

ÉCOLE DOCTORALE DES SCIENCES CHIMIQUES

Laboratoire de Bioimagerie et Pathologies – UMR 7021

THÈSE

Lucie HAYE

soutenue le : **15 décembre 2023**

pour obtenir le grade de : **Docteur de l'université de Strasbourg**

Discipline/ Spécialité : Chimie des polymères – Chimie des matériaux

Conception et caractérisation de nanoparticules polymériques luminescentes pour la bioimagerie et la biodétection

THÈSE dirigée par :

Dr. Andreas REISCH

Maître de conférences, Université de Strasbourg

RAPPORTEURS :

Pr. Rachel MEALLET

Professeure, Université de Paris Sud - Saclay

Dr. Fabienne GAUFFRE

Directrice de recherches, Université de Rennes

AUTRES MEMBRES DU JURY :

Dr. Delphine CHAN-SENG

Chargée de recherches, Université de Strasbourg

Pr. Sébastien LECOMMANDOUX

Professeur, Université de Bordeaux

A mon père,

Acknowledgements

Le travail présenté dans cette thèse est le résultat de 3 ans d'efforts, d'échecs et de réussites, qui n'aurait jamais pu aboutir sans l'aide et le soutien de diverses personnes.

Je tiens tout d'abord à remercier Andreas, pour m'avoir guidée tout au long de ma thèse. Cela a été un réel plaisir de travailler au quotidien avec toi. Tu m'as beaucoup appris scientifiquement, merci pour ton temps, tes explications et réponses à mes nombreuses questions. Mais tu m'as également beaucoup appris sur le plan humain et j'espère pouvoir mettre en œuvre tous ces enseignements dans ma vie professionnelle comme au-delà.

Un grand merci à tous les collaborateurs sur les différents projets, avec une mention particulière pour Niko Hildebrandt, Loïc Charbonnière et Xavier Le Guével pour leur aide et leurs conseils tout au long de cette thèse.

Je remercie également Andrey Klymchenko pour son accueil dans son équipe, sa bonne humeur, le partage de ses connaissances et sa grande maîtrise du barbecue. Je tiens à remercier tous les membres de l'équipe nanochimie et bioimagerie pour avoir participé à la bonne ambiance du laboratoire, leur soutien, ainsi que tous les échanges scientifiques, l'entraide, les gâteaux, les repas, les barbecues et les diverses activités que nous avons partagé. Un grand merci à Elisabete et Sophie, avec qui j'ai eu le plaisir de travailler mais qui sont rapidement passées de collègues à amies, avec qui j'ai toujours grand plaisir à réinventer le monde autour d'un verre de vin. Merci également à Caterina, avec qui il a été un plaisir de partager un bureau durant quelques mois, ainsi que de nombreux fous rires et photos d'Hélios. Une grosse pensée pour Antoine, avec qui j'ai partagé de nombreux souvenirs, à commencer par un bureau, puis l'aventure MiFoBio et enfin le voyage en Guadeloupe. Un grand merci à Deep, qui a été présent tout au long de ma thèse, pour ta gentillesse, ta créativité et ton excellente cuisine. Une autre personne présente tout au long de ma thèse a été Rémi, je te remercie car j'ai beaucoup appris avec toi et j'ai été heureuse d'être présente à ton mariage, et partager ce moment important de ta vie. Un grand merci à Carla pour ton soutien (d'autant plus marqué pendant ces derniers jours de rédaction !), ton amitié, ça a été un plaisir de te côtoyer au quotidien et je garde un très bon souvenir de notre escapade entre le Vercors et la Drôme. Merci à Lazare pour ces discussions passionnées de science, m'avoir transmis cette passion pour le Lakowicz et tout ce qu'il m'a appris. Un grand merci à Tanushree pour sa bonne humeur, le partage de sa culture et nos nombreux rires. Merci à Abdel pour sa gentillesse, ses conseils et son soutien tout au long de ma dernière année de thèse. Merci à Sonia pour sa bonne humeur, sa gentillesse et sa motivation pour nos activités labo, mais aussi à Nathan pour ses histoires étonnantes et farfelues aux poses café. Cela a été également un plaisir de partager le quotidien du labo avec Paraskevi, Valentine, Fei, Bohdan, Valeria, Pankaj et les différents stagiaires qui sont passés par notre équipe.

Je tiens à remercier également Clémentine et Cinthia qui sont l'exemple même que les voisins aussi peuvent devenir des vrais amis sur qui on peut compter. Un grand merci à Marine, Antoine et Thomas, mais aussi Nadège et Edouard pour leur amitié et leur soutien depuis toutes ces années. Un immense merci à Valentine pour tous ses encouragements, conseils et soutien durant toute ma thèse. Partager nos différentes expériences et émotions liées à nos thèses m'a énormément appris, motivée et renforcé notre amitié. Merci aux Chaud'Caen, May, Lanou, Sassou, Lolo, Max, Sim, Clem, Paulo, Bibi, Tho, Coincoin, vous qui êtes depuis l'école d'ingénieur comme une deuxième famille, pour votre amitié, votre soutien dans les meilleurs moments comme dans les pires, et les innombrables souvenirs tous ensemble.

Ma famille est et a toujours été très importante dans ma vie, elle façonné la personne que je suis et aidé à réaliser mes projets. Un merci tout particulier à mes grands-parents qui m'ont beaucoup appris, encouragée et soutenue depuis toujours. Un merci à Tomàs pour son soutien et sa bienveillance, ainsi qu'à ma sœur Cécile qui est là pour moi, malgré la distance. Un immense merci à ma mère pour son amour, pour tout ce qu'elle m'a appris, l'éducation qu'elle m'a donnée. Tu m'as toujours encouragée, motivée, tout fait pour m'aider, avec tes actions et tes paroles tu m'as donné les clés nécessaires pour réussir. Je n'aurais pas les mots suffisants pour remercier mon père, qui a et aura toujours une place primordiale dans ma vie. Toi qui m'as tout donné, toujours fait de mieux, a façonné la personne que je suis, m'a soutenue, donné le courage et la force d'aller au bout de ce projet malgré les obstacles. Tu as toujours cru en moi, m'a permis de prendre confiance en moi-même et bien plus encore, merci pour tout, je t'aime papa.

General Introduction

Luminescence based bioimaging and biosensing are attractive methods in the biomedical field, for both the study and diagnosis of living system. To enhance the signal detected and thus the imaging and sensing quality, a luminescent contrasting agent is frequently used. This addition to the biological systems studied enables to achieve a fast, highly specific and sensitive detection of biomarkers. It also permits to achieve bioimaging with a high spatio-temporal resolution. As fluorescent compounds can naturally be found complex biological systems, this generates autofluorescence. This parasitic signal creates a noise that degrades the detection ability which is measured with the signal-to-noise ratio (SNR). The design probes focus on increasing their brightness in order to improve the SNR. However, it is still a challenge to reach a SNR sufficient for efficient luminescence imaging and sensing in complex biological media. Indeed, applications such as deep tissue imaging or specific biomarker detection in biological fluids cannot be achieved with a sensitivity and resolution satisfactory enough to be applied in medicine.

Alternative luminescence modes have been identified and can be explored to develop autofluorescence free bioimaging and sensing. First, there is a great interest to shift into spectral region with low autofluorescence, like the Shortwave Infrared region (SWIR, 900 – 1700 nm), commonly designated as the biological window. In this wavelength range, biological tissues absorption is reduced, enabling a deeper penetration of light and a reduction of the scattering from the probe signal. Another strategy is the use of up converting emitters, that will absorb photons of low energy to emit a single photon from higher energy. Up-conversion (UC) does not occur in biological systems, ensuring a background free detection of the probe signal. Last, time-gated (TG) detection of light record the signal of long-lifetime emitting probes while discarding the autofluorescence, enhancing thus the signal-to-noise ratio. However, the number of contrasting agents displaying at least one of these features is restricted. Their brightness is usually lower than “classical” emitters in the visible region and dimer when introduced in aqueous media. Furthermore, the nature of these probes is usually very different from the components of biological systems and induce a low biocompatibility. Thus, the development of efficient emitters for SWIR, UC or TG applications in complex biological media is a challenge.

To overcome these problems, we propose to decouple the brightness properties from the surface properties of luminophores by encapsulating them in polymeric nanoparticles. Indeed, polymeric based materials are of high interest in the development of luminescent nanoprobes, offering a high tunability, biocompatibility and targeting ability. We use the nanoprecipitation technique, to synthesize polymeric nanoparticles loaded with different metallic based luminophores in order to create bright and biocompatible nanoprobes. The different projects presented are realized in collaboration with other research laboratories. Loïc Charbonnière (IPHC, Strasbourg) and his team developed transition-metal and lanthanides-based complexes for applications in respectively in TG and UC. Xavier Le Guével (IAB, Grenoble) synthesized and

characterized SWIR gold nanoclusters and worked on the phantom model and *in vivo* imaging. Niko Hildebrandt and his team realized some photophysical characterizations and cellular imaging. Laurent Cognet and his student tested the ability of probes for single-particle tracking in the SWIR.

During this thesis, first the encapsulation of rhenium-based complexes with or without organic dyes was investigated for application in time-gated imaging. The characterization with different physico-chemical and photophysical analysis enabled to understand the PL mechanisms undergoing inside the polymeric nanoparticle and extract information about the internal luminophore organization. In a second time, this encapsulation process was aimed to enable the transfer of molecular up-conversion properties of a nona-nuclear lanthanide complex from organic solvent to aqueous media. After characterization of the obtained nanohybrid, their potential for autofluorescence free bioimaging was assessed *in cellulo*. Eventually, new SWIR contrasting agents were developed by trapping luminescent gold nanoclusters into polymeric nanoparticles. A thorough physico-chemical characterization confirmed the quantitative encapsulation in the polymer matrix and photophysical characterization revealed their great brightness. Furthermore, experiments first in phantom models and then *in vivo* confirmed their ability to be used as contrasting agents for blood vessel imaging. At last, the study of their brightness at the single particle level with super-localization microscopy showed that these nanoprobe are promising contrasting agents for single-particle tracking.

Together, these studies enable to enlighten the possibilities that offers the combination of metallic-based luminophores and polymeric nanoparticles in the development of contrasting agents for bioimaging and sensing.

Table of Content

Acknowledgements	I
General Introduction	V
Table of Content	IX
Acronyms and Abbreviations.....	XIII
CHAPTER I: State of the art.....	1
1. Luminescence based Bioimaging and Biosensing	1
1.1 Creation of contrast	3
1.2 Characterization of the contrast	4
1.3 Challenges for luminescent probes.....	8
2. Alternative luminescent modes	11
2.1 Shortwave Infrared.....	11
2.2 Up Conversion	13
2.3 Time Gating	15
2.4 General Problems and Challenges	18
3. Polymeric Nanoparticles and Encapsulation	19
3.1 PNPs preparation from monomers	19
3.2 PNPs preparation from polymers.....	22
3.3 Encapsulation of metallo-based compounds.....	25
3.4 Biocompatibility	27
4. Objectives and Approaches	28
Materials and Methods	32
1. Polymer Synthesis	32
1.1 Polymer Index	32
1.2 Free Radical Polymerization	33
1.3 RAFT Polymerization	34
1.4 Block Copolymer	36
2. Nanoparticles Preparation and Characterization	37
2.1 PNPs Synthesis	37
2.2 Size Determination.....	38
2.3 Further characterization	42
3. Spectroscopic Characterization	44

3.1	Instrumentation	44
3.2	Quantum Yields	46
3.3	FRET.....	47
3.4	Fluorescence Correlation Spectroscopy (FCS).....	48
CHAPTER II:	Co-encapsulation of organic dyes and metallic complexes for TG Imaging	50
1.	Rhenium Loaded PNPs	51
1.1	Synthesis and characterization of Re complexes	51
1.2	Synthesis and characterization of NPs loaded with Re complexes	52
1.3	Spectroscopic Characterization.....	54
1.4	Time-Resolved Characterization	56
2.	Co-encapsulation of Re complexes and cyanine dyes	56
2.1	PNPs Formation and Steady State Spectroscopy	57
2.2	Time Resolved Spectroscopy.....	59
2.3	In vitro Application.....	64
3.	Conclusion	66
CHAPTER III:	Molecular Up-conversion within PNPs for Live-Cell Imaging	68
1.	Formulation and optimization.....	69
2.	PNPs Characterization	72
2.1	Transition to deuterated media	72
2.2	Spectroscopic Characterization.....	74
3.	Cellular Imaging.....	78
4.	Conclusion	80
CHAPTER IV:	Gold Nanoclusters loaded PNPs for SWIR Imaging	82
1.	AuNC encapsulation	83
2.	Photophysical Characterization	85
2.1	Steady State	86
2.2	Time Resolved	89
3.	Brightness evaluation for <i>in vivo</i> applications.....	91
3.1	Blood Vessel Imaging	92
3.2	Single Particle Tracking.....	93
4.	Biointerfacing	98
4.1	Immunotoxicity	98
4.2	Toward surface protection and <i>in vivo</i> imaging	100

5. Conclusion	103
General Conclusion.....	107
References	111
Annexes	132
1. Polymer Characterization	132
2. Co-encapsulation of organic dyes and metallic complexes for TG Imaging	136
2.1 Rhenium Loaded PNPs	136
2.2 Co-encapsulation of rhenium complex and cyanine dyes	145
3. Molecular Up-conversion within PNPs for Live-Cell Imaging	151
3.1 Formulation and optimisation	151
3.2 Characterization in deuterated media	156
3.3 Imaging.....	159
4. Gold Nanoclusters loaded PNPs for SWIR Imaging	160
4.1 AuNCs encapsulation	160
4.2 Photophysical characterizations	161
4.3 Brightness evaluation for <i>in vivo</i> applications	164
4.4 Biointerfacing	166
Résumé de thèse	171
1. Introduction.....	171
2. Nanoparticules pour l'imagerie résolue dans le temps	172
3. Nanoparticules pour l'imagerie en conversion ascendante.....	174
4. Nanoparticules pour l'imagerie dans le proche infrarouge	177
5. Conclusion générale	179

Acronyms and Abbreviations

ACQ: Aggregation Caused Quenching	PNP: Polymeric Nanoparticle
AIBN: Azobisisobutyronitrile	QD: Quantum Dot
AuNC: Gold Nanocluster	QY: Quantum Yield
ATRP: Atom Transfer Radical Polymerization	RAFT: Reversible Addition-Fragmentation chain-Transfer
BBB: Brain Blood Barrier	RDRP: Reversible-Deactivation Radical Polymerization
BSA: Bovine Serum Albumin	ROP: Ring-Opening polymerization
CD: Carbon Dot	ROS: Reactive Oxygen Species
CMC: Critical Micelle Concentration	RT: Room Temperature
CTA: Chain Transfer Agent	SNR: Signal to Noise Ratio
DLS: Dynamic Light Scattering	SPT: Single Particle Tracking
DP: Degree of Polymerization	SWCNT: Single-Walled Carbon Nanotubes
EDL: Electrical Double Layer	SWIR: Shortwave Infrared
EGFP: Enhanced Green Fluorescent Protein	TG: Time Gating
EtOH: Ethanol	UC: Up Conversion
F6-TPB: Tetrakis(3,5-bis(trifluoromethyl)phenyl)borate)	ZP: Zeta Potential
FBS: Fetal Bovine Serum	
FRET: Förster Resonance Energy Transfer	
FRP: Free Radical Polymerization	
GFP: Green Fluorescent Protein	
Ln: Lanthanide	
LOD: Limit of Detection	
LPS: Lipopolysaccharide	
MLCT: Metal-to-Ligand Charge Transfer	
NIR: Near InfraRed	
NMP: Nitroxide-Mediated Polymerization	
NP: Nanoparticle	
PBS: Phosphate Buffer Serum	
PDT: Photo-Dynamic Therapy	
PEG: Poly(ethylene glycol)	
PEMA: Poly(ethyl methacrylate)	
PL: Photoluminescence	
PLGA: Poly(lactic-co-glycolic acid)	

CHAPTER I: State of the art

Photoluminescence (PL) is widely used in the biomedical field, from fundamental research where it enables to reveal biological structures and processes, to point of care assays for diagnosis. This interest rises partially from the possibility to do bioimaging and sensing at different scales, going from the whole animal to the single emitter. Moreover, PL based analysis can be achieved rapidly with high specificity and sensitivity. All these features are keys to reach both high spatial and temporal resolution required for the study of the complex biological systems.

To develop further this technic efficiency and the range of applications associated, the design of adapted tools is crucial. Indeed, an efficient PL bioimaging or sensing detection relies generally on the introduction of a luminescent probe. Therefore, the design, synthesis and optimization of contrasting agents is crucial to meet the different requirements for imaging and sensing in living systems. First, these luminescent compounds need to be easily detectable, *i.e.* bright, to ensure a high sensitivity, and enable high spatio-temporal resolution. For applications in complex biological systems such as deep tissue imaging or biosensing in blood, a very high signal from the probe is required and is still challenging to achieve.

Furthermore, a probe should be tunable, to be adapted for different applications. For the detection and/or quantification of an object of interest, the probe has to be specific, meaning able to recognize a given target with a high preference over the rest of the system. The nature and composition of the studied biological system can vary a lot, going from the whole animal, to a tissue, a cell or a biological fluid so the probe design is to be adapted to ensure an efficient contrast in every case. Furthermore, as it is destined to be used in complex biological systems an essential feature of the probe is to be biocompatible, meaning that it should be able to be in contact with a living system without producing an adverse effect.¹ Moreover, a good stability and the absence of non-specific interactions with the biological system are necessary to optimize its performance. Before designing and synthesizing a probe, a good comprehension of the luminescence phenomenon and the parameters that create and characterize a contrast is required.

1. Luminescence based Bioimaging and Biosensing

Luminescence encompasses a group of phenomena in which matter emits light after an electronic or vibrational excitation. The notion of “cold light” has been introduced by Fortunio Liceti² to describe this kind of emission and is to be opposed to incandescence, where light is originated by heating. Various types of luminescence can be found in nature, sparking the interest of scientists, with for example the first reported observation of fluorescence, in 1565 by Nicolás Monardes (1602 for phosphorescence).³ During the 19th century, these two phenomena were studied and characterized by different scientists, leading Eilhard Wiedemann to introduce the term of luminescence.⁴ Nowadays, due to the discovery of

numerous types of luminescence such as radioluminescence, electroluminescence or chemiluminescence. Fluorescence and phosphorescence have been regrouped under the sub-category of photoluminescence.

PL is a process of light emission by a substance after absorption of photons. This absorption is triggered by irradiation of the substance with a light having photons from the same energy than the gap, e.g., between the singlet ground state S_0 and an excited state, *i.e.* a state of higher energy (excitation). This leads to the rapid transfer (10^{-15} s) of an electron from S_0 to the first S_1 or second S_2 excited state (Figure 1). In the ground state, electrons are paired with opposite spin and it is to be noted that during the absorption, the spin of the excited electron remains unchanged when going into the singlet state, thus conserving the pairing with the electron in the ground state. Once in the excited state, the energy can be redispersed in different ways.

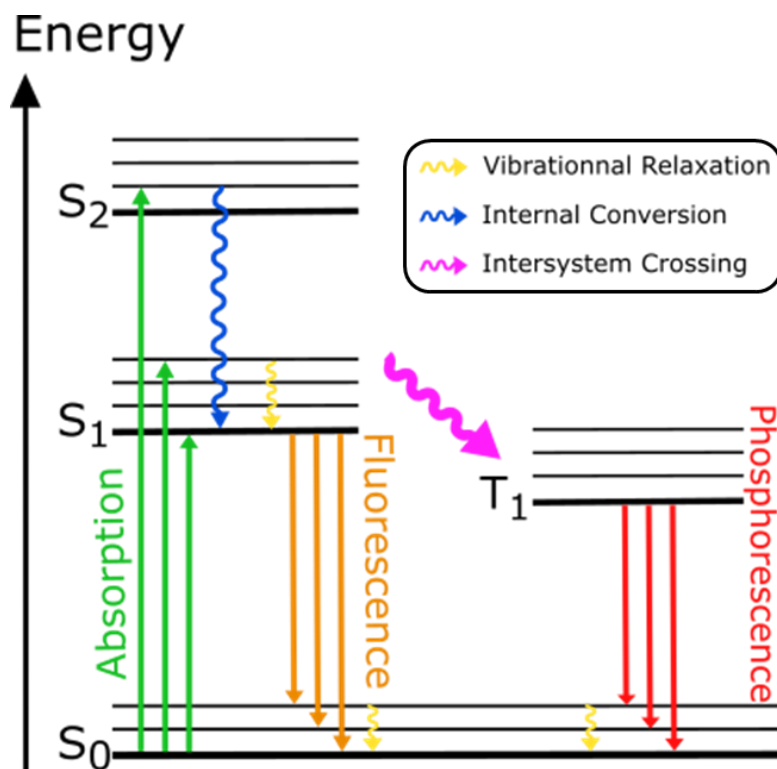


Figure 1: Adapted Perrin-Jablonski diagram

Vibrational Relaxation: Each electronic state is composed of several vibrational state. The electron in the excited state undergoes a fast non radiative relaxation (10^{-12} to 10^{-10} s) to the lowest vibrational level of the state. When the S_1 and S_2 states are close in energy an internal conversion can be observed.

Fluorescence: From the lowest vibrational level of an excited state, the electron can go back to the ground state by liberating energy (10^{-10} to 10^{-7} s), this phenomenon being called a radiative decay. As some of the energy has been lost through non radiative processes, the

energy of the emitted photon is generally lower than the one of the absorbed photons, which translates physically by a wavelength of emission longer than the excitation source.

This displacement is called Stokes shift, in reference to Georges Stokes who described first the phenomenon in 1852⁵ and introduced the term of florescence one year later.

Intersystem crossing: This radiationless transition can be observed between two electronic states with different spin multiplicity. On the contrary of the $S_0 \rightarrow S_1$ transition, this process occurs between the excited singlet state and the triplet state T_1 and implies a change of spin of the excited electron, provoking the loss of the pairing with the electron in the ground state. This transition is observed on timescale close to those of fluorescence (10^{-10} to 10^{-8} s) but has low probability to occur as it is “forbidden”.

Phosphorescence: Once the electron in the T_1 , the observation of the radiative decay of the electron to the ground state is possible. However, non-radiative de-excitation processes also exist, such as triplet-triplet annihilation or internal conversion. All these transitions require a new change of the electron spin to be paired again with the other ground electron and thus occur on relatively long timescales (10^{-10} to 1s).

Various systems, *e.g.* single molecules, nanoparticles (NPs) or films, are capable of emitting light through PL, we will take a particular interest in those under the form of single emitter that will be designated in this work as luminophores. An important point to keep in mind is that numerous luminophores don't exhibit only one of the processes described above, but rather an accumulation of the different processes weighted on their probability of occurrence.

1.1 Creation of contrast

A luminescent probe for bioimaging and sensing must meet different requirements to be efficient. It is important to understand the context in which the probe is used, and all the parameters attached to it to be able to optimize it. For an image or a test to reveal interesting information, the goal is to create a contrast between the object of interest and the rest of the system. A contrast is by definition the difference in luminance or color that makes an object distinguishable from its environment. Identifying the parameters that makes this contrast possible is crucial to understand the different challenges to overcome in order to create efficient luminescent probes.

In bioimaging and sensing, under illumination the probe will emit a **flux of photons** that will be harnessed by a device (camera, detector...), resulting in a signal. The probe being introduced in a complex environment, other unwanted signals from different nature (light, vibrations, electronic...) exist and are designed as **background**. These parasite signal may also be recorded by the device, thus creating a **noise**. The **signal to noise ratio** (SNR) is a quantitative tool used in microscopy and more generally in different types of imaging to estimate the efficiency of a probe to distinguish itself from its environment. It directly

compares the amount of signal and noise recorded. For that, the background that the device receives is recorded in the absence of the probe and used to create a threshold that discriminates the noise from the object of interest. Improvement of the SNR can be achieved either by enhancing the signal from the probe or reducing the one from the background. An important parameter determining the amount of signal emitted by a probe is the **brightness**. The brightness of a probe corresponds to the number of photons per time unit that a probe emits upon excitation with a given light intensity. In this work, we express the brightness as:

$$B = \varepsilon * QY \quad (1)$$

With ε the extinction coefficient and QY the **quantum yield** of the emissive entity. The extinction coefficient represents the capacity of a luminophore to absorb photons at a given wavelength.

When a luminophore absorbs light, the energy stored can be dispersed in radiative or non-radiative pathways (Figure 1). The QY is the efficiency of a luminophore to re-emit the photons that it absorbs, *i.e.* follow a radiative pathway. Calculation of the QY can be achieved either by absolute or relative methods and during this work I used the latter (described in §3.2 Quantum Yields). The process of luminescence is not instantaneous and occurs over a more or less long amount of time depending on the luminophore. Indeed, before emitting a photon, the luminophore spend some time in the excited state. The **fluorescence lifetime** is the average value of time spent in the excited state.^{6,7} This time is characterized by one or several exponential decays depending on the radiative pathways followed by the probe.

1.2 Characterization of the contrast

Differentiating an object from its environment is not an easy task and a qualitative assessment of the probes used is necessary to ensure its reliability. Sensitivity and specificity are notions largely used in bioimaging and biosensing to evaluate the efficiency of luminescent probes, however, both notions have different definitions. To try a clear explanation of these notions, we will consider the case of a luminescent probe designed to target a given protein only expressed by cancer cells. When imaging, the objective is to be able to differentiate cells that have the proteins (sick) from the one that don't (healthy) and to see where the protein is in the cell.

Statistical definitions:⁸

Here, some statistical notions have to be defined:

- True positive: Cells that have the protein and are detected
- False positive: Cells that don't have the protein but are detected
- False negative: Cells that have the protein but aren't detected
- True negative: Cells that don't have the protein and aren't detected

The **statistical sensitivity (S_{Se})** is the ability to detect the specimens with the object of interest in a population. In the chosen example, we want to be able to see how many cells in a given sample are sick. It is mathematically defined as:

$$SSe = \frac{\text{Number of TP}}{\text{Number of TP} + \text{Number of FN}} \quad (2)$$

With TP = True positive and FN = False negative (Figure 2)

The **statistical specificity (SSp)** is the ability to correctly identify an object as being not the one of interest. For our case, we want to be sure the “undetected” cells are healthy, otherwise a treatment based on that analysis would fail to correctly eliminate all sick cells. It is mathematically defined as:

$$SSp = \frac{\text{Number of TN}}{\text{Number of TN} + \text{Number of FP}} \quad (3)$$

With TN = True negative and FP = False positive

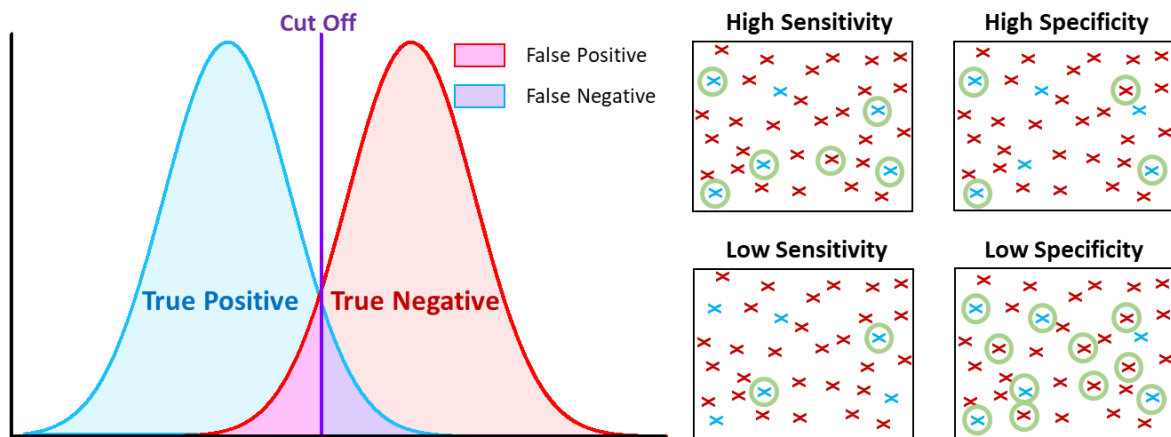


Figure 2: Left: Schematic representation of the statistical notions. Right: Example of high/low sensitivity and specificity in a sample

Analytical definitions:⁹

The **analytical sensitivity** is the ability to detect a low concentration of an object of interest in a biological sample. A synonym usually used is the **limit of detection (LOD)**, a threshold below which the signal detected is considered as noise. It depends on a probe brightness, but also the noise of the sample and the detection capability of the device. In our case, the probe has to be able to detect very small amount of the protein of interest in the middle of all the constituent of the cell, to make the identification of sick cells easier.

The **analytical specificity** is the ability to exclusively identify a targeted substance among similar ones. The probe from our example should only bind with the protein of interest, to avoid mistaking a healthy cell for a sick cell.

Every notion described above have to be taken into account when designing and evaluating the quality of a luminescent probe, for they each participate to enhance the veracity of the final result.

Once the quality of a probe assessed, its use in bioimaging will generate signals, which are then translated into a picture of the region of interest. A notion to estimate the quality of a picture is the **spatial resolution**, which is defined as the minimum distance separation

between two objects, such as they can still be distinguished. This characteristic can depend on the probe used, through its brightness, but is also associated to the imaging device. Abbe established in 1873 that the minimum resolvable distance d for optical imaging is a function of the wavelength of the incident light:¹⁰

$$d = \frac{\lambda}{2n \sin \theta} \quad (4)$$

With λ the wavelength of the light, n the refractive index and θ the half-angle of convergence to the spot of the light. For blue light, this diffraction limit is around 200 nm. For biological imaging this implies that structures such as cells (10 to 100 μm) or bacteria (1 μm) can be resolved but smaller ones such as viruses (100 nm) or proteins (10 nm) fall under this limit. The relatively recent development of super-resolution imaging enables to cross this diffraction limit, lowering the limit of spatial resolution for light based imaging to a few tens of nanometers.¹¹ On 2D imaging, spatial resolution is defined on two axis, x and y , but for 3D imaging takes also into account the depth axis (z) and the spatial resolution of an imaging technique can differ depending on the axis studied. This resolution is also limited by the device abilities, as the final picture is divided in pixels. In Figure 3A, the quality of the picture from a pine needle degrades, when the number of pixels diminishes, losing first the ability to see the smaller cells (in green), then the bigger one, before eventually not being able to recognize the object.

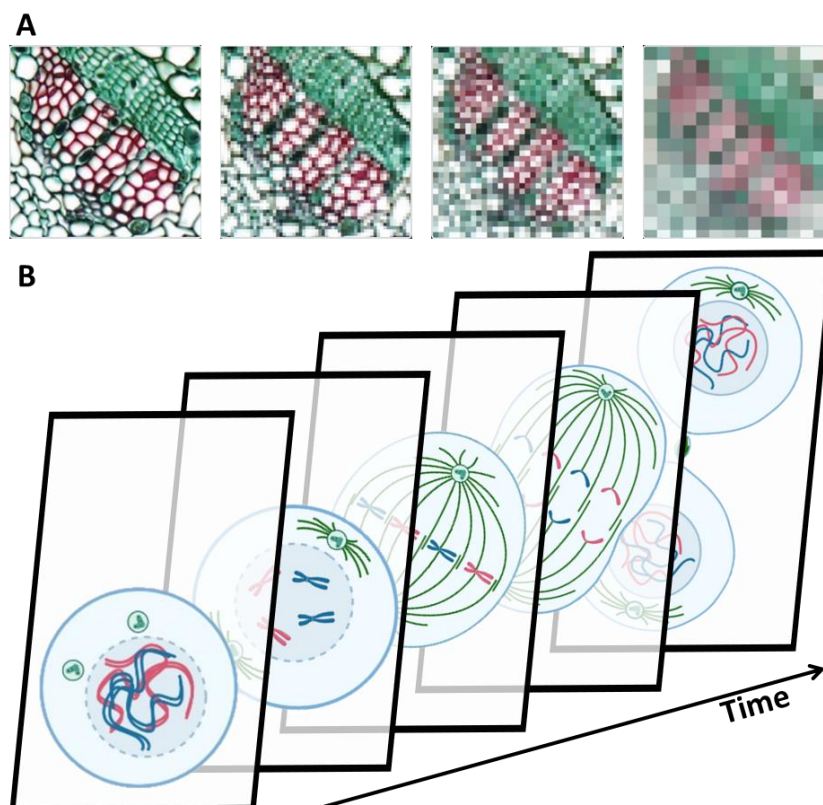


Figure 3: Illustrations of resolution: A) Loss of spatial resolution due to the number of pixel (pictures from <https://www.microscopyu.com>) B) Frames of a cell taken at different moments enlightening the process of cell division

Resolving objects on the nanometer scale enables to extract various structural and organizational information but leave out an important parameter: time. Biological processes

imply changes or movements that occur on different time scales and their study often requires the acquisition of several pictures of the same object over time. The **temporal resolution** is defined as the precision of a measurement with respect to time. In imaging, an ensemble of pictures (frames) of the same area in a sample will be taken at known intervals of time to obtain a film that recount the evolution of the system (Figure 3). The choice of the time between the frames will depend on the timescale of the studied process and the probe should be tuned accordingly. Indeed, the flux of photon during the acquisition period should be high enough to ensure an easy differentiation from the background. In the meantime, the probe has to be stable enough to emit on a timescale larger than the studied process to capture it entirely. Eventually, the camera used for recording has a minimal time between which it is capable to take two frames that has to be taken into account.

Finding a good balance between spatial and temporal resolution is important to apprehend at best what we observe. In this idea, single-particle tracking (SPT) can reveal various information about a biological system. The development of single molecule microscopy enabled to detect luminescent probes on the single object scale with sizes down to a few tens of nanometers and follow them over time.

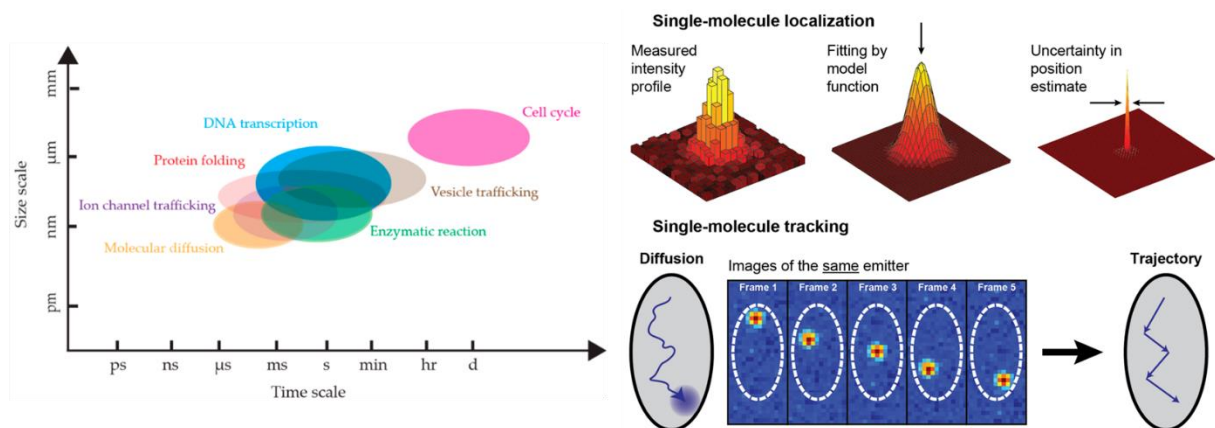


Figure 4: Spatio-temporal scale of different biological processes (left)¹² and Illustration of probe localization and tracking (right)¹³

Probes are usually detected under the form of large spots due to diffraction limit, so their precise position is defined by fitting their intensity profile with two or three Gaussian functions and is called point-spread function (PSF). This first step of the SPT technic, called super localization, gives a high spatial resolution to the probe. Then in a second step called linking, different localizations of the probe are connected frame by frame, thus modeling the probe's trajectory and giving time resolution.¹⁴ The resolution of a probe is directly proportional to the number of photons emitted, as it enhance the precision of the position of the probe in its environment.¹⁵ The high spatial resolution of SPT shows for example probe distribution in the biological system, from which the structural organization can be extracted. Time resolution informs about dynamic parameters such as the velocity or viscosity of the system, the combination of all these information revealing the system evolution over time.

1.3 Challenges for luminescent probes

The race to produce brighter probes is still going on with a wide range of materials that has been developed over the years. Luminescent requirements to be efficient bioimaging probes are conditioned by the devices used for their detection and the environment they are introduced in. First, a major limitation is the fluorescent emission displayed by biological media in the visible range (400 to 700 nm), like the “classical” emitters presented above. Indeed, proteins, NAD(P)H, fatty acids, vitamin A, flavins or porphyrins present in complex biological systems have been identified as fluorescent emitters in the visible region.¹⁶ This autofluorescence of biological systems creates a background for bioimaging and thus a brightness competition between the media and the probes. This is why the design of probes focuses a lot on their brightness, to enhance the SNR and eventually get a better spatial resolution. Furthermore, the constituents of tissues, skin or fat also absorb the light of this spectral window, limiting greatly the penetration depth and thus the possibility to do deep tissue imaging.

Among the luminescent probes, a widely developed and used category are fluorescent molecules,¹⁷ designated usually as fluorescent dyes. These small organic molecules are based on several motifs such as rhodamines, cyanines, BODIPYs or fluoresceins¹⁸ that have been chemically modified over time to extend their properties. An efficient fluorescent molecule has extinction coefficient values around $10^5 \text{ M}^{-1}\text{cm}^{-1}$ and QY close to the unity. Their high tunability enables to modify their spectral properties and photostability making them sensitive to their environment. Modification of dyes is also used to target specific functions.

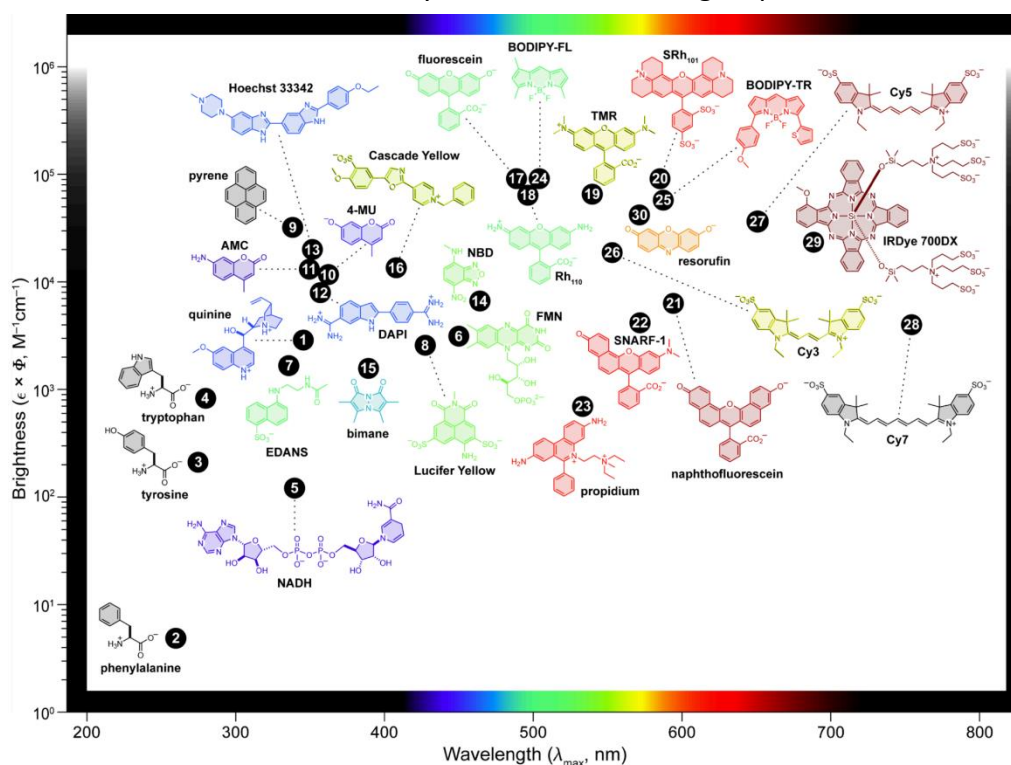


Figure 5: Brightness versus maximum absorption wavelength of different fluorescent dyes¹⁷

However, the small Stokes shift and low photostability of organic dyes are limiting for bioimaging and sensing applications. Indeed, organic molecules have a tendency to bleach, *i.e.* to irreversibly turn off after a certain time of exposition to a light source. Furthermore, because of they emit in the visible region where tissues have a high absorbance coefficient, they are not suited for application such as deep tissue imaging.

Bigger organic structures such as proteins or peptides are used as probes for bioimaging applications. Their fluorescence comes from fluorophores formed naturally inside the protein structure. In nature fluorescent proteins can be found, the first and most known one being probably the Green Fluorescent Protein (GFP), where the fluorophore is formed thanks to a favorable conformation. After that, a large palette of fluorescent proteins have been identified and/or engineered, with spectral properties covering the entire visible region.¹⁹ Entities can be genetically modified to express the protein gene, creating specific labelled objects with high targeting abilities within a large range of size, going from protein, organelles or cells up to whole organism.²⁰ As not all proteins are luminescent, methods have been developed to couple a protein of interest with a fluorescent dye, expanding the range of tools available for protein based bioimaging and biosensing applications.²¹ Eventually, peptides are short amino acid based chain (molecular weight under 10 kDa) possessing high specificity and tissue penetrability. As proteins they can be fluorescent naturally or after dye coupling, and gained interest from scientists for biological applications.^{22,23} However, the quantity of proteins present in a sample depends on their expression, which can be low and inhomogeneous. As organic molecules, their range of emission is mostly restricted to the visible region, suffering from limited depth penetration and high background noise due to autofluorescence.

Another large family of luminescent probes are nanoparticles. Quantum dots (QDs) are inorganic semi-conducting NPs composed of a small number of atoms and a reference in the field of PL bioimaging and biosensing. This structure, intermediate to the molecule and the bulk material, creates quantum confinement (Figure 6), *i.e.* a limited number of energy levels, on the contrary to bulk which has valence and conduction bands.²⁴ As the number of atoms govern both the size of the NP and the band-gap energy, size and color of QDs are intrinsically linked (Figure 6). Photophysical properties of QDs are highly tunable, by modifying their size, alloy composition or by doping with other elements. However, small spherical shaped emitters such as QDs have a high surface to volume ratio, so any defect can reduce drastically their PL intensity and stability. Furthermore, bare QDs suffer from low solubility in aqueous media and are toxic for the body. Different strategies have been developed to chemically modify their surface, in order to increase their water solubility or targeting abilities.²⁵

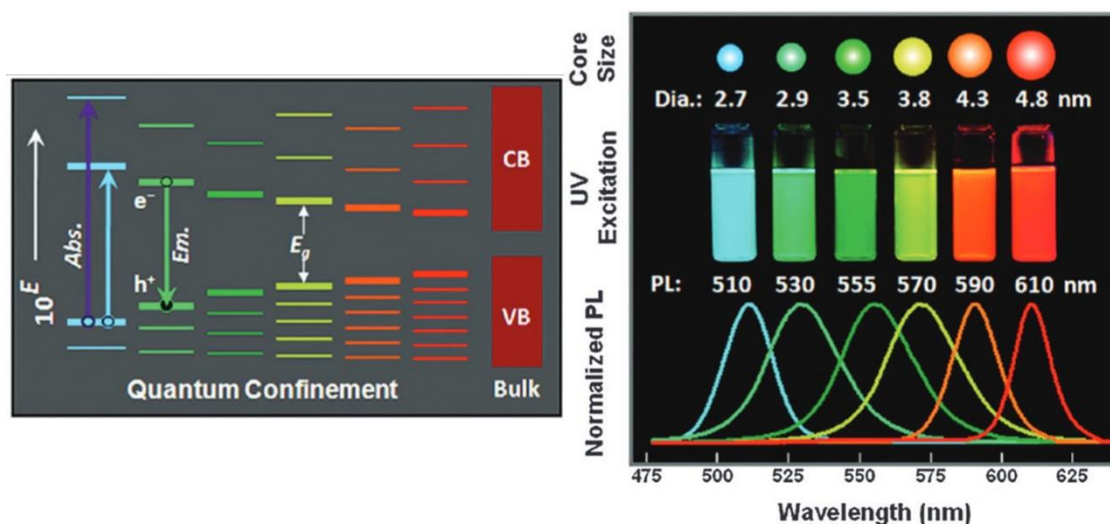


Figure 6: Schematic representation of quantum confinement in QDs (left) and the associated optical properties²⁶

Carbon based materials are an emerging category of luminescent probes. Carbon dots (CDs), often compared to QDs for their similar luminescent mode, exist under various shapes and are looked up for their high quantum yield, photostability or biocompatibility.²⁷ These features associated to their small size (1 to 10 nm usually) makes them good candidates to overcome high challenges such as crossing the Brain-Blood Barrier (BBB) in bioimaging. Moreover, their encapsulation ability and surface tunability expand the range of application to drug delivery.²⁸ As QDs, defects can drastically reduce the PL abilities of the probes. Other types of carbon based materials have been developed such as fullerene, carbon nanotubes or graphene, each presenting interesting properties for biological imaging.²⁹ Among them a strong interest has been taken into Single-Walled Carbon Nanotubes (SWCNT). These materials can be assimilated to a graphene layer rolled up in a 1D tube, with a diameter close to 1 nm and a length up to the μm range.³⁰ The chirality of the SWCNT tunes its optical and photophysical properties from which various application for sensing and imaging have been developed.³¹ These materials being insoluble in water, a functionalization or coating is required to be used as biosensors. This functionalization, but also the nanotube dimensions will determine the cytotoxicity of the final probe.

If toxicity can be intrinsic to the probe, it can also come from the imaging setup itself. As these probes exhibit mostly a fluorescent emission in the visible region, powerful UV/Visible excitation sources are necessary for them to emit. However biological samples are also sensitive to light, generating toxicity which is susceptible to degrade the studied sample.

Eventually, a probes design will also be adapted to its application and one may prioritize some features above others. Often, improvement of spatial resolution will imply diminution of temporal resolution and vice versa: exposing a probe to a powerful excitation source may increase the final signal but also lead to faster bleaching. In SPT, as the signal is recorded from single emitters, they have to be very bright to ensure the collection of enough photons to detect it.

Altogether, the probes described above have been developed and optimized for bioimaging and sensing through intense enhancement of their brightness to stand out of the autofluorescence background. However, the final SNR is not always sufficient for imaging and sensing in complex biological media, limiting the possible applications in “real-life” medicine. A complementary strategy to the increase of brightness to improve the SNR is the reduction of the background. For these, the exploration of alternative luminescent modes is to be conducted.

2. Alternative luminescent modes

As aforementioned, a lot of molecules naturally present in the body generate autofluorescence and the background created from it diminishes the final imaging resolution and thus its possible exploitation. However, light can be emitted following different pathways, that have been theorized and later proved experimentally. First, downshifting is a process characterized by the absorption of a photon followed by the emission of a photon of lower energy and its efficiency is characterized by the QY which can go up to 100 % (the totality of the absorbed photons is re-emitted). This is the most common and known process where you can find for example the fluorescence. This must be differentiated from downconversion, where a photon, usually with a high energy, is absorbed and more than one photon of lower energy is re-emitted. This process, also called photon cascade emission or quantum cutting, enable to get photons with a lower energy than excitation with a QY that can be above 100 % and can be achieved following different mechanism.³² On the contrary, Up Conversion (UC) is a process where multiple photons are absorbed by a compound and the resulting emitted photon has a higher energy than the incident photon. As autofluorescence follows a classic downshifting emission, it can be greatly reduced by developing probes using different luminescent processes that are not common in biological media.

2.1 Shortwave Infrared

A strategy to overcome autofluorescence while using a downshifting PL is to shift the window of observation toward longer wavelengths. Shortwave InfraRed (SWIR), also called NIR-II, is a spectral region between 900 and 1700 nm often depicted as the optimal window for *in vivo* fluorescence imaging. SWIR is divided between NIR-IIa (1000-1400 nm) and NIR-IIb (1500-1700 nm), which corresponds to the two regions where tissues have a very low absorption (Figure 7A). Nowadays, a strong interest is growing for SWIR imaging, more particularly since the development of InGaAs camera³³ that enables a better detection of the light emitted in the SWIR (Figure 7B).

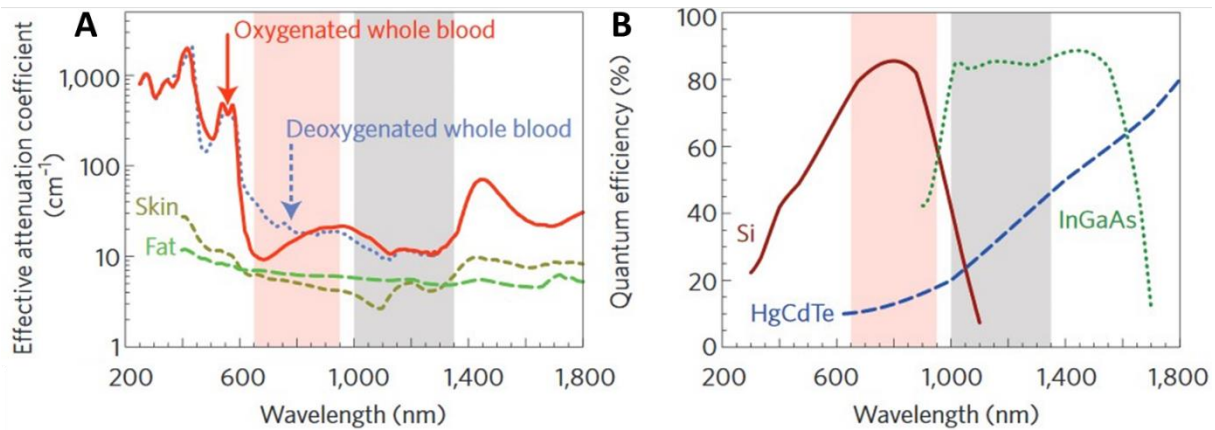


Figure 7: A) Absorption coefficient of different tissues B) Efficiency of detection of different cameras. Red region: NIR I; Grey region NIR II-a³³

The low ability of tissues to absorb SWIR light has multiple advantages for an efficient imaging: the autofluorescence is very reduced and the incident light can penetrate deeper into tissues, increasing greatly the spatial resolution in the z axis. The emitted light will also be less scattered, improving again the resolution.³⁴ Moreover, the power source used for this imaging is less energetic than classical UV-Vis emitting lasers, diminishing the phototoxicity and bleaching. It was recently shown that an additional NIR illumination on classical fluorescent imaging can slow down the photobleaching of EGFP and reduce the global cytotoxicity.³⁵

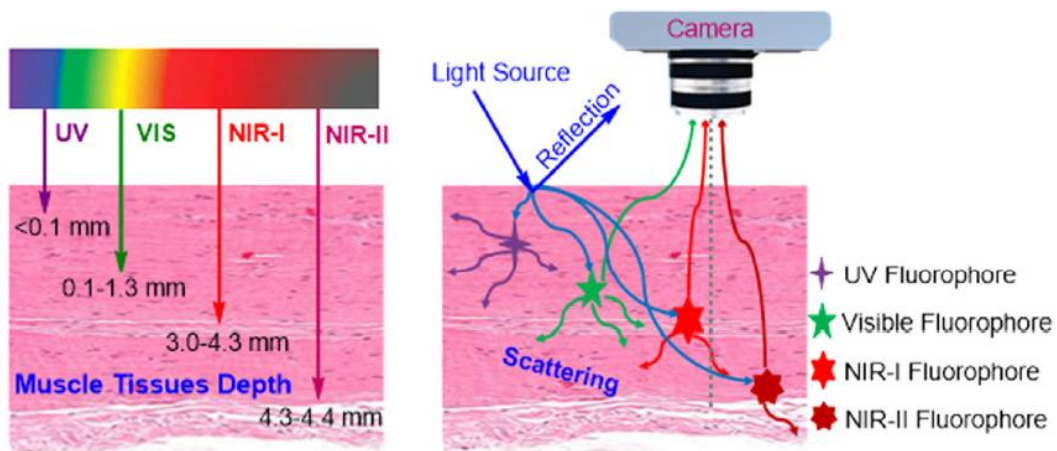


Figure 8: Illustration of NIR II light tissue penetration (left) and the advantages (right)³⁴

One of the challenges in improving SWIR imaging is to develop bright contrasting agents for this region. Fluorescent dyes that have their emission properties tuned toward the SWIR region, suffer from a low brightness compared to visible region³⁶. Indeed, in Figure 9, the fluorophores described have brightness up to $10^3 \text{ M}^{-1}\text{cm}^{-1}$ which is two to three orders of magnitude smaller than the fluorophores shown in Figure 5, and it is due to the low QY and coefficient absorption. Moreover, most of the photophysical data were recorded in organic solvents, showing the difficulty to obtain results in aqueous media.

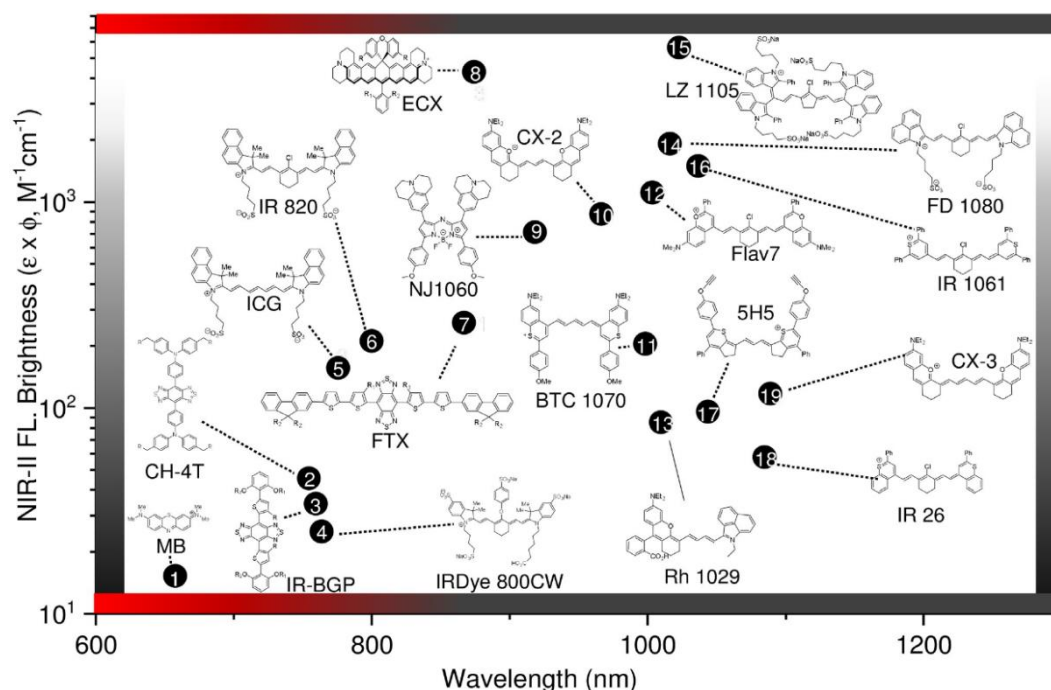


Figure 9: PL brightness of fluorophore emitters in SWIR depending on their absorption maxima³⁶

In consequence, SWIR emitters with various nature are being developed, such as gold nanoclusters (AuNCs),^{37,38} but also different types of luminescent nanoparticles (NPs), notably lanthanide based NPs³⁹ and QDs.⁴⁰ SWCNTs have also been described as efficient probes for SWIR bioimaging and sensing.³⁰ Recently, dye nanoassembly⁴¹ or conjugated polymer based NPs emitting in NIR-II have been described with an emission up to 1400 nm.^{42–44} Eventually, the few examples of organic NIR-II dyes encapsulated in polymers resulted in rather large objects (> 100 nm).^{45–47}

2.2 Up Conversion

Another strategy to develop a background free imaging is to use probes with an Up Conversion based PL. Indeed, this phenomenon, manifested physically by an Anti-Stokes process (Figure 10), *i.e.* a wavelength of emission inferior to the wavelength of excitation, is not encountered in biological system. Various UC process have been identified and can be separated into two categories: the non-linear process such as two photon absorption excitation or second harmonic generation, and the process with successive absorption of photon. The latter was proposed by Bloembergen in 1959⁴⁸ and demonstrated during the next decade by different scientist. Different mechanisms can lead to this phenomenon⁴⁹ and can be generalized as seen in Figure 10. Briefly, upon excitation a first photon is absorbed, populating the first excited state L^* which has a relatively high stability. This feature enables the absorption of a second photon, populating a higher excited state L^{**} . Eventually, the photon emitted from the L^{**} excited state has a higher energy than the absorbed one. The relative stability over time of the first excited state is a key parameter to ensure UC rather than downshifting emission.

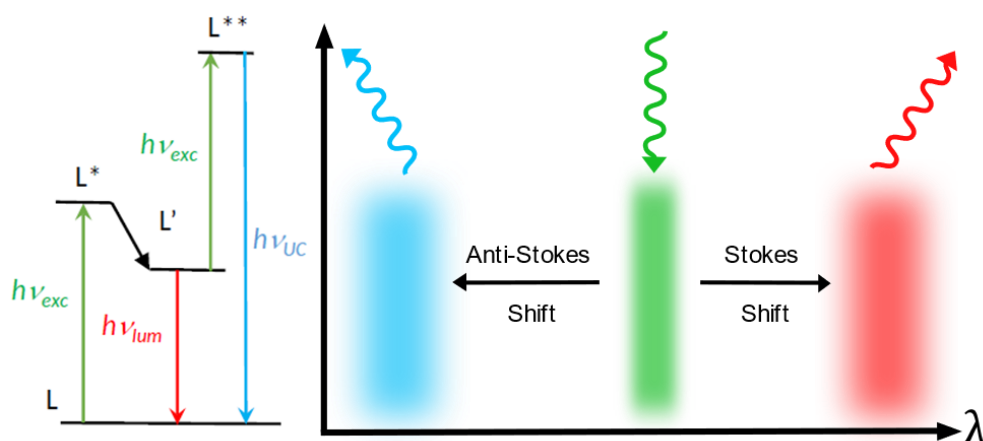


Figure 10: Scheme of general Up Conversion process (left)⁴⁹ and implication on the wavelength of emission (right)

Lanthanides (Ln) have unique luminescent properties due to their electronic structure. Indeed, the f electrons of Ln^{3+} ions are protected from their chemical environment by the electrons from the 5s and 5p subshells, the forbidden f-f electronic transitions electrons give the lanthanides stable excited states and generate an abundant number of ladder-like energy levels⁵⁰ that can be climbed upon sufficient excitation.⁵¹ This, associated with multiple active energy level translates into narrow emission bands, which are very characteristic for each Ln (Figure 11). Moreover, their forbidden transition ensures long lifetime of the excited state, a crucial feature to promote UC radiative pathway and thus, make Ln particularly suited for the development of UC emitting probes. Moreover, they can exhibit PL features under different forms such as metallic complex, inorganic nanoparticles or crystals. To this day, these unique properties make the lanthanides the most used materials for UC applications. In particular, inorganic nanoparticles (NPs) based on a crystalline lattice (e.g. NaYF_4) into which lanthanide ions are doped both as sensitizers (e.g. Yb 10 – 20%) and as activators (e.g. Er ~2%) have been optimized and are currently leveraged for various applications.^{52–54} With this wide development, numerous bioimaging applications emerged over the years.⁵⁵

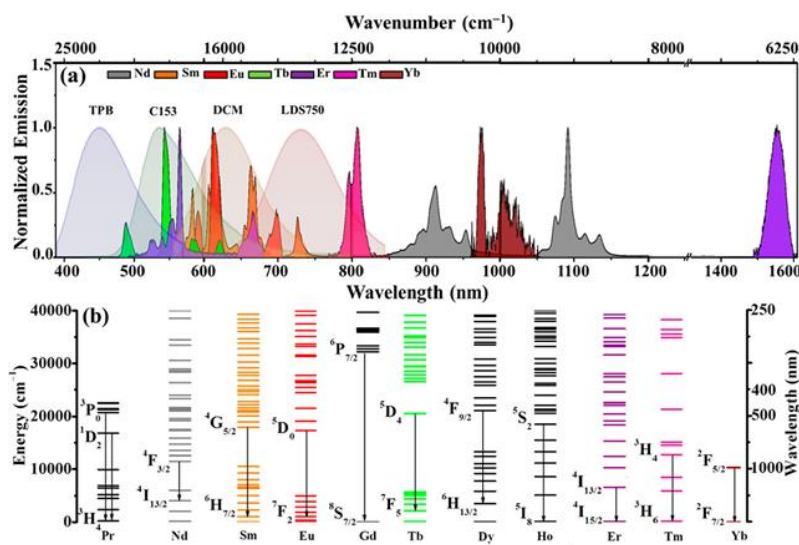


Figure 11: Ln emission spectra with their most emissive electronic transition

If UC has been widely described in solids or inside NPs, its observation at the molecular level is more recent. One of the challenges to observe molecular UC⁵⁶ in solution is to minimize the non-radiative deactivation processes in order to achieve long excited state lifetimes. Indeed, a molecule in solution can easily transfer its energy to the solvent and thus is more prompt to energy loss than when inside a solid, so limiting the interactions between the UC emitter and the solvent is crucial. In literature, molecular UC is mostly described mostly in organic solvent.^{57,58} The non-radiative rate constant in a medium increase exponentially with the associated vibrational energy, which is very high in the case of water. As a result, molecular UC is difficult to transpose to aqueous media and thus to adapt to imaging and sensing in biological systems, with only a few examples described in deuterated or protic water.^{49,59,60} Nonetheless, the entrapment of up converter into polymeric micelles recently reported offered a beginning of solution to this challenge.^{61,62}

2.3 Time Gating

Fluorescence imaging usually relies upon the brightness of the luminescent probes used in contrast to the autofluorescence of the biological media and uses continuous-wave (CW) excitation to ensures these probes are re-excited directly after emitting. However, depending on probes properties, different fluorescent lifetimes are observed. Organic molecules, proteins and other components of the biological system have short (few ns) fluorescence lifetimes, but other compounds have lifetimes in the μs or ms range (Figure 11). This feature offers the possibility to add a time dimension into the development of bioimaging techniques with suppression of the autofluorescence.

Time-gating (TG) uses pulsed excitation to generate luminescence, associated with probes having long lifetimes (μs or ms scale usually). To segregate their signal from autofluorescence, the acquisition of the signal is delayed from the excitation, once the autofluorescence signal faded (Figure 12). This excitation-delay-acquisition process is repeated to record a high number of pictures from the same area, the time between two pulses being adapted to record enough signal from the probes while keeping the total acquisition time relatively short. The superposition of these frames enables to enhance the SNR.

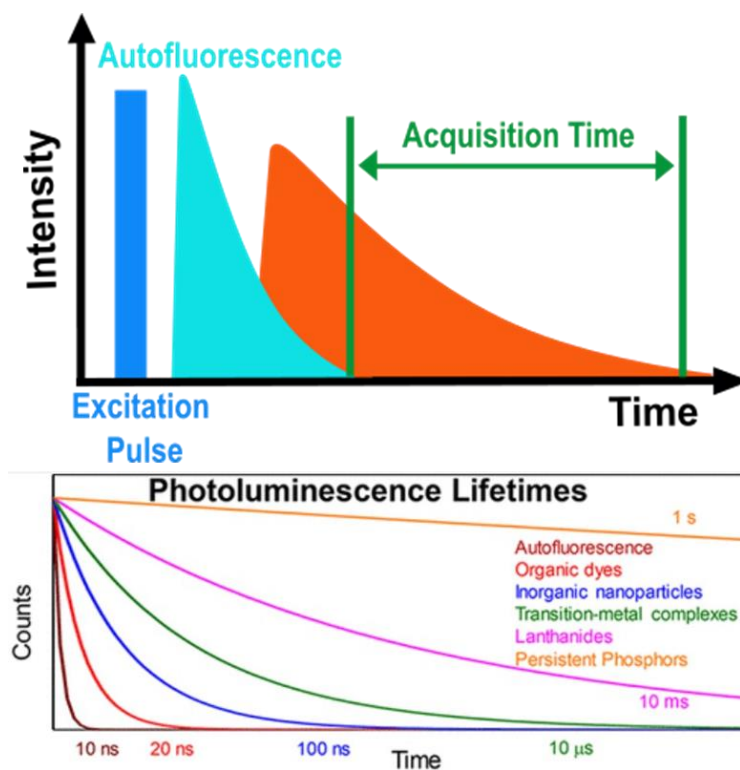


Figure 12: and Principle of Time-Gated Imaging (top) and PL Lifetime for different types of emitters (bottom)⁶³

As organic dyes have lifetimes in the same range as bio-molecules, they are not suitable for TG imaging and developing adapted probes implies the use of other materials. Metals, such as transition metals or lanthanides have shown long lifetime properties (Figure 12), going up to the ms scale and making them solid candidates for developing TG probes.^{63,64} In particular, transition metal complex such as Rhenium, Ruthenium or Iridium are interesting probes for their luminescence can be initiated from different electronic transition such as ligand centered, metal centered or metal-to-ligand charge transfer (MLCT). The design of probe can be adapted By modifying the metal or the number and nature of ligands, PL properties such as the wavelength of emission but also the PL lifetime. Moreover, the PL of these probes is very sensitive to their environment, which makes them well suited for sensing applications. Indeed, metal complexes based probes have been reported for sensing ions, reactive oxygen species (ROS), enzymes or thiols.⁶⁵ They can be tuned to do specific targeting, owing them applications in the field for anti-cancer therapy.⁶⁶

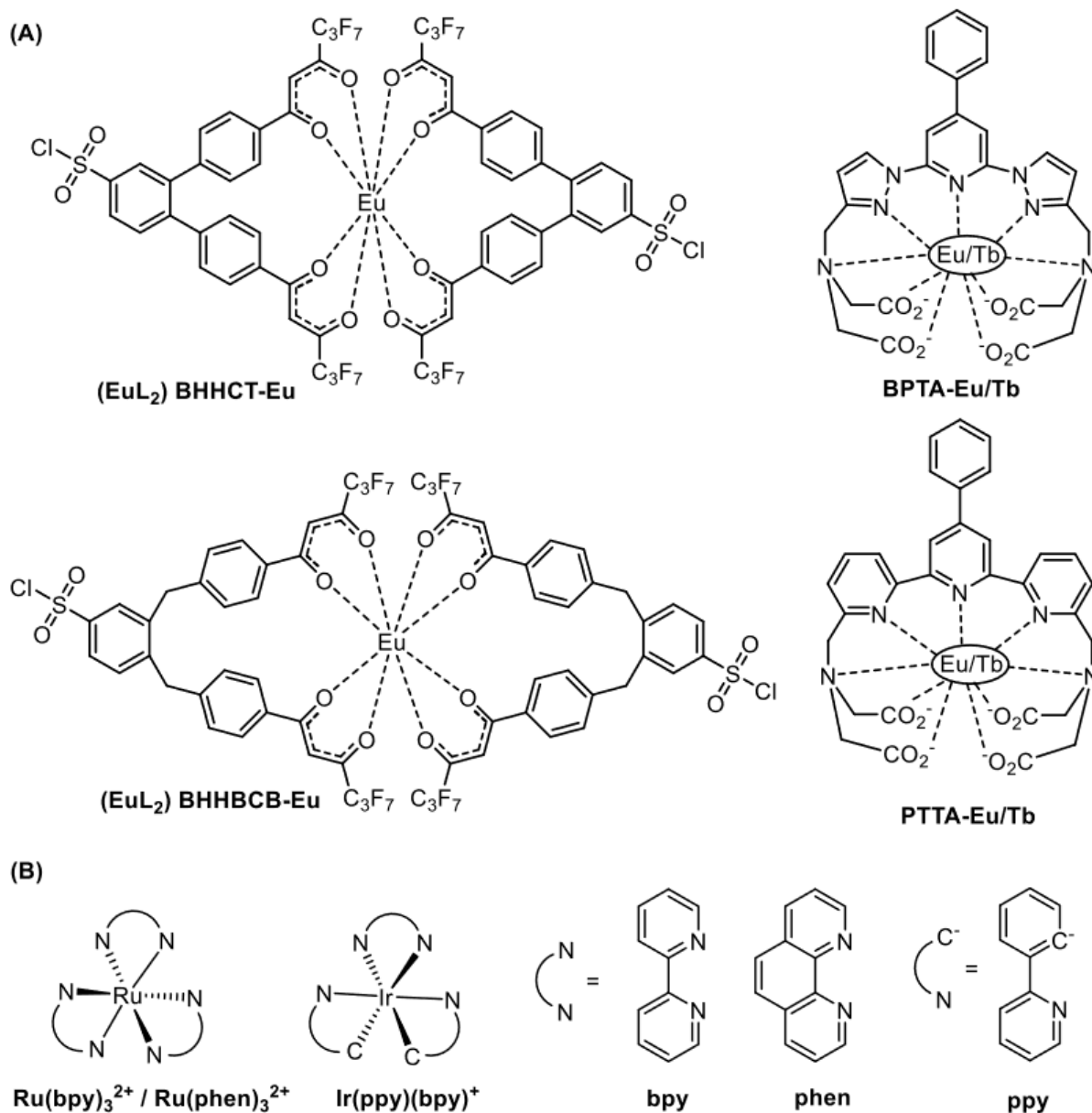


Figure 13: Examples of probes for TG bioimaging and sensing using A) lanthanides or B) transition metals⁶⁴

Moreover, a luminophore lifetime can be composed of different decay time, each corresponding to a de-excitation pathway. As a de-excitation pathway can be privileged over another under given condition, the probe's lifetime variation will depend on its environment and this property can be exploited for sensing applications. Förster resonance energy transfer (FRET) phenomenon is extensively used in bioimaging for its PL properties are very sensitive to environment changes. A wide range of sensitive probes in TG imaging have been developed taking advantage of both FRET associated lifetimes and low autofluorescence background.⁶⁷

2.4 General Problems and Challenges

As attractive as these luminescence modes are, creating probes that exhibit this kind of features is not an easy task. Among the luminescent probes described earlier, only a limited number can be tuned to display at least one of these photophysical properties. Furthermore, the same luminophore can undergo various processes of de-excitation, radiative or not and thus, an adapted design of the probe is required to favor the chosen path of radiative emission. Indeed, an efficient contrasting agent requires a high brightness in the mode of emission chosen (SWIR, UC or TG), associated with a good photostability. Another key requirement is the water solubility and stability to ensure the continuity of the desired PL properties in complex biological systems. Eventually, the biocompatibility of the probe is necessary for applications like deep tissue bioimaging or molecular sensing in biological fluids. The existing contrasting agents generally lack some of these requirements to be applied in complex biological environments.

For example, SWIR emitting probes have generally a low QY, with values up to a few percent at best. Indeed, the low energy of the radiative transition is close to vibrational transitions, causing a high energy loss through non-radiative processes. This phenomenon, associated with low to moderate extinction coefficients, results in a restricted brightness of the final probe.

In the case of upconversion, the probability of de-excitation through downshifting stays high despite the stability of the excited state. For achieving optimal UC efficiency in inorganic Ln NPs, a doping level must be found that maximizes absorbance while minimizing concentration quenching, that leads to decreasing upconversion efficiency.⁶⁸ This implies a precise tuning of the organization and local environment of the Ln emitters, however such control is difficult to achieve with the current doping strategies. Molecular UC emitters suffer currently from two major limitations: firstly, the low absorption cross section of lanthanide ions strongly limits the brightness of systems containing less than ten lanthanide ions. Furthermore, vibronic overtones of first and second sphere OH, NH, and CH oscillators, in particular H₂O, leads to enhanced quenching in such small molecular entities, strongly limiting their transposition to aqueous media.

The principal TG emitters, lanthanides, have very low coefficient absorption so they require a powerful excitation source that can be toxic for the media. In response to that problem, lanthanide ions are associated with ligands that can be excited and then transfer their energy to the metallic center to emit. This also induces a limited brightness, which translates to a reduced photon flux. However, this limitation, due to the forbidden energy transitions, are the same generating the long lifetimes properties. Thus, one can't enhance the brightness of the probe by excluding this de-excitation pathway and must find a balance between the two features.

Another challenge to overcome in the development of probes with these alternative luminescent modes is their adaptability to complex biological media. Indeed, most of the luminophores see their photophysical features greatly diminished when transferred from organic solvent to aqueous media, questioning the possibility to use them in biological media. Thus, this water quenching has to be reduced by shielding the luminophore from water molecules. This, associated to a low biocompatibility, means that the probe must be modified to be inserted in an unharmed way inside the biological system. Furthermore, the design of the probe should avoid non-specific interactions with the constituents of the system, while guaranteeing its targeting abilities.

Due to these limitations, the emerging luminescent emitters for SWIR, UC or TG applications are often metal based, with a precise atomic organization. As they are, per nature, very different from the constituents of complex biological media, their use and transposition for bioimaging and biosensing can be challenging, so improving their brightness and biocompatibility is necessary. The approach we chose to resolve this issue is to try to decouple brightness and surface properties of our probes by encapsulating bright emitters into polymeric nanoparticles (PNPs). This approach has the double benefit of shielding the emitters from the aqueous media to preserve their luminescent properties and in the meantime regroup a high number of emitters in a small volume to create very bright nano-objects. In this case we consider that the brightness is proportional to the number of luminophores N encapsulated:

$$B = N * \epsilon * QY \quad (5)$$

This strategy requires to form PNPs with adapted size and surface properties, while ensuring a good encapsulation of the luminophores.

3. Polymeric Nanoparticles and Encapsulation

Polymer-based NPs were first reported at the end of the 1970's as promising nanocarriers for anti-cancer drug delivery.⁶⁹ Since then, a large range of PNPs have been reported for application of drug delivery or contrasting agent, with increasing performances in sensitivity, specificity as well as biocompatibility. The nature and structure of the polymer used will induce the final properties of the PNPs and can be tuned to answer specific problems. In our case, the polymer chemistry is a tool to modulate the size and surface properties of the PNPs as well as ensuring the encapsulation of high amount of luminophores. Furthermore, it will be used to optimize the stability and biocompatibility of the final colloidal suspension in complex biological systems. Different methods have been developed to synthesize PNPs and will be overviewed in the following.

3.1 PNPs preparation from monomers

Monomers are the starting material for the synthesis of polymers and can also be at the origin of the PNPs formation. These methods imply a polymerization reaction and the conditions to conduct it will dictate the PNPs final features.

3.1.a) Emulsion polymerization

A first way to prepare PNPs from monomers is conventional emulsion polymerization. Monomers with low water solubility are dispersed in an aqueous solution with surfactants in concentration above the critical micelle concentration (CMC). As a result, surfactants assemble into micelles (10 nm) containing a few monomers and the majority of monomers forms droplets (around 10 μm diameter) stabilized by surfactants. The introduction of a water-soluble initiator in the system leads to the generation of radicals that can travel through the continuous phase and be absorbed and desorbed in the micelles or droplets. The polymerization process occurs into micelles, because they have a larger surface to volume ratio so radicals are more likely to be captured in it. The FRP (see Free Radical Polymerization for mechanism details) starts with the particle nucleation, *i.e.* the addition of the radical on a monomer, creating a polymer chain, followed by the particle growth with the addition of multiple monomers. The droplets are considered to be reservoirs as they contain the majority of monomers, they supply monomers to the particle-swollen micelles through the aqueous phase, enabling the particle growth up to their disappearance. This process eventually gives polymeric PNPs with sizes between 50 and 500 nm, intermediate of those of micelles and droplets. Encapsulation of cargo (luminophore, drugs...) inside these PNPs can be achieved during the NP formation with the cargo in the organic phase of the emulsion.⁷⁰ However, this implies that the cargo must diffuse through the aqueous phase from the droplets to the micelles and can lead to inhomogeneous distribution of cargo inside the PNPs.

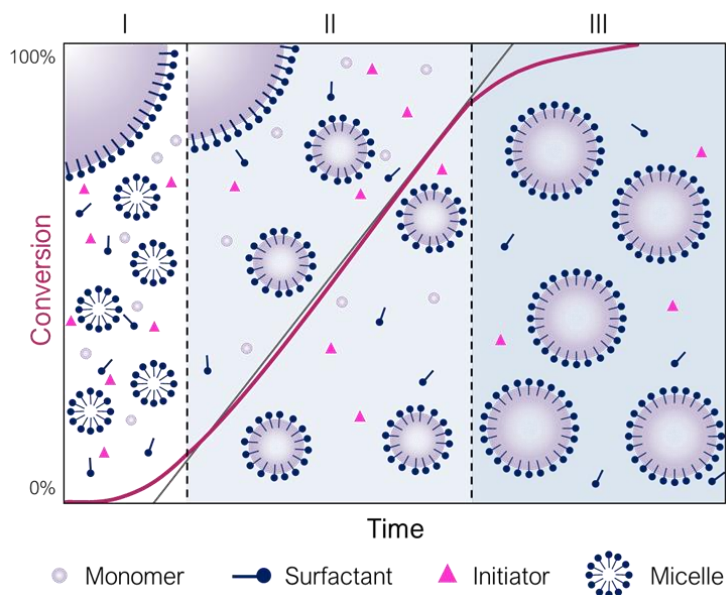


Figure 14: Scheme of emulsion polymerization steps

Other types of emulsion polymerization exist, like the mini emulsion polymerization that uses surfactants with the concentration usually under the CMC. In this case, droplets are generated by applying shear forces such as rapid stirring or sonication and have smaller sizes, below 0.5 μm . They are stabilized by the surfactants, helping the prevention of micelles formation and thus becoming the polymerization reactors. This process doesn't require monomer

transportation into the aqueous phase, which can be an issue for non-water-soluble monomers and the synthesized PNPs are smaller, 30 to 200 nm, compared to conventional emulsion polymerization.⁷¹ Micro-emulsion is another way to synthesize smaller PNPs (5-50 nm) using this time a huge amount of surfactants. Indeed, in this case the monomer represents only 5 to 10 wt%, leading to the formation of thermodynamically stable emulsion where the polymerization can occur.⁷² These variations of the emulsion polymerization are better suited for cargo encapsulation as they are directly trapped inside the forming nanoparticle.

3.1.b) PISA

Polymerization-induced self-assembly (PISA) is a process, where the growth of a polymer chain on a previously prepared polymer leads to a spontaneous organization of the obtained material. This method is based on reversible-deactivation radical polymerization (RDRP), where a first polymer block is synthesized using a chain transfer agent (CTA).⁷³ Once this macro-CTA formed, a second block with monomers of a different nature, with low solubility in the solvent of reaction, is grown on the first one. When the second block reaches a certain size (*i.e* a critical degree of polymerization (DP), Figure 15) the overall polymer becomes insoluble in the reaction media and self-assemble. This method avoids the use of molecular surfactant like in emulsion polymerization, reducing the problem of purification of the final product.

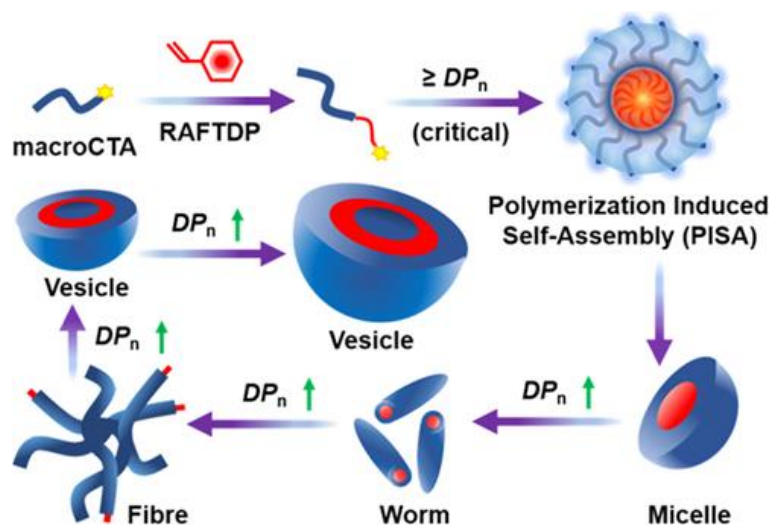


Figure 15: Different self-assembly architectures enabled by PISA⁷⁴

PISA can be performed using different polymerization techniques such as nitroxide-mediated polymerization (NMP), atom transfer radical polymerization (ATRP) or ring-opening polymerization (ROP)⁷⁵, but most of the time the RAFT technique is preferred. Different shapes of nano-objects can be obtained upon PISA method such as PNPs, micelles, worms, fibers or vesicles (Figure 15) and the shape can be determined by the DP but also by external triggers such as the temperature.⁷⁶ This method enables also the encapsulation of different cargo of interest such as biomolecules, where different approach can be used to ensure an efficient encapsulation.⁷⁷ However, the encapsulation of inorganic materials can be more difficult.

3.2 PNPs preparation from polymers

Forming PNPs starting from monomers has drawbacks such as the need to eliminate the unreacted monomers or surfactants used for the polymerization. This purification steps linked to the polymer formation after the PNPs synthesis can be bypassed by preparing the PNPs with already synthesized polymers. Furthermore, the encapsulation ability of such methods is limited and can be improved when using pre-formed polymers.

3.2.a) Polymer Self Assembly

Under certain conditions, amphiphilic copolymers can spontaneously self-assemble into nano-objects, which can be polymeric micelles or polymersomes. Micelles are constituted of a hydrophobic core surrounded by a hydrophilic shell, whereas polymersomes are vesicles constituted of a hydrophobic membrane (Figure 16). The self-assembly occurs when the system reaches the critical micelle concentration (CMC), typically forming a thermodynamic equilibrium.⁷⁸ A modification of the system may thus disrupt the created equilibrium, making the self-assembly reversible. For example, in the case of micelles, a dilution over a threshold CMC will induce the dissociation of the nano-objects. This process is observed for polymer having two (or more) blocks with different properties and various intrinsic parameters of the polymer can be used to tune the polymersome properties.⁷⁹ Indeed, the chemical nature, volume fraction or molar mass of the two blocks but also the overall architecture of the polymer will influence the final characteristics of the polymeric nano-object. The polymer chemistry enables also to tune the membrane properties such as the thickness, permeability or functionalization. Furthermore, the environment of the polymer, like the polymer concentration, type of solvent, pH or ionic strength can be used to tune the polymersomes properties. For some applications, the disruption of the system has to be avoided, so the polymersomes can be modified by cross-linking of the polymer to fix the structure.

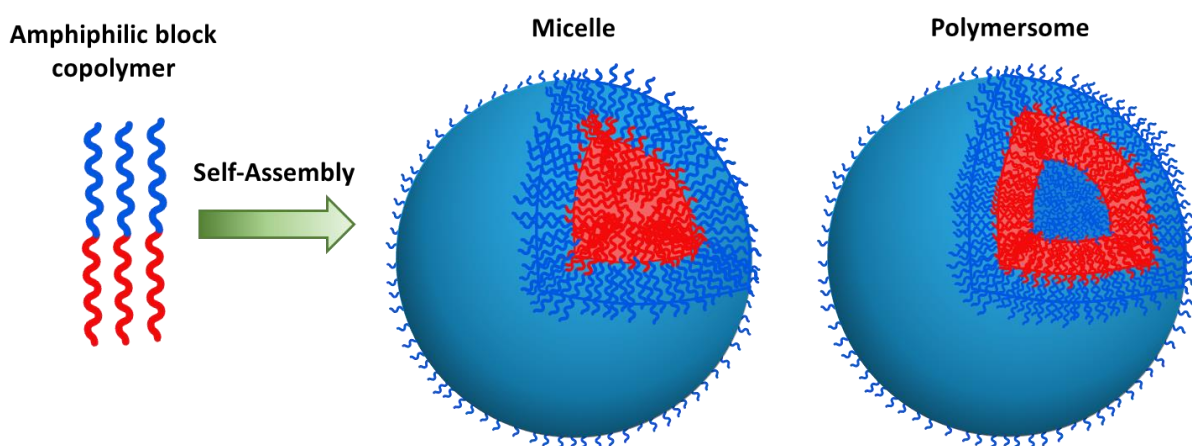


Figure 16: Scheme of Micelle and Polymersome organization. The hydrophilic and hydrophobic parts of the polymer are respectively blue and red

The described polymer nanocarriers are attractive material for cargo encapsulation and delivery in biological systems, thus various studies have been achieved to characterize their

stability, loading capacity and release ability.^{80,81} Through this method, the loading various cargo has been achieved, such as drug,⁸² proteins,⁸³ or quantum dots.⁸⁴

3.2.b) Emulsification evaporation

The assembly of polymers into NPs can also be achieved following the emulsification evaporation method.^{85,86} Here, the polymer and the cargo to encapsulate are dissolved in an organic phase non miscible with water and put with an aqueous phase containing stabilizers. First the solution is emulsified using either sonication or high-pressure homogenizer to form an o/w emulsion. This process enables to obtain nano-sized droplets of organic phase containing both the polymer and the cargo, which stability is ensured by the stabilizers. It is to be noted that the size of the droplets is directly linked to the final size of the NPs, so the size can be tuned by playing with the different parameters (organic to water ratio, polymer concentration, energy and method of emulsification...) involved in this step. Then the organic solvent is evaporated to provoke the aggregation of the polymer chains inside the droplets and thus form the NPs. Eventually, a purification step is added where NPs are centrifuged and washed several times to remove the stabilizers.

This method enables to have a good control over the concentration of the encapsulated cargo but can be applied only for lipophilic cargo. A hydrophilic cargo can be encapsulated following a variation of this method, the double emulsion evaporation. Briefly, a w/o emulsion is made to trap the hydrophilic cargo in an organic phase, which is then emulsified to obtain a w/o/w emulsion. However, this variation is more tedious to put in place with generally a lower encapsulation efficiency.

3.2.c) Nanoprecipitation

A technique often compared to emulsification-solvent evaporation for the synthesis of NPs for medical application is nanoprecipitation. Also called solvent displacement, this method is based on the Ouzo effect⁸⁷, phenomenon eponymous from the Greek equivalent of Pastis. In this alcoholic beverage, the addition of an excess of water provokes the precipitation of the aromatic compounds which gives the cloudy aspect of the turbid solution. This phenomenon can be represented on a ternary diagram (Figure 17). Here, the red line shows the transition between the initial system, a polymer (solute) diluted in a solvent, that is mixed with a high fraction of non-solvent (usually water). When the mixture composition is in the Ouzo region, which is part of the metastable region, the spontaneous self-assembly in PNPs occurs. To apply this process, both polymer and load are dissolved in a water miscible solvent, here acetonitrile, and the resulting solution is added to an aqueous phase. Mixing and inter-diffusion of the organic and aqueous phase leads to a mixture, in which the polymer and the load are not soluble anymore, creating supersaturation, which is in turn the driving force for particle formation. Because particle formation in this case is a kinetically controlled process, it allows trapping of the load. Once formed the PNPs are a colloidal suspension stabilized by the charges or hydrophobic groups present at the surface. On the contrary to micelles, upon dilution in an aqueous media there is no CMC below which the particle will dissolved to return under the

form of single polymer chains. This method of preparation is straightforward, fast and doesn't require the use of surfactants, making the purification steps easier. Furthermore, a scale up of the production is possible with the use of microfluidics.⁸⁸

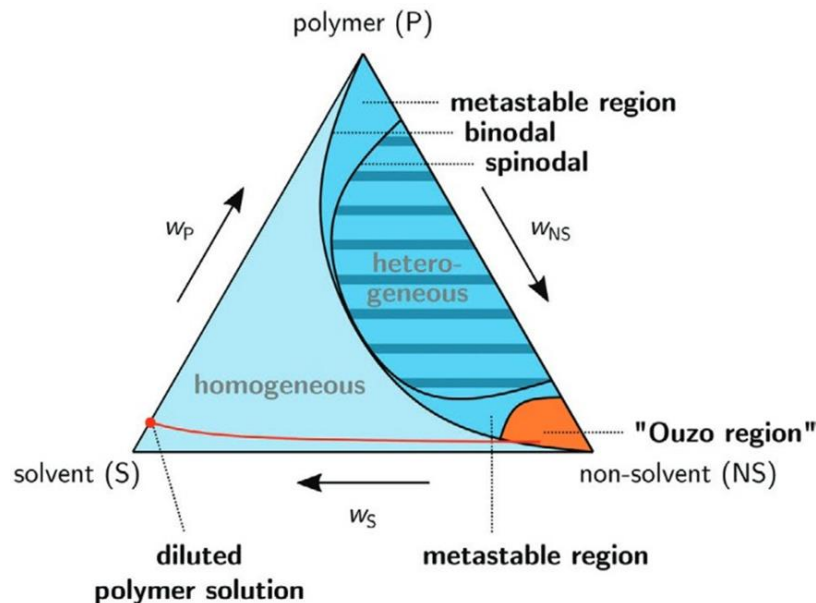


Figure 17: Ternary Diagram of polymer/solvent/non-solvent mixture⁸⁹

A wide range of parameters play a role in the formation of the PNPs and will influence their final physico-chemical properties. Indeed, the choice of solvents for the organic phase, through its water miscibility,⁹⁰ viscosity, or concentration^{87,91,92} will modify the size of the PNPs formed. For the aqueous phase, the presence or not of salt but also the pH of the solution can favor or not the formation of PNPs and modify their size.⁹³ The mixing conditions can also influence the PNPs formation: the particles can be prepared by hand or with different kind of microfluidics mixers, and optimized condition can lead to the obtention of smaller PNPs with narrower size distribution.^{94,88} In the case of encapsulation of cargo, the PNPs formation can be modified, either in a beneficial or detrimental way. The loading can impact the PNPs size and formation^{87,95} and a proper encapsulation will require a sufficient hydrophobicity^{96,97} from the cargo.

Apart from the assembly conditions, the nature of the polymer can be used to optimize encapsulation and modify the organization of cargo inside PNPs.⁹⁵ The polymer used must have a minimum hydrophobicity to self-assemble, and this characteristic can be used to tune the PNPs size.⁹⁸ The self-assembly of amphiphilic block copolymer can also be achieved and enable to create PNPs with peculiar hydrophilic/ hydrophobic phase arrangement.⁹⁹ Positive or negative charges can be added in the polymer structure, an increasing amount having a tendency to decrease the size of the PNPs.^{91,93} Furthermore, PNPs with both type of charges at their surface can be engineered.¹⁰⁰

3.3 Encapsulation of metallo-based compounds

In the literature, the notion of encapsulation is used to describe the synthesis of different materials. Here, this notion will be restricted for the phenomenon of gathering a more or less high number of cargos inside a single nano object. All the processes consisting in covering a single emitter with polymers by capping, adsorption, linking and other methods will be defined as **coating** and these cases fall out of the scope of our work. As described above, encapsulation of cargo inside a PNP can be achieved using different techniques and brings advantages for the elaboration of luminescent probes. Indeed, regrouping a high number of luminophores into a restricted volume enables to create very small and bright objects. However, when luminophores are put in close proximity, they may interact with each other and this can modify their luminescence properties. At high local concentrations, luminescent emitters frequently undergo one of two opposed phenomena: aggregation-induced emission (AIE) and aggregation-caused quenching (ACQ). If the first is somewhat positive in the design of bright objects, the second implies that there is a limit above which the brightness of the NP decreases with increasing luminophore concentration. In consequence, a good comprehension and control of the luminophore organization inside the PNP is essential.

The objective of this thesis being to create luminescent nanoprobes for either SWIR, UC or TG imaging and sensing, the choice of luminophore must be done accordingly. Metal based luminophores, such as transition metals or lanthanides, are the most suitable reported candidates to exhibit these PL properties. They encounter a growing interest for biological applications, with the description in the literature of a very large variety of compounds, their PL properties that are often used as sensor for various biological parameters. They can also be encapsulated into polymeric NPs to form nano-hybrids, that are thus a mix between organic and inorganic materials, like for example hybridosomes.¹⁰¹ Different examples of luminescent nano-hybrids obtained from encapsulation of metallic compounds into polymeric PNPs have been described, with applications in PL bioimaging, sensing or photodynamic therapy (PDT).

Determination of the concentration in luminophores encapsulated inside the PNPs is a key parameter to better understand the internal organization and structure. Indeed, these data are useful to characterize the behavior of the synthesized probes but also for comparing them with other nanocarriers. However, the calculation or measurement of the effective concentration of the object of interest inside the PNP is not always easy to achieve, particularly because of the large diversity of methods employed to create PNPs. The different examples introduced below are describing the process of small metallic emitters encapsulation of PNPs, evidencing the different possibilities to create such nanohybrids. There is no universal way to express the cargo concentration, as units related to volumes, mass or molecular weight can be used, but also sometimes concentrations are relative to the polymer and other to the solution. From this arise another problem: the evaluation of the **encapsulation efficiency**. Indeed, not all the metal starting material is encapsulated and often the excess is washed away without being properly quantified. Generally, absorbance measurements are the proposed quantification method for the encapsulation of cargo inside PNPs is achieved through.

Nonetheless, from the different examples cited before a common observation done is that the encapsulation of these luminophores have a minor or negligible effect on their PL properties.

Using the NP preparation methods described before, AuNCs¹⁰² and QDs¹⁰³ have been encapsulated through emulsion polymerization, yielding PNPs with size between 50 and 200 nm. To ensure that the metal is trapped inside the PNPs, a strategy is to complex the metal onto the monomer before the emulsion polymerization.^{104–106} In the same spirit, europium and terbium based complexes have been complexed on already formed polymer to form potential fluorescent makers.¹⁰⁷ An interrogation rising from this is to know whether it is preferable to complex the metal complex before or after the polymerization step to enable a better encapsulation. Kusumaatmaja et al. achieved the synthesis of star PMMA with either sequential or simultaneous introduction of an europium complex and showed that the final concentration, determined by absorption, was almost a hundred times higher when the polymerization was done with the complex already attached.¹⁰⁸ This linkage to the polymer can also be a covalent bond in the case of AuNCs, followed then by self-assembly.¹⁰⁹ Furthermore, the metallic emitters can play a role in the creation of the network that structures the final PNP through its coordination. Indeed, examples of chemical precipitation between lanthanide ions and polymers yielding NPs with sizes of a few tens of nanometers have been reported, with applications as PL and MRI probes.^{110,111} This strategy, inspired from the MOF construction, also enables to synthesize lanthanide loaded nanodiscs.¹¹² However, the self-assembly of polymers and metals can also be achieved without linking them, by simply trapping them into the polymer matrix.^{113,114} Through the emulsification/solvent evaporation method, CdSe nano-pellets and Ruthenium complexes were encapsulated into PNPs^{115,116} and despite the similarity in the method of preparation of the PNPs, the luminophore loading is expressed with two different ways. Indeed, one loading is based on the initial volume ratio between polymer and CdSe nano-pellet, without further characterization after the PNPs formation, whereas the other uses absorbance calibration curve to determine the concentration, estimated around 40 %. Eventually, nanoprecipitation has also been used to prepare ruthenium or europium loaded PNPs, with application in O₂ sensing, live cell imaging and PDT therapy.^{117–119} Depending on the nanoprecipitation conditions and polymer used, a wide range of sizes between 10 and 300 nm could be obtained, with up to 50 wt% of metallic complex encapsulated.

Eventually, over the last decades, different classes of materials filling the gap between molecules (or complexes) and NPs have been developed. These extend a precisely defined composition and controlled structure, like usually found in molecules, to arrangements made of a few to tens of atoms or ions, often held in place by ligands, with sizes in the low nanoscale (often < 2nm), leading to the appearance of new types of properties, particularly for optical applications.^{120–122} This opens further the range of emitters that can potentially be encapsulated inside PNPs, giving the possibility to enhance the number of probes for biosensing and imaging in complex biological media.

3.4 Biocompatibility

During synthesis and photophysical characterization, the luminescent materials are generally studied either in organic solvents or water when the solubility enables it. However, when put in a complex biological media, the NPs are in contact with various entities that can modify their stability and properties. As we want to use our PL for bioimaging, they must stay intact and avoid non-specific interactions with the constituents of the biological media they are in so stealth properties are a requirement. The surface characteristics of the NPs such as the charge or hydrophobic/ hydrophilic character will determine their properties. Without adapted surface, proteins can adsorb at the surface of the NP, creating a protein corona which can lead to a rapid elimination or destabilization of the probe. Thus, a fine tuning of the surface is crucial to ensure stealth properties.

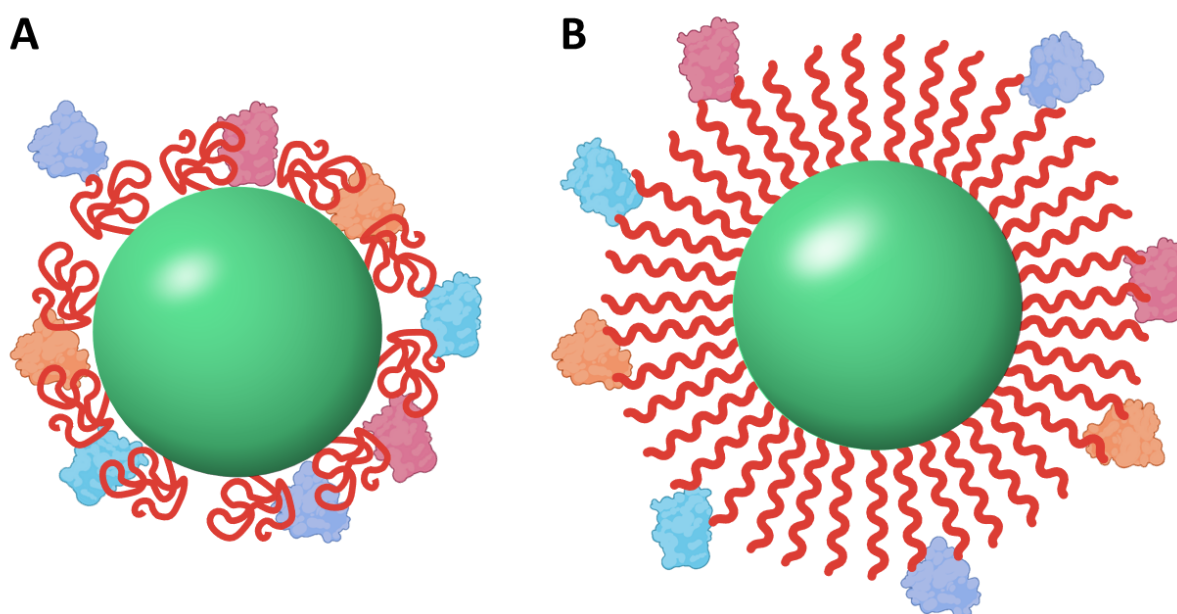


Figure 18: A) Low PEG (red) density: Mushroom conformation, and formation of protein corona through protein adsorption at the surface of the NP B) High PEG density: Brush conformation and protein repulsion

Poly(ethylene glycol) (PEG) is widely used in pharmaceutical application, for it is FDA approved and has shown to be efficient in protecting NPs from interactions.¹²³ Pegylation of NPs, polymeric or not can be achieved using different methods such as covalent coupling (chemical or enzymatic), adsorption or self-assembly of block-copolymers.¹²⁴ Depending on the PEG length, the molecular weight, the dispersity or the density of grafting at the NPs surface, the polymer chain can adopt in majority two different conformations.¹²⁵ At low density, the PEG chain will have tendency to adopt a mushroom conformation which usually does not prevent the protein corona formation. When increasing this density, the chain will elongate to adopt a brush conformation and improve the stealth character of the NPs (Figure 18).

4. Objectives and Approaches

Light based bioimaging and sensing are attractive methods to study complex biological systems. The quality of the result depends strongly on the probe used. Indeed, the introduction of a probe is frequently required to detect and differentiate an object of interest from the system studied. Thus, the probes photophysical properties have to be optimized to enhance the imaging sensitivity and resolution. For a luminescent contrasting agent, a high PL brightness is key to achieve an efficient detection, especially in systems like tissues or biological fluids. As the probe is destined to be used in living and/or complex biological systems, the probe must be biocompatible, meaning able to interact with the living system without degrading it, but the reverse is also true. Thus, stealth properties must be developed for the contrasting agent, without interfering with its targeting abilities.

An important limitation in luminescence based bioimaging and sensing is the natural autofluorescence of biological systems that induces a high background and deteriorated SNR. Thus, the design of new probes using luminescence modes different from fluorescence is an attractive solution in the development of autofluorescence free imaging. In our case the focus was done on three modes: shortwave infrared, upconversion and time gated detection. Expanding the number contrasting agent displaying these peculiar luminescent modes is necessary to help the development of innovative imaging methods and its application to biomedicine. Indeed, the existing probes for TG, UC and SWIR suffer from limited brightness, especially in aqueous media, low biocompatibility and are generally not well adapted for *in vivo* application. In particular, the aim is to enhance the brightness of the contrasting agents to improve the SNR, sensitivity and resolution reachable for applications such as the detection of small quantities of biomarkers in complex biological media. Once the PL properties optimized, the probe should be adapted biological system by increasing biocompatibility, while reducing the non-specific interactions.

For that our strategy is to decouple the photophysical properties from the bio-interface properties of our probes. The solution we propose is to encapsulate luminophores into polymeric nanoparticles, as they will ensure a PL emission with the desired optical properties, while the PNPs surface can be tuned to answer the biological property demands. To formulate these probes, we aim to use nanoprecipitation, as it is a straightforward and tunable method to synthesize PNPs with the possibility of encapsulating high concentration of cargo. The entrapment of luminescent emitters inside the polymer matrix will have a double beneficial effect: the polymer should protect the luminophores from water and enable to preserve their luminescent properties while gathering a high number of emitters in a small volume that is the PNP and creating bright nano-objects.

The objective of this thesis is to develop luminescent probes by formulating bright NPs through encapsulation of luminophores with different nature. These PNPs are designed to present optimized properties for Time-Gated, Up Conversion or Shortwave Infrared imaging. Using as starting point the extensive studies done previously in the team on the encapsulation of small

organic molecules, we gradually transition to the encapsulation of larger metal-organic and metallic compounds.

First, the encapsulation of rhenium-based complexes, either alone or with organic fluorophores, is investigated in order to design long lifetime emitters for Time-Gated Imaging. The combination of thorough physico-chemical and photophysical analysis enabled to characterize precisely the optical properties of the final nanoprobe, but also to extract valuable information about the encapsulation and luminophore organization inside the PNPs. In a second time, we take an interest into hetero-nonanuclear lanthanide complexes as molecular up-converters and focus our efforts on transposing this feature into biological media. After optimization we were able to present PNPs loaded with molecular upconverters capable of emitting in the visible region upon excitation at 980 nm. A careful study of the nanoprobe PL brightness and stability encouraged us to use them for bioimaging and successful experiments showed that *in cellulo* imaging was possible. Eventually, we designed AuNCs loaded PNPs to be bright emitters in the SWIR region. After formulation and optimization of the PNPs, a detailed characterization confirmed the good encapsulation of AuNCs at high concentration inside the PNPs, and their ability to emit in the SWIR. A brightness evaluation revealed a high potential for bioimaging and sensing, both at the solution and single-particle level. It was also shown that these nanoprobe present are not cytotoxic. Eventually, a reduction of the non-specific interactions of the SWIR emitters was achieved by pegylation of their surface and the final PNPs were tested as contrasting agents for *in vivo* blood vessel imaging, confirming their potential.

Materials and Methods

1. Polymer Synthesis

1.1 Polymer Index

The polymer chemistry plays an important role in the formulation of PNPs as explained in the introduction. For this reason, various polymers were used during this PhD and are summarized in this part.

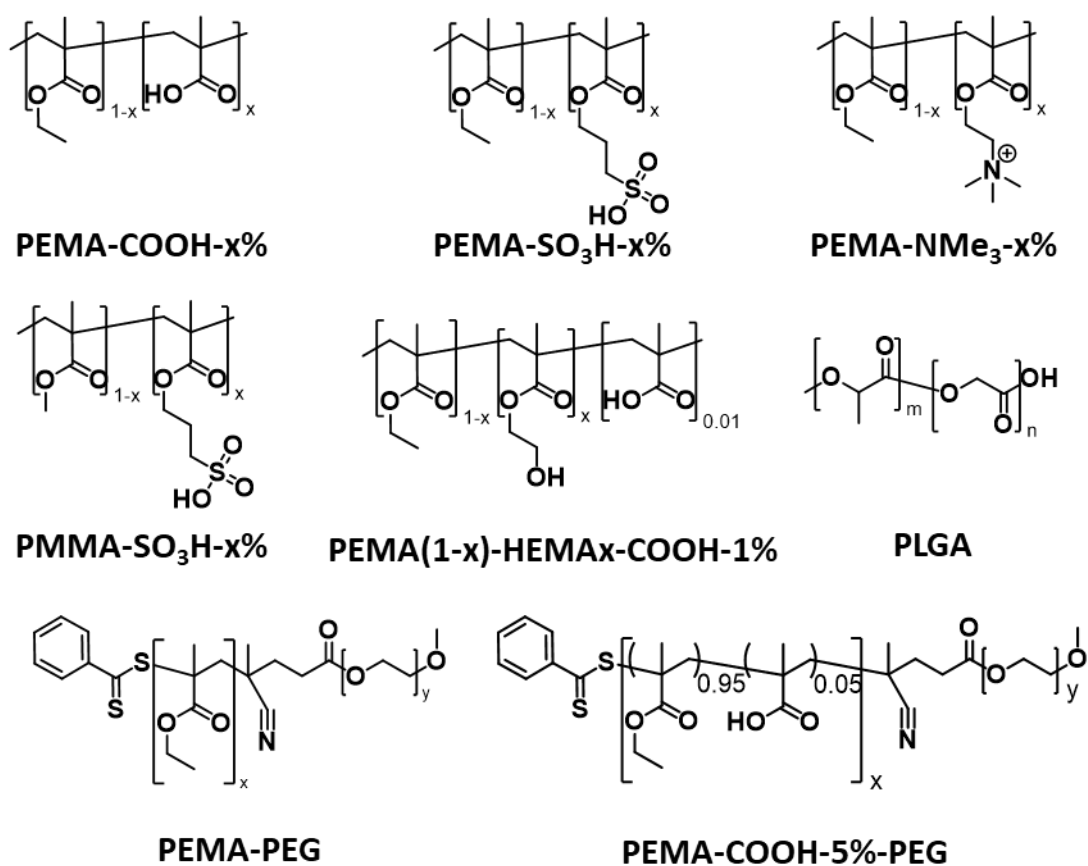


Figure 19: Chemical structure of the polymer used in the different projects

1.2 Free Radical Polymerization

FRP is a polymerization process widely used for it enables to prepare polymers of various natures in an easy and cheap way. The mechanism of this process is divided in 4 steps as shown in Figure 20:

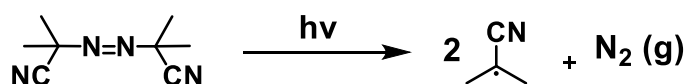
Radical Formation: An initiator such as AIBN is decomposed either thermally or by irradiation, the heterolytic rupture of a covalent bond generating two radicals.

Initiation: After having been generated, the radical reacts with the double bond of a first monomer, starting the formation of a new polymeric chain and transferring the radical to the monomer.

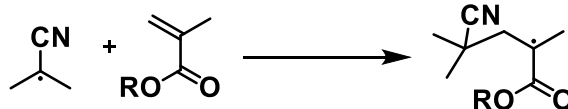
Propagation: The polymeric chain reacts with new monomers, adding them one by one and making the polymer chain grow. This process occurs either until all monomer are consumed or the radical is quenched.

Termination: The reaction stops when the polymer chain loose its radical. Two main termination processes can be distinguished: combination (Termination A in Figure 20) and disproportionation (Termination B in Figure 20).

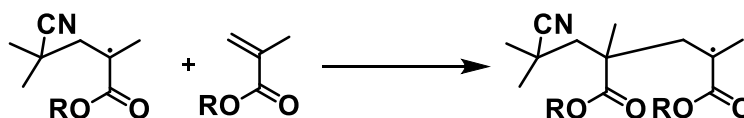
I - Radical Formation



II - Initiation



III - Propagation



IV - Termination

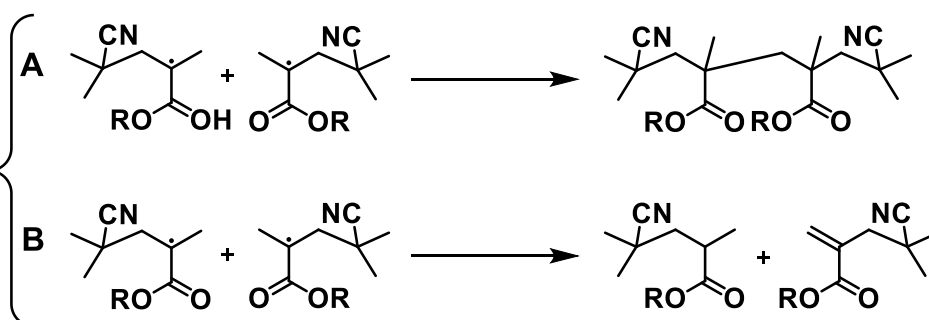


Figure 20: Free radical polymerization mechanism

We used FRP principally for the synthesis of statistical copolymers. When synthesizing copolymers with FRP, two monomers can have different reactivity, meaning that the addition on the polymer chain will not follow the initial monomer ratio. It's possible to predict the composition of the polymer from initial ratio using the Mayo-Lewis equation¹²⁶, from a

theoretical point of view, or the Wiley Database of Polymer Properties¹²⁷ from an experimental point of view. In our case, we copolymerized monomers with similar chemical structures (methacrylate) and chose to stop the polymerization reaction for conversion rate of monomer between 25 and 30 % to ensure a similitude between monomers initial ratio and polymer final composition.

Procedure (PEMA-COOH-5%): Monomers were dissolved in DMSO at a concentration of 2 M. 35 mL of EMA (70.1 mmol, 0.95 eq) and 1.85 mL of MAA (3.7 mmol, 0.5 eq) solutions were placed in a 100 mL round-bottom flask. 61 mg of AIBN (0.37 mmol, 0.005 eq) were added and the mixture was flushed with argon during 5 min. It was then heated at 70 °C under inert atmosphere for 30 min. ¹H NMR spectroscopy analysis of the reaction mixture was used to determine the conversion rate of the reaction. The ratio between the intensities of the O-CH₂-signals from the monomer and the polymer showed 20 % of conversion.

The mixture was precipitated in 400 mL of a methanol-water 90-10 mixture at -10°C. The polymer was recovered using centrifugation and redissolved in acetonitrile before a second precipitation in methanol-water 90-10 mixture at -10°C. The obtained polymer was dried under vacuum to give 1.44 g of white solid (overall yield 17 %). ¹H NMR (400 MHz, CDCl₃) δ (ppm): 4.04 (m, 2H), 1.92 – 1.82 (m, 2H), 1.25 (m, 3H), 1.04 – 0.88 (m, 3H).

1.3 RAFT Polymerization

Since its first description in 1998, reversible addition-fragmentation chain-transfer (RAFT) polymerization has become a widely used method to produce polymers. Its attracting controlled character¹²⁸ enables to synthesize polymers with predictable molecular weight, low dispersity and various architectures. The mechanism of the polymerization is based on an equilibrium between active and dormant chains assured by a CTA. As described in Figure 21, the reaction is initiated the same way as in FRP, by the radical formation and addition on the first monomer. Then the chain grows by alternating between the following steps:

RAFT Pre-Equilibrium: Here the polymer chain carrying a radical attach to the CTA, provoking the detachment of the leaving group and becoming dormant.

Re-Initiation: This new group reacts with one or several monomers by radical addition to form a second polymer chain.

RAFT Equilibrium: The addition/fragmentation equilibrium between active and dormant chain is ensured by the active polymer chain (*i.e.* carrying the radical) periodically attaching to the CTA and releasing the dormant chain. Ideally, the addition/fragmentation rate is higher than the monomer addition rate to enable an homogeneous chain growth and thus having polymer chains with a similar DP.

Termination: Eventually, the chain growth ends through a bi-radical recombination process, creating dead chain and stopping the polymerization. The number of chains undergoing termination can be predicted from the original quantity of initiator and CTA introduced into the system and this parameter is to take into account for putting in place an efficient polymerization system.

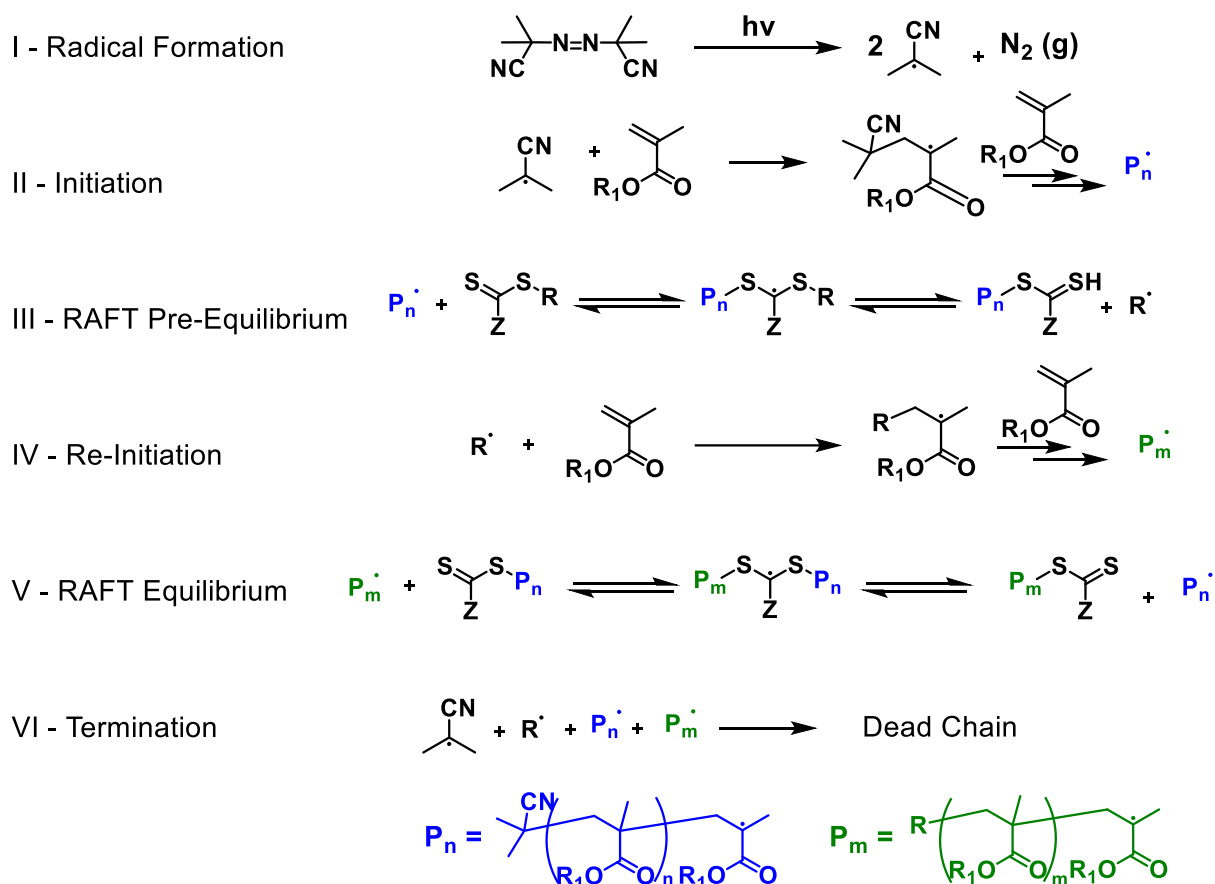


Figure 21: General mechanism of RAFT polymerization

The number fraction of living chains, named Livingness (Liv), can be evaluated as follow:

$$\text{Liv} = \frac{[\text{CTA}_0]}{[\text{CTA}_0] + 2f[\text{I}_0](1 - e^{-k_d t})(1 - \frac{f_c}{2})} \quad (6)$$

With $[\text{CTA}]_0$ and $[\text{I}]_0$ the initial concentration in CTA and initiator respectively, f the efficiency to give radicals and k_d the decomposition rate of the initiator, and f_c the radical coupling factor. This living character has a great interest in the synthesis of block copolymer as after the polymerization and purification of the first block, a second block can be grown on the pre-formed chain.

As appealing as this technique is, an efficient polymerization requires a good adjustment of the different reagents used. A wide range variety of CTA can be used and their choice is adapted to the monomer composition, reactivity or hydrophilicity. Moreover, the presence of initiator in the reaction mixture may lead to a competition between RAFT and FRP polymerizations if the proportions of CTA and initiator aren't optimized and the formation of non-living polymer chains.

Procedure (PEMA-COOH-5%): Monomers were dissolved at a concentration of 2M in DMF. 2.19 mL of EMA (4.38 mmol, 397 eq) and 112 μL of MAA (0.22 mmol, 21 eq) were placed into a Schlenk. 2.4 mg of CTA (0.011 mmol, 1 eq) and 0.18 mg of AIBN (1.1×10^{-3} mmol, 0.1 eq) previously dissolved in solution were added to the reaction mixture. The Schlenk was put

under argon and is submitted to 3 freeze-thaw cycles. The reaction is heated at 80°C for 24h under argon and stirring. A conversion rate of 76 % was determined by ^1H NMR spectroscopy. The polymer was precipitated in a MeOH-NaCl(1M) 80-20 mixture at -10°C. The obtained solid was dried on the rotary evaporator, redissolved in 1.5 mL of acetonitrile and precipitated in a MeOH-NaCl(1M) 70-30 mixture at -10°C. After drying under a vacuum, 180 mg of a light pink solid were obtained (yield 44 %). ^1H NMR (400 MHz, CDCl_3): δ (ppm) 4.04 (m, 2H), 1.92-1.82 (m, 2H), 1.26 (m, 3H), 1.04-0.88 (m, 3H).

1.4 Block Copolymer

There is a huge interest in synthesizing block copolymer with different nature to generate materials with the properties of both blocks. Indeed, amphiphilic polymers are characterized by a unique proximity between polymers with opposite features, leading to the creation of a material with hybrid properties, normally incompatibles.⁷³ In our PNPs formulation most of the used polymer are based of PEMA. Thus, we aimed to synthesize a PEMA based polymer linked covalently with a PEG polymer (designated as PEMA-PEG). First, a OH terminated PEG chain was coupled with a CTA containing a carboxylic acid group through Steglich addition. 1D and 2D NMR analysis enabled to assess the coupling and thus formation of the PEG-CTA. In a second step the PEG-CTA is used as macro chain transfer agent for the synthesis of the PEMA block through RAFT polymerization. After purification ^1H NMR analysis is used to calculate the final units number of the PEMA block using the PEG signal. Among the PEMA-PEG synthesized some are prepared using a small amount of methacrylic acid monomers to introduce acidic functions into the hydrophobic block. The quantification of the exact amount of carboxylic group is difficult to achieve on the final polymer as the proton of this function can't be seen on our ^1H NMR spectrum. Thus, a small quantity of this polymer is modified using a methylating agent and measure the percentage of carboxylic acid function.

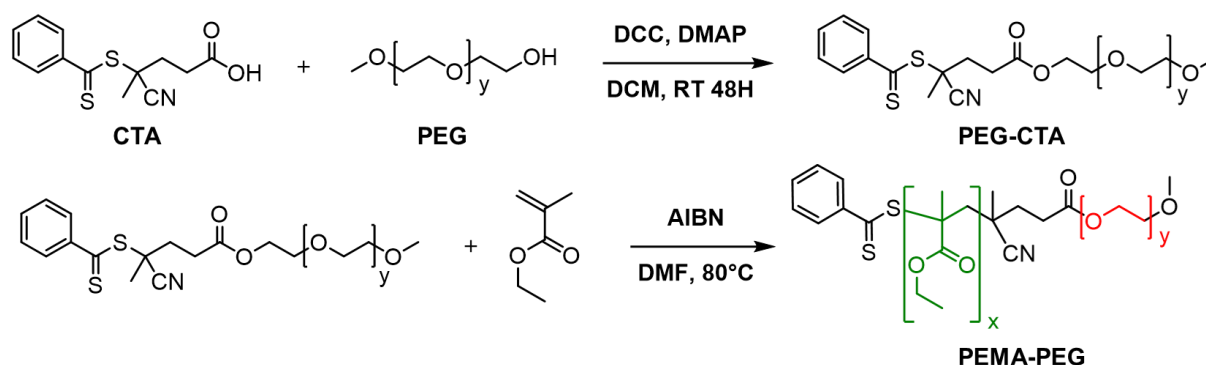


Figure 22: Synthesis scheme of PEMA-PEG

Procedure PEG and chain transfer agent coupling

1 g of PEG(1,9k) (0.53 mmol, 1eq) and 221 mg of CTA-COOH (0.79 mmol, 1.5 eq) were dissolved in 20 mL of DCM. The reaction mixture was put in an ice bath and 130 mg of DCC (0.63 mmol, 1.2 eq) previously dissolved in 2 mL of DCM were added slowly. 7.7 mg of DMAP (0.063 mmol,

0.12 eq) were added to the reaction mixture. The ice bath is removed and the reaction is stirred for 48h at R.T.

The reaction mixture is filtered to remove the dicyclohexylurea formed during the reaction. The precipitate was concentrated on the rotary evaporator then precipitated twice in cold diethyl ether. After drying under vacuum, 790 mg of PEG-CTA were obtained ($\eta = 79 \%$).

Procedure P(EMA)-b-PEG synthesis

Solutions of ethyl-methacrylate and methacrylic acid at 2 M were prepared in DMF. 1.827 mL of ethyl-methacrylate solution (417 mg, 3.65 mmol, 199 eq) and 93 μL of methacrylic acid solution (16 mg, 0.18 mmol, 10 eq) are introduced into a Schlenk. 40 mg of PEG-CTA ($1.8 \cdot 10^{-2}$ mmol, 1 eq) are added to the reaction mixture and stirred up to dissolution. To this are added 0.3 mg of AIBN ($1.8 \cdot 10^{-3}$ mmol, 0.1 eq) beforehand dissolved in DMF. The reaction mixture is put under Argon and is undergoing 3 freeze-pump-thaw cycles before being heated at 80°C for 48 h. NMR of the reaction mixture showed a conversion rate of 35 % after 24 H and 80 % after 48 h. The reaction mixture was precipitated in a 70-30 MeOH-NaCl 1M cold mixture. The precipitate is dried on the rotary evaporator, redissolved in acetonitrile and precipitated a second time in a 70-30 MeOH-NaCl 1M cold mixture. The precipitate is lyophilized and the final mass of polymer recovered was 158 mg ($\eta = 41 \%$)

Procedure for methylation:

20 mg of P(EMA-COOH-5%)-PEG ($8.05 \cdot 10^{-3}$ mmol of COOH groups, 1 eq) are dissolved in 1 mL of THF. To this are added dropwise 40 μL of (trimethylsilyl)diazomethane solution ($8.05 \cdot 10^{-2}$ mmol, 10 eq). The reaction mixture is stirred for 3 h at RT. After this time the reaction mixture is diluted with EtOH to neutralize the excess of (trimethylsilyl)diazomethane. The solvent is evaporated on the rotary evaporator and yielded a quantitative product.

2. Nanoparticles Preparation and Characterization

2.1 PNPs Synthesis

PNPs are synthesized using the nanoprecipitation technique presented in Nanoprecipitation.

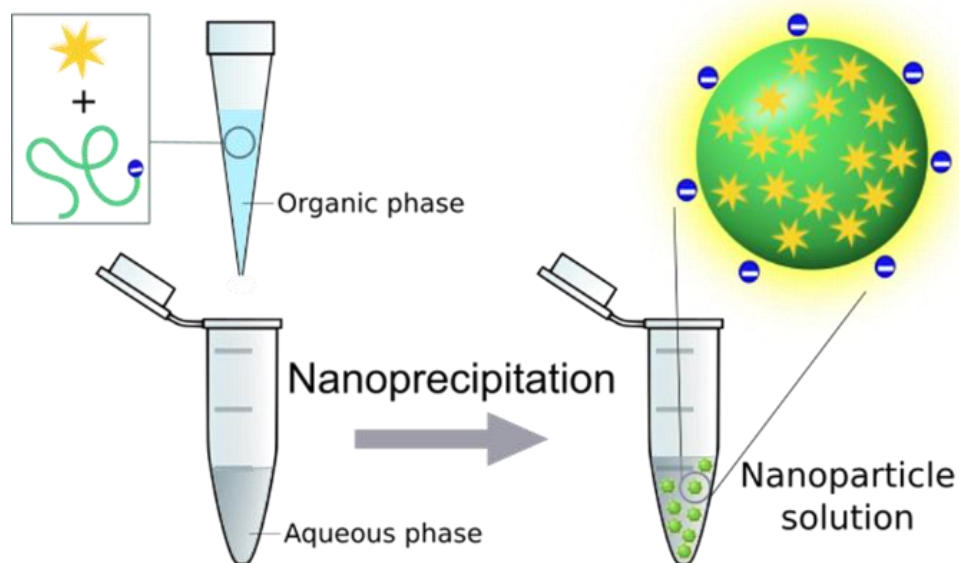


Figure 23: Nanoprecipitation scheme for the encapsulation of luminophore (star) inside a polymer

PNPs with different concentrations of luminophore encapsulated inside can be inside. This concentration, called loading (L) and expressed in wt%, is defined as followed:

$$L = \frac{m_{Lum}}{m_{Lum} + m_{Polymer}} \quad (7)$$

With m_{Lum} and $m_{Polymer}$ being respectively the mass of luminophore and polymer in the solution.

Procedure: Stock solutions of polymers were prepared at a concentration of 10 g L^{-1} in acetonitrile. These solutions were diluted to 2 g L^{-1} in acetonitrile, with the desired amount of luminophore. $50 \mu\text{L}$ of the mixture were quickly added to $450 \mu\text{L}$ (a 9-fold volume excess) of aqueous phase under shaking (Thermomixer comfort, Eppendorf, 1050 rpm at 21°C), followed by further dilution to the desired concentration.

Different aqueous phases can be used to tune the size of the NPs: MilliQ water, phosphate buffer, borate buffer, tris buffer. The buffers are prepared at 20 mM concentration and the pH can be adjusted.

2.2 Size Determination

2.2.a) Dynamic Light Scattering (DLS)

A key element parameter in the characterization of NPs is their size, for it informs about the homogeneity, stability and good quality of the prepared nanomaterial. Size influences the ability of nanomaterials to move or cross barriers in biological media⁹³, and can be limiting parameter for bio-applications such as cellular uptake or drug delivery. Moreover, when producing the nanomaterial the size distribution of the formulation can be more or less monodisperse, which will also have an impact on the probe capability. DLS has emerged as a

popular method to determine the size of a colloidal suspension, as it is a simple, fast, non-invasive method with minimal sample preparation and affordable instrumentation.

Individual elements such as molecules or NPs move following a random pattern in suspension called Brownian motion, the speed of motion being proportional to the size of the element. Moreover, colloidal suspensions scatter the light, as states the Tyndall effect, with the intensity of the scattered light inversely proportional to the wavelength. This scattering becomes independent of the incident angle (Rayleigh scattering) when the particle size is 10 times smaller than the incident light, which is why DLS instrumentation typically uses 633 nm lasers to generate isotropic scattered light on a NPs solution.¹²⁹ Because of the Brownian motion, the intensity of the scattered light fluctuates and can be recorded over time, these fluctuations depending directly on the NP size (Figure 24).

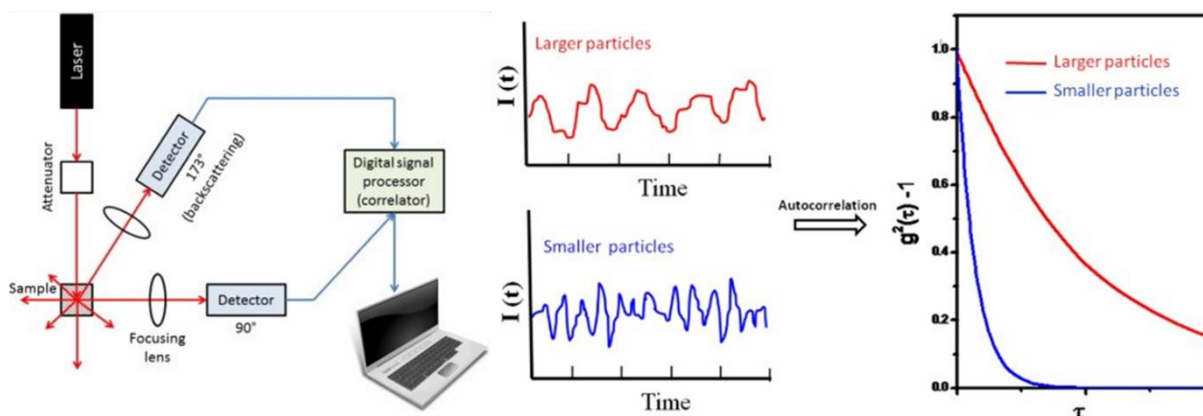


Figure 24: Schematic of the DLS instrumentation (left) and fluctuation in the intensity of scattered light with their associated correlation functions for small and big NPs¹³⁰

An autocorrelation function is generated from the signals recorded, taking into account the intensity at a given time $I(t)$ and after a delay time $I(t + \tau)$ over time. From the fitting of the autocorrelation function can be extracted the translational diffusion coefficient D , directly related to the Brownian motion. Eventually, the hydrodynamic radius R_h of the NPs can be calculated using the translational diffusion coefficient in the Stokes-Einstein equation:

$$R_h = \frac{k_B T}{6\pi\eta D} \quad (8)$$

With k_B the Boltzmann constant, T the temperature and η the viscosity.

As the autocorrelation function is automatically created and fitted from the raw data and the user has a direct access on the software to the calculated size, this technique is widely used today in nanomedicine. Understanding the factors involved in size determination is essential to keep a critical eye on the obtained results. The initial method is designed to characterize monodisperse populations using the Z-Average function, thus the analysis of a mix of populations with different size will lead to an average size of all the populations. To avoid this problem, a multimodal fitting of the raw data using as weight either their intensity, number or volume can reveal the size and proportion of each population. Moreover, the intensity of the scattering increasing strongly with the NPs radius, a small proportion of aggregate in a suspension will impact greatly the final displayed size.

More specific of our case, luminescent compounds may interfere with the DLS analysis if they absorb at the laser emission wavelength. Indeed, the signal intensity will be greatly diminished and the noise enhanced, deteriorating the SNR and making the analysis impossible.

Another point to take into account and highlighted by the Stokes-Einstein equation is the dependence between the NPs radius and the viscosity of the medium. In our case, most of the NPs were prepared and analyzed in aqueous medium. At some occasions they were prepared in deuterated aqueous medium, so the data were analyzed using a corrected viscosity.

In the case of biological applications, DLS has been used to study stability of NPs in biological fluids¹³¹ and protein adsorption on the NPs.¹³² However, as biological medium are composed of ions, vitamins or proteins, these element can also scatter light and increase the noise, leading to misinterpretation of the obtained data.

Procedure: The size of the NPs was measured on a Zetasizer Nano series ZSP (Malvern Instruments). Each sample was measured 10 times with a run length of 10 s each. Volume-averaged values, determined by the Zetasizer software based on Mie theory, were used. Mean values give the average over at least three independent preparations, error bars correspond to standard error of the mean.

2.2.b) Transmission Electron Microscopy (TEM)

Transmission electron microscopy is an imaging technique using the scattering of electrons. After the establishment of the light diffraction limit by Abbe (see Characterization of the contrast), electrons were considered to push further the limit of spatial resolution in imaging. Indeed, electron have a wave-particle duality and their wavelength is inversely proportional to their speed. In TEM, an electron beam is applied onto a sample and the power of the beam will define the electron speed and thus their wavelength. Electrons interacts with matter by scattering and their signal can be focused and magnified using electromagnetic lenses from which an image of the sample can be projected. A very high spatial resolution can be reached, going down to the subatomic level at 0.39 Å.¹³³ Electrons interactions with matter increasing to the power four with the atomic number, heavy atoms are easier to image with this technique.

Soft matter (composed mostly of H, C, N and O atoms) is in consequence harder to properly image, because the scattering amplitude is very low compared to the unscattered electrons, so the generated contrast is very slim.¹³⁴ A solution to improve contrast is to apply on the sample staining agents composed heavy atoms such as uranium. The contrasting agent can deposit everywhere on the sample, resulting in brighter spots on the image where the soft matter is, it is called negative staining. Otherwise, it can accumulate on the sample, this time creating positive staining, *i.e.* dark spots for soft matter.

Overall, this technique enables a great improvement of spatial resolution compared to light-based imaging, but suffers from several drawbacks. First, samples have to be imaged in vacuum to limit electrons interactions with other matters that would create noise. This parameter is

important because our NPs are normally in water so the diameter measured in DLS is the hydrodynamic diameter, whereas in TEM, the measured diameter corresponds to the hard-core surface. More generally, working under vacuum implies the loss of temporal resolution, the sample being frozen into a given position. The TEM device should also be stable to limit vibrations and has to be cooled by liquid nitrogen to minimize heating and electric charge accumulation. Furthermore, samples can be damaged by the electron dose, thus a limited exposure time and reduced power should be applied. To conjugate these requirements with the need of high resolution, imaging of sample in TEM is usually done in two steps. First, a “low dose” mode enables to search at low magnification (e.g. 2650x)¹³⁵ the appropriate area for imaging on the sample. Then, the focus and recording of the picture is achieved at higher magnification (e.g. 40000x) and higher power.

Procedure: Solutions of NPs (5 μL) were deposited onto carbon-coated copper–rhodium electron microscopy grids following amylamine glow-discharge. They were then treated for 20 s with a 2% uranyl acetate solution for staining. The obtained grids were observed using a Tecnai F20 Twin transmission electron microscope (FEI Eindhoven Holland) operating at a voltage of 200 kV. Images (2,048 pixels \times 2,048 pixels) were recorded using a US1000 camera (Gatan) and analyzed using the Fiji software. At least 200 particles per condition were analyzed.

2.2.c) Cryo-TEM

A derived technic to TEM is cryogenic-TEM (cryo-TEM), that uses also the electron scattering to image matter, where the object of interest isn't observed under vacuum. Indeed, in this case the drop of sample deposited on the grid and undergoes an ultra-fast cooling to vitrify the aqueous phase containing the nano-object. The vitrification, in opposition to the freezing, ensures that water molecules don't have time to rearrange when transitioning from liquid to solid state and thus limits the risk of denaturation or modification of the observed system. However, an efficient vitrification can be difficult to put in place and sample preparation for cryo-TEM imaging can be tricky. Cryo-TEM is an effective way to gain temporal resolution as it is capable to capture metastable intermediates that can help resolve assembly mechanisms of complex systems.¹³⁶

Procedure: 3 μL of sample was deposited onto freshly plasma-cleaned (Fishione 1070) 300 mesh Quantifoil R2/2 grids (Quantifoil Micro Tools GmbH, Jena, Germany) and the grids were plunge-frozen using a Vitrobot Mark IV (FEI) with 95% chamber humidity at 15°C (blot force 5, blotting time 2 s). CryoEM imaging was performed on Glacios(FEI) microscopes operated at 200 keV acceleration voltage and equipped with a K2 Summit camera (Gatan, Inc., Pleasanton, CA) using *SerialEM* software. All images were acquired at a target defocus of 1.5 μm with a dose of $\sim 40 \text{ e}^- \cdot \text{\AA}^{-2}$ in super-resolution mode at a nominal magnification of 45 000 \times , corresponding to a pixel size of 0.90 \AA .

2.3 Further characterization

2.3.a) ζ -Potential

NPs and other colloidal suspensions have charges at their surface that ensures their stability. These electric charges have a huge role in the ability of NPs to be non-toxic, stealth and mobile in biological media. The presence of charges at the particle surface can be explained with the DLVO theory which states that the particle stability in solution is dependent to its total potential energy.¹³⁷ A competition between Van der Waals attractive forces and electrostatic repulsions occurs to form the NP up to the point where repulsion forces become predominant. At that moment is formed an electrical double layer (EDL) with a strong adhered layer (Stern layer, Figure 25) charged oppositely to the NP and located directly at the surface of the NP. This layer is surrounded by a diffused layer composed of both charges. The Zeta Potential (ZP) is the electrical potential developed at the slipping plane, *ie* the solid (NP)-liquid (dispersant) interface.

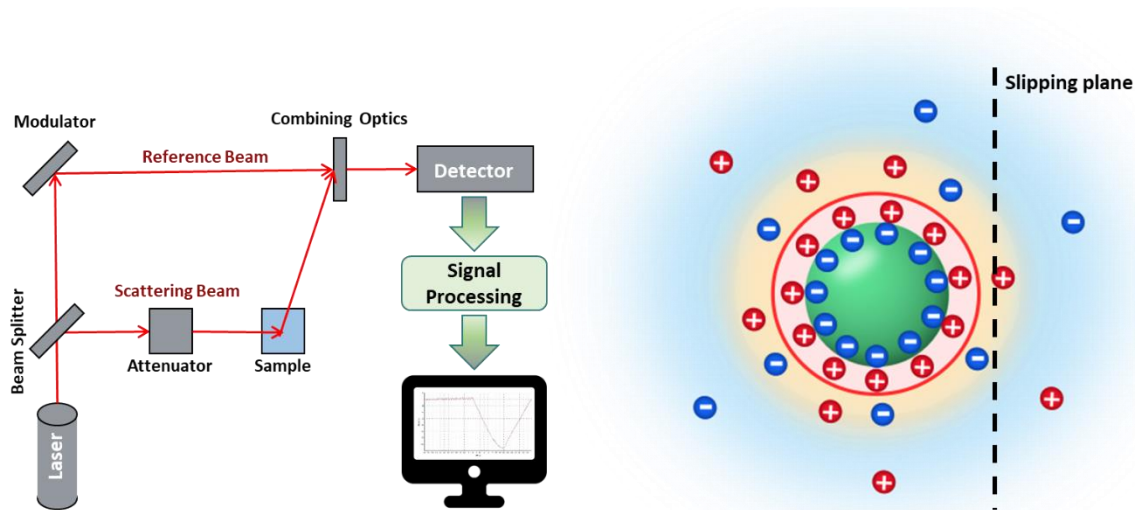


Figure 25: Left: Instrumentation for zeta potential measurement. Right: Scheme of the charges repartition around a NP

Determination of the ZP is achieved by measuring the electrophoretic mobility μ of NPs under an applied electric field:

$$\mu = \frac{V}{E} \quad (9)$$

With V the NPs velocity and E the electric field strength. In practice, a solution of NPs is put in a cell with two electrodes and an electric field is applied to the system, causing the movement of NPs toward the oppositely charged electrode. This movement scatters the light of an incident laser, creating a frequency shift proportional to the speed of the NPs, called Doppler shift. This shift is measured by splitting before the sample the laser beam into two, with only one passing through the sample and then recombining the two signals (Figure 25). From this can be determined the particle velocity and thus the ZP using the Henry equation:¹²⁹

$$\mu = \frac{2\varepsilon_r\varepsilon_0\zeta f(Ka)}{3\eta} \quad (10)$$

with ε_r the relative permittivity, ε_0 the vacuum permittivity, ζ the ZP, $f(Ka)$ Henry's function and η the viscosity of the dispersant. In the case of the EDL being much smaller than the NPs radius, either for large NPs or high salt concentration ($10^{-2}M$) the value of $f(Ka)$ is approximated as 1.5, using the Helmholtz-Smoluchowski equation.

The ZP value is a good indicator of colloidal dispersion stability, the most common ranges being:

- 0 to 5 mV: Fast aggregation
- 5 to 20 mV: Low stability
- 20 to 40 mV: Moderate stability
- Above 40 mV: High stability
-

However, ZP of a colloidal suspension is dependent on external parameters, the pH being the most important for an aqueous solution. Indeed, with the increase of ion (H^+ and HO^-) concentration in solution, charges at the surface of the NP will be neutralized gradually up to a point called isoelectric point where it will be equal to zero. The ionic strength and valency of ions, which varies from one biological media to another, also influence the EDL thickness and thus modifies the ZP.

Eventually, one has to take into account that not only electric charges play a role in the colloid stability but consider also the steric interactions. It has been demonstrated on diverse type of NPs suspension that addition of poly(ethylene glycol) (PEG) helped improve the colloid stability while reducing the ZP.

Procedure: The ζ -potential of the obtained NPs was measured on a Zetasizer Nano series ZSP (Malvern Instruments). Each sample were diluted 10 times (concentration of NPs in solution 0.2 g/L) and 1 mL was introduced into folded capillary cells DTS 1070. Three successive measurements per sample were made combining electrophoretic mobility and laser Doppler velocimetry. Every measurement had at least 10 runs each carried out with an applied potential of ± 150 V.

2.3.b) Number of luminophore per NP

The volume of one NP (V_{NP}) was calculated based on the mean NP diameter determined by TEM. The NP mass (m_{NP}) was then estimated using the calculated volume of NP and the density of the polymer ($\rho_{Polymer}$):

$$m_{NP} = \rho_{Polymer} * V_{NP} \quad (11)$$

The mass of luminophore per particle (m_{Lum}) was calculated using:

$$m_{Lum} = m_{NP} * L \quad (12)$$

With L the loading. The number of luminophores per NP (N_{Lum}) was calculated by taking into account the molar mass of the luminophore (M_{Lum}) and N_A the Avogadro constant:

$$N_{Lum} = \frac{m_{Lum} * N_A}{M_{Lum}} \quad (13)$$

Uncertainties on the obtained values originate from the size measurement but are difficult to estimate. It has to be noted that for the AuNCs loaded NPs (Chapter IV), the loaded objects have a high density compared to the polymer and are encapsulated at high concentration. Thus, it was decided in that case to use a mean density (ρ_{NP}), based on the loading of AuNCs inside the particle (L) and the densities of Au (ρ_{AuNC}) and of the polymer ($\rho_{Polymer}$):

$$\rho_{NP} = \frac{1}{\frac{1-L}{\rho_{Polymer}} + \frac{L}{\rho_{AuNC}}} \quad (14)$$

2.3.c) Distance between luminophores

Nearest neighbor:

In the case of an isotropic random distribution the average nearest neighbor distance between two luminophores can be estimated according to:¹³⁸

$$d = \frac{0.554}{\sqrt[3]{C}} \quad (15)$$

with C the concentration (number of luminophores per volume) inside NPs.

Average distance:

In the case of an isotropic random distribution the average distance (assuming cubic packing) can be estimated through:

$$d = \frac{1}{\sqrt[3]{C}} \quad (16)$$

3. Spectroscopic Characterization

3.1 Instrumentation

The projects developed during this PhD were mostly conducted in collaboration with other laboratories. This led to the use of an important number of devices for the different spectroscopic characterization.

3.1.a) Absorption Spectra

Absorption spectra of the different luminophores and loaded were recorded on a Cary 5000 Scan ultraviolet–visible spectrophotometer (Varian).

3.1.b) PL Excitation Spectra

A luminophore can be excited at different wavelength, depending on its structure. The potential of a certain wavelength to excite the luminophore into following a radiative process

can be assessed by recording excitation spectra. This analysis is complementary to the absorbance spectrum of a luminophore because absorption of energy doesn't always result in a radiative transition. The excitation spectra of NPs prepared during the PhD were recorded on a FS5 Spectrofluorometer (Edinburgh Instruments).

As this spectrometer is equipped with a UV-Vis detector, the excitation spectra of SWIR emitting NPs were recorded with a Fluorolog-3 (Horiba Instruments) equipped with a near-infrared detector. As measurement of the NPs inside a quartz cuvette revealed to be complicated to apply, the excitation spectra were recorded using another procedure.

Procedure: 0.1 mg/mL of the samples were loaded into capillary tubes to reduce the light pathlength and thus, the light scattering in the samples. The emission wavelength was fixed to 1050 nm and the excitation spectra were measured from 360 to 1000 nm. The excitation slit was set to 3 nm, whereas the emission slit was set to 8 nm. Raw excitation spectra were corrected by dividing the excitation signal by the corrected lamp signal (T1/R1c). An empty capillary tube was measured as the blank control. T1/R1c of the blank was subtracted from T1/R1c of the sample to obtain the final excitation spectra of the samples.

3.1.c) PL Emission Spectra

Rhenium loaded PNPs:

PL spectra of the rhenium complexes were recorded on a FS5 Spectrofluorometer (Edinburgh Instruments) using a Xenon flash lamp as the excitation source.

PNPs for UC:

Steady-state emission spectra were recorded on an Edinburgh Instruments FLP920 working with a continuous 450 W Xe lamp and a red sensitive R928 photomultiplier from Hamamatsu in Pelletier housing for visible detection (230 to 900 nm) or a Hamamatsu R5 509-72 photomultiplier cooled at 77 K for the Vis-NIR part. 395 nm high pass cut-off filter was used to eliminate the second order artefacts for the visible part and an 850 nm high pass cut-off filter for the NIR part.

Steady-state upconversion emission spectra were recorded on a FLP920 spectrometer using a 980 nm LED from Edinburgh Instrument with an 850 nm high pass filter between the source and the sample to remove any potential visible excitation. The power of the LED was calibrated using a FieldMate power meter from Coherent Technology. An 850 nm high pass filter between the source and the sample to remove any potential visible excitation has been used.

AuPNPs:

PL spectra were recorded on a WP NIR1 spectrometer (Wasatch Photonics) using 405 and 730 nm lasers (LCC Oxxius) and 808 nm laser (Pro-Lite Technology) as excitation sources.

3.1.d) PL Lifetime

Rhenium loaded PNPs:

Fluorescence lifetimes of Re complexes and Re/Cy5 loaded NPs were measured with a NanoLed-303 from Horiba Jobin Yvon Fluorolog. PL decay curve of the Re (alone or inside NPs) was recorded for the emission at 515 ± 8 nm using a 13 μ s window and a 50 kHz repetition rate. PL decay curve of the Cy5 was recorded for the emission at 700 ± 8 nm using a 13 μ s window and a 50 kHz repetition rate. Complementary measurements were done for Cy5 using this time a 200 ns window and 500 kHz repetition rate.

PNPs for UC:

Lifetimes for downshifting emission were measured on a FLP920 spectrometer in the Multi Channels Spectroscopy mode and using a Xenon flash lamp as the excitation source. Errors on the luminescence are estimated to $\pm 10\%$.

AuPNPs PL lifetimes were measured on a Fluorolog-3 with 400 μ L of samples in quartz cuvettes with a 0.5 cm path length. PL decay curves were measured at three emission wavelengths, namely 950 nm, 1050 nm, and 1200 nm using two different picoseconds pulsed diode lasers from Edinburgh Instruments: 1. EPL 405 (Serial number: 083/405/11/11) with a pulse width of 56.3 ps and emission peak centered at 404.2 nm; 2. HPL 670 (Serial number: 010/670/04/21) with a pulse width of 104.4 ps and emission peak centered at 675.4 nm.

3.2 Quantum Yields

3.2.a) Quantum Yield of downshifting

QYs were determined from the absorbance values at the excitation wavelength ($A_{x,\lambda_{ex}}$) and the integral over the whole emission range (F_x) using a simplified relative method with a reference, according to the formula:

$$QY_{NP} = QY_{Ref} \frac{F_{NP} A_{NP,\lambda_{ex}} n_{H_2O}^2}{F_{Ref} A_{Ref,\lambda_{ex}} n_{SolventRef}^2} \quad (17)$$

where "NP" corresponds to solutions of the NPs in aqueous media and n to the respective refractive indices of the solvents.

3.2.b) Upconversion Quantum Yields

The UCQY was measured on concentrated solutions (*ca.* 1-2 mM) using the definition of the luminescence QY as the ratio of the number of emitted photons to the number of photons absorbed. The emitted signals was compared to [TbGlu(H₂O)]Na ($\varphi_{UC} = 31\%$)¹³⁹ as reference.

3.3 FRET

Fluorescence Resonance Energy Transfer (FRET) is a process of non-radiative energy transfer between two luminophores, that occurs when the emission spectrum of the donor is overlapping the absorbance spectrum of the acceptor (Figure 27). The theory behind this phenomenon considers the luminophores as oscillating dipoles with similar resonance frequency that enables the energy exchange.¹⁴⁰ This energy transfer can be originated from different mechanisms but in our case we consider only the Förster mechanism, occurring in long range distance, going up to 10 nm. This energy transfer depending on both the donor and acceptor properties, but also the distance between the two. Thus, the study of this phenomenon enables to extract structural information concerning the FRET pair and is widely used in bioimaging and sensing in complex biological media.

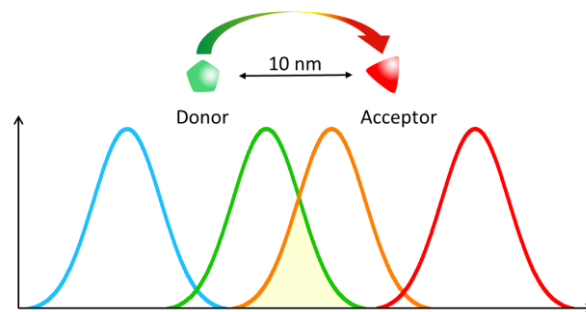


Figure 26: Schematic of the FRET phenomenon

Different parameters to describe FRET properties with calculation methods described below.

3.3.a) FRET efficiency

The FRET efficiency can be calculated using steady state or time resolved spectra. For the steady state the following formula is applied:

$$E = 1 - \frac{F_{DA}}{F_D} = 1 - \frac{\tau_{DA}}{\tau_D} \quad (18)$$

With the relative fluorescence intensity of the donor in the absence (F_D) and the presence (F_{DA}) of the acceptor (middle part of the equation). Another way to determine it is to use the lifetime of the donor in the absence (τ_D) and the presence (τ_{DA}) of the acceptor.

The Time-Resolved method applied to evaluate the FRET efficiency was developed by our collaborators and is very specific, also it is explained in details in the Annexes.

3.3.b) Förster Radius

The Förster radius can be calculated using the spectroscopic properties of the donor and acceptor, first by determining the overlap integral $J(\lambda)$ between the donor emission and the acceptor absorption:

$$J(\lambda) = \int_0^{\infty} F_D(\lambda) \varepsilon_A(\lambda) \lambda^4 d\lambda \quad (19)$$

λ is the wavelength (nm), $F_D(\lambda)$ is the fluorescence intensity of the donor normalized to unity and $\epsilon_A(\lambda)$ ($M^{-1}\cdot\text{cm}^{-1}$) is the extinction coefficient of the acceptor at λ . From this, the Förster distance (in Å) is given by:

$$R_0^6 = 8.79 \times 10^{-5} (\kappa^2 n^{-4} QY_D J(\lambda)) \quad (20)$$

with $\kappa^2 = 2/3$, n the refractive index of the medium (in water $n = 1.33$), QY_D the quantum yield of the donor alone

3.4 Fluorescence Correlation Spectroscopy (FCS)

Molecules and nanosized objects naturally diffuse freely in solution and their velocity is directly correlated with their size. Indeed, the smaller the molecule, the faster it will diffuse through a given spherical volume. Thus, a measurement of this diffusion enables to extract information such as the size of the object of interest, in our case the nanoprobe. However, in biological media, a high number of constituents have a size within the same range as the probe, making its direct observation impossible. As the probe is luminescent, this feature can be used to study its evolution in complex biological media. FCS is a method that can reach a single-molecule detection sensitivity by monitoring the fluctuations over time of the PL intensity from nanosized luminescent objects due to their diffusion. To do so, a setup of confocal microscopy is used, as it provides a confined observation volume (~ 0.5 fl), which enhances the SNR of FCS significantly. This volume is illuminated by a laser that will excite the luminescent species when they cross the observation volume (Figure 27).

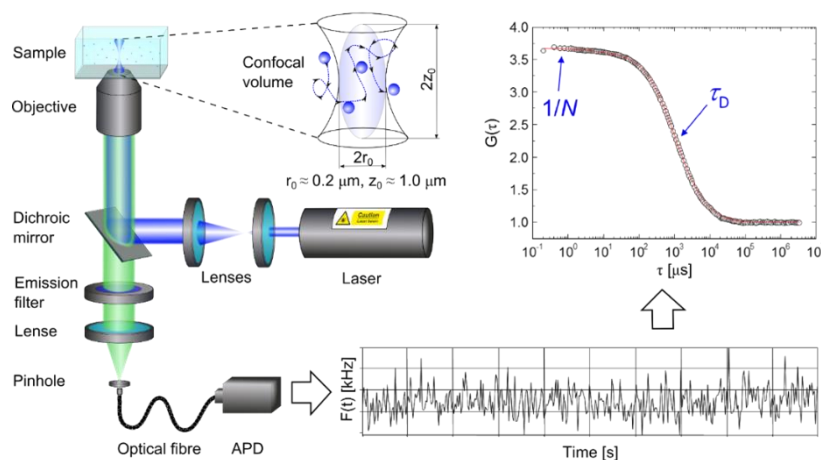


Figure 27: Schematic representation of FCS setup. ¹⁴¹

A correlation analysis of these fluctuations yields information on the diffusion coefficients of the species but also the average number of the molecules passing through the open detection volume the setup. From these parameters the size of the nano-objects also their fluorescence brightness or concentration can be extracted. This method is interesting to study colloidal suspension and their photophysical properties such as photobleaching. Furthermore, it also enables to evaluate the luminescent nanoprobe stability and interactions in a complex biological media.

CHAPTER II: Co-encapsulation of organic dyes and metallic complexes for TG Imaging

Among the modes allowing background-free imaging, Time-Gating is particularly attractive because it enables to circumvent autofluorescence through the recording of the signal of long lifetime emitters. An objective of this thesis is thus to develop PNPs with luminescent properties adapted for time-gated imaging. In order for this type of imaging to work, the probe should exhibit long PL lifetime and photostability over time, so the choice of luminophore to encapsulate must be done accordingly.

From the large diversity of existing contrast agents, photoactive transition-metal complexes that include the d^6 species Ru^{II} ,¹⁴² Os^{II} ,¹⁴³ Ir^{III} ,¹⁴⁴ and Re^I ^{145,146} are known to be photostable and long-lifetime luminophores, which enable time-gated detection for suppression of short-lifetime background autofluorescence.^{147–150} They exhibit large Stokes shifts, principally due to charge transfer between the ligand and the metal, facilitating separation of excitation and emission wavelengths and limiting PL self-quenching. These photophysical features make such transition-metal complexes interesting candidates for *in cellulo* imaging. However, most of the photophysical properties of these complexes are reported in organic solvents¹⁴⁷ because of their low solubility in aqueous media, which induces a non-controlled aggregation and a loss of PL.

To transfer their PL brightness and long lifetime to a complex biological system they must be shielded from the surrounding environment. To this end, a strategy is to encapsulate the luminophores inside polymeric NPs, as it should provide protection from the aqueous media. Up to now, transition-metal complexes have been mainly encapsulated in inorganic structures such as crystals¹⁵¹, zeolites^{152,153} or silica nanoparticles¹⁵⁴ with the purpose of improving their catalytic performance. More particularly, ruthenium complexes have also proven to be good candidates for anticancer therapy when encapsulated in single-walled carbon nanotubes¹⁵⁵ but also in organic matrices such as liposomes,¹⁵⁶ micelles,¹⁵⁷ or polymeric NPs.^{117,158,159} However, encapsulation of PL transition-metal complexes have rarely been explored,^{160,161} and from these examples few information about the concentration of luminophore inside the NPs or their organization can be extracted.

Because of this lack of knowledge, the properties and the performance of PNPs loaded with high amounts of luminescent transition-metal complexes are largely unknown, and a systematic investigation of such nanohybrids should be conducted. In this spirit, the formulation of PNPs loaded with different concentrations of rhenium complexes was achieved. Polymers with different nature or bearing different amounts of charges were used for the formulation of the luminophore loaded PNPs. The loading and PNPs preparation conditions were varied to offer a large panel of nanoprobes. The sizes, PL intensities and lifetimes of the

formed PNPs were measured and compared in order to study the influence of the complex loading and polymer chemistry.

The complexes revealed to have an enhanced brightness when encapsulated inside PNPs but their good encapsulation remained difficult to prove and their emission located in a region of strong autofluorescence. To try and answer both problems, the transition-metal complexes were co-encapsulated with cyanine dyes inside PNPs. Due to FRET phenomenon, these new systems exhibited an emission shifted in the NIR region (700 – 900 nm) and presented important variations in their PL lifetimes. These new characteristics were studied with both steady-state and time-resolved analysis and enabled to better understand the encapsulation and organization of the luminophores inside the PNP. Eventually, the potential of the designed nanohybrids was evaluated for bioimaging applications.

1. Rhenium Loaded PNPs

1.1 Synthesis and characterization of Re complexes

As luminescent compounds, we selected two types of Re-based $^3\text{MLCT}$ emitters. Indeed, $[\text{Re}(\text{diimine})(\text{CO})_3\text{L}]$ emitters display impressive QYs up to 41% under anaerobic conditions,¹⁶² making them ideal candidates for exploration in this study. Two types of Re-based $^3\text{MLCT}$ emitters of the general formula $[\text{Re}(\text{diimine})(\text{CO})_3(\text{MeCN})]$ with the diimine being either 2,2'-bipyridine or 1,10-phenanthroline (MeCN = acetonitrile) were synthesized by a partner lab. It was previously shown that bulky hydrophobic counterions form highly apolar salts with cationic dyes and thus ensure effective encapsulation into the apolar matrix of polymer NPs with minimized dye leakage and aggregation caused quenching (ACQ).^{163,164} It was decided to apply the same strategy with the rhenium complexes so the bulky hydrophobic counterion F6-TPB (tetrakis(3,5-bis(trifluoromethyl)phenyl)borate) was introduced through ion-exchange to produce compounds of the general formula $[\text{Re}(\text{diimine})(\text{CO})_3(\text{MeCN})] \text{F6-TPB}$ (diimine = 1,10-phenanthroline or 2,2'-bipyridine, abbreviated Re(phen) and Re(bipy), Figure 28). All compounds were characterized by ^1H , ^{13}C , ^{11}B , and ^{19}F NMR, mass spectrometry, and elemental analysis (Annexes, Figure 68 to Figure 77).

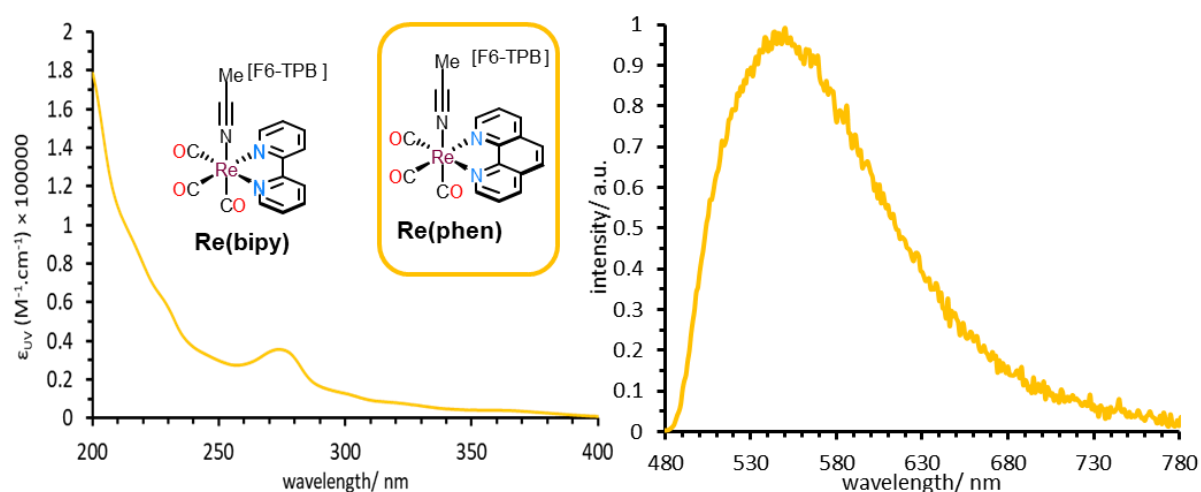


Figure 28 : Absorbance (left) and emission(right) spectra of Re(phen) in ACN. Inset: Structures of Re(bipy) and Re(phen)

The spectroscopic properties of the molecular Re complexes were explored in aerated acetonitrile (Table 1). The absorption spectra for the free Re complexes showed two main features (Figure 28, Annexes Figure 78), with ligand centered π - π^* transitions dominating <320 nm, and broad visible maximum apparent at *ca.* 280 nm, corresponding to the 1 MLCT absorption band. The steady state photoluminescence spectra of both complexes gave broad structureless 3 MLCT emission at *ca.* 550 nm (Figure 28, Annexes Figure 79). Time-resolved measurements revealed mono-exponential decays for the 3 MLCT of 150 ns and 247 ns for Re(bipy) and Re(phen), respectively (Annexes Figure 80, Figure 81). QY measurements gave similar results for both complexes, 6-7% in aerated acetonitrile solutions.

Table 1. Photophysical properties (absorption and emission maxima λ_{abs} and λ_{em} , PL lifetime τ , and PL QY Φ) of the obtained Re complexes in aerated acetonitrile at 298 K. ^a Excitation at 452 nm ^b Using [Ru(bipy)₃Cl₂] in water ($\Phi = 0.04$; $\lambda_{exc} = 450$ nm) as a reference.¹⁶⁵

	λ_{abs}/nm ($\epsilon / M^{-1}.cm^{-1} \times 10^5$)	λ_{em}/nm	τ/ ns (% component) ^a	$\Phi/ \%$ ^b
Re(bipy)	268 (23,800), 306 (15,700), 317 (19,500), 350 (4,300)	558	150 (100%)	7
Re(phen)	273 (35,500), 366 (3,700)	548	247 (100%)	6

1.2 Synthesis and characterization of NPs loaded with Re complexes

Once the transition metal complexes characterized, they were encapsulated in polymeric nanoparticles using the nanoprecipitation method. In a first step, we optimized encapsulation of the Re complexes by varying their amount and the used polymer (Figure 29). In particular, poly(ethyl methacrylate) (PEMA) based polymers bearing different amounts of charged methacrylic acid (noted COOH) to tune the particle size were used. On the other hand,

copolymers of EMA with the hydrophilic hydroxyethyl methacrylate (HEMA), and poly(lactic-co-glycolic acid) (PLGA), a polymer known for its biocompatibility and biodegradability, were used to investigate the influence of polymer nature and hydrophobicity. Nanoprecipitation of both complexes, Re(phen) and Re(bipy), with the different polymers yielded NPs over the entire investigated range of loadings (9 to 29 wt%), with sizes ranging from 20 to 70 nm according to DLS (Figure 29). From all the formulations analyzed, different observations can be made: First, both complexes yielded very similar results for the studied polymers and loadings, showing that small ligand modification on the encapsulated complex doesn't influence the encapsulation. Moreover, the amount of encapsulated complex led to no noticeable change in the size of the PNPs for a given polymer. Varying the polymer, however, enabled to increase up to a factor 3 the size of the PNPs. The hydrophilicity of the polymer also enabled to decrease the particle size, but not as strongly as the modification of charge. The smallest NPs of about 20 nm were obtained with PEMA-COOH-5%, the polymer having the highest fraction of charged groups, this trend being similar as when encapsulating organic dyes.⁹⁸ The use of PLGA implied a total change in the polymer backbone and hydrophobicity which didn't prevent the formation of NPs with relatively small size of about 35 nm. PLGA based NPs encapsulating Re(phen) were prepared either in milliQ water or phosphate buffer and yielded very different sizes, illustrating the influence of the aqueous media on PNPs formation. For selected examples, the sizes were also measured through TEM (Figure 29), yielding smaller sizes because TEM provides a number average of the hard-core diameter, but confirming the formation of spherical NPs with a monodisperse size distribution.

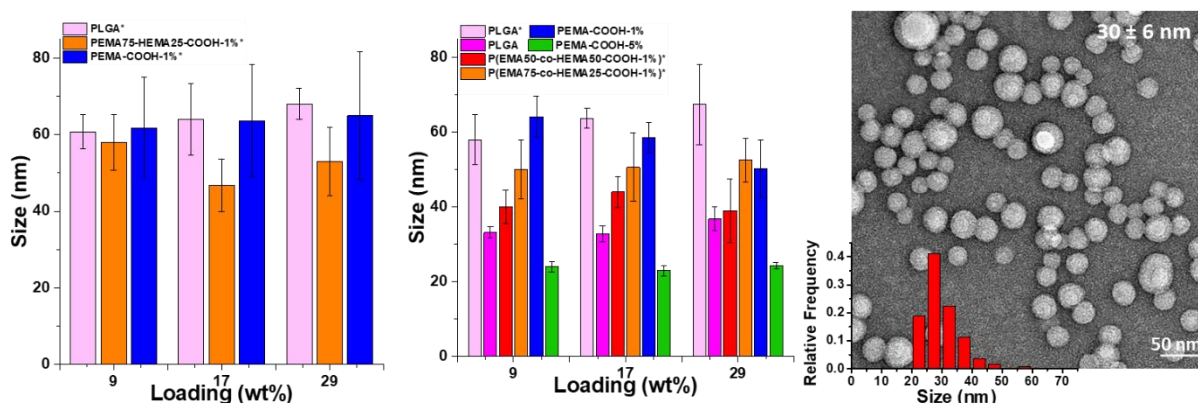


Figure 29: Size measured in DLS for PNPs loaded with Re(bipy) (left) and Re(phen) (middle), in legend * means the nanoprecipitation was made in milliQ water, otherwise in phosphate buffer (20 mM, pH 7.4). TEM picture of NPs with 29 wt% Re(phen) loading in PEMA-COOH-1%

From the size determined by DLS, the number of complexes encapsulated per PNP could be estimated using the size of the particle and the concentration of the Re complexes inside the NPs, going up to 11,000 Re complexes for the biggest NPs with the highest loadings (Table 2, see Materials and Methods for calculations). These numbers are directly depending mostly on the PNPs volume and the loading, the polymer density having a lower influence. These results allowed us to estimate the distances between Re complexes inside the NPs based on the Re complex concentration. Assuming that the Re complexes were homogeneously distributed inside the PNP, the mean center to center distance ranged from 2.8 nm for a loading of 9 wt%

in Re complex to 1.9 nm for the highest loading, which suggested proximal Re complexes inside the PNP.

Together, this yielded a high tuning potential, as the size of the PNPs could be finely controlled by modifying the structure of the polymer over a wide range of loadings. This detailed characterization suggested that our nanoprecipitation approach allowed us to obtain Re complex-loaded polymer NPs (metallo-organic nano-hybrids) with excellent control over size and loading. However, it should be noted that nanoprecipitation of Re complexes alone, *i.e.* without the polymer, under identical conditions also yielded nano-assemblies with circa 30 nm diameter. As preparation of PNPs with and without complex yielded NPs with different size, the aforementioned results were insufficient to quantify the actual encapsulation of the Re complexes within the NPs and consequently more characterizations are necessary to investigate the encapsulation ability of our system.

1.3 Spectroscopic Characterization

We were able to form stable solutions of monodisperse PNPs and tune their size by playing with the polymer chemistry. Moving forward into the characterization of the obtained PNPs, we aimed to assess their luminescent abilities. Absorption spectra of the Re complex loaded PNPs (Figure 30 for Re(phen), Annexes Figure 82 for Re(bipy)) showed a peak around 275 nm for Re(phen) and at around 320 nm for Re(bipy), similar to those observed for the complexes alone in acetonitrile solution and characteristic of the ligand-centered transitions. Noticeably, the difference between the absorbance spectra of the Re complex in ACN and in PNPs at the same concentration was relatively low, this demonstrated that scattering was quite moderate by comparison with absorption. Together with the linear increase of absorbance with loading, this suggested a good encapsulation efficiency of the Re complexes inside the polymer matrix.

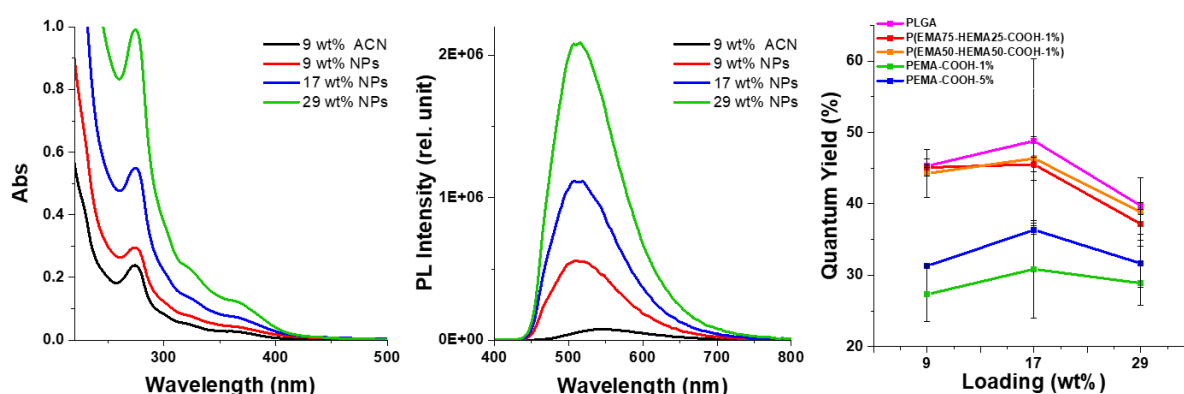


Figure 30: Absorbance (left) and PL intensities (right) $\lambda_{ex} = 275$ nm spectra of Re(phen) in solution in acetonitrile or encapsulated in PEMA-COOH-1%. (Samples marked 9 wt% ACN and 9 wt% NPs have the same concentration in Re(phen)). Right: QYs for different NPs loaded with Re(phen), using Re(phen) in ACN as a reference

Excitation of the Re(phen) and Re(bipy) loaded PNPs at, respectively, 275 and 320 nm, resulted in both cases in a broad emission between 450 and 700 nm (Figure 30 and Annexes Figure 82). The PL intensity increased linearly with the loading, with maxima at around 510 nm for Re(phen) and 515 nm for Re(bipy) loaded NPs, somewhat blue shifted compared to the

corresponding Re complexes in acetonitrile solution ($\lambda_{\max} \approx 550$ nm). Interestingly, the emission intensity increased more than fivefold, when encapsulating the Re complexes in polymer NPs, compared to their simple dissolution in acetonitrile (for corresponding concentrations). For further characterization, we then focused on Re(phen) loaded polymer NPs, which exhibited a higher PL intensity than Re(bipy) when encapsulated in NPs. QY measurements in the case of the Re(phen) loaded NPs revealed that Re(phen) showed QYs up to 8-fold higher when encapsulated inside NPs (QY between 25 and 50%, Figure 30) compared to when dissolved in organic solvent (QY = 6%, Table 1). One might anticipate that energy transfer from the $^3\text{MLCT}$ state of Re to triplet oxygen, which is one of the major quenching pathways of the luminescence, may be reduced by a decreased diffusion of oxygen in the solid NPs. Considering the measured QYs, two groups of Re(phen) loaded NPs appeared depending on the used polymers: the PNPs made with the more hydrophilic polymers (PLGA and EMA/HEMA copolymers) had higher QYs than the more hydrophobic PEMA based ones. We could also see that the extent of loading had little, or at least no clear, influence on the QY, suggesting that ACQ was not very important for these complexes. This is in line with the very large Stokes shift of these complexes, which limits homo-energy transfer and self-quenching. The brightness per NP was estimated based on the number of encapsulated Re complexes per NP, the QY, and the extinction coefficient of the Re complexes (Table 2). The brightness increased with the loading and the particle size and a maximum brightness of $1.4 \times 10^8 \text{ L mol}^{-1} \text{ cm}^{-1}$ was achieved for P(EMA50 –HEMA50-COOH-1%) PNPs. These observations suggested that the encapsulation of the Re complexes inside polymeric NPs was a good way to enhance its emission and offered the possibility to create very bright Re PL.

Table 2: Photophysical properties of PNPs

Polymer	Loading (wt%)	Number of complexes per PNP	$\epsilon_{\text{PNP 273nm}}$ ($\text{M}^{-1} \cdot \text{cm}^{-1}$)	Brightness ($\text{M}^{-1} \cdot \text{cm}^{-1}$)
PEMA-COOH-1%	9	6157	2,2E+08	6,0E+07
	17	8844	3,1E+08	1,0E+08
	29	9227	3,3E+08	9,5E+07
PEMA-COOH-5%	29	1020	3,6E+07	1,1E+07
PEMA75-HEMA25-COOH-1%	29	4379	1,6E+08	6,0E+07
PEMA50-HEMA50-COOH-1%	29	10990	3,9E+08	1,4E+08
PLGA	29	4649	1,7E+08	6,6E+07

1.4 Time-Resolved Characterization

To complete our PNP analysis, we studied the influence of encapsulation of Re(phen) complexes inside polymer NPs on their PL lifetimes. Compared to Re(phen) in solution (250 ns) the average PL lifetime strongly increased to over 3 μ s inside the polymer NPs (**Table 3**), which provided good evidence for strongly reduced PL quenching when the Re(phen) complexes are protected from the environment by the polymer matrix. The double-exponential PL decay of Re(phen) in the NPs showed a shorter (~ 1.0 μ s) and a longer (~ 4.6 μ s) component, most probably related to Re(phen) complexes closer to the NP surface (prone to quenching *via* the environment, named quenched Re) and closer to the NP center (better protection from the outer environment, named unquenched Re). Increased Re(phen) loading (from 9 wt% to 29 wt%) resulted in an overall better protection of the complexes from quenching by the environment, as shown by an amplitude increase of the longer component for high loaded NPs and thus, increasing amplitude-averaged PL lifetimes (3.1, 3.4, and 3.6 μ s, respectively).

Table 3 : Fit from Re(phen) PL decay curves, lifetimes (τ), amplitude fractions (α) and overall amplitude-averaged lifetimes ($\langle \tau \rangle$)

Loading (wt%)	τ_{D1} (μ s)	α_{D1}	τ_{D0} (μ s)	α_{D0}	$\langle \tau_D \rangle$ (μ s)	rel. errors
9	0.88	0.43	4.69	0.57	3.07 \pm 0.18	3%
17	0.96	0.33	4.64	0.67	3.42 \pm 0.21	3%
29	1.14	0.27	4.51	0.73	3.61 \pm 0.22	3%

2. Co-encapsulation of Re complexes and cyanine dyes

Re complexes emit in a spectral region with strong autofluorescence in biological environments, inducing high background signals. Hence, we aimed at shifting the emission wavelength towards the NIR, which would significantly reduce autofluorescence background. NIR-emitting cyanine dyes are a typical example of fluorescent probes for autofluorescence-free and/or deep-tissue imaging.¹⁶⁶ In the case of transition-metal complexes, tuning the emission can be achieved by varying the energy landscape, which requires to profoundly change the chemical structure of the ligands.^{167–170} An alternative approach is the use of Förster resonance energy transfer (FRET) to NIR dyes, which can also induce a bathochromic shift in the emission of the luminescent system. This possibility was shown for a Ru-cyanine dyad, consisting of a Ru complex covalently linked to a Cyanine 5 dye.¹⁷¹ The dyad could be used to induce long-lifetime downshifted PL, in which emission of Cyanine 5 ($\lambda_{em} = 660$ nm) was induced through excitation of the Ru ¹MLCT absorption band ($\lambda_{ex} = 450$ nm), which was operated *via* a FRET mechanism. Here, we used a similar FRET approach to shift the emission of the Re complexes into the NIR *via* a simple co-encapsulation of cyanine dye FRET acceptors. A Cyanine 5 based DiD was selected as FRET acceptor and combined with the bulky hydrophobic F5-TPB as counterion, noted Cy5/F5-TPB or simply Cy5 in the following (Figure 31), to improve encapsulation and avoid ACQ.¹⁷²

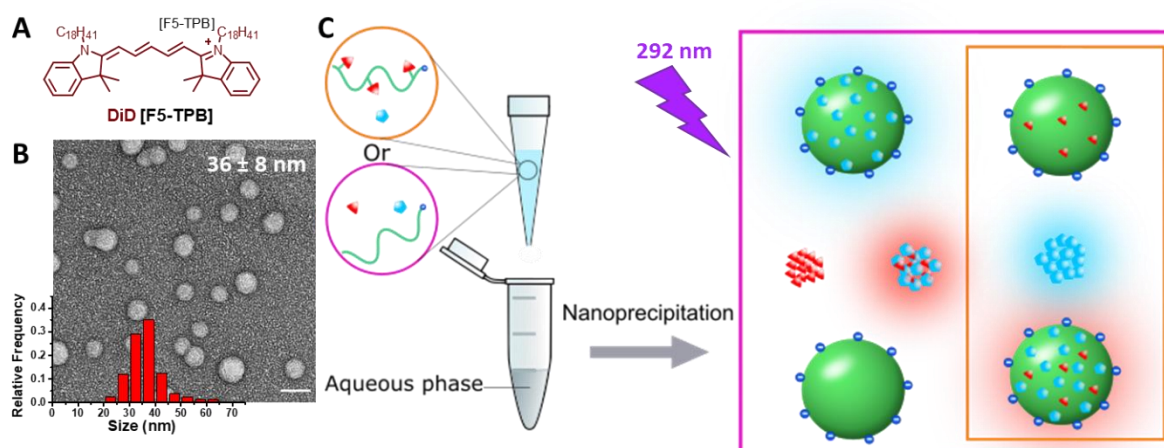


Figure 31: A) Structure of DiD F5-TPB (Cy5) B) TEM picture of Rephen 29 wt% and Cy5 2wt% in PEMA-COOH-1% PNPs C) Nanoprecipitation scheme for co encapsulation, with the Cy5 grafted or not to the polymer. In the magenta square are the different possible nano-assemblies for the non-grafted polymer and in the orange for the grafted polymer

2.1 PNPs Formation and Steady State Spectroscopy

The co-encapsulation of 29 wt% of the Re(phen) complex with increasing amounts of Cy5 from 0.1, 0.5, 1, 2, to 5 wt% in PEMA-COOH 1% yielded PNPs with only slight influence of the dye on the particle size as shown by TEM imaging (Figure 31). DLS characterization is not possible not possible due to Cy5 absorption (see DLS, Introduction).

Indeed, theoretically during the nanoprecipitation process the rhenium complex, the cyanine and the polymer can assemble into very different nano-objects (Figure 31). Indeed, apart from the wished co-encapsulation inside PNPs, only one or none of the luminophore can be encapsulated in the PNPs, creating empty PNPs and luminophores aggregates. Here again, the luminophores may aggregate together or separately. The study of the PL of the formed suspensions will help identify what phenomenon occurs with this system. In particular, study of the resulting FRET between Re(phen) and Cy5 is an excellent method to extract information on the nanometer scale organization of the luminophores inside the PNPs. Absorption spectra of the obtained PNPs (Figure 32A) showed a linear increase of the absorbance of Cy5 with loading and constant Re(phen) absorbance, suggesting a good encapsulation of both luminophores. The emission spectra showed a continuous decrease in the Re(phen) complex PL intensity with increasing Cy5 loading (Figure 32B). This decrease shows that the two luminophores are interacting and thus rules out the possibility of Re(phen) assembling without the Cy5 either in or out of the PNPs. At the same time, Cy5 emission appeared even at the lowest Cy5 loading, and increased up to 2 wt% Cy5 loading. Considering the PL intensities in the presence and in the absence of the acceptor (Cy5), the FRET efficiencies of these systems (Table 4) could be calculated (See MM FRET efficiencies). Globally, the FRET efficiency

increased continuously with the amount of acceptor dyes going from 10 to 90 %. The evaluation of the PL intensity of Cy5 by direct excitation (292 nm) resulted in only very low contribution. (Table 4, Annexes Figure 83) In this context it is noteworthy that the Re(phen) donor PL was only slightly quenched when adding 0.1 wt% of Cy5 acceptor, whereas the acceptor PL increased significantly, which means that the overall PL brightness of the Re(phen)-Cy5 PNP system was improved via Re(phen)-to-Cy5 FRET.

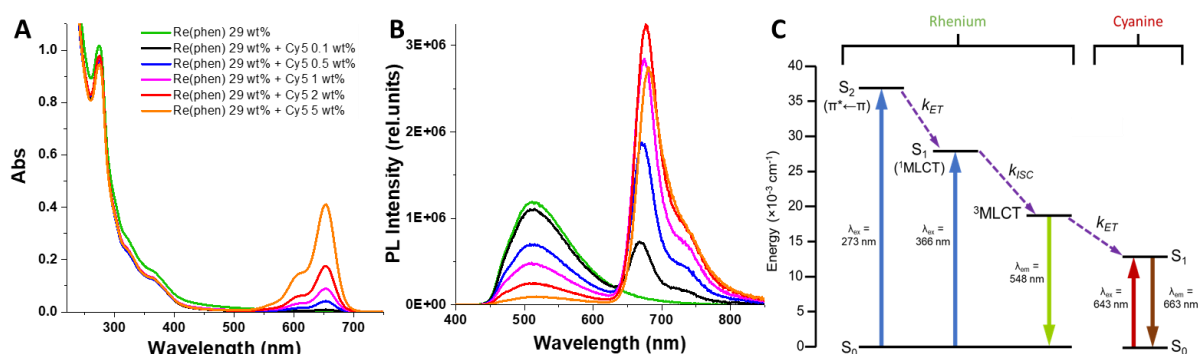


Figure 32 : A) Absorption and B) PL Intensity spectra of NPs loaded with 29 wt% of Re(phen) and increasing amounts of Cy5, $\lambda_{ex} = 292$ nm. C) Energy level diagram for downshifting energy transfer processes within Re(phen) and Cy5 loaded NPs.

This set of FRET experiment enabled to show that the two luminophores are interacting but could prove their encapsulation inside the polymer matrix. Nonetheless, energy transfer can also offer the possibility to further study the actual encapsulation of the Re complexes inside the polymer NPs. For this, Re(phen) were encapsulated into PNPs made with a polymer previously covalently grafted with Cy5 (Figure 31). In this case, FRET can only occur for Re(phen) encapsulated within the polymer NPs, and not for NPs formed from the Re(phen) complexes alone (Figure 31). Excitation of the Re(phen) complex gave a PL spectrum (Annexes Figure 84) corresponding to a Cy5 emission, accompanied by a strong decrease of the donor Re(phen) emission compared to NPs loaded with just Re(phen). The obtained decrease of Re(phen) emission was of the same order as for coencapsulation of Re(phen) and Cy5 at equivalent concentrations, indicating a very close proximity of Re(phen) and Cy5 attached to the polymer. In consequence, this result together with the arguments presented earlier, namely control of size through polymer and linear absorbance and PL of Re loaded NPs, supports the conclusion that the rhenium complexes are encapsulated inside the PNPs. Furthermore, the encapsulation efficiency can be estimated from the donor signal. If just a small portion of the Re(phen) were encapsulated, the remaining signal from the complexes not interacting with the Cy5 would be high. Here, the Re(phen) signal is very low, confirming the very good encapsulation efficiency.

Table 4. FRET efficiencies for NPs loaded with 29 wt% Re(phen) and increasing amounts of Cy5, according to PL intensities. a) Calculated for 50 nm NPs as described in ESI. b) for a Re(phen) loading of 29 wt%.

Cy5 loading (wt%)	Number of Cy5 dyes per NP ^a	Average distance between Cy5 molecules (nm)	Number of Re(phen) per Cy5	FRET efficiency (%)	Contribution of Cy5 to PL intensity without FRET (%)
0.1	32	12.7	287	8	0.46
0.5	160	7.4	58	42	1.25
1	319	5.9	29	60	1.34
2	632	4.7	15	79	1.57
5	1534	3.5	6	92	3.32

2.2 Time Resolved Spectroscopy

In order to better understand the photophysics of PNPs loaded with Re complexes and Cy5, these systems were further investigated *via* time-resolved PL spectroscopy. In particular, we wanted to study very high local concentrations of Re(phen) complexes and FRET between Re(phen) complexes and Cy5 dyes. Understanding the photophysics of such hybrid systems is essential for an efficient implementation into biosensing and bioimaging applications. The energy-level diagram depicted in Figure 32C gives a schematic view of the assumed downshifting behavior of the system co-encapsulating Re(phen) and Cy5. In the absence of Cy5 the Re(phen) ³MLCT emission can be engendered *via* excitation of the ligand-centered S₁ ($\pi^* \leftarrow \pi$) or ¹MLCT absorption bands. Consequently, in the co-encapsulation particles containing Re and cyanine – and considered the very efficient FRET behavior – either of the Re(phen)-based absorption bands give rise to a populated ³MLCT state which thus sensitizes the S₁ absorption band of the Cy5 dye at 643 nm with resultant Cy5 emission at 663 nm.

In a next step, the influence of the presence of Cy5 acceptors was studied by measuring the PL decays of both Re(phen) and Cy5 (Figure 33). The intrinsic PL lifetime of Cy5 (few ns) being around 1000-fold shorter compared to the Re(phen) PL lifetime (~3.6 μ s, Table 3), the more efficient the FRET is, the faster the Re(phen) PL lifetimes should be quenched. The first observation was that quite significant differences are found between the Re(phen) donor (Figure 33A) and Cy5 acceptor (Figure 33B) PL decays. The Re(phen) PL decays were relatively long, with amplitude-averaged PL decay times ranging from 3.26 μ s (Re(phen) with 0.1 wt% Cy5) to 0.67 μ s (Re(phen) with 5 wt% Cy5). The Cy5 PL decays were significantly shorter, with amplitude-averaged PL decay times ranging from 0.69 μ s (Re(phen) with 0.1 wt% Cy5) to 0.06 μ s (Re(phen) with 5 wt% Cy5). The corresponding system-averaged FRET efficiencies calculated with the obtained lifetime, designated as $\langle E^*_{\text{FRET}} \rangle$ have values of ~80% and ~98% (Table 5, Annexes for details on calculations). In addition, the PL intensities of the Cy5 dyes on the very

short time scale (below ~ 200 ns in Figure 33B) were extremely high compared to those on the longer time scale (>500 ns). This very different decay behavior of FRET-quenched Re(phen) and FRET-sensitized Cy5 strongly suggested that there were many Re(phen) donors that did not interact with Cy5 acceptors and thus, $\langle E^*_{\text{FRET}} \rangle$ values were much lower when measured via Re(phen) PL intensity.

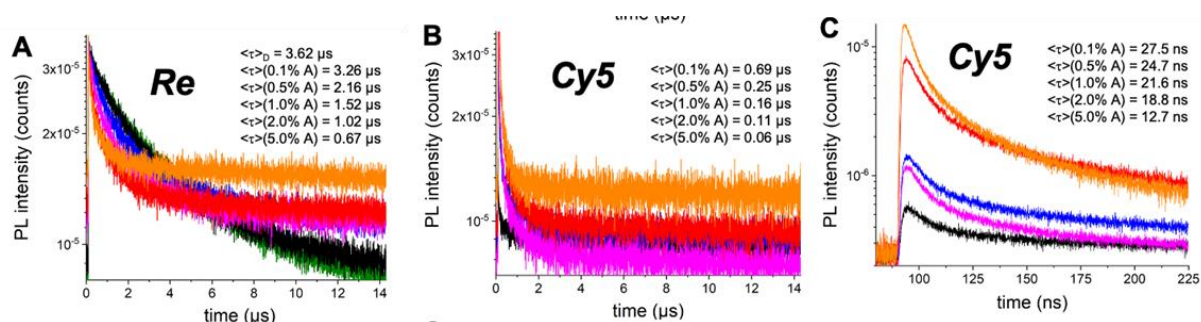


Figure 33: PL decays (intensities in each graph were normalized by the number of excitation pulses) and amplitude-averaged lifetimes of Re(phen) loaded NPs containing distinct fractions of Cy5 (green: 0%; black: 0.1%; blue: 0.5%; magenta: 1%; red: 2%; orange: 5%) measured for Re(phen) donor (A: 515 ± 8 nm,) and Cy5 acceptor (B and C: 700 ± 8 nm, observation window 14 μs and 200 ns, respectively,) emission. Excitation via a 303 ± 10 nm light emitting diode (pulse length < 1.2 ns).

A high fraction of non-interaction Re(phen) is possible, in particular when the acceptor doping is very low. Indeed, in this case the number of Re(phen) donors per Cy5 inside the NPs is very high (Table 4). Therefore, the FRET efficiencies calculated by donor PL intensity (Table 4) represent the system-averaged FRET efficiencies ($\langle E^*_{\text{FRET}} \rangle$), which takes into account both interacting and non-interacting Re(phen) donors and do not provide any donor-acceptor distance information. This means that different luminophore organizations inside the PNP can lead to the same final donor intensity, e.g., 100% donors with 50% FRET efficiency result in the same system-averaged FRET efficiency as 50% non-interacting donors plus 50% donors with 100% FRET efficiency. Taken literally, this would correspond to an organization where, in the first case (Figure 34A), all donors (blue) are equally spaced from the acceptor, with a distance close to the Förster radius and thus each contributing to the FRET with a 50% efficiency. In the second case (Figure 34B), half of the donors are really close to the acceptor, thus interacting strongly and contributing to the FRET with an efficiency of 100% whereas the other half are too far to interact. Hence, the actual FRET efficiencies (which only include donors that transfer energy to an acceptor) are most probably much higher than shown in the Re(phen) PL decays and the steady-state PL spectra. This assumption would also explain why the Cy5 acceptor sensitization is substantially stronger than the Re(phen) donor quenching (Figure 32C). Very efficient Re(phen)-to-Cy5 FRET becomes the preferred energy pathway compared to Re(phen)-Re(phen) homo FRET (which leads to self-quenching due to the increasing probability of ending up in a dark state with an increasing number of homo-FRET steps)¹⁷³ or Re(phen) PL quenching *via* the environment. This FRET configuration with reduced PL losses results in an overall emission amplification of the donor-acceptor system compared to the NPs loaded with Re(phen) alone, as observed in Figure 32B. Thus, the PL QY of Re(phen) is not the same for

Re(phen) loaded NPs and Re(phen)-Cy5 loaded PNPs and the Re(phen) loaded PNPs PL spectrum cannot be used as correct donor-only FRET reference.

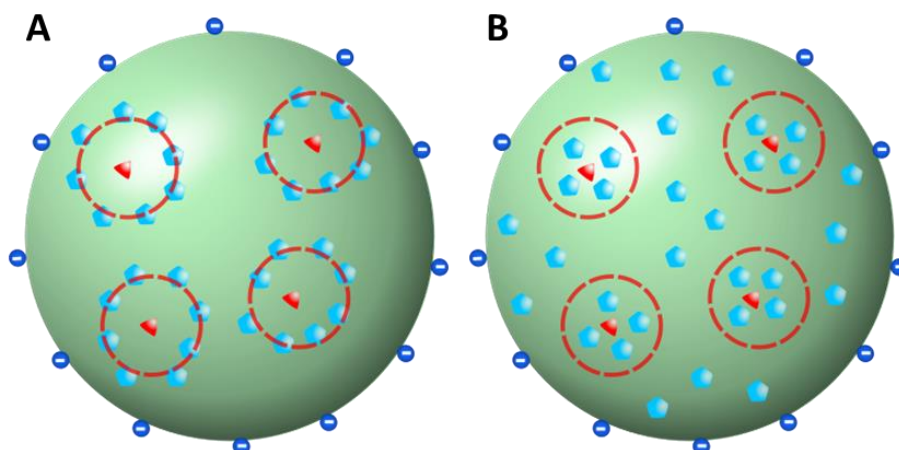


Figure 34: Example of luminophore loaded PNPs with a FRET efficiency of 50 %. Red dashed circle represents the Förster radius R_0 . A) All donors are participating equally to the FRET with a 50 % efficiency each B) 50 % of the donors are participating to the FRET with 100 % efficiency and 50 % are not participating

The time-resolved measurements showed the limitations of the information that can be extracted from the steady-state PL intensities, but a more careful analysis from these data can also reveal these missing informations. Indeed, PL decays could, in principle, be distinguished between the interacting and non-interacting components for FRET. If the non-interacting Re(phen) component can be identified in the decay curves, it is possible to extract it from the FRET components and an actual FRET efficiency, which considers FRET-pairs only, can be calculated. However, this can be quite challenging when the donor alone already possesses a multi-exponential decay (due to environmental quenching), which was the case of our Re(phen) complex-loaded NPs. Therefore, an approach previously described was applied, based on the fitting of decays from lanthanide complexes with multiexponential decays that are used for FRET (see Equations 8 to 13 in ESI).^{174,175} The method, briefly described in the following, has been applied to both Re(phen) and Cy5 decays measured on the 14 μs window (Figure 33A, B). Previously, the component of unquenched (and thus non-interacting) Re(phen) has been identified as the long decay time of Re(phen) loaded PNPs ($\tau_{D0} = 4.51 \mu\text{s}$, Table 3). The PNPs containing both Re(phen) and Cy5 were fit with a 3-exponential function, for which this long decay time of Re(phen) was fixed to account for the contribution of non-quenched Re(phen). The short decay component of Re(phen) ($\tau_{D1} = 1.14 \mu\text{s}$), corresponding to the complexes with a free emission (quenched but non-interacting with Cy5), could not be extracted from the FRET decays by fixing because it had the same time range as the FRET decays. Therefore, an amplitude correction factor (z_D , Equation 11 in the ESI)^{174,175} was used to correct for this contribution of free Re(phen) emission. By applying this method, two FRET decay times (τ_{DA1} and τ_{DA2}), their relative amplitudes (α_{DA1} and α_{DA2}), a relative donor amplitude (α_{DA0}), the donor correction factor (z_D), an average FRET decay time ($\langle\tau_{DA}\rangle$), an average FRET efficiency ($\langle E_{\text{FRET}} \rangle$), an average decay time of the complete decay ($\langle\tau\rangle$), and a system-averaged FRET efficiency ($\langle E^*_{\text{FRET}} \rangle$, taking into account quenched and unquenched components) could be determined (Table 5 for Cy5 decay, Annexes Table 7 for Re(phen)).

Whereas the overall amplitude-averaged decay time ($\langle\tau\rangle$) resulted in FRET efficiencies ($\langle E^*_{\text{FRET}}\rangle$) that corresponded quite well to the ones determined by steady-state intensities (because also the PL decay contains all donor components – *vide supra*), the FRET decay times ($\langle\tau_{\text{DA}}\rangle$) and FRET efficiencies of the actual FRET pairs ($\langle E_{\text{FRET}}\rangle$) were significantly larger, in particular for the NPs containing few Cy5 (0.1, 0.5, and 1 wt%), which showed strong contributions of Re(phen) unquenched PL (61, 34, and 20% relative donor amplitude). For the PNPs with higher amounts of Cy5 (2 and 5 wt%), the differences were not that strong because of the significantly lower contributions of non-quenched Re(phen) (13 and 10% relative donor amplitude) to the PL (Annexes Table 7). This important contribution of the unquenched Re(phen) inevitably led to large errors, which were even larger (due to error propagation) when calculating FRET efficiencies (see, e.g. FRET efficiencies for Re(phen) loaded NPs with 0.1% Cy5, Annexes Table 7)

Table 5: Fit (from Cy5 PL decay curves in **Figure 33B**) lifetimes (τ) and amplitude fractions (α) and calculated correction factors (z_A), amplitude averaged FRET lifetimes ($\langle\tau_{\text{AD}}\rangle$), average FRET efficiencies ($\langle E_{\text{FRET}}\rangle$), overall amplitude-averaged lifetimes ($\langle\tau\rangle$), lifetime system-averaged FRET efficiencies ($\langle E^*_{\text{FRET}}\rangle$), and intensity system-averaged FRET efficiencies (int. $\langle E^*_{\text{FRET}}\rangle$).

Cy5	τ_{AD1} (μs)	α_{AD1}	τ_{AD2} (μs)	α_{AD2}	α_{AD0}	rel. errors
0.1%	0.031	0.16	0.41	0.84	0.128	5%
0.5%	0.025	0.21	0.35	0.79	0.036	5%
1.0%	0.021	0.22	0.31	0.78	0.020	5%
2.0%	0.020	0.27	0.25	0.73	0.012	5%
5.0%	0.014	0.37	0.14	0.63	0.006	5%

Cy5	z_A	$\langle\tau_{\text{AD}}\rangle$ (μs)	$\langle E_{\text{FRET}}\rangle$	$\langle\tau\rangle$ (μs)	$\langle E^*_{\text{FRET}}\rangle$	int. $\langle E^*_{\text{FRET}}\rangle$
0.1%	0.0466±15%	0.309±0.046	0.91±0.19	0.691±10%	0.81±0.13	0.08±0.02
0.5%	0.013±15%	0.268±0.031	0.93±0.16	0.248±10%	0.93±0.15	0.41±0.08
1.0%	0.0071±15%	0.244±0.026	0.93±0.16	0.161±10%	0.96±0.15	0.60±0.12
2.0%	0.0042±15%	0.183±0.020	0.95±0.16	0.110±10%	0.97±0.16	0.80±0.16
5.0%	0.0021±15%	0.093±0.010	0.97±0.16	0.059±10%	0.98±0.16	0.92±0.18

Relative errors provided in the table are related to τ and α and were estimated. Errors for z_A , $\langle\tau_{\text{AD}}\rangle$, $\langle E_{\text{FRET}}\rangle$, $\langle\tau\rangle$, $\langle E^*_{\text{FRET}}\rangle$, and int. $\langle E^*_{\text{FRET}}\rangle$ (intensity calculated system-averaged FRET efficiency with intensity errors estimated as 10%) were calculated using error propagation.

Because the FRET-sensitized Cy5 emission (700±8 nm) contained almost no background from non-quenched Re(phen), evaluation of the PL decays of Cy5 (Figure 33B) could possibly reveal more accurate FRET efficiencies. The results clearly show that even for very low Cy5 fractions

(0.1 wt% and 0.5 wt%), the FRET efficiencies were very high (>90%), which confirmed that the intensity and lifetime evaluations of the Re(phen) donor emission strongly underestimated the FRET efficiencies. This also confirmed that the Re(phen) donor emission at low Cy5 fractions contains a strong contribution from non-quenched Re(phen). The FRET efficiencies constantly increased from 0.91 (for 0.1 wt% Cy5) to 0.97 (for 5 wt% Cy5), suggesting that for increasing Cy5 fractions not only more FRET pairs were formed but also the average donor-acceptor distance decreased. Considering the Re(phen)-Cy5 FRET pair Förster radius of $R_0 = 3.7$ nm (see Introduction for calculation) and the measured FRET efficiencies, the average donor-acceptor distance decreased from 2.5 to 2.1 nm. These values were not accessible by simply considering the NP sizes and Re(phen) and Cy5 loading ratios. However, those volume-concentration considerations are still useful for evaluating the FRET distance calculations. When going from 0.1 to 5 wt% Cy5 loading, the average distance between Cy5 dyes in the NPs decreases from more than 12 nm to 3.5 nm, which means that at 5 wt% loading on average all Re(phen) complexes lie within a distance of less than 1.8 nm to a Cy5 dye. However, in the case of 0.1 wt% the majority of Re(phen) complexes are at distances $>R_0$.

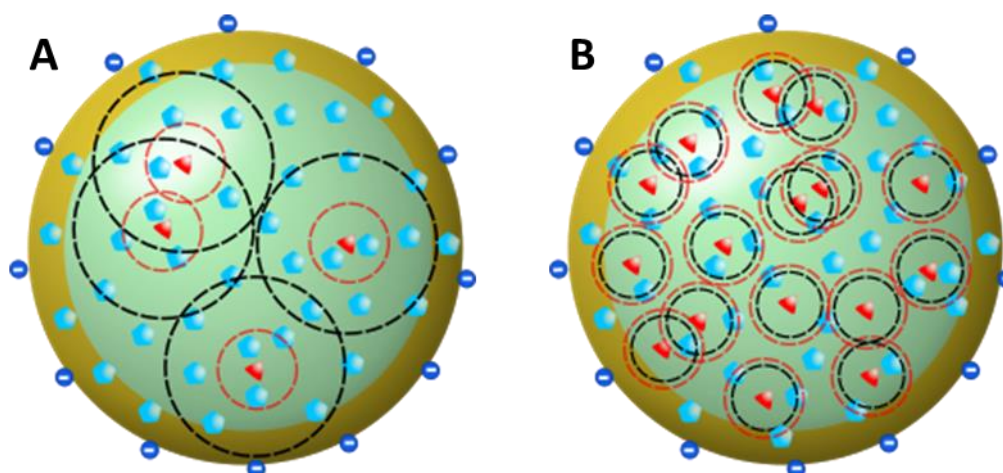


Figure 35: Scheme of the theoretical luminophore organization (with Re(phen) in blue and Cy5 in red) inside the PNP for A) low concentration and B) high concentration in Cy5. The unquenched Re(phen) are in the middle of the PNP (green) whereas the quenched NPs are at the surface (orange). Red dashed circle represents the Förster radius and black dashed circle represents the average Cy5 distance.

Whereas the average FRET distance estimations are within a reasonable range when considering the size and loading ratios of the Re(phen)-Cy5 PNPs, they still seem to be slightly overestimated. Considering that the very short PL decay component of Cy5 (Figure 33B) could not be properly resolved on the 14 μ s time scale that was necessary to appropriately fit the Re(phen) donor decays, we also recorded Cy5 PL decays in a 200 ns window after pulsed excitation (Figure 33C). These fit results (Equation 19 to 21 in the ESI) revealed very short decay time components (amplitude-averaged lifetimes between 12.7 ns and 27.5 ns) that correspond to FRET efficiencies of $\sim 100\%$ and further confirmed that the formed Re(phen)-Cy5 donor-acceptor pairs provided very high FRET efficiencies, *i.e.*, all Cy5 dyes were in very close contact to at least one Re(phen) donor. These observations, associated with the steady-state analysis, are compatible with the hypothesis of an homogeneous distribution of the luminophores inside the PNPs.

The very efficient FRET and very close donor-acceptor distances revealed by time-resolved spectroscopy are very interesting, as they allow to efficiently shift the PL of these NPs into the NIR through simple coencapsulation of the Re(phen) complexes and Cy5, without the need to chemically link the two. This results in luminescent NPs with a very large Stokes shift and a very high particle brightness through the high loading with Re(phen) complexes and a nearly complete absence of ACQ. Yet, the intuitively very positive result of high FRET efficiencies also comes with a drawback: The microsecond PL lifetimes of Re would have been very beneficial for time-gated FRET detection,⁶⁷ providing higher photon flux compared to lanthanide-based time gating (because a microsecond decay allows for 1000 times more excitations per time than millisecond decays) while still efficiently suppressing autofluorescence background (in the nano- to micro-second range). However, with a FRET efficiency close to unity, the interesting capability of shifting the emission to the NIR region (Cy5) cannot work for microsecond time-gating because the FRET-sensitized Cy5 PL decay is too fast.

2.3 In vitro Application

Steady state and Time-Resolved analysis of NPs with Re(phen) and Cy5 co-encapsulated revealed that the luminophore assembly forms an efficient FRET system inside the PNPs. The donor to acceptor ratio strongly modulates the NPs luminescent properties, pushing to the NIR region their emission but reducing strongly their PL lifetime in the meantime. After these characterizations, the developed nanoprobe are tested for both TG applications and cell imaging.

In a first time, the inadaptability to conventional microsecond time-gating was confirmed, by using the NPs co-encapsulating Re(phen) and Cy5 for both time-gated PL detection on a conventional benchtop fluorescence plate reader and time-gated imaging inside live cells. Using pulsed excitation at 303 nm and the shortest possible integration time of 20 μ s (gate time), and shifted the detection windows for both Re and Cy5 emission intensity maxima from 0 to 20 μ s (delay time). After 10 μ s of delay, the afterglow of the microsecond flash lamp started to decay until almost background emission was reached at a delay of 20 μ s (Annexes Figure 85). The decay of the PL signal of the Re(phen) loaded NPs was slightly longer, whereas increasing fractions of Cy5 resulted in a progressive decrease of the additional delay toward the pure decay of the lamp afterglow. The progressive decrease of the signal delay reflected the FRET-quenched PL lifetime and intensity found during the spectroscopic characterization (*vide supra*). For the Cy5 detection channel, all signals were very similar, which confirmed the much faster PL decay of the FRET-sensitized Cy5 inside the NPs. These results were confirmed on a microsecond time-gated microscope, for which the Cy5 emission channel could not measure any Cy5 PL (data not shown because the signal only consisted of background noise).

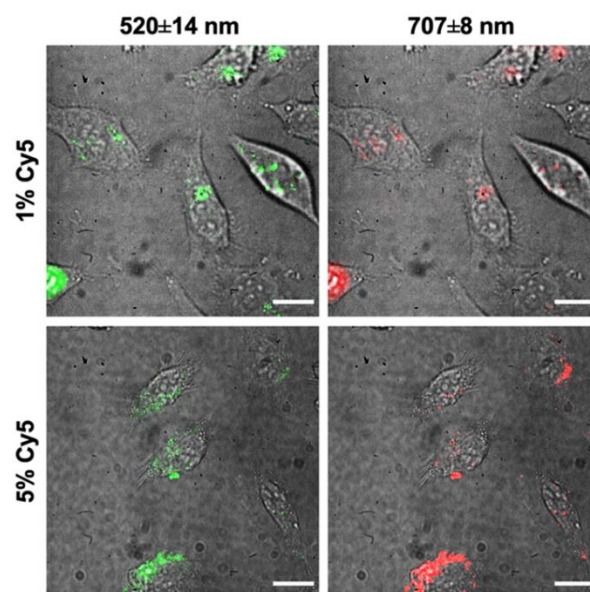


Figure 36: Cellular Imaging of PEMA-COOH 1% NPs loaded with 29 wt% Re(phen) and 1 or 5 wt% Cy5, excitation (λ_{exc}) at 320 ± 20 nm and emission (λ_{em}) at 520 ± 14 nm (green) for the donor channel and 707 ± 8 nm (red) for the acceptor channel. The images show the overlay of DIC and fluorescence. The first-row show images of NPs loaded with 29 wt% [Re(phen)] and 1 wt% Cy5 and the second-row show images of NPs loaded with 29 wt% [Re(phen)] and 5 wt% Cy5. Scale bars are $20\ \mu\text{m}$

In a second time, we investigated the peculiar PL emission of Re(phen) Cy5 loaded NPs for bio-application. Indeed, the very strong quenching-sensitization of the Re(phen)-Cy5 donor-acceptor pair and large spectral separation between excitation (~ 300 nm) and emission (680 nm, and up to 800 nm) associated to the large gap between Re(phen) and Cy5 emission could potentially be exploited for ratiometric sensing with significantly lower autofluorescence from the Cy5 NIR PL. Thus, the live cell imaging performance of the PNPs coencapsulating Re(phen) and Cy5 was evaluated with conventional steady-state fluorescence microscopy. HeLa cells were incubated for 3 h with the Re(phen)-Cy5 PNPs at different loading ratios (1 wt% and 5 wt% Cy5) and then performed live cell fluorescence imaging at 520 ± 14 nm (Re(phen) emission) and 707 ± 8 nm (Cy5 emission) under 320 nm excitation. Taking into account that for Re(phen)-Cy5 NPs in solution the Re(phen) emission was strongly quenched and Cy5 emission strongly sensitized (Figure 32), we selected a spectral bandpass filter for Re(phen) (~ 28 nm bandwidth) approximately twice as large as the one for Cy5 (~ 16 nm bandwidth).

For both Cy5 fractions (1 wt% and 5 wt%), clear PL signals of both Re(phen) and Cy5 could be detected inside the HeLa cells (Figure 36) with intensities that were adequate for ratiometric detection. The relative Cy5-to-Re(phen) PL intensities clearly increased with increasing Cy5 fraction (Annexes Figure 86), which confirmed the FRET behavior found for NPs in solution (Figure 32). Control experiments showed that there was no significant Cy5 emission detectable when Re(phen) loaded NPs (without Cy5) were incubated with HeLa cells (Annexes, Figure 87) and only autofluorescence (in the Re(phen) detection channel) and very faint Cy5 fluorescence (in the Cy5 detection channel) were detectable when Cy5 loaded NPs (without Re(phen)) were incubated with HeLa cells (Annexes Figure 88). Eventually, the imaging from top to bottom (z-

stacking) through the HeLa cells incubated with NPs confirmed their good internalization inside the cell (Annexes, Figure 89). The morphology of all imaged cells was unaffected, which showed that the endocytosis of the NPs had no significant impact on the live cells.

3. Conclusion

In this chapter, very high amounts of luminescent transition-metal complexes were successfully encapsulated in PNPs. Variation of the polymers used allowed tuning of particle size, from 20 to 70 nm, encapsulating up to 29 wt% of Re complexes corresponding to close to 10,000 Re complexes per PNP. The PL QYs of the Re complexes increased strongly upon encapsulation in polymer NPs, reaching close to 50% in some cases, which resulted in probes with PL brightness of up to $10^8 \text{ M}^{-1} \text{ cm}^{-1}$ and lifetimes of the order of 3-4 μs . Encapsulation thus helped to create very bright luminescent probes for use in bioimaging based on luminescent Re complexes. However, in view of excitation in the UV and emission around 500 nm, a strong autofluorescence background was expected in bioimaging applications. This problem can be overcome by co-encapsulation of the NIR dye Cy5 in the Re complex loaded PNPs. The nanoprobe containing both types of luminophores exhibited a shift in their emission into the NIR due to energy transfer, which revealed to be very efficient thanks to lifetime measurements and analysis. Going further, the combined analysis of steady-state and time-resolved data confirmed the efficient encapsulation of the transition-metal complexes inside the PNPs and suggested a very close proximity and homogeneous distribution of the encapsulated luminophores. This resulted in very bright, visible and NIR emitting NPs, which could be used for cellular imaging and showed good internalization and high contrast in the two wavelength regions. Thus, simple co-encapsulation of different luminescent compounds, proved to be a powerful strategy to tailor and optimize the emission properties of nanoprobe - without requiring a covalent link - even for such differing entities as organic fluorophores and transition metal compounds, opening the way to new classes of luminescent probes. This study also enlightens the challenges encountered when formulating these systems and the difficulty to conjugate all the desired features, which in our case was the NIR emission and long PL lifetimes. Indeed, a limitation of the Re-Cy5 PNPs was the inability to preserve the μs range lifetimes obtained for Re loaded PNPs. This very efficient FRET made microsecond time-gated imaging in the NIR impossible, the resulting objects showed a high brightness in combination with lifetimes in the range of hundreds of nanoseconds. In this way, by relying on set-ups allowing very fast TG, sub- μs TG imaging may become possible, combining higher photon flux than what is typically obtained in La and transition metal-based millisecond and microsecond TG with efficient background removal.

CHAPTER III: Molecular Up-conversion within PNPs for Live-Cell Imaging

Another strategy to reduce the background emission in bioimaging and biosensing is to take advantage of the Up-conversion (UC) emission of some luminophores. Indeed, on the contrary to downshifting (DS) processes such as fluorescence, UC does not occur naturally in complex biological media. Upconverting emitters, allow the generation of high energy photons through the combination of two or more low energy photons, and the resulting blue shifted emission is thus very specific from the probes. The most popular probes for this kind of imaging and sensing are up-conversion nanoparticles (UCNPs) based on an inorganic crystalline lattice into which lanthanide ions are doped both as sensitizers and activators have attracted large interest notably for their potential applications in bioimaging and biosensing, allowing background-free detection in complex biological media.^{176,177}

Following the seminal work of energy transfer up-conversion (ETU) by Piguet and co-workers in 2011,^{178,179} another type of UC material, namely molecular UC complexes, with precisely defined positions of the lanthanide ions within molecular structures has been in the recent focus of UC research.¹⁸⁰⁻¹⁸² Such molecular systems now include the full suite of UC mechanisms, namely (ETU),¹⁸³ excited-state absorption (ESA),^{184,185} cooperative luminescence (CL),¹⁸⁶ and cooperative sensitization (CS) UC.^{181,182} Here, the distance and even the type and number of neighbors can be precisely designed, which allows optimizing the upconversion efficiency using molecular design principles. The importance of the up-scaling of the local control on the molecular scale to many active centers or emitters has been exemplified by the recent appearance of molecular cluster aggregates,¹⁸⁷ while they do not resolve the problem of shielding them from the environment. However, up to now molecular up-conversion have been mainly reported in organic solvent, and only a few examples in water (deuterated or protonated).^{49,59,60} To enable the development of sensing and imaging applications using molecular UC, the first step is to transfer this luminescent process to aqueous media. For that, two major limitations have to be overcome: firstly, the low absorption cross section of lanthanide ions strongly limits the brightness of systems containing less than ten lanthanide ions. Furthermore, the OH vibronic overtones of water lead to strong quenching the PL of such small molecular entities, strongly limiting their possibilities for use in bioimaging and biosensing applications.

Herein, we introduce a new approach - exploiting the benefits of both the molecular and nanoparticular regimes - to achieve observation of molecular UC in aqueous media and thus to create brighter UC probes for bioimaging: Encapsulation of large amounts of molecular UC complexes in polymer NPs to achieve bright metalorganic UC emitters suitable for bioimaging, which remains an isolated approach.⁶¹ We chose a previously described nonanuclear UC complex, $[Yb_5Tb_4(acac)_{16}(OD)_{10}](OD)$ (acac = acetylacetonate), abbreviated Yb_5Tb_4 in the following.^{188,189} The complex (Figure 37A) can undergo an CS UC process when exciting two

proximate Yb(III) ions via excitation at 980 nm, followed by transferring its energy to a terbium ion, leading to upconverted emission in the visible region (Figure 37B).¹⁸⁸ The structure of this Ln complex is more elaborated than the rhenium complex encapsulated before, with 9 metallic centers that must stay in close proximity in order to preserve their PL properties. Up to date little studies have been dedicated to the encapsulation and organization of large metal-organic entities in polymer NPs at high loadings. Recently, Demina et al. have encapsulated upconversion nanoparticles (UCNPs) inside polymers to create large multifunctional NPs for chemo and photothermal therapy.⁶² This arrangement enabled to reduce the toxicity of the UCNPs, while ensuring colloidal stability with high PL intensity in aqueous media.

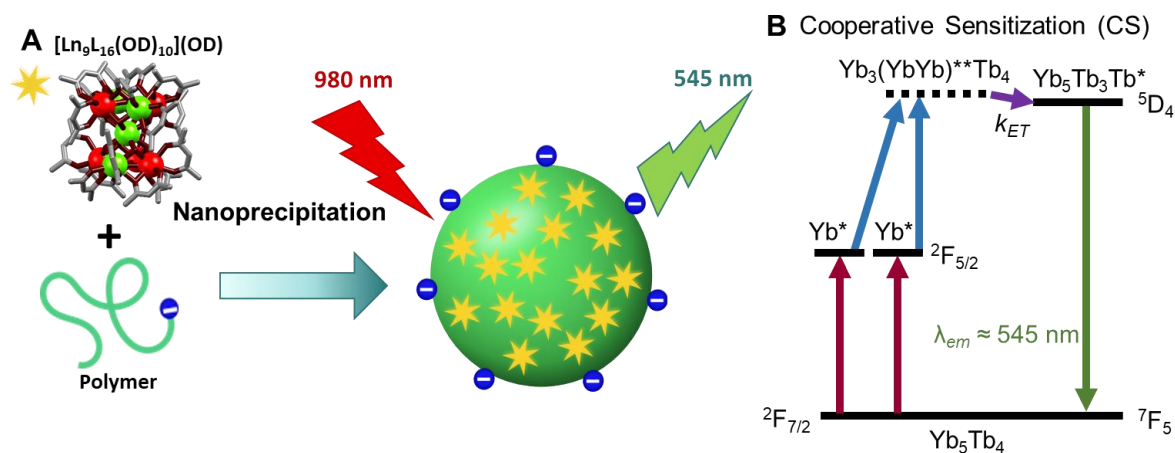


Figure 37: A) General Scheme of synthesis of UC PNP. B) Mechanism of cooperative sensitization

In this study, the possibility of encapsulation of hetero-nonanuclear UC complex, $[\text{Yb}_5\text{Tb}_4(\text{acac})_{16}(\text{OD})_{10}](\text{OD})$ in polymer NPs was investigated. The two major objectives therein were to achieve efficient and very high loadings inside the PNPs and transferring molecular CS UC to biological systems. First the encapsulation was optimized through adaptation of the complex, notably by varying the counterion, through the choice of the polymer, and by adjusting the assembly parameters. Then, the downshifting and up-converting emission of the prepared nanohybrids were measured and compared for a series of different PNP formulations. From these results, the influence of the complex loading and the size of the PNPs on the PL properties was discussed. This study was then extended to the influence of different environments and the stability of the UC emission in these, building the basis for the application of the obtained UC PNPs to cellular imaging.

1. Formulation and optimization

In the first step, the aim was to assemble PNPs of controlled size while encapsulating high amounts of Yb_5Tb_4 complexes. To achieve this, the nature of the load and the nature of the used polymers were varied but also the assembly conditions like concentrations, composition of solvents and aqueous phase and mixing conditions. Here, the outcome of nanoprecipitation was evaluated first by verifying the formation of PNPs using dynamic light scattering, followed by analysis of the absorbance, by finally measuring the extent of down-shifting

photoluminescence. The optimization of encapsulation and PNP formation was initially conducted in protic aqueous media (H₂O and phosphate buffer) but the first attempts to encapsulate the putative perdeuterated nonanuclear [Tb₉(acac)₁₆(OD)₁₀](OD) complexes proved to be challenging, resulting often in the formation of large aggregates rather than PNPs. By screening the different nanoprecipitation conditions, some polymer/complex combination yielded PNPs with a monodisperse size but poor down-shifting PL emission intensity of the Tb atoms when exciting the acac ligands (Annexes Figure 90).

Based on previous studies with fluorescent dyes,^{190,191} it was hypothesized that the increased hydrophobicity of the complex is a key to optimize encapsulation. Therefore, the original hydrophilic hydroxide counterion was exchanged for the bulky, hydrophobic tetrakis(3,5-bis(trifluoromethyl)phenyl)borate (F6-TPB) counterion (Figure 38A), known to facilitate encapsulation for organic dyes and metalorganic complexes.¹⁹¹ For the anion metathesis reaction, tests were performed on a protic diamagnetic analogue. The final compound, [Y₉(acac)₁₆(OH)₁₀](F6-TPB) was fully characterized by NMR (¹H, ¹³C, HSQC, HMBC, Annexes Figure 91 to Figure 95), which confirmed full exchange of hydroxide for the bulky lipophilic counterion. These conditions were then applied to the perdeuterated hetero-nonanuclear congener, resulting on the encapsulation of the resulting [Yb₅Tb₄(acac)₁₆(OD)₁₀](F6-TPB) complex (abbreviated Yb₅Tb₄/F6-TPB).

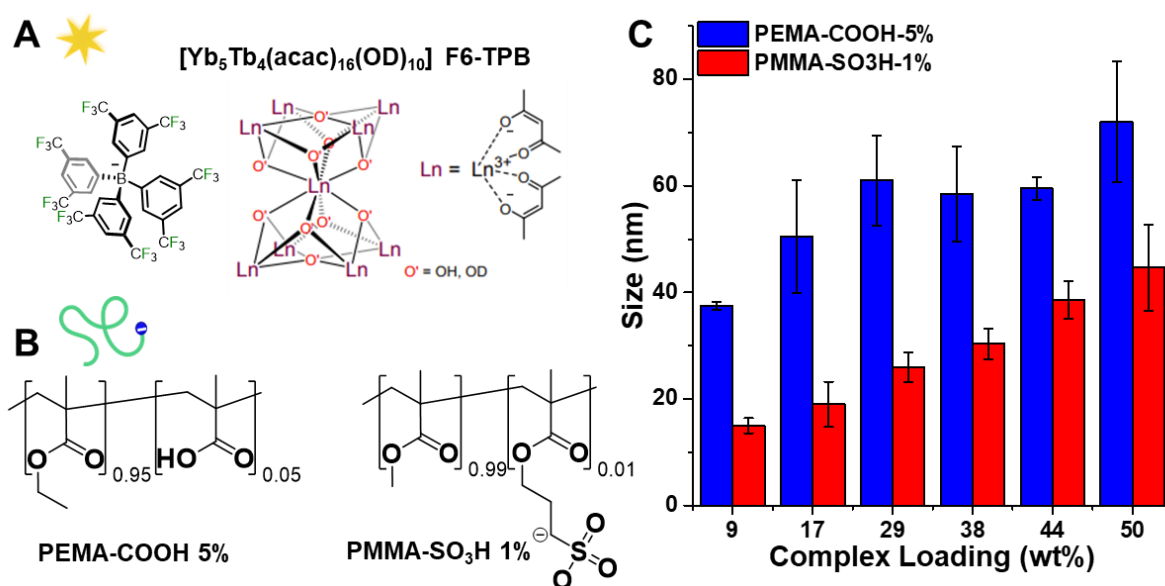


Figure 38: A) Structure of the nona-nuclear complex and the counterion F6-TPB, overall [Yb₅Tb₄acac₁₆(OH)₁₀](F6-TPB) (artistic representation) B) Structure of polymers used for the NPs synthesis C) Size of the formulated PNPs.

Methacrylate-based copolymers enabled PNP formation with various concentrations of the Yb₅Tb₄/F6-TPB complex. After a new round of formulation and optimization, the following investigation focused on the complex loaded PNPs obtained with two polymers (Figure 38B). PEMA-COOH-5% gave NPs with sizes between 40 nm and 70 nm according to DLS, with an initial increase of size with loading. PMMA-SO₃H-1% formulations resulted in smaller PNPs, with an increasing of size from 15 to 40 nm with loadings (Figure 38C). In this way, PNPs with controlled sizes from 15 to 80 nm could be obtained and it was, in particular, possible to control

the size for a given loading using polymer chemistry. Complementary size characterization was made using Transmission Electron Microscopy (Annexes Figure 96), showing smaller sizes compared to DLS (33 nm in TEM against 58 nm in DLS for 38 wt% in PEMA-COOH-5%). This difference is due to the fact that TEM yields the number distribution of the hard core diameter, while DLS yields the volume distribution of their hydrodynamic diameter.¹⁹² Both techniques showed a monodisperse population of NPs.

UV/vis measurements showed a continuous increase in the absorbance of the peak around 280 nm, attributed to the acac ligands, with loading for PEMA-COOH 5% based NPs up to 38 wt% (Figure 39A). For higher loadings a shift to lower wavelengths and a relative decrease in the intensity were observed, suggesting a limit in the encapsulation ability of these systems. For PMMA-SO₃H-1% based PNPs a continuous increase of the absorbance with the loading was observed. To try and evaluate the concentration of lanthanide complex encapsulated, the extinction coefficient of the acac ligands from the [Yb₅Tb₄(acac)₁₆(OD)₁₀][F6-TPB] complex was determined experimentally. When dissolved in methanol, a value of $19.7 \times 10^4 \text{ M}^{-1} \text{ cm}^{-1}$ (for $\lambda = 292 \text{ nm}$) was obtained, very close to what was measured for the analogue with the hydroxy counterion.¹⁸⁹ A comparison between the absorbance spectra of the complex in solution and inside the PNPs revealed the presence of scattering due to the size of the PNPs (Annexes Figure 97). This artifact induces an overestimation of the concentration of complex but a correction on the spectra to suppress it is difficult. Using the measured extinction coefficient in methanol, the expected absorbance of the complex ligand encapsulated inside the PNPs was calculated (Annexes Table 8). The comparison revealed a difference (approx. factor 2) between the theoretical and measured absorbance, suggesting a lower final concentration of complex encapsulated. The absorbance spectrum of an identical amount of complex was measured in water, showing a decreased absorbance relative to methanol. As the complex structure in water is most uncertain, several explanations are possible: first, there is a possibility that the complexes are aggregating together or are being degraded, but also that the extinction coefficient of the ligand changes with the environment. Another possibility is a change of the protonation state of the acac ligand, which has been reported to lower the extinction coefficient and blue shift the peak maximum.¹⁹³ This behavior was observed in this study for PEMA-COOH-5% PNPs with 44 and 50 wt% loading of complex, systems for which we supposed the encapsulation did not occur properly. Due to all these possibilities, making a reasonable calculation of the complex concentration is impossible without further experiments. Furthermore, these absorbance values are an indirect measurement of the real lanthanide encapsulation as they are from the ligands. A partial loss of the ligand during encapsulation is possible, however difficult to prove, and the direct measurement of absorbance of the lanthanide is tricky to measure directly due to very low extinction coefficient ($\epsilon_{\text{Yb}} = 29 \text{ M}^{-1} \text{ cm}^{-1}$, for [Yb₅Tb₄(acac)₁₆(OD)₁₀](OD)).¹⁸⁹ Thus, the absolute concentration of Yb₅Tb₄/F6-TPB complexes cannot be determined with these data, however, the general linear increase suggests a good encapsulation of the complex.

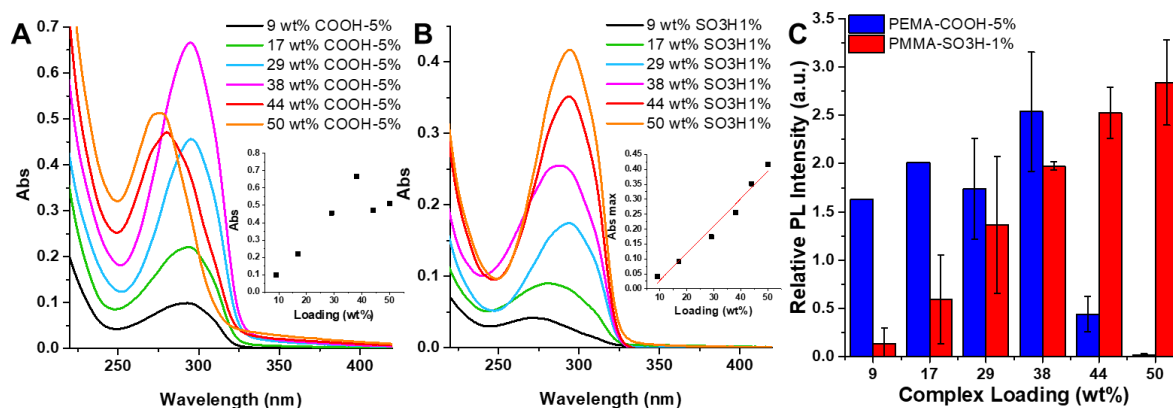


Figure 39: Absorption spectra of A) PEMA-COOH-5% and B) PMMA-SO₃H-1% based PNPs with different concentration in complex. Inset: Max of absorbance for different PNPs. C) Relative intensities of [Yb₅Tb₄(acac)₁₆(OD)₁₀](F6-TPB) loaded PNPs prepared in protic aqueous media. The intensities were calculated by integrating the area of the PL downshifting emission of Tb atoms. To be compared they were divided by the PL intensity of the complex at 9 wt% in acetonitrile solution; $\lambda_{ex} = 340$ nm.

To help select the best candidates the downshifting PL spectra of Tb were recorded for the different PNPs and their intensity was normalized by the Tb emission of Yb₅Tb₄/F6-TPB at 9 wt% in organic solution (Figure 39C). The PNPs formulated with PMMA-SO₃H-1% showed a regular increase of their PL intensity with loading, whereas the ones with PEMA-COOH-5% showed a good relative PL intensity up to 38 wt% of complex. This is in good agreement with the absorbance spectra showing a decrease and wavelength shift above this loading, suggesting that the system reaches a limit of encapsulation and explaining the drop of emission for PEMA-COOH-5% PNPs with higher loading. The striking difference in the success of assembly of loaded PNPs between complexes with hydroxide and F6-TPB counterions underlines the importance of adjusting the hydrophobicity of the load, and that this can be readily achieved by choosing the right counterion.

2. PNPs Characterization

2.1 Transition to deuterated media

One of the challenges to observe molecular UC in solution is to minimize the non-radiative deactivation processes in order to achieve long excited state lifetimes, which is required such that the initial mono-excited state persists long enough to undergo a second excitation. The latter is notably limited by energy transfer from the complex excited-state to overtones of ligand vibrations in the first coordination sphere or outer-sphere solvent oscillators, leading to non-radiative excited-state deactivation. In this sense a judicious choice of ligands and limiting the interactions between the Ln complex and the solvent is crucial. Knowing that the non-radiative rate constant in a medium increases exponentially with the energy of its associated vibrations, the investigation of the PNPs photophysical properties was further investigated with their preparation in deuterated aqueous medium, owing to the lower vibrational energy than its non-deuterated analogue (*cf.* 3300 cm⁻¹ for O-H vs. 2500 cm⁻¹ for O-D).¹⁸⁹ At the same

time this should limit exchange of bridging deuteroxide ligands in the first coordination sphere. Therefore, in order to maximize our chances to observe UC, the best candidates for UC were identified from the synthesis in protic media (H_2O) and then transferred their synthesis to deuterated media (D_2O).

Using PMMA-SO₃H-1% and PEMA-COOH-5% as before, two series of loaded PNPs with different sizes, between 15 and 35 nm for PMMA-SO₃H-1% and between 55 and 65 nm for PEMA-COOH-5% according to DLS, could be obtained: (Figure 40A). The size revealed to be quite independent of the loading, especially in the case of PEMA-COOH-5%. TEM analysis showed again a slightly lower core size than DLS (Figure 40B,C) and confirmed a very similar size of NPs prepared in protic and deuterated media. From the measured core diameter of the NPs and the loading of Yb₅Tb₄/F6-TPB, the number of Yb₅Tb₄/F6-TPB complexes encapsulated inside the PNPs could be estimated.

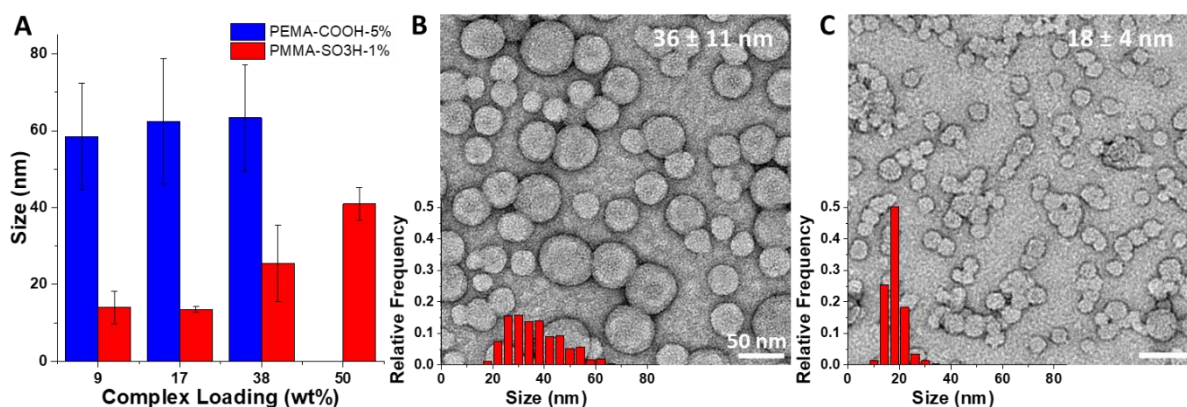


Figure 40: A) DLS sizes of [Yb₅Tb₄acac₁₆(OD)₁₀](F6-TPB) loaded NPs prepared in deuterated medium. TEM picture of NPs (Left bottom: distribution size) with 38 wt% [Yb₅Tb₄acac₁₆(OH)₁₀](F6-TPB) loading in B) PEMA-COOH-5% and C) PMMA-SO₃H-1%

The number of encapsulated Yb₅Tb₄/F6-TPB complexes increased practically linearly with loading, going from 600 to 1700 complexes per NP (Annexes Table 9). The highest number being obtained for PEMA-COOH-5% PNPs containing 38 wt% of Yb₅Tb₄/F6-TPB with a hard core size of 36 nm. At the same loading, PMMA-SO₃H-1% based NPs have a hard core size of 18 nm, and in consequence contained approximately 225 Yb₅Tb₄/F6-TPB complexes. Another parameter that could be determined is the average center to center distance between two Yb₅Tb₄/F6-TPB complexes inside the NP, which is directly linked to their concentration. If we consider that the complexes are homogeneously distributed inside the NP, the average closest neighbor distance between complexes (center to center) goes from 2.2 nm for the lowest loading to 1.3 nm for the 38 wt% loading (Annexes, Table 9). Taking into account the size of the complexes, the distance between the lanthanide ions in different complexes can reach down to about 0.7 nm, showing their great proximity.

2.2 Spectroscopic Characterization

The optimization of the PNP synthesis enabled preparation of nanoparticles with high amounts of $\text{Yb}_5\text{Tb}_4/\text{F6-TPB}$. The next step was to characterize the photophysical properties of the obtained nanohybrids prepared in deuterated media. Absorbance spectra clearly showed the absorbance due to the acac ligands with a large absorption band around 280 nm, in good accordance with what was observed in protic medium. Excitation of the acac ligands at 340 nm enables to observe the downshifting PL of both Tb ($^5\text{D}_4 \rightarrow ^7\text{F}_J$ with $J=6$ to 3) in the visible region and Yb ($^2\text{F}_{5/2} \rightarrow ^2\text{F}_{7/2}$) in the Near InfraRed (NIR) region (Figure 41A, B and Annexes Figure 99). For all PNPs, the emission intensity both in the visible and the NIR region increased when increasing the loading of encapsulated complex (Figure 41C).

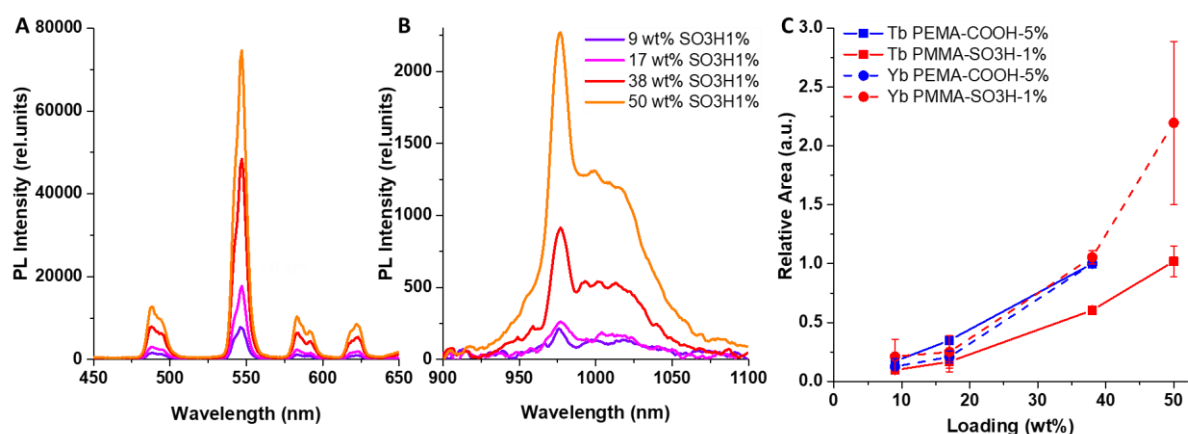


Figure 41: Downshifting PL of $[\text{Yb}_5\text{Tb}_4(\text{acac})_{16}(\text{OD})_{10}](\text{F6-TPB})$ loaded PNPs. Absolute emission spectra of A) Tb and B) Yb when loaded inside PNPs. C) Relative Integrated Area of Tb (square) and Yb (circle) down-shifting PL for different PNPs. Integration of the intensity was made between 450 and 650 nm for Tb emission and 900 and 1100 nm for Yb emission, area relative to the Area of 38 wt% in PEMA-COOH-5% PNPs. $\lambda_{\text{ex}} = 340$ nm

The steady state analysis was completed with measurement of the DSL decay curves for both the terbium and ytterbium atoms, and for all PNPs in deuterated media (Figure 42 for PMMA-SO₃H-1%, Annexes Figure 100 for PEMA-COOH-5%). A multiexponential fitting enabled to extract the amplitude average lifetime (Annexes, Table 10). The PL lifetime of the Tb inside the PNPs was calculated to be between 408 and 489 μs depending on the PNP. This is approximately a factor two lower than the lifetime of the $[\text{Yb}_5\text{Tb}_4(\text{acac})_{16}(\text{OD})_{10}](\text{OD})$ complex reported in methanol¹⁸⁹ and confirm that the Tb DS emission is well preserved inside the PNPs. Interestingly, the PEMA-COOH-5% based PNPs have longer PL lifetimes than the PMMA-SO₃H-1% based ones. One may impute this lower value to a higher surface quenching due to the smaller size of the latter formulations, generating a higher surface to volume ratio. However, this trend is rather reversed for the Yb DS lifetime with slightly higher values for PMMA-SO₃H-1% based PNPs, the overall being between 5 and 10 μs . One exception is the 50 wt% loaded PNPs with PMMA-SO₃H-1% with a PL lifetime of 49 μs , identical to the corresponding complex with the hydroxy counterion in methanol.

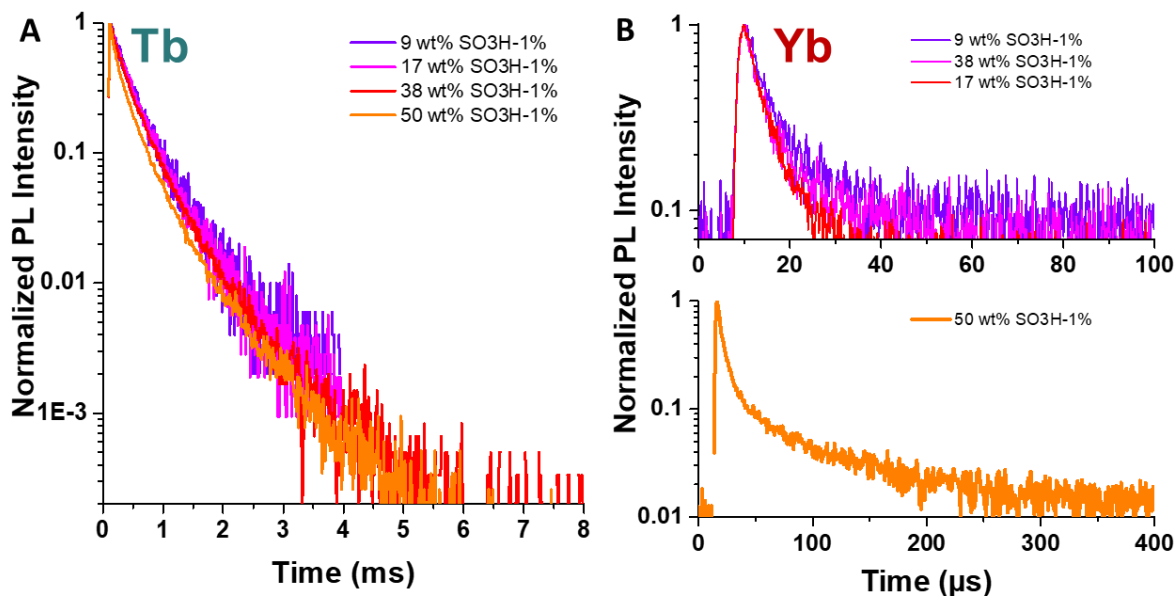


Figure 42 : Normalized PL Decay curves for the downshifting emission of A) Tb and B) Yb for different PMMA-SO₃H-1% PNPs, $\lambda_{ex} = 340 \text{ nm}$

To test the ability not only in downshifted emission but also in UC, PNPs were irradiated with a 980 nm laser ($P = 6.9 \text{ W cm}^{-2}$) to excite two proximate Yb ions and trigger cooperative energy transfer to Tb. PL spectra were recorded and showed that all studied NPs exhibited UC emission in deuterated aqueous media (Figure 43A). Comparison of the relative integrated area (Figure 43B) showed that the emission intensity was increasing with loading over the studied range, and followed a trend similar to what was observed for the Ln downshifting emission. At the same time, UC emission intensity was practically the same for PNPs made from PEMA-COOH-5% and PMMA-SO₃H-1%. The UC QY for PEMA-COOH-5% based PNPs with 38 wt% loading in complex was determined to be $6.77 (\pm 1.04) \times 10^{-8}$ in deuterated aqueous media, which is about 40 times lower than that obtained for the $[\text{Yb}_5\text{Tb}_4(\text{acac})_{16}(\text{OD})_{10}](\text{OD})$ complex in deuterated methanol.¹⁸⁹

Understanding the influences of different parameters related to the complex encapsulation on the UC PL of these systems is essential to predict their behavior and allow future improvements. In particular, the influence of loading, size, and environment inside and around the PNPs is to be discussed, as the luminescence properties of polymeric NPs are particularly complex to disentangle. As introduced before, the optically active elements of these systems are polynuclear complexes able to produce cooperatively sensitized UC through the interaction between the lanthanide ions. It is important to keep in mind that the description of the properties of such UC molecules is difficult by itself, since it depends on the Yb/Tb ratio (so their inter-nuclear distances), and their interactions with the surrounding environment.¹⁸⁹

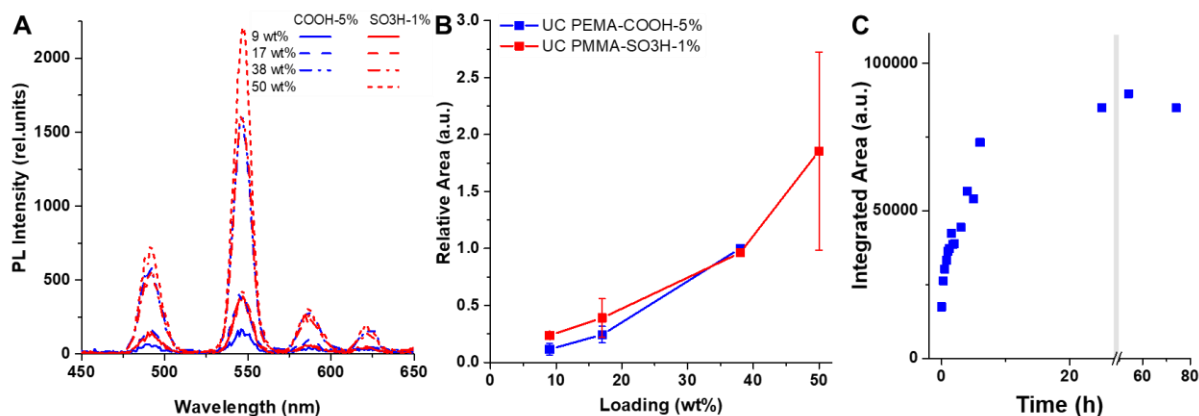


Figure 43: UC PL of [Yb₅Tb₄(acac)₁₆(OD)₁₀](F6-TPB) loaded PNPs. A) UC emission spectra of PNPs, either prepared with PEMA-COOH-5% (blue) or PMMA-SO₃H-1% (red), $\lambda_{ex} = 980\text{nm}$ ($P = 6.9\text{ W cm}^{-2}$). B) Relative Integrated Area. Integration of the intensity was made between 450 and 650 nm, area relative to with the area of 38 wt% in PEMA-COOH-5% PNPs C) UC relative Intensities of PNPs prepared either with deuterated or non-deuterated acetonitrile over time

Considering the size influence, a dependency of luminescence properties related to the size of the PNP could be expected. This hypothesis is based notably on the fact that with an increasing size, the fraction of luminophore close to the surface of the PNP will decrease, if a homogeneous distribution of the complexes is considered. Inversely, in smaller PNPs, a larger fraction of these would be close to the surface, influencing notably the importance of solvent-related quenching, due to energy transfer between solvent vibrational modes and non-radiative relaxations of the Ln energy levels.^{194,195} In this study, the size of the PNPs was tuned by modifying the polymer. Interestingly, for a given loading, both DS and UC PL were generally very close for PNPs made from PEMA-COOH 5% and PMMA-SO₃H 1%, with the only exception of Tb DSL, which was lower for the latter. This indicates that the PL of the complex loaded PNPs was largely independent of particle size and mainly depended on the loading and the efficient encapsulation of the complexes.

It is expected that the complex loading in the NPs will exert some effect on luminescence. While a linear increase in the luminescence with the loading could be expected, also different effects could start to play a role in highly loaded PNPs deviating from this linearity. As an example, making a comparison with inorganic systems, some luminescence detrimental ion-ion interactions are commonly observed with relatively high doping of some lanthanides, as cross-relaxation or parasitic energy migration, leading to the so-called “concentration quenching effects”.^{68,196–199} In the present case, the situation is more complicated, because the lanthanide presence is focused in clusters (the nonanuclear complexes), with inter-ionic distances under 1 nm, distributed in the nanoparticle at variable distances dependent on the concentration (between 2 and 1 nm for the nearest neighbors). Looking at the experimental data obtained for the different PNPs, it is possible to notice a general increase of the DSL and UCL with the loading for all studied PNPs. An initial slow increase between 9 and 17 wt% is followed by a steeper increase up to 50 wt% loading for the PMMA-SO₃H 1% based PNPs and 38 wt% for PEMA-COOH 5%. For the latter, this value corresponds to the threshold for efficient

encapsulation inside the PNPs, as evidenced by absorbance measurements. Nonetheless, the intensity doesn't increase linearly with the loading, suggesting some quenching, potentially due to aggregation of the complex inside the PNPs.

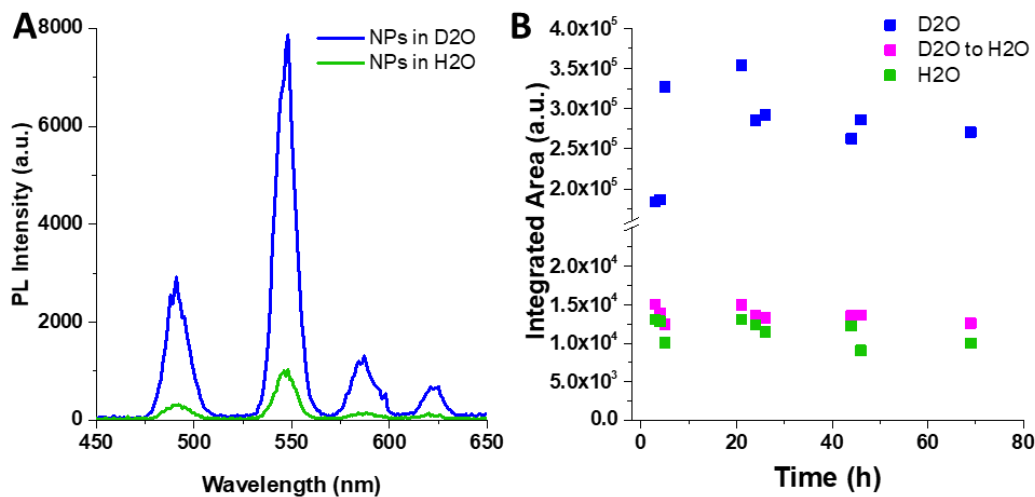


Figure 44: A) Comparison of PL UC emission spectra of PNPs diluted in deuterated or non-deuterated water B) Evolution of the area of UC emission over time for PEMA-COOH 5% NPs loaded with 38 wt% $[[Yb_5Tb_4(acac)_{16}(OD)_{10}](F6-TPB)$ prepared in different aqueous media. D_2O and D_2O to H_2O NPs were prepared in deuterated aqueous medium then the D_2O to H_2O were concentrated and redispersed in protonated water. H_2O NPs were prepared in protonated aqueous media.

The study of the behavior of the UC PL was pushed further by measuring its evolution over time and in different media. In a first step, the stability of the signal with time was studied from the moment of assembly of the PNPs. The PL was evaluated by measuring the intensity of the $^5D_4 \rightarrow ^7F_5$ transition over time. This kinetic study (Figure 43C) revealed a first phase, between $t=0$ (*i.e.* the PNPs formation) and 4 h, where the signal intensity increased regularly by approximately a factor of 5. It was followed by a second phase, where the signal intensity is stabilized and remained stable over more than three days. It should be noted that practically the same behavior was observed when non-deuterated acetonitrile was used for particle preparation instead of deuterated acetonitrile (Annexes Figure 101). In case of the slow increase, no influence from the extent of deuteration of the acetonitrile used during synthesis was observed, indicating that a slow leaching of the solvent is not at the origin of this behavior. In view of the time scale of several hours a process involving the rearrangements of the polymer chains is likely to be at the origin of the increase. This can be realized either through a rigidification of the direct environment of the complexes or through the slow removal of water molecules.

To further access their applicability in biological environments, the UC emission of loaded PNPs was evaluated over time for different situations: PNPs synthesized in D_2O , concentrated and then redispersed either in D_2O or H_2O or PNPs synthesized in H_2O (Figure 44B). In all cases, after the initial increase described above, the UC emission showed an excellent stability over time, for a period of at least 3 days. These experiments further revealed that the signal of PNPs prepared in D_2O then transferred into H_2O was very similar to the one of PNPs prepared

directly in H₂O (both approximately 8 times lower than the one prepared and kept in D₂O). The fast decrease of the UCL upon transfer into H₂O, is supposed to be related to quenching by ET transfer to vibrational modes of H₂O, which is generally much more efficient in case of the higher energies associated with H₂O compared to D₂O. In principle, quenching by water molecules in the first coordination sphere or outer-sphere solvent oscillators could be possible. Water content in methacrylate based plastic materials is reported to be very low (<2%),²⁰⁰ as is the case of diffusion of water in these materials ($D \sim 10^{-12} \text{ m}^2 \text{ s}^{-1}$).²⁰¹ However, in view of the small size of the PNPs used here, the characteristic diffusion time can be estimated to be less than milliseconds. In consequence, slow diffusion of only a few water molecules into the outer coordination sphere of the encapsulated complexes could effectively be at the origin of the observed decrease in UC. These results indicate that, at least on the time scale of our measurements, the presence of D₂O or H₂O had a much larger influence than whether the PNPs were prepared in either medium.

3. Cellular Imaging

After evaluation of the UCL properties in different media, it was confirmed that our systems are able to emit in UC not only in deuterated but also protic aqueous media. These promising results allowed to consider trying these nanoprobe in biological media. Indeed, fully exploiting anti-Stokes behavior allows to obtain outstanding signal-to-noise ratio images with very simple experimental setups. In particular, the absence of NIR-induced autofluorescence in the visible region renders sophisticated instruments such as time-gating devices, or extremely bright and long lasting fluorophores unnecessary.^{202,203} To demonstrate the potential of the presented polymeric UC NPs for bioimaging, they were used directly as contrast agents for cellular imaging.

After incubation for 3 h with Cos7 cells, followed by rinsing, the polymeric UCNP luminescence can be clearly seen (Figure 45A, B). After examining the raw luminescence, a second major point is to check the PNPs localization to confirm the cell uptake. To verify the effectiveness of PNP inclusion inside the cells, a z-axis scan, acquiring luminescence images with the focal point in different positions are collected (Figure 45C). Interestingly, the upconverted luminescence of the polymeric UCNPs can be seen inside the cell and not only on the membrane, confirming their uptake. This demonstrate that the UC complexes encapsulation is an effective method to exploit the interesting properties of molecular upconverters in an aqueous environment and, first of its kind, in biological systems.

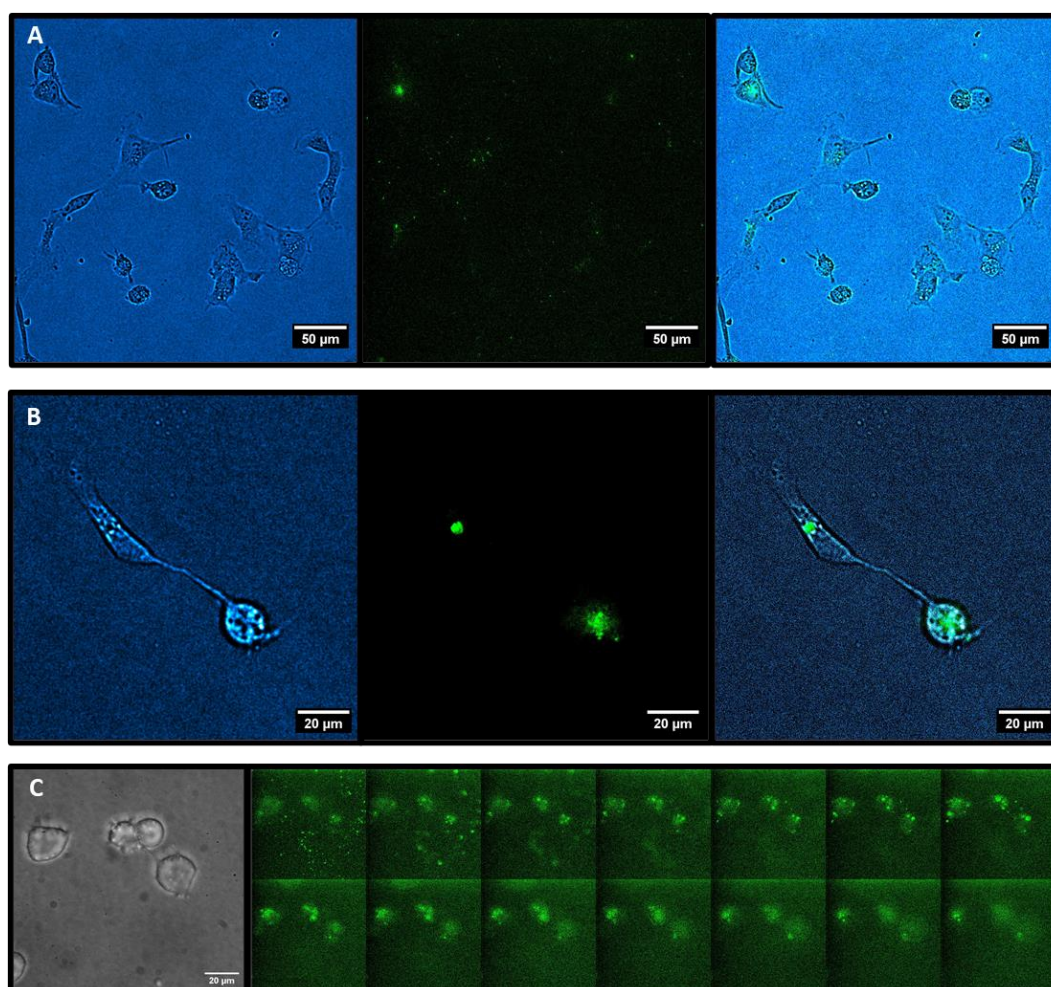


Figure 45: DIC, green channel under 980 nm excitation and composite image of polymeric UCNPs in Cos7 cells with (A) 40x and (B) 100x magnification. (C) Reference DIC image and scan along z-axis of green channel for polymeric UCNPs

In order to give a better idea of the current performance of the presented polymer UCNPs, we compared their luminescence properties in cell imaging with standard inorganic UCNPs.²⁰⁴ As reference inorganic UCNPs, a simple NaYF₄ matrix with a core-shell nanoarchitecture was used, in which the core is doped with Yb³⁺ and Er³⁺ ions (20 and 2% respectively) while the inert shell's function is to prevent surface-related quenching.²⁰⁵ As expected, the polymeric UCNPs luminescence is weaker compared to the inorganic ones, as can be deduced from the higher noise. Nevertheless, under identical experimental conditions the polymeric UCNPs luminescence can be clearly seen alongside the inorganic ones (Annexes Figure 102, Figure 103 for the raw images). It should be noted that, in the inorganic UCNPs, the upconversion is based on sequential energy transfers (energy transfer upconversion, ETU) from the Yb³⁺ to the Er³⁺ ions, and due to the favorable energy level structure of Er³⁺, the ETU mechanism is by definition more efficient than the cooperatively sensitized (CSUC) implemented in molecularly upconverting complexes. In principle, it would be preferable to compare between polymeric and inorganic nanoparticles operating by the same UC mechanism. While ETU has been reported at the molecular scale,¹⁷⁸ it is exceeded in efficiency by several orders of magnitude by the CSUC complexes utilized in this study. Furthermore, inorganic systems based on CSUC

are surpassed and not as widely used as ETU-based ones. For this reason, it was chosen to compare the synthesized PNPs to the most efficient upconverters employed up to now, and the results show that the performance of the first generation of UC complex loaded polymer NPs is encouraging.

4. Conclusion

The principal objective of this study was to effectively produce a molecular up-converting emitter capable to be detected in aqueous media and biological systems. This could be achieved by combining the properties of hetero-nonanuclear lanthanide complexes with polymeric NPs. A modification of the $[\text{Yb}_5\text{Tb}_4(\text{acac})_{16}(\text{OD})_{10}](\text{OD})$ complex hydrophobicity proved to be necessary to ensure a good encapsulation inside the polymeric matrix and the polymer chemistry enabled a variation in the size of the final PNPs. Even if an absolute concentration of the encapsulated complex was impossible to measure, linear increase of the absorbance of the ligand with the loading enabled to encapsulate a high number of complex, going up to 1700 per PNP. After optimization of the formulations, the PNPs were prepared and characterized in deuterated medium, to better observe the UC properties. Downshifting emission of both the terbium and ytterbium atoms could be measured when exciting the acac ligand, their intensities increasing with the loading. UC signal could also be measured when exciting directly the Yb atoms, with a UC quantum yield of 6.77×10^{-8} . After an increase in the intensity in the first hours following the PNPs preparation, the UC intensity proved to be stable over a period of at least 3 days. The UC PL could also be observed in protic aqueous media, with an intensity approximately 8 times lower than in deuterated media. Encouraged by these results, the experiments were pushed further, going to a direct application in biological system. The synthesized nanohybrids were used for up-conversion bioimaging of cells and were compared to classic UCNPs. Whereas the PNPs proved to be less bright than commercial UCNPs, it was possible to do imaging of the cells with both NPs using the same experiments parameters. This result proved the capacity of our nanoprobe to achieve UC based bioimaging and with a relatively good efficiency for a first generation probe.

CHAPTER IV: Gold Nanoclusters loaded PNPs for SWIR Imaging

A quite recent strategy to perform background free imaging is to shift the PL properties toward the second near-infrared window (NIR-II) between 1000 and 1700 nm, also known as shortwave infrared (SWIR). Light in this wavelength range can penetrate deeper into tissues due to reduced scattering.²⁰⁶ Autofluorescence is also negligible compared to the visible or NIR region,³⁴ making it possible to enhance the SNR, key parameter for *in vivo* imaging, and thus achieving high spatio-temporal imaging resolution.^{207,208} The interest for imaging in this wavelength region greatly increased with the development of InGaAs cameras that have an improved detection ability in this region. Despite intense efforts over the last years, contrast agents for this wavelength region remain limited. In general, the brightness of the probes remains low, thus developing more efficient probes is a crucial challenge in the improvement of SWIR imaging.

Among the probes developed over the last two decades, ultra-small gold nanoclusters (AuNCs) are an intriguing class of luminescent materials, with core sizes below 3 nm, made-up of several tens of Au-atoms most often stabilized with thiolated ligands.²⁰⁹⁻²¹¹ Both, the Au(0) core as well as charge transfer states involving the ligands contribute to their photoluminescence (PL) emission, but the precise mechanism is still under debate.²¹² Interestingly, several members of the AuNC family emit in the NIR-II region,^{213,214} and they have been recently employed for protein tracking, blood vessel imaging, and molecular imaging.²¹⁵⁻²¹⁷ The ligand shell (nature of the ligand, rigidity) has a profound influence on the emission properties, notably in view of achieving emission in the NIR-II,^{213,218} but determines also the solubility properties and interactions with the biological media.^{218,219} Thus, a compromise must be found between the emission properties of the probe and its biocompatibility. A possible approach to decouple surface and emission properties is to encapsulate AuNCs into polymer NPs, such that the ligands are not in contact with the media and only modulate the AuNC emission, while the interface is controlled by the polymer. A second advantage of encapsulation of high amounts of NIR-II-emitting AuNCs in polymer NPs would be a significant enhancement of the overall brightness, as the individual clusters are combined in one probe. Examples of AuNCs encapsulated into polymers can be found in the literature, as described in the introduction. However, these approaches have not been extended to nanoclusters emitting in the SWIR/NIR-II region. SWIR emitting AuNCs are larger and highly inorganic compared to the luminophores that were encapsulated in the precedent chapters. Thus, their ability to be encapsulated in PNPs while preserving their PL properties must be tested.

In the present work, monodispersed nanohybrids were assembled, that are polymer NPs encapsulating SWIR-emitting AuNCs at loadings up to 50 wt% (called AuPNPs), through nanoprecipitation with the aim to accomplish bright NIR-II fluorescent nanoprobos. By

controlling both the size of NPs and the concentration of encapsulated AuNCs, it was possible to evaluate both physico-chemical and photophysical properties of the AuPNPs. In particular, a progressive shift of the PL emission to longer wavelengths was observed with increased loading. Multi-wavelength PL lifetime measurements allowed us to assign this redshift to increasing interactions between the AuNCs within the NPs.

Once the AuPNPs characterized thoroughly, their potential for bioimaging was quantified. First, by imaging them in tissue phantom models to mimic blood vessel bioimaging. Second, by evaluating the brightness at the single particle level and the possibility to track single particles over extended period of time. The observation of such small objects is made possible by the super localization microscopy approach, which has the capacity to bypass the diffraction limited resolution of optical microscopes. In particular, single particle tracking localization microscopy allows to interrogate molecular dynamics at the nanoscale in a variety of environments including biological specimens such as biological tissues^{220,221}. SWIR probes for SPT enable to achieve this type of study with an enhanced depth, unlocking new kinds of information. The analysis conducted showed a great brightness at the single particle level, opening further the possible range of application for these SWIR emitters.

Another key parameter in the development of efficient contrasting agents for complex biological systems is the biocompatibility. Thus, the potential cytotoxicity and intracellular accumulation of AuPNPs were tested and was completed by an evaluation of their potential anti-inflammatory character. This study confirmed the absence of cytotoxicity and suggested an anti-inflammatory response of the macrophages when in contacts with the PNPs. To enhance the stability and circulating performances of the AuNPs in complex biological systems, the PNPs were modified by adding a pegylated coating, either by adsorption of Pluronic or by design of amphiphilic polymers. The stealth properties in biological fluid of the pegylated PNPs was investigated by FCS and yielded encouraging results. Eventually, the coated and uncoated AuPNPs were used for *in vivo* blood vessel imaging.

1. AuNC encapsulation

To develop our SWIR emitting NPs, we chose AuNCs with dodecanethiol (DDT) ligands in order to achieve a high hydrophobicity of the resulting AuNCs to facilitate their encapsulation. Synthesis of these AuNCs was achieved by a partner lab following a well-established protocol²²² that ensures a good control of the NC size. The obtained products after purification had a diameter of 1.84 ± 0.34 nm, as determined by HR-TEM (Annexes Figure 104).²²³ The absorbance profile of our AuNCs, notably with the band at ~ 700 nm, is characteristic of the presence of Au₂₅ NC species.^{121,224} Together, these results indicate that the obtained product is composed of a majority of Au₂₅DDT₁₈ clusters, though a certain distribution of cluster sizes is certainly present.

These AuNCs were encapsulated through nanoprecipitation into PNPs (Figure 46C) to yield AuNC loaded PNPs (AuPNPs). Poly(ethyl methacrylate) (PEMA) based polymers were chosen

for the formulation, as they have shown very good results for the encapsulation of hydrophobic fluorescent dye salts with high QYs.^{98,225} The polymers contained 5 or 10 mol% of COOH groups in order to control the size of the resulting AuPNPs (Figure 47).^{91,226–228} AuNCs could be encapsulated at high concentration, with loading going up to 50 wt%.

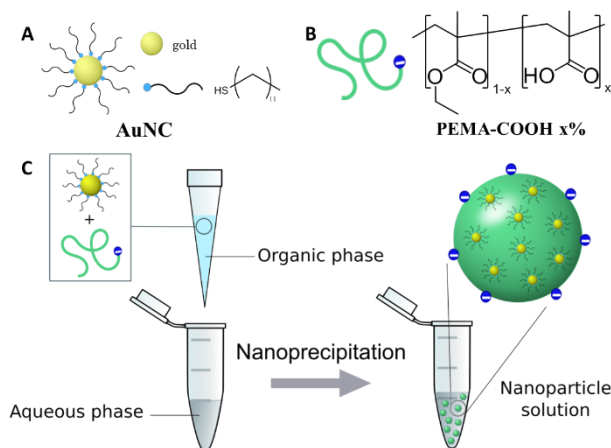


Figure 46: A) Structure and representation of gold nanoclusters stabilized by dodecanethiol (AuNC). B) Structure and representation of the polymer. C) Principle of NP synthesis through nanoprecipitation

Dynamic light scattering (DLS) confirmed the formation of AuPNPs and showed increasing sizes of the obtained PNPs with increasing AuNC loading (Figure 47). Polymers with 10% of charged groups gave AuPNPs roughly half the size of those bearing 5%, and the sizes of the highest loaded AuPNPs had hydrodynamic diameters of 41 ± 7 nm and 68 ± 6 nm, respectively. Certain AuPNPs based on the polymers bearing 5% charged groups were further investigated by TEM imaging (Figure 47), showing monomodal size distribution and a slightly smaller diameter (60 ± 13 nm) compared to DLS. The latter can be attributed to the fact that DLS measures the hydrodynamic diameter that is usually larger than the TEM hard sphere diameter. TEM images also showed an increasing contrast with increasing AuNC loading (in the absence of contrast agent, Annexes Figure 105), confirming the encapsulation of AuNCs inside the PNPs. High resolution cryo-TEM images further revealed the presence of small dots with sizes ≤ 2 nm, corresponding to the size of the AuNCs, whose numbers per particle increased with loading (Figure 47). No obvious organization, *e.g.* clustering that would be expected to yield zones of much higher contrast, was observed when examining a large number of nanohybrids at different loadings (Figure 47 and Annexes Figure 105). ICP-MS analysis of AuPNPs, purified through ultrafiltration to evacuate all non-encapsulated materials, indicated a linear increase of the amount of gold with loading and an excellent agreement with the calculated expected gold content (Figure 47). Together, these results indicated a practically quantitative encapsulation of the AuNCs in the PNPs.

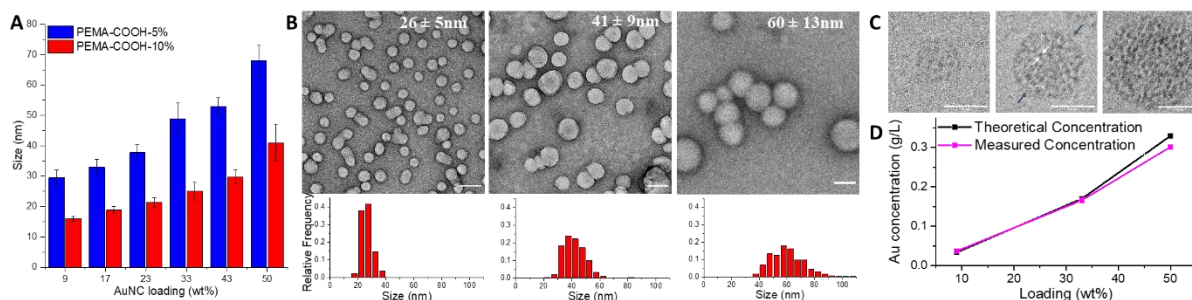


Figure 47: A) NP size (hydrodynamic diameter) measured by DLS for two polymers. B) TEM images of AuPNPs (from left to right) for 9, 33 and 50 wt% of AuNC loading and their size (hard sphere diameter) distributions. Scale bars: 50 nm. C) Cryo-TEM images of AuPNPs (from left to right) for 9, 33 and 50 wt% of AuNC. Dark arrows show NP and white arrows show AuNC (~ 2 nm). Scale bars: 20 nm. D) Gold concentration inside AuPNPs as measured by ICP-MS compared to calculated concentration.

The combination of different analysis shows that we have an encapsulation efficiency close to 100 %. This data, associated to the size of the AuPNPs obtained from TEM and the mass concentration of clusters inside the NP, were used to approximate the number of clusters encapsulated per NP. Taking into account densities of the polymer material and gold and their weight fractions, an estimation of the mean density of the AuPNPs was calculated (See Material and Methods). As both polymers exhibited similar encapsulation ability, the following results are focused on PEMA-COOH-5% based PNPs.

For AuPNPs loaded with 9 wt%, we estimated that around 100 AuNCs were encapsulated in one NP, this number growing strongly with the loading and reaching almost 14,000 for the highest loading (50 wt%, Table 6). These values are in qualitative agreement with the obtained high resolution cryo-TEM images, though the latter do not allow a quantitative assessment of the number of AuNCs. Once we knew the cluster concentration inside a NP, we could estimate the average distance between clusters. This distance (being highly linked to the loading) was approximately half between the lowest and the highest loading (Table 6). At 50 wt% loading it reached an average center to center distance of about 2 nm (assuming a cubic lattice) and an average nearest neighbor distance of 1.1 nm (assuming an isotropic random distribution).²²⁹

2. Photophysical Characterization

The AuNCs used for encapsulation are hydrophobic when introduced into aqueous media and thus aggregate, which results in a quenched PL. As they were successfully encapsulated into AuPNPs, their photophysical properties have to be evaluated to confirm their ability to emit in aqueous media. Moreover, their entrapment into the polymer matrix forces a close proximity, which may modify their properties. In the following, the PL properties and photophysical characteristics of the assembled AuPNPs are studied through steady-state and time-resolved experiments.

2.1 Steady State

PNPs loaded with AuNCs showed broad absorption spectra, ranging from the UV region to the NIR with two main peaks around 416 and 708 nm (Figure 48), very similar to the spectrum of the clusters in organic solvent. While the absorbance increased linearly with loading, reinforcing the hypothesis of an encapsulation efficiency close to unity, the shape of the spectra remained practically unchanged. From the absorption spectra were extracted the extinction coefficient of the AuNCs when trapped inside the AuPNPs, with values around $14,000 \text{ M}^{-1} \text{ cm}^{-1}$ at 730 nm, and five times higher at 405 nm. This, associated to the calculated number of AuNCs per NP, were used for the determination of the particle extinction coefficient at the two major absorption wavelengths, reaching values of circa $1 \times 10^9 \text{ M}^{-1} \text{ cm}^{-1}$ (at 405 nm) and $2 \times 10^8 \text{ M}^{-1} \text{ cm}^{-1}$ (at 730 nm). The measurement of PL excitation spectra showed a good fitting with the absorption spectra, thus confirming that the latter did not contain significant amounts of scattering (Annexes Figure 106). A further investigation of the PL properties linked to these two peaks was achieved by exciting respectively with a 405 nm and a 730 nm laser (Annexes Figure 107). For both excitation wavelengths the spectroscopic properties revealed to be similar, apart from the PL intensity, which was directly linked to the difference of absorbance between the two regions. In consequence, the next experiments focus on the results obtained with excitation at 730 nm, as this wavelength is better suited for *in vivo* imaging.

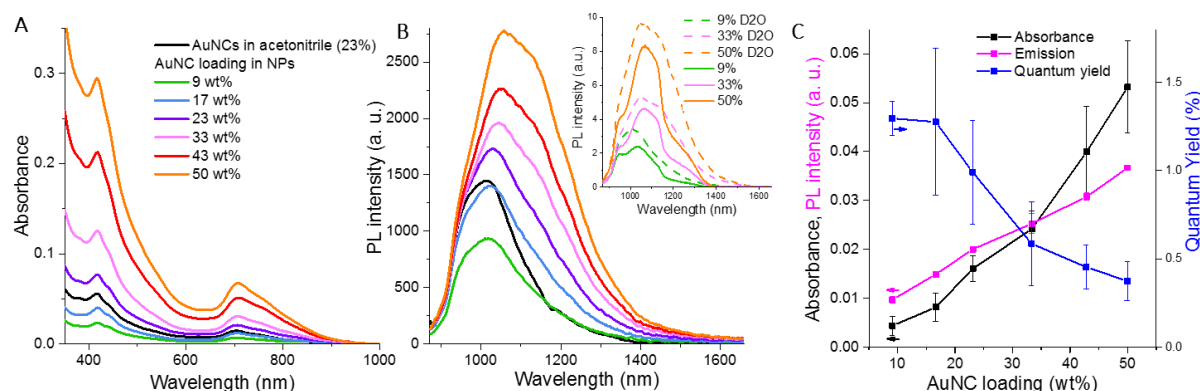


Figure 48: Absorbance (A) and PL (B) spectra of PEMA-COOH 5% AuPNPs loaded with different amounts of AuNCs (λ_{exc} . 730 nm). Inset of B) Comparison of PL spectra in deuterated and non-deuterated media. C) Evolution of absorbance, PL intensity, and QY with loading.

When studying the photophysical properties in the NIR-II, the influence of solvents has to be considered. Indeed, H₂O has various absorption peaks in the emission range of the AuPNPs (Annexes Figure 106), which are absent for D₂O. A comparison of the absolute PL emission of AuPNPs prepared in H₂O and D₂O revealed that the shape of the PL emission spectrum changes between the two conditions, in particular with a decrease of the measured intensity in H₂O in the regions 930-1050 nm and 1100-1250 nm, corresponding to the absorption of water (Annexes Figure 108). On the other hand, we observed little difference between the maximum intensity of AuPNPs prepared in the two aqueous media (Figure 48), suggesting that the clusters are well trapped inside the polymer matrix and have limited contact with water. Together these results indicated that the differences in the PL spectra stem mainly from the

absorption of the emitted PL by H₂O, and not from interactions of H₂O with the encapsulated AuNCs. The same results were obtained for AuPNPs prepared in H₂O and subsequently transferred to D₂O, indicating that preparation in D₂O did not alter the particles themselves. In order to study the properties of AuPNPs without the solvent bias, all following experiments were realized in deuterated water.

Table 6: Summary of characteristics of AuNC-loaded PNPs. a) Average size of > 200 AuPNPs \pm width at half maximum; b) Estimated based on equation 3; c) Estimated based on equation 4; d) Calculated according to $\epsilon_{NP} = \text{Number of AuNCs} * \epsilon_{AuNC}$; e) Measured using IR1061 as reference; f) Calculated according to brightness = $\epsilon_{NP} * QY$.

Loading AuDDT (%)	Size in DLS (nm)	Size in TEM (nm) ^a	Number of AuNCs per NP ^b	AuNC distance inside PNPs ^c (nm)	ϵ_{NP} 730nm (M ⁻¹ .cm ⁻¹) ^d	QY (%) ^e	Brightness 730 nm M ⁻¹ .cm ⁻¹) ^f
9	30 \pm 3	26 \pm 5	120	2.6	1.7 x 10 ⁶	1.3	2.3 x 10 ⁴
33	49 \pm 6	41 \pm 9	2 300	1.4	3.3 x 10 ⁷	0.6	2.0 x 10 ⁵
50	68 \pm 6	60 \pm 13	14 000	1.1	2.0 x 10 ⁸	0.4	7.6 x 10 ⁵

PL spectra of the AuNCs loaded PNPs showed a broad PL emission starting around 850 nm and reaching up to 1500 nm, achieving the objective of synthesizing NIR-II-emitting nanohybrids. The absolute emission intensity of the AuPNPs increased continuously with AuNC loading (Figure 48B), showing that a high concentration of cargo keeps having a beneficial effect on the global PL. To further evaluate the PL efficiency of our AuPNPs, the QYs for different AuNC loadings were measured using the dye IR1061 as reference²³⁰ (Figure 48C). The free AuNCs in organic solution (acetonitrile) had a QY of 1%, in good agreement with previously measured QY values.²¹⁷ At low loadings of the AuNCs in the nanohybrids, the QYs were of the order of 1.3%, and they decreased with increasing loading to attain 0.4% at the highest loading, suggesting an ACQ-like phenomenon.¹⁹¹ Owing to the strongly increasing absorbance with increasing loading, the absolute PL intensity of AuPNPs still increased even with the highest AuNC content (Figure 48C), showing that the increasing number of clusters inside AuPNPs significantly compensated the decrease in QY.

To try and quantify the influence of these parameters, the nanohybrid brightness can be estimated by multiplying the QY and the per-particle extinction coefficient. The elevated number of nanoclusters per nanohybrid at high loadings (up to 14,000) resulted in per-particle brightness values of up to 3.8 x 10⁶ M⁻¹ cm⁻¹ and 7.6 x 10⁵ M⁻¹ cm⁻¹ for excitation at 405 nm and 730 nm, respectively. These values can be compared to those of other NIR-II contrast agents (Annexes Table 11): Typical NIR-II dyes, such as ICG or IR-E1050, have a brightness (in water) of the order of a few 10 M⁻¹ cm⁻¹,²³¹ which is also the order of magnitude for chromophores specifically developed for use in blood.²³² Somewhat higher brightness values are obtained for nanostructures, such as gold nanorods (1200 M⁻¹ cm⁻¹),²³³ organic NPs based on chromophores undergoing AIE (27,000 M⁻¹ cm⁻¹),²³⁴ or QDs (e.g., 12,000 M⁻¹ cm⁻¹).^{235,236} Thus, our nanohybrids are four orders of magnitude brighter than dyes emitting in the same

wavelength range, and one to two orders of magnitude brighter than typical NIR-II emitting NPs. Brighter SWIR objects such as SWCNTs exist, but their 1D geometry is very different from our 0D probes.

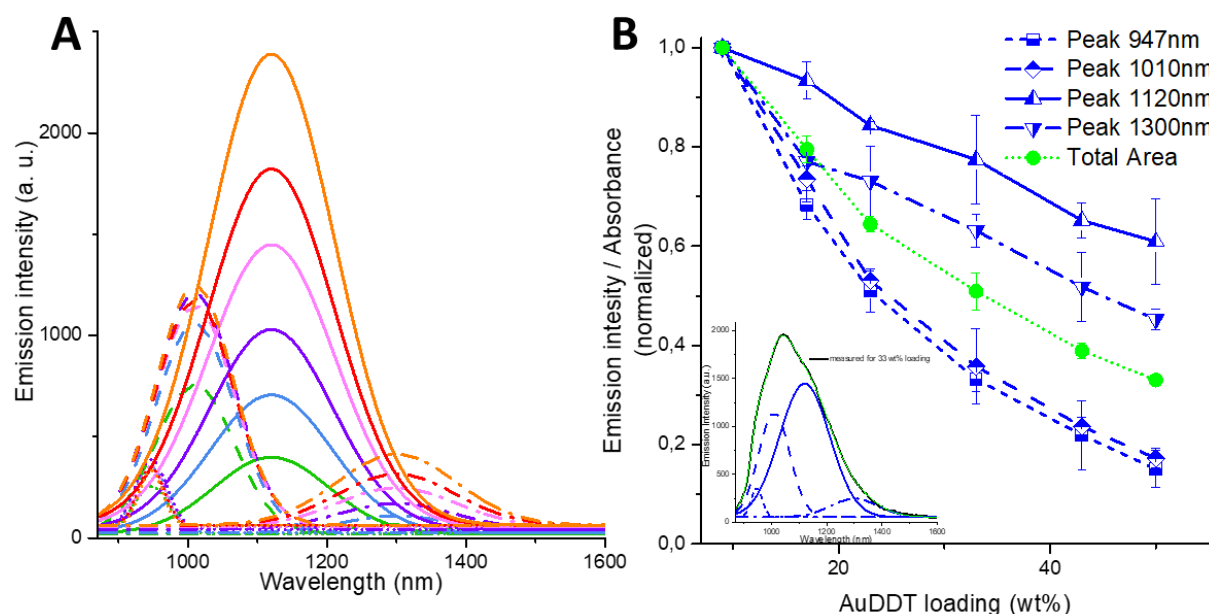


Figure 49: A) Gaussian peak fit for AuPNPs with different loadings. B) Ratio between peak area and absorbance, normalized to the value at 9 wt% for comparison between the different peaks. Inset: Representation of the deconvolution of the PL emission spectrum of AuPNPs,

To further study the influence of AuNC loading on our nanohybrids, the PL spectra were normalized (Annexes Figure 108), revealing that an increase in the AuNC concentration induced a shift in the PL toward longer wavelengths. For a better understanding of this evolution, we performed deconvolutions of the observed emission spectra (Figure 49A). For simplicity, we chose to decompose the spectra into different Gaussian curves and the best fitting results were obtained for four Gaussians with maximum intensities at 947, 1010, 1120, and 1300 nm, respectively (Figure 49A). This model was then applied to the spectra of AuPNPs loaded with different AuNC concentrations and the absolute intensities of each peak were compared. In Figure 49, two trends emerge from comparison of the peaks: at lower wavelength (947 and 1010 nm), the absolute PL intensity remained nearly constant, independent of the AuNC concentration. On the contrary, absolute PL intensities of the two longer wavelength peaks (1120 and 1300 nm) increased with increasing AuNC concentrations. The resulting relative decrease/increase of lower/higher wavelength intensities was found for both 730 nm (Annexes Figure 108) and 405 nm excitation. Taking into account that the absorption also increases with increasing loading, a comparison of the absolute PL intensities of the different peaks can be misleading. Therefore, similar to the global PL analysis, the ratio between each PL peak intensity and its corresponding absorbance value (Figure 49B) was calculated and, as expected (cf. QY in Figure 48), all ratio values decreased while increasing the loading. However, the decrease was significantly less strong for the longer wavelength peaks. This suggests that the PL at longer wavelengths is less sensitive to an ACQ-type quenching behavior. Through variation of the fraction of charged groups on the polymers used for

nanoprecipitation, it was possible to obtain nanohybrids with different sizes but the same loading of AuNCs (Figure 47A). PL measurements on nanohybrids with 33 wt% AuNC loading and sizes of 49 nm and 25 nm, respectively, showed that the overall PL was about 15% higher in case of the bigger sizes (Annexes Figure 109). This difference mainly stems from a higher emission at the shorter wavelengths (950 and 1010 nm).

2.2 Time Resolved

The steady state spectroscopy results enabled to highlight variations of the PL properties of our nanohybrids depending on the emission range observed (Figure 48). This difference in the PL behaviour has been attributed to a difference of sensitivity towards AuNC quenching inside the PNPs. Indeed, the inter-AuNCs distances within the AuPNPs decrease with increased loading, meaning that the probability of AuNC interactions would increase at the same time. To further investigate this wavelength dependent behaviour, PL decay kinetics have been measured at 950 and 1050 nm for the short wavelength and 1200 nm for the longer wavelength. The wavelength of 1200 nm was chosen because it is significantly separated from the short wavelength peaks and still provides sufficient PL intensity for kinetic analysis. Moreover, different AuNC PL studies suggested that excitation at the distinct absorption peaks resulted in preferential PL from either the AuNC core (700 nm excitation) or from the AuNC surface via ligand-metal interactions (400 nm excitation).^{121,237,238} Thus, we investigated the PL kinetics using two different excitation lasers with wavelengths of 404 and 675 nm.

The multiexponential PL decays of AuNC loaded PNPs (Figure 50) clearly show different AuNC concentration-dependent behaviors for the different emission wavelengths. Whereas 950 nm emission presented a strongly pronounced longer decay time component, 1200 nm emission mainly showed faster decays, and the 1050 nm emission decay behavior was in between the two others. The fitted PL decay times (Figure 50, center) and amplitude fractions (Figure 50, bottom) confirmed this trend. The 1200 nm emission was insensitive to the AuNC concentrations with two unchanged PL lifetimes and amplitude fractions, resulting in a stable average PL lifetime. Emission of pure AuNCs (data points at 0 wt%) was measured in ethanol and was very weak at 1200 nm, which explains the slightly lower decay time values. 950 nm and 1050 nm PL decays also showed two distinct PL lifetimes. However, whereas the shorter lifetime (τ_1 , black) was stable over the entire AuNC concentration range and corresponded very well to the one at 1200 nm, the longer decay time (τ_2 , red) was much higher at low AuNC loading and decreased toward the τ_2 value at 1200 nm with increasing AuNC loading. The long lifetime component was also significantly stronger for the 950 nm decay compared to 1050 nm, which showed that the influence of AuNC loading was stronger for the shorter emission wavelength. This trend is also visible in the amplitude-averaged PL lifetimes (blue data points in Figure 50, center). These results are in agreement with the steady-state spectroscopy, which showed that the redshift of the AuPNPs with increasing AuNC concentration was mainly caused by a stronger PL decrease at shorter wavelengths (Figure 49).

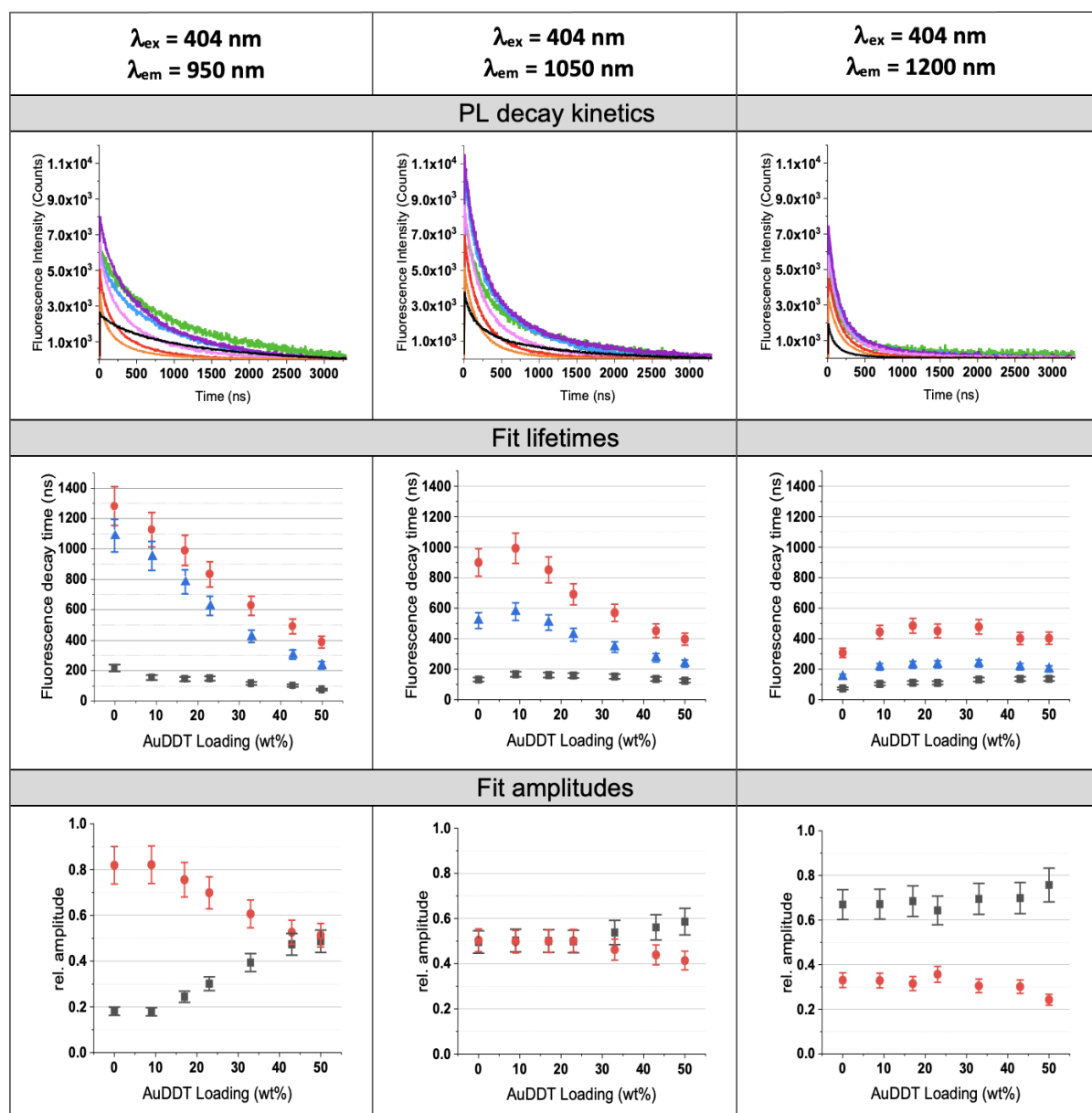


Figure 50: Intensity-comparable (the curves from each graph were normalized for similar excitation intensity and similar absorption and background) PL decays (top row - brown: AuNCs; orange: 50 wt%, red: 43 wt%; magenta: 33 wt%; purple: 23 wt%; blue: 17 wt%; green: 9 wt%), fit PL lifetimes (black: τ_1 ; red: τ_2 ; blue: $\langle \tau \rangle$), and fit amplitude fractions (black: x_1 ; red: x_2) of AuNCs (in ethanol) and AuPNPs (AuDDT in D_2O) for excitation (λ_{ex}) at 404 nm and emission (λ_{em}) at different wavelengths (950, 1050, and 1200 nm). 0 wt% loading corresponds to AuNCs in ethanol. Raw PL decay curves and the different normalization steps are shown in SI Figure S7.

Another interesting point concerns high AuNC loading (50 wt%), for which the single and amplitude-averaged PL lifetimes are very similar for all emission wavelengths (Figure 50, center). This behaviour can be interpreted by a decreasing distance between the AuNCs with increasing loading. The longer PL emission wavelengths (>1200 nm) showed a long (~400 ns) and a short (~100 ns) lifetime component, which did not change with AuNC loading (Figure 5, center right). Considering that the PL intensity at 1200 nm was very weak for AuNCs in solution (Figure 50, top right) and that it was quenched less than the shorter wavelength PL intensity

with increased loading (Figure 49B), the longer PL wavelengths can be attributed to strongly interacting AuNCs. The shorter PL emission wavelengths (<1200 nm) showed a relatively strong long (>1 μ s) decay component together with a relatively weak short (\sim 100 ns) component (Figure 5, center left). The very long decay component is longest and strongest for AuNCs in solution (Figure 50, left). The higher the AuNC loading, the stronger it is quenched, until reaching the value of \sim 400 ns, which presents the one of the strongly interacting AuNCs at 1200 nm. Therefore, the shorter wavelengths mainly present non-interacting or weakly interacting AuNCs, whose fraction strongly decreases with increasing loading due to shorter inter-AuNC distances within the AuPNPs. Both the differences of luminescence decays at short (950 and 1050 nm) and long (1200 nm) emission wavelengths for lower AuNC loading (<50 wt%) and the red shift of the PL with increasing AuNC concentration (Figure 48B) can therefore be attributed to increasing AuNC interactions (closer inter-AuNC distances) that favor longer wavelength over shorter wavelength PL emission.

Interestingly, excitation at 675 nm (instead of 404 nm) resulted in very similar PL decay kinetics, including PL lifetimes and amplitude fractions (Annexes Figure 110). These findings show that there is no difference of exciting the AuNCs in the short or long wavelength absorption band and that there is no excitation-wavelength dependent emission of the AuNC core or ligand-metal-surface states. Although this result is contradictory to previous studies,^{121,239} it has to be noted that the size distribution and the nature of the ligand often has a significant impact on PL emission properties notably in the near infrared region. Indeed, in our case we did not observe AIE behaviour, as was previously described for aggregation of AuGSH NCs.²⁴⁰ A possible reason might be the poorly efficient ligand-metal and ligand-metal-metal charge-transfer of the aliphatic DDT ligands here, compared to electrophilic GSH ligands.^{121,241} While our results provide a new perspective on interaction-dependent AuNC emission behavior, more studies with detailed and comprehensive AuNC PL characterization of many different types of AuNCs will be necessary to fully understand AuNC PL.

The synthesized AuPNPs have been characterized through different spectroscopic experiments that brought complementary information that helped understand the organization of the AuNCs inside the AuPNPs. It highlighted their increasing proximity with the increase of concentration and revealed the evolution of the photophysical properties resulting from this arrangement.

3. Brightness evaluation for *in vivo* applications

Theoretical calculation of the AuPNPs brightness suggested a great potential for imaging application, but remains to be tested in term of *in vivo* bioimaging. Thus, the potential of the nanohybrids was tested first for deep tissue imaging and second for single particle tracking.

3.1 Blood Vessel Imaging

To evaluate the suitability of our nanohybrids for SWIR imaging in terms of photophysical properties, their PL was measured with a NIR-II camera at different tissue depths, using an appropriate phantom model system. In a first step, the PL intensities of concentrated nanohybrid solutions were measured with different AuNC loadings, from 0 to 50 wt%, selecting different sub-optical windows in the SWIR and using NIR excitation ($\lambda = 808 \text{ nm}$ - which is not ideal for AuNC absorption but better suited for tissue penetration compared to excitation in the visible wavelength region). To quantify the PL signal from AuNC loaded AuPNPs in the different sub-optical windows (Figure 51A) a signal to noise ratio was calculated, taking the signal of AuPNPs without AuNCs as background. This experiment clearly indicated that most of the PL was emitted below 1319 nm with a linear increase with AuNC loading. However, signal could also be detected in the NIR-IIb above 1400 nm for the highest loadings, with a SNR that remained higher than 3 for AuPNPs loaded with 33 and 50 wt% of AuNCs for concentrated (Figure 51A) and diluted samples (Annexes Figure 111) This suggest that highly loaded nanohybrids may even be applicable as *in vivo* contrast agents in the NIR-IIb region.

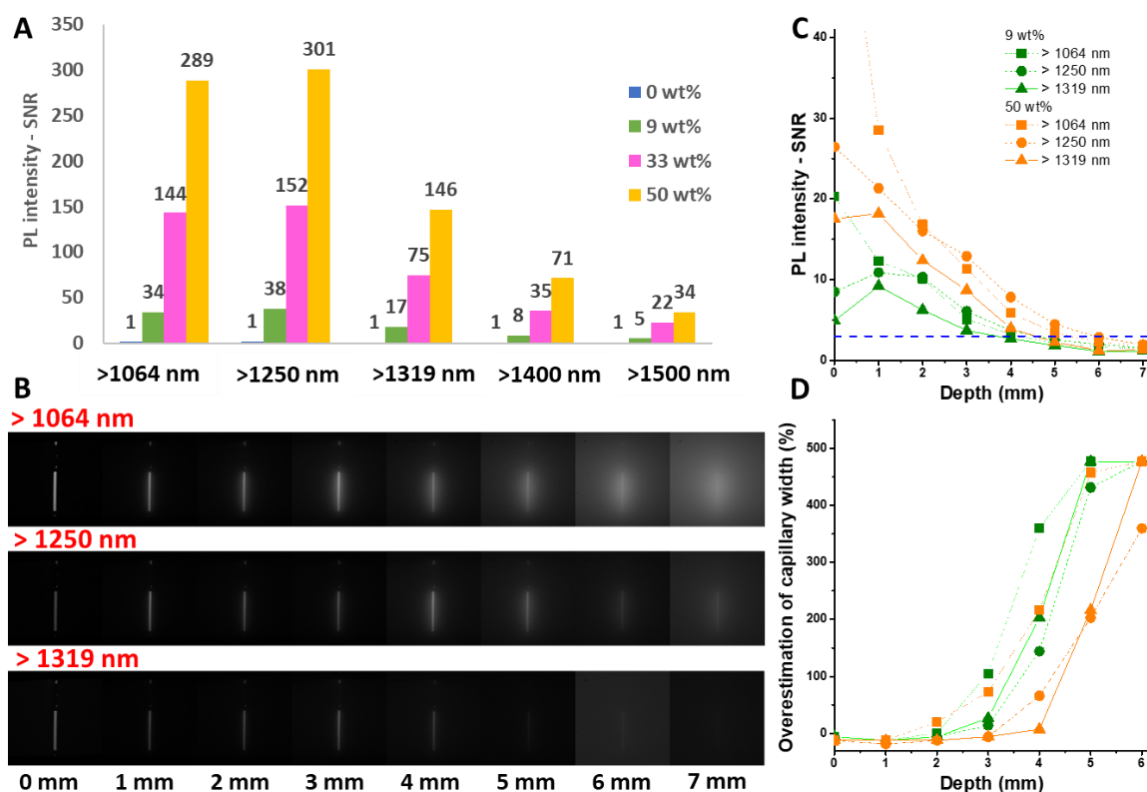


Figure 51: SWIR imaging of Au-PEMA solutions in tubes and capillaries. A) PL intensity expressed in SNR of AuNC NP solution ($300\mu\text{g}/\text{mL}$) at different AuNC loading. B) PL images of capillaries filled with AuPNPs (50 wt% of AuNC) at different depths in intralipid solution (1%) using LP1064 nm, LP1250 nm, and LP1319 nm. C) PL intensity profiles of AuPNPs in capillaries at different intralipid heights using different LP filters. D) Overestimation of the capillary width (%) at different intralipid heights using different LP filters. SNR threshold = 3. $\lambda_{\text{exc.}}$ 808 nm.

In a next step the aim was to quantify how the loading of the nanohybrids with AuNCs influences the depth and the resolution that can be reached, *e.g.*, for imaging blood vessels *in*

vivo. Instead of sacrificing animals, a much better approach for characterizing tissue penetration depth and spatial resolution for blood vessel imaging is the use of tissue mimicking phantom models composed of nanohybrid-filled capillaries placed at different depths in a 1% intralipid solution (Annexes Figure 112).²⁴² Indeed, this model allows simulating the imaging of blood vessels at different depths below the skin, with the possibility to precisely position the capillaries and to evaluate and compare the performance of the different contrast nanoagents. Two of the most important parameters for imaging are the sensitivity of detection and the overestimation of the widths of capillaries, *i.e.* the resolution, which were determined as a function of the tissue phantom depth and the AuNC loading. As expected from the wavelength-dependent PL intensities, and the intralipid-induced absorption and scattering, the PL intensities originating from the capillaries decreased with increasing emission wavelengths and higher depths (Figure 51B). Although increasing tissue thicknesses also resulted in a more scattered (blurred) image of the capillaries (Figure 51B from left to right), increasing PL wavelengths clearly reduced the scattering (Figure 51B from top to bottom).

Quantification of images measured with nanohybrids at different AuNC loading and in different sub-optical windows are presented in Figure 51C and D. A SNR of 3 was used as detection limit for evaluating the detection sensitivity.²⁴³ While there was no significant benefit of selecting a sub-optical window at wavelengths beyond 1250 nm (due to the decreasing PL intensities), there was a clear improvement of the sensitivity when using AuPNPs with the highest AuNC loading. For instance, AuPNPs loaded with 50 wt% of AuNCs could be detected above the defined SNR threshold at 5 mm depth using a >1250 nm long pass filter with a SNR of 3, whereas lower AuNC loadings did not allow to reach sufficiently high SNR at this depth (Figure 51C and SI Figure S13). The overestimation of the capillary width directly provides a measure of the accomplishable spatial resolution. Indeed, generally placing fluorescent objects in diffuse environments leads to a strong scattering enhancement with a rapid overestimation of their real size.²⁴³ So the percentage of overestimation of the capillary width, extracted from the NIR-II images, was plotted as a function of the tissue phantom depths (Figure 51D and SI Figures S14 - S17). Reduced scattering using both longer wavelengths and higher AuNC loading could be clearly observed. For example, selecting the >1319 nm wavelength range and 50 wt% loading of AuNCs made possible to detect capillaries with a good spatial resolution, which corresponded to less than 20% of overestimation, at 4 mm depth in intralipids.

This first evaluation of the PNPs loaded with AuNCs brightness proved that they display a high brightness when put in solution, and confirmed the possibility to go deep into tissue model with a good sensitivity and resolution. Moreover, associating the AuPNPs with the highest loading with the appropriate filter confirmed their potential for use in *in vivo* imaging.

3.2 Single Particle Tracking

Bioimaging can be used to reveal the structure and functioning at the very different scales from the simple molecule level. This requires different probe designs to answer the requirements of the corresponding imaging scales. In the case of SPT, it can be used for example to monitor

the behavior of individual molecules or to study the μm structure and properties of complex biological systems. The probes are used in a very dilute condition to be observed individually. The next step of the brightness evaluation of the synthesized AuNCs loaded PNPs is to test their detectability at the single particle level in the SWIR and compare it to other probes. A suitable single particle probe should possess the following properties: high photoluminescence (PL) brightness for super-localization well below the emission wavelength, excellent photostability for long recording and small dimensions for accessing restricted environments.

For this application small PNPs loaded AuNCs were used (17 wt% in PEMA-COOH-10%). Water soluble ultra-small AuNCs surface-functionalized with short dithiol-terminated poly(ethylene glycol) molecules were chosen for the comparison, as they are similar species to the one encapsulated in the AuPNPs. To complete the study, SWCNTs solutions were prepared by modifying raw SWCNT material with phospholipid-PEG (18:0 PEG5000 DSPE, Laysan Bio), a well-known suspending agent for biological applications^{244,245}. Indeed, luminescent single walled carbon nanotubes (SWCNTs) of 200 to 800 nm length and 1 nm diameter, have proved extremely valuable for single particle tracking (SPT) applications in tissues^{246,247}. Nevertheless, the one-dimensional SWCNT probes display singular diffusion properties in crowded environment²⁴⁸ and would benefit from other SWIR emitting nanoparticles having complementary morphologies. Developing SWIR AuPNPs with small size and spherical morphologies would thus be key to control their accessibility in specific areas of biological tissues.

The studied AuNCs have core sizes below 3 nm (according to high-resolution TEM, Annexes Figure 113), display a broad absorption range from visible to near-infrared and corresponding PL emission in the SWIR from 800 to 1200 nm (Figure 52B) with QY reaching 6.5% previously identified at the ensemble level (Annexes Table 12). AuPNPs size was measured by DLS and gave a mean hydrodynamic particle size of 27 ± 2 nm. TEM micrographs showed a narrow monomodal size distribution with a mean size of 18 ± 3 nm. The absorption and emission spectra remained similar to the ones described in Figure 48, as the same AuNCs are encapsulated, and a PL QY of 0.65 % was measured. The chosen SWCNTs have a (7,5) nanotube chirality²⁴⁹ that displays strong absorption at 660 nm while emitting at ~ 1025 nm (Figure 52D) making them a fair standard for the Au-based objects investigated in this work. One has to take into consideration that each type of nano-object displays different absorption spectra and are therefore not strictly optimally excited at the same excitation wavelengths, yet the choice of a common excitation wavelength at 660 nm is a good compromise since AuNC-based emitters display broad absorption spectra around this wavelength.

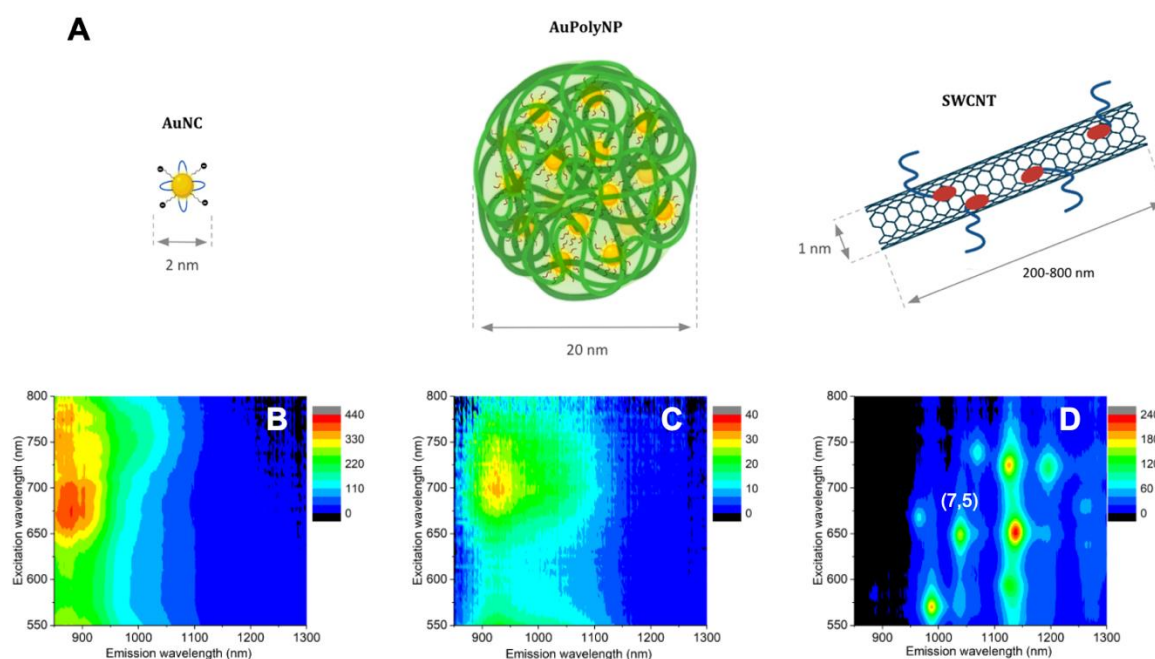


Figure 52: A) Scheme of the different SWIR emitters. 2D PL maps of AuNCs (B), AuPAuPNPs (C) and SWCNTs (D). The peak corresponding to the (7,5) chirality is indicated

The optical properties of AuNCs, AuPNPs and SWCNTs were inspected at the single particle level using a single molecule fluorescence microscope optimized for SWIR imaging. Figure 53 shows typical images of AuNCs, AuPNPs and SWCNTs dispersed on a glass-slide and recorded with 30 ms integration time at identical excitation laser intensities. AuNCs could not be observed at the single particle level in an aqueous environment, which was expected from the per particle brightness determined in ensemble, see Table 12. Yet it becomes possible to detect them at the single particle level in dried condition with PL levels of the order of that of SWCNTs. This behavior may be related to previous observations having shown significant PL enhancement by surface charge injection^{250,251}. AuPNPs and SWCNTs are easily detected both in dried and aqueous environments. Indeed, from images displayed in Figure 53(top), the detection of diffraction limited points (having Full Width at Half Maximum close to the diffraction limit given by $0,61\lambda/NA \sim 480$ nm) is a first indication that AuNCs and AuPNPs are detected at the single particle level. Note the presence of few elongated particles in Figure 53C as expected for SWCNTs with longer lengths than the diffraction limit.

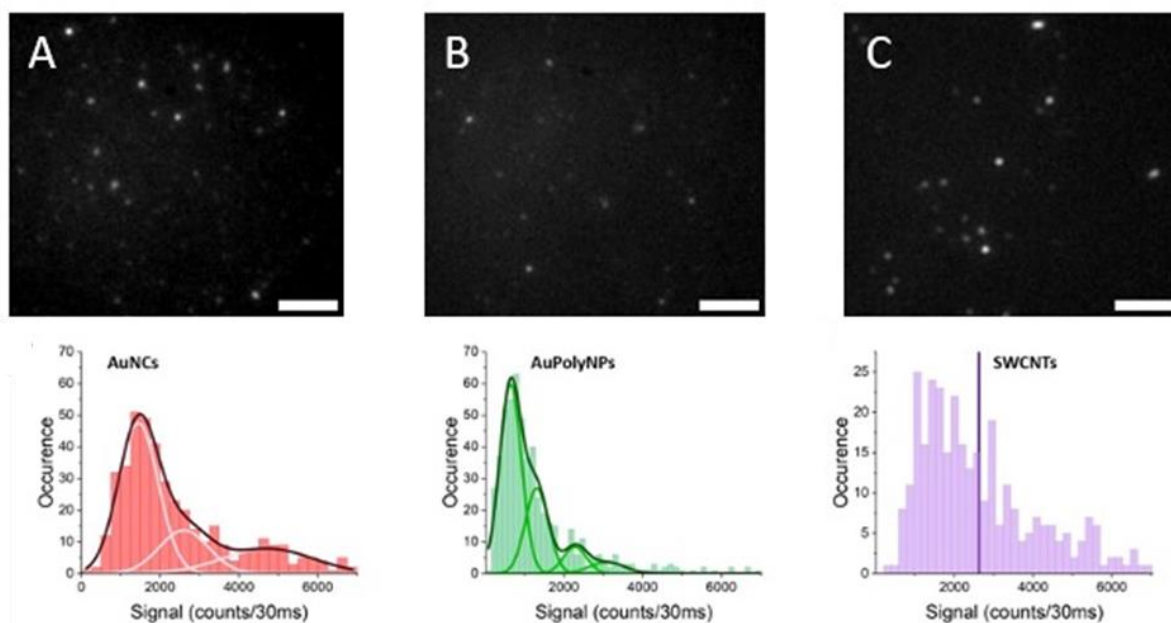


Figure 53: Top: Fluorescence images of individual A) AuNCs, B) AuPNPs, C) SWCNTs immobilized on coverslips excited at 660 nm (700 W/cm^2). Scale bar: 5 μm . Bottom: Evidence for single NP detection. Histogram of the signals for the 3 different samples, AuNCs (dried), AuPAuPNPs (aqueous), SWCNTs (aqueous). The distributions in A and B are well fitted by multiple Gaussian curves. The histogram in C is broader with median equal to 2700, reflecting a polydisperse distribution as expected for SWCNTs of several lengths.

In order to confirm that the great majority of resolved discrete spots may be attributed to single AuPNPs, we constructed the histograms of signal intensities corresponding to each spot by fitting the diffraction limited signals to 2D Gaussian curves having width equal to the microscope diffraction limit (Figure 53, bottom). For AuNCs and AuPNPs, the signal intensity histograms revealed the presence of one main population and minority subpopulations having signals that are multiple of the main population (Figure 53, bottom). This indicates that single particles correspond to the first populations while the subpopulations represent the situation of two or more particles detected within the diffraction limited spot. For SWCNTs, the signal distribution is less monodisperse as expected by the dispersion of length of nanotube preparations (spanning typically from 200 nm up to 800 nm). On the other hand, AuPNP emission of single particles (~ 650 counts/30 ms) is found to be only ~ 4 times lower than that of SWCNTs (median ~ 2700 counts/30 ms) that are known to be very bright emitters, bearing in mind that AuPNPs and SWCNTs are also very differently shaped objects. Indeed, AuPNPs are small spherical AuPNPs ($\sim 20\text{-}30$ nm) in contrast to SWCNTs that are thin and long 1D objects (typically, 400 nm length, 1-3 nm diameter).

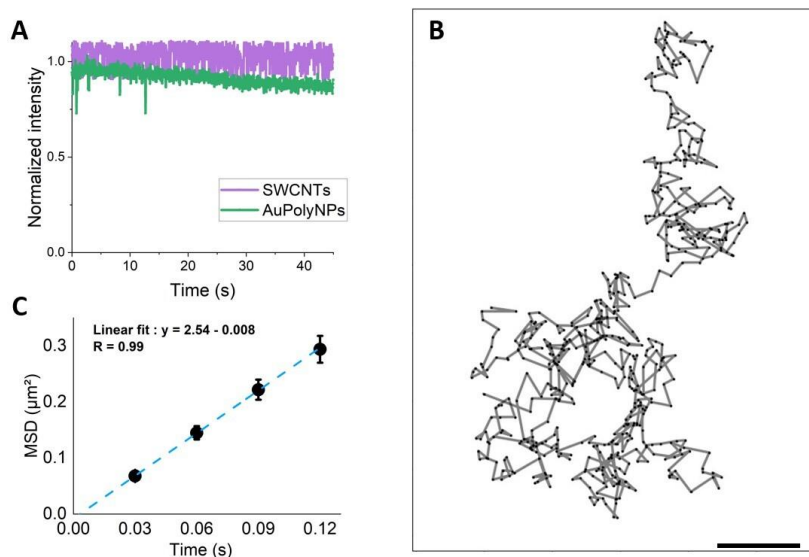


Figure 54: A) Photostability of a single AuPNP and a single SWCNT (normalized emission intensity). B) Example trajectory of a single AuPNP recorded by SPT. Scale bar = 1 μm. C) average MSD plot of 191 trajectories with a linear fit.

Once the detectability of the AuPNPs at the single particle level was assessed, their ability to be tracked in the same conditions as SWCNT was investigated, as the latter have already demonstrated great promise in biological studies due to their SWIR emission range^{252,253}. For that, single AuPNPs were immobilized as in Figure 53B and they could be continuously detected at high imaging rate (30 ms integration time) during tens of seconds with low photobleaching (Figure 54A). This excellent photostability constitutes a key prerequisite for realistic SPT applications. Then, single AuPNPs were imaged, localized and tracked freely diffusing in a water/glycerol (1:2 vol/vol) solution. From that, the trajectories of individual AuPNPs were recorded and reconstructed while AuPNPs were captured in the depth-of-focus range of the microscope (Figure 54B) to analyze their diffusion characteristics. For this, the average mean square displacement (MSD) of 191 AuPNPs trajectories was calculated and found to be linear as expected for Brownian diffusion (Figure 54C).

Interestingly, knowledge of the viscosity of the medium (0.026 ± 0.002 Pa.s)^{254,255} allowed us to determine the diffusion constant of the particles and thus retrieve their hydrodynamic diameter from the slope of the MSD using the Stokes-Einstein equation and taking into account localization precision of this experiment. The average hydrodynamic diameter, measured with a single molecule approach, has a value of 26 ± 3 nm, which is in excellent agreement with the diameter of 27 ± 2 nm measured by DLS at the ensemble level. Eventually, the per particle brightness of AuPNPs was evaluated upon excitation at 660 nm and compared with that of SWCNTs owing to the determination of the size of AuPNPs obtained by our SPT analysis presented above, and to the knowledge of their molar extinction and quantum yield (Annexes Table 12). A brightness of $14\,000$ M⁻¹.cm⁻¹ was found for AuPNPs to be compared to $130\,000$ M⁻¹.cm⁻¹ for (7,5) SWCNTs. This represents a brightness ratio of ~ 9 in fair agreement with that obtained from our single-particle study (~ 4 fold) shown in Figure 53 given the uncertainties on the molar extinction and QY data in ensemble measurements.

4. Biointerfacing

The development and optimization of AuNC loaded polymeric nanoparticles lead to the obtention of bright nanoprobes for the SWIR region. Indeed, their PL properties and potential for bioimaging was assessed both in solution and at the single particle level. Another requirement for a probe to be used as contrasting agent is to be biocompatible, *i.e.* harmless for the biological system it is put in contact with. Thus, the cytotoxicity and intracellular accumulation of the AuPNPs is studied to test their biocompatibility. Then pegylation of the surface of the PNPs with two methods is investigated in order to increase their stealth properties in complex biological media. Eventually, the AuPNPs are tested in *in vivo* SWIR imaging.

4.1 Immunotoxicity

Because the first line of cells in contact in the body are innate immune cells, immunotoxicity assays should be tested on innate phagocytic cells such as macrophages.²⁵⁶ In this spirit, the interaction and the intracellular accumulation of the AuPNPs in macrophages were first investigated. Then, the capacity of AuPNPs to modulate the responses of macrophages with or without stimulation with lipopolysaccharide (LPS) was evaluated. For this study AuPNPs with a loading of 10 wt% in AuDDT in PEMA-COOH-5% (33 ± 3 nm in DLS) were used. The surface charge determined by zeta potential confirmed also their negative charge (-31 mV) in water at pH 7, in line with the observed good colloidal stability over several months (at 4°C). Furthermore, no PL decrease over a period of a few weeks nor photobleaching during the cellular studies were noticed, demonstrating the robustness of the protocol to load hydrophobic Au NCs such as AuDDT inside these polymeric NPs.

Cell viability of J774.1A macrophages in presence of AuPNPs was evaluated by Presto-Blue assays after 24 h and 48 h incubation using AuPNPs concentrations between 1 and 100 $\mu\text{g}/\text{mL}$ (Annexes Figure 114: A) LDH assays on J774.1 cells at 24h with different concentrations of AuPNPs. B) PrestoBlue assays and C) LDH assays on NIH-3T3 cells lines at 24h with different concentrations of AuPNPs. Figure 114). This test revealed no cytotoxicity on J774.1A and this observation was confirmed using an LDH assay and also on another cell line such as NIH-3 T3 mouse embryonic fibroblasts. In order to determine whether the PNPs can penetrate the membrane of the cells, AuPNPs were tracked through confocal fluorescence microscopy using a highly sensitive APD camera that enables the detection of the fluorescence signals up to 1000 nm suitable for the NIR-II emission of the AuNCs emitters. In Figure 55, the accumulation of AuPNPs (in red) in the cytoplasm was clearly observed after 24 h incubation at 50 $\mu\text{g}/\text{mL}$ AuPNPs concentration. Kinetic experiments conducted at short incubation times (5 min, 30 min) indicated a fast interaction of the AuPNPs with the cellular membrane after 5 min, followed by their rapid internalization at 30 min. This particle uptake, in line with data previously reported for dye-loaded PNPs,^{172,257} is commonly associated with an endocytic process where particles are first interacting with the cell membrane and then are engulfed into endosomes vesicles until their late storage in lysosomes.²⁵⁸

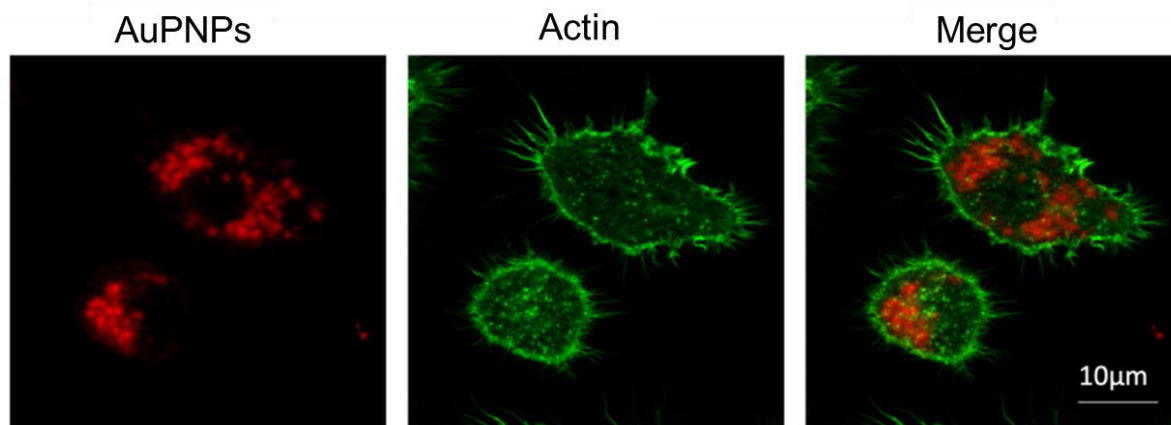


Figure 55: Confocal microscopy. CLSM of J774.1A macrophages were incubated with AuPNPs (red) at 50 $\mu\text{g}/\text{mL}$ for 24 h and labelled for actin (green)

Then the immunological response of J774.1A macrophages was investigated in presence of AuPNPs (33 ± 3 nm) or with the unloaded PNPs (27 ± 1 nm) by first looking at their activation and their cytokine secretion. Using CD86 and MHCII detection, a slight activation of the unstimulated macrophages in presence of the unloaded PNPs only was detected (Annexes Figure 115). Then, macrophages activated after a stimulation with *E.coli* lipopolysaccharide (LPS) were studied in the presence of loaded and unloaded PNPs. However, no significant impact on the activation of LPS stimulated macrophages in the presence of PNPs or AuPNPs was found (Annexes Figure 115). This suggested that the polymer with or without AuNCs did not alter the activation of these macrophages. To determine whether these AuPNPs elicited pro-inflammatory or an anti-inflammatory response, the levels of indicative cytokines (IL-6, TNF- α , IL-10) secreted by macrophages were checked. For stimulated and unstimulated macrophages, the variations levels of the different cytokines were not statistically significant (Annexes Figure 115). These data suggest a moderate, if any, anti-inflammatory effect after stimulation due to the presence of the PNPs. This anti-inflammatory effect has been reported with other polymeric nanoparticles such as PLGA and PLA PNPs.^{259,260} These effects appear independent from the presence of AuNCs, since they are observed with unloaded and Au loaded PNPs.

To further seek for a potential anti-inflammatory effect of the AuPNPs, the production of reactive oxygen species (ROS) and of nitric oxide (NO) was analysed, as they both play an essential role in cell regulation and are associated to inflammation.^{261,262} First observation is that no production of NO by unstimulated macrophages could be detected, even in the presence of PNPs or AuPNPs demonstrating the lack of proinflammatory potential. During the LPS-induced inflammatory response, macrophages release NO which is a key proinflammatory mediator.²⁶³ As expected, cells stimulated with LPS produced a high NO level (30 μM) (Figure 56A). However, a striking decrease of the NO production was observed in presence of AuPNPs and was not affected by the Au loading of the PNPs, since we observed a similar decrease for loaded and unloaded s in a dose-dependent manner. For instance, NO production decreased by 30 % at 10 $\mu\text{g}/\text{mL}$ of AuPNPs and by more than 85 % at 50 $\mu\text{g}/\text{mL}$ of AuPNPs. Independency

from the presence of Au is further supported by the fact that AuNPs do not affect NO.²⁶⁴ These findings corroborated the previous results suggesting the possible anti-inflammatory effect of PNPs as depicted by the heat map summarizing the modulations induced by AuPNPs, (Annexes Figure 116). Next, the ROS production by the unstimulated macrophages was investigated and no difference were observed when they were exposed to AuPNPs or to PNPs compared to control cells (Figure 56B). The same conclusion was drawn for macrophages after LPS stimulus. In general, a similar behavior between the NO and the ROS level is expected, as observed in many instances reporting the scavenging of ROS in cells by some AuPNPs.²⁶⁵ Therefore, PNPs seemed to interfere with NO and ROS productions by independent pathways.

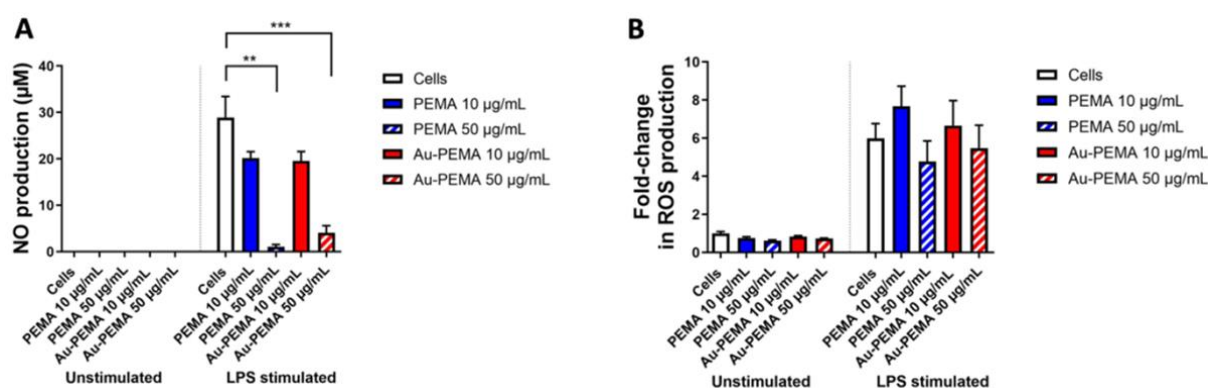


Figure 56: Effect of AuPNPs on NO and ROS production. A) NO production by J774.1A macrophages after 24 h exposure to AuPNPs, followed by a 24 h of LPS stimulation. Mean \pm SE. PEMA control groups $n = 3$; other groups $n = 7-8$. B) Fold-change in ROS production by J774.1A macrophages after 24 h exposure to AuPNPs, followed by a 24 h of LPS stimulation. Data are normalized to unstimulated cells. Mean \pm SE, $n = 5$.

Altogether, our data support an overall anti-inflammatory response of the macrophages exposed to PNPs, characterized by decreases of some cytokine secretions and NO, which are the hallmark of the response of M1 inflammatory macrophages. Nonetheless, at this stage more work is requested to fully elucidate the immuno-metabolism mechanism occurring in macrophages in the presence of PNPs.

4.2 Toward surface protection and *in vivo* imaging

The developed AuPNPs did not show any toxicity for the cells, but investigation of similar PNPs system have been done in our team, showing the poor stability of the bare PNPs in complex biological media and thus compromising their application *in vivo*.²⁶⁶ The formation of a protein corona around the PNPs label them as intruders and prevent a long stay in living system, thus improving their stealth properties is crucial. Pegylation is a method widely used in the pharmaceutical field to generate stealth surface properties. Pluronic is a triblock polymer composed of a poly(propylene oxide) (PPO) bloc attached to two PEG blocs and Pluronic with various size of PPO and/or PEG blocs are commercially available. When added in a solution of AuPNPs, the PPO bloc, more hydrophobic, is adsorbed onto the surface of the AuPNPs, whereas the PEG chains stay in the aqueous media, creating a protection around the NP.²⁶⁶ as described in the introduction, the PEG chain can take different conformations, depending on

the PEG length and grafting density at the surface of the PNP. The bare AuNC loaded PNPs displayed a size of 49 nm in DLS before Pluronic addition and 66 nm after, showing that a 9 nm thick layer of Pluronic has come to coat the PNP surface. The theoretical length of an ethylene oxide being 0.35 nm¹²⁴ and the PEG chains of the Pluronic used having a molar mass of 4700 g.mol⁻¹ (*i.e.* 107 units) the calculated PEG length gives a value around 37 nm, way larger than the one observed. That suggests that the PEG do not elongate into a brush conformation. This length being in similar range than the diameter of the PNPs, further experiments will be needed to test the stealth properties of the coated probes.

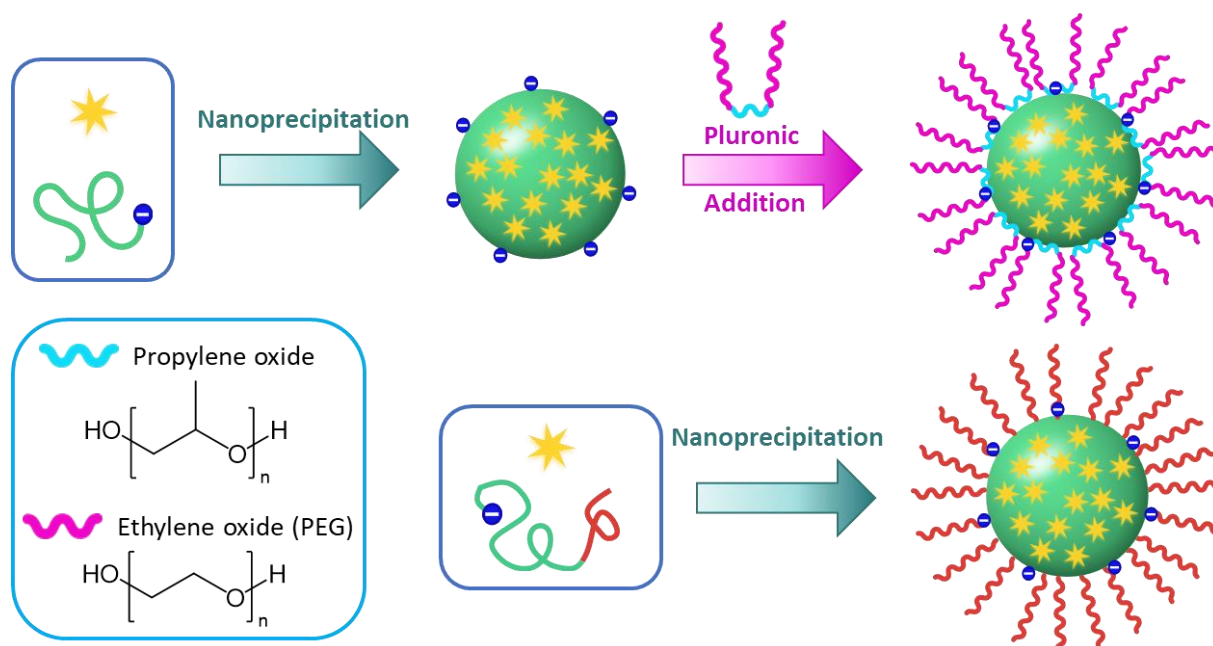


Figure 57: Pegylation of AuPNPs. Top: By Pluronic addition. Bottom: By nanoprecipitation of amphiphilic block copolymer

If the coating with Pluronic is attractive through its simplicity to be put in place, the simple adsorption of the protective shell around the AuPNPs may not be enough. Another strategy is to use block copolymers with a PEMA based block and a PEG based block. Synthesis of different PEMA-PEG is described in the Materials and Methods. Briefly, a PEG chain with an OH termination was coupled with a RAFT chain transfer agent. Two macro-CTA were synthesized, using PEG with 1900 (1.9k) and 5000 (5k) g.mol⁻¹ molecular weight. After removal of the unreacted chain transfer agent, the PEMA block is synthesized through RAFT polymerization using the prepared macro-CTA. This method enabled to obtain PEMA-PEG with different molecular weight of both the PEMA and the PEG block. Additionally, PEMA blocks with 5 mol% of methacrylic acid monomers were synthesized, to approach the PEMA-COOH-5% structure used in previous experiments. Formulation of AuPNPs with these polymers was done to evaluate their encapsulation ability for both rhodamine dyes and AuNCs. Four PEMA-PEG were used for this study. The first one is a PEG(5k) linked to a PEMA(40k) and the three other are PEMA-COOH-5% -PEG with different sizes of hydrophilic and/or hydrophobic block.

To evaluate the stealth properties of the different PNPs (coated with Pluronic or prepared with PEMA-PEG), PNPs prepared in aqueous media then diluted either in phosphate buffer serum (PBS), bovine serum albumin (BSA) or fetal bovine serum (FBS). PBS represents a medium where the PNPs are stable, whereas BSA is rich in albumin and FBS is a complex biological fluid. Then FCS analysis of the PNPs in the different media were achieved to evaluate their stealth properties. The bare PNPs, *i.e.* without any coating, displayed a low stability in complex biological media as shown in Figure 58, where the size of the PNPs in BSA and FBS is largely increased (from 45 to 80 nm) compared to the PBS. This suggested the formation of a protein corona around the PNPs, attracted by the bare negative charges, followed by a moderate aggregation of the PNPs.

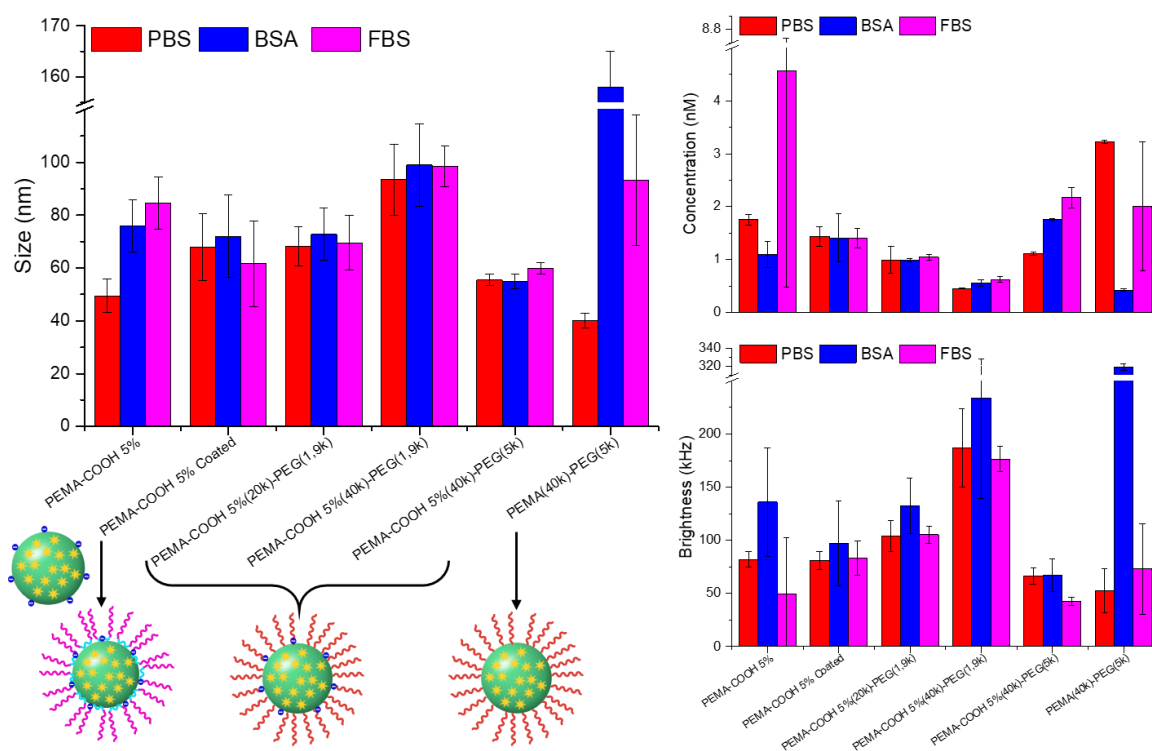


Figure 58: Size, concentration and brightness for different AuPNPs measured in different aqueous media by FCS. Size measured in FBS were reduced with a 10% factor to compensate the difference of viscosity between phosphate buffer and FBS

Then, it could be observed that Pluronic coated PNPs keep the same size around 70 nm, suggesting a good stability in both BSA and FBS. This observation is reinforced by the regularity of the values of the concentrations and brightness measured for these PNPs in the different media. The synthesis of PEMA-COOH-5%-PEG based PNPs yielded particles with sizes going from 37 to 70 nm depending on the polymer used. This difference may be attributed to the difference of block size between the different polymer, the smaller PNPs being formed with the polymer having the longest PEG chain. This suggests that during the nanoprecipitation, the growth of PNPs is stopped more rapidly because of the hinderance generated from the rather long chains. In term of stability, all formulations displayed similar features, having stable sizes, concentration and brightness values independently from the medium of dilution. For PEMA-COOH-5% (40k)-PEG(1.9k), the rather large uncertainties on size and brightness can be

partially explained by the fact that the setup is set mostly for the observation of small objects like single molecules and this PNP is the biggest of the experiment. The last formulation with PEMA-PEG based PNPs yielded particles that were not stable when put both in PBS or FBS, the large size and brightness recorded suggesting the formation of big aggregates. This behavior can be attributed to the lack of charges on the hydrophobic bloc, that normally participate to the stabilization of the colloid suspension. Altogether, these results show the importance of presence of both the charges and the hydrophilic groups at the surface of the PNP to ensure its stability in complex biological media.

Eventually, the AuPNPs were tested for *in vivo* imaging in mice. The efficiency of the Pluronic coating was evaluated by injecting mice either with bare or Pluronic coated AuPNPs and measuring their PL signal in mice plasma over time. As expected, the bare PEMA-COOH-5% AuPNPs with 50 wt% loading were rapidly eliminated (half-life = 10 min) from the mice system, whereas the similar but coated AuPNPs circulated for an extended amount of time, their half-life being around 11h (Figure 59).

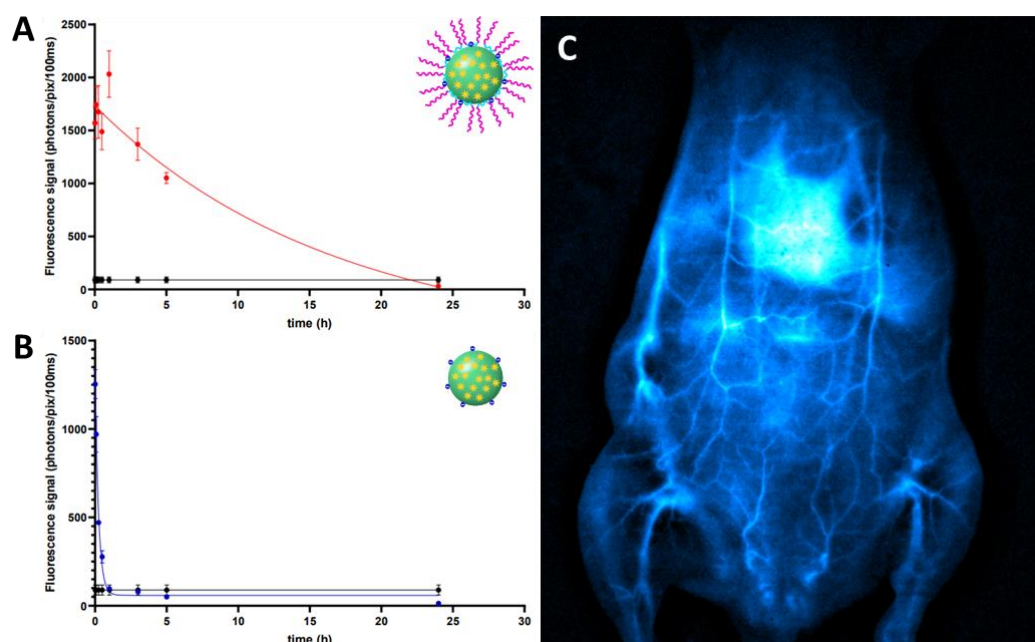


Figure 59: PL signal after injection in mice for A) Pluronic coated AuPNPs and B) Bare AuPNPs. Black line is the signal for non-injected mice. C) *In vivo* SWIR Imaging of a mice after injection of Pluronic coated AuPNPs and post Monte-Carlo reconstruction

SWIR Imaging using a 1250 nm Longpass, *i.e.* recording the PL for wavelength over 1250 nm was achieved on the whole animal level. After imaging treatment using the Monte-Carlo method,³⁷ a reconstructed picture of circulatory system of the mouse could be achieved.

5. Conclusion

In this chapter, the different steps conducting the construction, characterization, evaluation and eventually testing of a new type of nanoprobe for SWIR imaging were exposed. First, the

assembly process of series of PNPs loaded with high amounts of AuNCs emitting in the NIR-II spectral region was described. From that, a thorough characterization using multiple methods enabled to study the efficient encapsulation of AuNCs within the polymer matrix, with loading going up to 50 wt%. This allowed to synthesize nanoparticles of about 60 nm containing over 10 000 clusters each and, even though a slight ACQ effect was observed, relatively good quantum yields could be obtained even at very high AuNC loadings. In this way, an exceptional particle PL brightness for the NIR-II region in the order of $4 \cdot 10^6 \text{ M}^{-1} \text{ cm}^{-1}$ could be reached, which places our nanohybrids among the brightest SWIR emitters. The high AuNC concentrations inside the particles further gave the possibility to study the PL properties at very small inter-cluster distances. Surprisingly, a bathochromic shift of the PL emission with loading was observed. Spectral deconvolution together with time-resolved PL measurements related different sensitivities of different emission modes to interactions between clusters: While emission from the Au core was little affected by the distance between clusters, emissions involving ligand-metal-surface states experience a relatively strong ACQ effect. In consequence, the PL maximum is shifted to longer wavelengths at higher loadings and thus further into the NIR II region. Our results stipulate that precisely engineering the distances and interactions of AuNCs can be a way of optimizing and tailoring their PL properties.

This characterization was followed by the evaluation of the potential of the AuPNPs for bioimaging and sensing applications. To do so, the brightness of the nanoprobe was measured in models at two scales: first at the ensemble level in solution and then at the single particle level. For the AuPNPs in solution, the combination of very high PL brightness with a bathochromic when increasing AuNCs loadings resulted in significantly improved detection and resolution in phantom models, down to 4 mm depth. These results confirmed the possibility to use the nanohybrids for *in vivo* blood vessel imaging. Another study was focused on the possibility to distinguish the AuPNPs at the single particle level in order to assess their potential for single particle tracking. The nanohybrids were successfully observed and showed a good photostability which is essential for this kind of application. The trajectories, diffusion behavior and constants of the probes could be measured, from this the size of the AuPNPs was extracted and revealed to be in excellent agreement with the one determined in DLS. Furthermore, the AuPNPs can exhibit comparable brightness and emission range under identical excitation conditions as well-known SWCNTs, confirming their potential for single particle tracking. This study also widens the range of available tools for this application in the SWIR region, adding 0D objects to the well-known 1D SWCNTs.

The study of AuPNPs in presence of murine macrophages showed the absence of toxicity from the developed nanoprobe, as well as their cell internalization by endocytosis. Furthermore, the poly(ethyl methacrylate) based NPs proved to have an anti-inflammatory effect accompanied by a down regulation of NO level and inflammatory cytokines on activated macrophages after LPS stimulation. These interesting results suggest a potential use of such nanocarriers for immunoregulatory applications or to label stem cells or immune cells for therapeutical applications. The development of a pegylated coating at the surface of the AuPNPs either using Pluronic or amphiphilic PEMA-PEG polymers was investigated to enhance

the stealth properties of the nanohybrids. FCS based analysis of the different NPs suggested a good stability of the PNPs in both BSA and FBS when a pegylated coating was applied, either originated from Pluronic or PEMA-PEG polymers. Encouraged by these results, *in vivo* imaging of the blood vessel system of mice was achieved, confirming the potential of the developed nanohybrids for bioimaging.

General Conclusion

Luminescence is a vast concept enveloping different processes that are attractive for bioimaging and biosensing applications. This thesis enlightened the obstacles to overcome in order to efficiently adapt PL based detection to complex biological media. A key for the successful achievement and improvement of PL imaging and sensing is the contrasting agent used in most applications. Indeed, a high brightness, biocompatibility and specificity are required to reach a high SNR despite the autofluorescence of complex biological systems, and obtain a spatio-temporal resolution. We took a particular interest in time-gating, up-conversion and shortwave infrared emission for the development of probes with PL properties that are not naturally observed in biological media. The final goal is to achieve background free bioimaging and biosensing, to enable the improvement of applications such as biomarker sensing in blood or deep tissue imaging. For that, we chose to synthesize through nanoprecipitation polymeric nanoparticles loaded with high amount of luminophore presenting the PL properties of interest. In this quest, we saw that metal based luminophores are the best candidates and thus investigated the possibility to encapsulate them inside the PNPs.

First, high amounts of luminescent transition-metal complexes were successfully encapsulated in PNPs in order to create probes with enhanced PL lifetimes. The size of the resulting nanoprobables could be tuned with polymer chemistry and PL QYs of the rhenium-based complexes increased strongly upon encapsulation in polymer NPs, with PL brightness of up to $10^8 \text{ M}^{-1} \text{ cm}^{-1}$ and lifetimes of the order of 3-4 μs . To shift the emission range of the probes toward the longer wavelength and reduce the autofluorescence, the rhenium complex was co-encapsulated with a cyanine based NIR dye. The nanoprobables containing both types of luminophores exhibited a shift in their emission into the NIR due to energy transfer, which revealed to be very efficient thanks to lifetime measurements and analysis. However, the same phenomenon decreased greatly the PL lifetime of the probes, making impossible time-gated detection on a μs scale. Nonetheless, this co-encapsulation enabled to extract information on the complex encapsulation and organization inside the PNPs. Indeed, the combined analysis of steady-state and time-resolved data confirmed the efficient encapsulation of the transition-metal complexes and suggested a very close proximity and homogeneous distribution of the encapsulated luminophores. Eventually, the bright PNPs could be used for cellular imaging and showed good internalization and high contrast in the two wavelength regions. Thus, simple co-encapsulation of different luminescent compounds, proved to be a powerful strategy to tune and optimize the PL properties of nanoprobables and opened the way to new classes of luminescent probes. This study also enlightens the challenges encountered when formulating these systems and the difficulty to conjugate all the desired features. The reduced lifetimes made microsecond time-gated imaging in the NIR impossible, but the final nanohybrids displayed a high brightness in combination with lifetimes in the range of hundreds of nanoseconds. This characteristic opens the possibility of achieving sub- μs TG imaging, and thus combine high photon flux than what is typically obtained in Ln complexes with autofluorescence free imaging.

Then, we focused our attention on the development of probes using molecular up-conversion. The objective of this study was to effectively produce a molecular up-converting emitter capable to be detected in aqueous media and biological systems. However, the number of emitters capable of exhibiting this kind of PL is restricted and their properties are mainly limited to organic solvents. The structure of this kind of emitter is more complex than previously encapsulated organic dyes or metallic complexes, in this case the complex was constituted of 9 lanthanide atoms, linked by numerous ligands to ensure their stability and proximity, features required for the UC emission. A modification of the $[\text{Yb}_5\text{Tb}_4(\text{acac})_{16}(\text{OD})_{10}](\text{OD})$ complex hydrophobicity proved to be necessary to ensure a good encapsulation inside the polymeric matrix and the polymer chemistry enabled a variation in the size of the final PNPs. After optimization of the formulations, the PNPs were prepared and characterized in deuterated medium, to better observe the UC properties. The downshifting emission of both the terbium and ytterbium atoms could be measured when exciting the acac ligand, their intensities increasing with the loading. UC signal could also be measured when exciting directly the Yb atoms at 980 nm, with the possibility to determine a UC quantum yield of 6.77×10^{-8} . The comparison of the PL properties of different PNPs formulations showed an absence of influence of the size. After an increase in the intensity in the first hours following the PNPs preparation, the UC intensity proved to be stable over a period of at least 3 days. The UC PL could also be observed in protic aqueous media, with an intensity approximately 8 times lower than in deuterated media. The synthesized nanohybrids were eventually used for up-conversion bioimaging of cells and were compared to classic UCNPs. Whereas the PNPs proved to be less bright than commercial UCNPs, it was possible to do imaging of the cells with both NPs using the same experiments parameters, which is encouraging for a first generation probe. This result proved the capacity of our nanoprobe to achieve molecular UC based bioimaging, a fact that has not been reported yet.

Eventually, we investigated the different steps conducting the construction, characterization, evaluation and testing of a new type of nanoprobe for SWIR imaging. We were able to prepare encapsulate a very high number of AuNCs within the polymer matrix, with loading going up to 50 wt%. A thorough characterization using multiple methods enabled to study the PL properties of the SWIR emitting nanohybrids. Even though a slight ACQ effect was observed, relatively good quantum yields could be obtained even at very high AuNC loadings, thus reaching an exceptional particle PL brightness for the NIR-II region in the order of $4 \cdot 10^6 \text{ M}^{-1} \text{ cm}^{-1}$. This result places our nanohybrids among the brightest SWIR emitters reported. Surprisingly, a bathochromic shift of the PL emission with loading was observed and studied through spectral deconvolution together with time-resolved PL measurements. This enabled to better understand the organization of the AuNCs inside the PNPs, showing that the emission from the Au core is little affected by the distance between clusters, whereas emissions involving ligand-metal-surface states suffer from a relatively strong ACQ effect. Altogether, this behavior is quite beneficial, as it shifts the PL maximum is toward longer wavelengths at higher loadings, and thus further into the NIR II region. This characterization was followed by the evaluation of the potential of the AuPNPs for bioimaging and sensing applications. To do so, the brightness of the nanoprobe was measured in models at two scales: first, in phantom models the AuPNPs

could be detected with a good sensitivity and resolution, down to 4 mm depth. These results confirmed the possibility to use the nanohybrids for deep tissue imaging. Second, their detection proved to be also possible at the single particle level. The nanohybrids were successfully observed and showed a good photostability which is essential for this kind of application, while exhibiting comparable brightness and emission range under identical excitation conditions as SWCNTs. Another key parameter for a contrasting agent being its biocompatibility, the cytotoxicity of the AuPNPs was evaluated. This study showed the absence of toxicity from the developed nanoprobe, as well as their cell internalization by endocytosis. Furthermore, it enlightened the anti-inflammatory effect, confirming altogether the possibility to use the nanohybrids in living systems. The development of a pegylated coating at the surface of the AuPNPs was achieved enhance the stealth properties of the nanohybrids. Eventually, *in vivo* imaging of the blood vessel system of mice could be achieved using the pegylated AuPNPs, confirming their potential for deep tissue imaging.

The different studies have shown the challenges related to the synthesis of nanoprobe presenting peculiar PL properties. Formulating bright polymeric nanoparticles requires a good control of the nanoprecipitation process to optimize the encapsulation and luminophore organization inside the polymer matrix. We were able to encapsulate large metal-based luminophore with complex structure and atom organization and study the effect of encapsulation on the final PL properties of the prepared nanohybrids. Three different types of PNPs could be obtained: first, probes with long PL lifetimes for fast time-gated detection were prepared using rhenium-based complexes. Then, molecular up-converting polymeric nanoparticles could be synthesized using a nonanuclear lanthanide complex, and applied in live-cell imaging. Eventually, gold nanocluster loaded polymeric nanoparticles were formulated for *in vivo* SWIR imaging. All these encouraging results show the possibility to expand the number of luminescent contrasting agents through combination of the interesting characteristics of both organic and inorganic materials, and improve their application in complex biological media.

References

- (1) Vert, M.; Doi, Y.; Hellwich, K.-H.; Hess, M.; Hodge, P.; Kubisa, P.; Rinaudo, M.; Schué, F. Terminology for biorelated polymers and applications (IUPAC Recommendations 2012). *Pure Appl. Chem.* **2012**, *84* (2), 377–410. <https://doi.org/10.1351/PAC-REC-10-12-04>.
- (2) Liceti, F. *Litheosphorus, Siue De Lapide Bononiensi Lucem in Se Conceptam Ab Ambiente Claro Mox in Tenebris Mire Conservante*; 1640.
- (3) Valeur, B.; Berberan-Santos, M. N. *Molecular Fluorescence: Principles and Applications*; Wiley-VCH Verlag GmbH & Co. KGaA: Weinheim, Germany, 2012. <https://doi.org/10.1002/9783527650002>.
- (4) Wiedemann, E. Ueber Fluorescenz Und Phosphorescenz I. Abhandlung. *Ann. Phys.* **1888**, *270* (7), 446–463. <https://doi.org/10.1002/andp.18882700703>.
- (5) Stokes, G. G. On the Change of Refrangibility of Light. *Philos. Trans. R. Soc. Lond. Ser. I* **1852**, *142*, 463–562.
- (6) *Principles of Fluorescence Spectroscopy*; Lakowicz, J. R., Ed.; Springer US: Boston, MA, 2006. <https://doi.org/10.1007/978-0-387-46312-4>.
- (7) Yang, W.; Chen, S.-L. Time-Gated Fluorescence Imaging: Advances in Technology and Biological Applications. *J. Innov. Opt. Health Sci.* **2020**, *13* (03), 2030006. <https://doi.org/10.1142/S1793545820300062>.
- (8) Parikh, R.; Mathai, A.; Parikh, S.; Chandra Sekhar, G.; Thomas, R. Understanding and Using Sensitivity, Specificity and Predictive Values. *Indian J. Ophthalmol.* **2008**, *56* (1), 45–50.
- (9) Saah, A. J.; Hoover, D. R. “Sensitivity” and “Specificity” Reconsidered: The Meaning of These Terms in Analytical and Diagnostic Settings. *Ann. Intern. Med.* **1997**, *126* (1), 91–94. <https://doi.org/10.7326/0003-4819-126-1-199701010-00026>.
- (10) Abbe, E. Beiträge zur Theorie des Mikroskops und der mikroskopischen Wahrnehmung. *Arch. Für Mikrosk. Anat.* **1873**, *9* (1), 413–468. <https://doi.org/10.1007/BF02956173>.
- (11) Wang, B.; Barbiero, M.; Zhang, Q.; Gu, M. Super-Resolution Optical Microscope: Principle, Instrumentation, and Application. *Front. Inf. Technol. Electron. Eng.* **2019**, *20* (5), 608–630. <https://doi.org/10.1631/FITEE.1800449>.
- (12) Hou, S.; Johnson, C.; Welsher, K. Real-Time 3D Single Particle Tracking: Towards Active Feedback Single Molecule Spectroscopy in Live Cells. *Molecules* **2019**, *24* (15), 2826. <https://doi.org/10.3390/molecules24152826>.
- (13) von Diezmann, A.; Shechtman, Y.; Moerner, W. E. Three-Dimensional Localization of Single Molecules for Super-Resolution Imaging and Single-Particle Tracking. *Chem. Rev.* **2017**, *117* (11), 7244–7275. <https://doi.org/10.1021/acs.chemrev.6b00629>.
- (14) Wang, Z.; Wang, X.; Zhang, Y.; Xu, W.; Han, X. Principles and Applications of Single Particle Tracking in Cell Research. *Small* **2021**, *17* (11), 2005133. <https://doi.org/10.1002/smll.202005133>.
- (15) Thompson, R. E.; Larson, D. R.; Webb, W. W. Precise Nanometer Localization Analysis for Individual Fluorescent Probes. *Biophys. J.* **2002**, *82* (5), 2775–2783

-
- (16) Croce, A. C.; Bottiroli, G. Autofluorescence Spectroscopy and Imaging: A Tool for Biomedical Research and Diagnosis. *Eur. J. Histochem.* **2014**. <https://doi.org/10.4081/ejh.2014.2461>.
- (17) Lavis, L. D.; Raines, R. T. Bright Ideas for Chemical Biology. *ACS Chem. Biol.* **2008**, *3* (3), 142–155. <https://doi.org/10.1021/cb700248m>.
- (18) Hermanson, G. T. Fluorescent Probes. In *Bioconjugate Techniques*; Elsevier, 2013; pp 395–463. <https://doi.org/10.1016/B978-0-12-382239-0.00010-8>.
- (19) Day, R. N.; Davidson, M. W. The Fluorescent Protein Palette: Tools for Cellular Imaging. *Chem. Soc. Rev.* **2009**, *38* (10), 2887–2921. <https://doi.org/10.1039/B901966A>.
- (20) Chudakov, D. M.; Matz, M. V.; Lukyanov, S.; Lukyanov, K. A. Fluorescent Proteins and Their Applications in Imaging Living Cells and Tissues. *Physiol. Rev.* **2010**, *90* (3), 1103–1163. <https://doi.org/10.1152/physrev.00038.2009>.
- (21) Toseland, C. P. Fluorescent Labeling and Modification of Proteins. *J. Chem. Biol.* **2013**, *6* (3), 85–95. <https://doi.org/10.1007/s12154-013-0094-5>.
- (22) Wang, W.; Hu, Z. Targeting Peptide-Based Probes for Molecular Imaging and Diagnosis. *Adv. Mater.* **2019**, *31* (45), 1804827. <https://doi.org/10.1002/adma.201804827>.
- (23) Maity, D. Selected Peptide-Based Fluorescent Probes for Biological Applications. *Beilstein J. Org. Chem.* **2020**, *16*, 2971–2982. <https://doi.org/10.3762/bjoc.16.247>.
- (24) Bera, D.; Qian, L.; Tseng, T.-K.; Holloway, P. H. Quantum Dots and Their Multimodal Applications: A Review. *Materials* **2010**, *3* (4), 2260–2345. <https://doi.org/10.3390/ma3042260>.
- (25) Díaz-González, M.; de la Escosura-Muñiz, A.; Fernandez-Argüelles, M. T.; García Alonso, F. J.; Costa-Fernandez, J. M. Quantum Dot Bioconjugates for Diagnostic Applications. *Top. Curr. Chem.* **2020**, *378* (2), 35. <https://doi.org/10.1007/s41061-020-0296-6>.
- (26) Algar, W. R.; Susumu, K.; Delehanty, J. B.; Medintz, I. L. Semiconductor Quantum Dots in Bioanalysis: Crossing the Valley of Death. *Anal. Chem.* **2011**, *83* (23), 8826–8837. <https://doi.org/10.1021/ac201331r>.
- (27) Hola, K.; Zhang, Y.; Wang, Y.; Giannelis, E. P.; Zboril, R.; Rogach, A. L. Carbon Dots—Emerging Light Emitters for Bioimaging, Cancer Therapy and Optoelectronics. *Nano Today* **2014**, *9* (5), 590–603. <https://doi.org/10.1016/j.nantod.2014.09.004>.
- (28) Wang, B.; Cai, H.; Waterhouse, G. I. N.; Qu, X.; Yang, B.; Lu, S. Carbon Dots in Bioimaging, Biosensing and Therapeutics: A Comprehensive Review. *Small Sci.* **2022**, *2* (6), 2200012. <https://doi.org/10.1002/smssc.202200012>.
- (29) Gaur, M.; Misra, C.; Yadav, A. B.; Swaroop, S.; Maolmhuaidh, F. Ó.; Bechelany, M.; Barhoum, A. Biomedical Applications of Carbon Nanomaterials: Fullerenes, Quantum Dots, Nanotubes, Nanofibers, and Graphene. *Materials* **2021**, *14* (20), 5978. <https://doi.org/10.3390/ma14205978>.
- (30) Pan, J.; Li, F.; Choi, J. H. Single-Walled Carbon Nanotubes as Optical Probes for Bio-Sensing and Imaging. *J. Mater. Chem. B* **2017**, *5* (32), 6511–6522. <https://doi.org/10.1039/C7TB00748E>.
- (31) Ackermann, J.; Metternich, J. T.; Herberich, S.; Kruss, S. Biosensing with Fluorescent Carbon Nanotubes. *Angew. Chem. Int. Ed.* **2022**, *61* (18), e202112372. <https://doi.org/10.1002/anie.202112372>.

-
- (32) Yu, D.; Yu, T.; Lin, H.; Zhuang, S.; Zhang, D. Recent Advances in Luminescent Downconversion: New Materials, Techniques, and Applications in Solar Cells. *Adv. Opt. Mater.* **2022**, *10* (12), 2200014. <https://doi.org/10.1002/adom.202200014>.
- (33) Smith, A. M.; Mancini, M. C.; Nie, S. Second Window for in Vivo Imaging. *Nat. Nanotechnol.* **2009**, *4* (11), 710–711. <https://doi.org/10.1038/nnano.2009.326>.
- (34) Dahal, D.; Ray, P.; Pan, D. Unlocking the Power of Optical Imaging in the Second Biological Window: Structuring NEAR-INFRARED II Materials from Organic Molecules to Nanoparticles. *WIREs Nanomedicine Nanobiotechnology* **2021**. <https://doi.org/10.1002/wnan.1734>.
- (35) Ludvikova, L.; Simon, E.; Deygas, M.; Panier, T.; Plamont, M.-A.; Ollion, J.; Tebo, A.; Piel, M.; Jullien, L.; Robert, L.; Le Saux, T.; Espagne, A. Near-Infrared Co-Illumination of Fluorescent Proteins Reduces Photobleaching and Phototoxicity. *Nat. Biotechnol.* **2023**, 1–5. <https://doi.org/10.1038/s41587-023-01893-7>.
- (36) Lei, Z.; Zhang, F. Molecular Engineering of NIR-II Fluorophores for Improved Biomedical Detection. *Angew. Chem. Int. Ed.* **2021**, *60* (30), 16294–16308. <https://doi.org/10.1002/anie.202007040>.
- (37) Yu, Z.; Musnier, B.; Wegner, K. D.; Henry, M.; Chovelon, B.; Desroches-Castan, A.; Fertin, A.; Resch-Genger, U.; Bailly, S.; Coll, J.-L.; Usson, Y.; Josserand, V.; Le Guével, X. High-Resolution Shortwave Infrared Imaging of Vascular Disorders Using Gold Nanoclusters. *ACS Nano* **2020**, *14* (4), 4973–4981. <https://doi.org/10.1021/acsnano.0c01174>.
- (38) Tsuboi, S.; Jin, T. Fluorescent Gold Nanoclusters for In Vivo Shortwave-Infrared Imaging. *ECS J. Solid State Sci. Technol.* **2021**, *10* (9), 096012. <https://doi.org/10.1149/2162-8777/ac258c>.
- (39) Fan, Y.; Zhang, F. A New Generation of NIR-II Probes: Lanthanide-Based Nanocrystals for Bioimaging and Biosensing. *Adv. Opt. Mater.* **2019**, *7* (7), 1801417. <https://doi.org/10.1002/adom.201801417>.
- (40) Montana, D. M.; Nasilowski, M.; Hess, W. R.; Saif, M.; Carr, J. A.; Nienhaus, L.; Bawendi, M. G. Monodisperse and Water-Soluble Quantum Dots for SWIR Imaging via Carboxylic Acid Copolymer Ligands. *ACS Appl. Mater. Interfaces* **2020**, *12* (32), 35845–35855. <https://doi.org/10.1021/acsmi.0c08255>.
- (41) Yan, D.; Li, T.; Yang, Y.; Niu, N.; Wang, D.; Ge, J.; Wang, L.; Zhang, R.; Wang, D.; Tang, B. Z. A Water-Soluble AIEgen for Noninvasive Diagnosis of Kidney Fibrosis via SWIR Fluorescence and Photoacoustic Imaging. *Adv. Mater.* **2022**, *34* (50), 2206643. <https://doi.org/10.1002/adma.202206643>.
- (42) Piwoński, H.; Wang, Y.; Li, W.; Michinobu, T.; Habuchi, S. Millimeter-Deep Detection of Single Shortwave-Infrared-Emitting Polymer Dots through Turbid Media. *Nano Lett.* **2020**, *20* (12), 8803–8810. <https://doi.org/10.1021/acsnanolett.0c03675>.
- (43) Zhu, Y.; Miao, Y.; Xue, T.; Liu, Y.; Zheng, C.; Ma, J.; Tan, W.; Wen, S.; Gu, C. The Short Wave Near-Infrared Fluorescence Properties of Two *p*-Azaquinodimethane (*p*-AQM)-Based Conjugated Polymers. *J. Innov. Opt. Health Sci.* **2020**, *13* (05), 2041003. <https://doi.org/10.1142/S1793545820410035>.
- (44) Gu, C.; Wang, H.; Wang, X.; Wen, S.; Liu, X.; Tan, W.; Qiu, M.; Ma, J. Dithieno[3,2-b:2',3'-d]Silole-Based Conjugated Polymers for Bioimaging in the Short-Wave Infrared Region. *RSC Adv.* **2021**, *11* (49), 30798–30804. <https://doi.org/10.1039/D1RA05097D>.

-
- (45) Chen, W.; Cheng, C.-A.; Cosco, E. D.; Ramakrishnan, S.; Lingg, J. G. P.; Bruns, O. T.; Zink, J. I.; Sletten, E. M. Shortwave Infrared Imaging with J-Aggregates Stabilized in Hollow Mesoporous Silica Nanoparticles. *J. Am. Chem. Soc.* **2019**, *141* (32), 12475–12480. <https://doi.org/10.1021/jacs.9b05195>.
- (46) Yakovliev, A.; Ziniuk, R.; Wang, D.; Xue, B.; Vretik, L. O.; Nikolaeva, O. A.; Tan, M.; Chen, G.; Slominskii, Yu. L.; Qu, J.; Ohulchanskyy, T. Y. Hyperspectral Multiplexed Biological Imaging of Nanoprobes Emitting in the Short-Wave Infrared Region. *Nanoscale Res. Lett.* **2019**, *14* (1), 243. <https://doi.org/10.1186/s11671-019-3068-x>.
- (47) Chepurina, O. M.; Yakovliev, A.; Ziniuk, R.; Nikolaeva, O. A.; Levchenko, S. M.; Xu, H.; Losytskyy, M. Y.; Bricks, J. L.; Slominskii, Yu. L.; Vretik, L. O.; Qu, J.; Ohulchanskyy, T. Y. Core–Shell Polymeric Nanoparticles Co-Loaded with Photosensitizer and Organic Dye for Photodynamic Therapy Guided by Fluorescence Imaging in near and Short-Wave Infrared Spectral Regions. *J. Nanobiotechnology* **2020**, *18* (1), 19. <https://doi.org/10.1186/s12951-020-0572-1>.
- (48) Bloembergen, N. Solid State Infrared Quantum Counters. *Phys. Rev. Lett.* **1959**, *2* (3), 84–85. <https://doi.org/10.1103/PhysRevLett.2.84>.
- (49) Nonat, A. M.; Charbonnière, L. J. Upconversion of Light with Molecular and Supramolecular Lanthanide Complexes. *Coord. Chem. Rev.* **2020**, *409*, 213192. <https://doi.org/10.1016/j.ccr.2020.213192>.
- (50) Dong, H.; Sun, L.-D.; Yan, C.-H. Energy Transfer in Lanthanide Upconverting Studies for Extended Optical Applications. *Chem. Soc. Rev.* **2012**.
- (51) Bünzli, J.-C. G. Benefiting from the Unique Properties of Lanthanide Ions. *Acc. Chem. Res.* **2006**, *39* (1), 53–61. <https://doi.org/10.1021/ar0400894>.
- (52) Wiesholler, L. M.; Hirsch, T. Strategies for the Design of Bright Upconversion Nanoparticles for Bioanalytical Applications. *Opt. Mater.* **2018**, *80*, 253–264. <https://doi.org/10.1016/j.optmat.2018.04.015>.
- (53) Mandl, G. A.; Cooper, D. R.; Hirsch, T.; Seuntjens, J.; Capobianco, J. A. Perspective: Lanthanide-Doped Upconverting Nanoparticles. *Methods Appl. Fluoresc.* **2019**, *7* (1), 012004. <https://doi.org/10.1088/2050-6120/aafa3d>.
- (54) Rostami, I.; Rezvani Alanagh, H.; Hu, Z.; Shahmoradian, S. H. Breakthroughs in Medicine and Bioimaging with Up-Conversion Nanoparticles. *Int. J. Nanomedicine* **2019**, *14*, 7759–7780. <https://doi.org/10.2147/IJN.S221433>.
- (55) Mettenbrink, E. M.; Yang, W.; Wilhelm, S. Bioimaging with Upconversion Nanoparticles. *Adv. Photonics Res.* **2022**, *3* (12), 2200098. <https://doi.org/10.1002/adpr.202200098>.
- (56) Nonat, A.; Chan, C. F.; Liu, T.; Platas-Iglesias, C.; Liu, Z.; Wong, W.-T.; Wong, W.-K.; Wong, K.-L.; Charbonnière, L. J. Room Temperature Molecular up Conversion in Solution. *Nat. Commun.* **2016**, *7*, 11978. <https://doi.org/10.1038/ncomms11978>.
- (57) Knighton, R. C.; Soro, L. K.; Francés-Soriano, L.; Rodríguez-Rodríguez, A.; Pilet, G.; Lenertz, M.; Platas-Iglesias, C.; Hildebrandt, N.; Charbonnière, L. J. Cooperative Luminescence and Cooperative Sensitization Upconversion of Lanthanide Complexes in Solution. *Angew. Chem.* **2022**, *134* (4), e202113114. <https://doi.org/10.1002/ange.202113114>.
- (58) Sun, G.; Xie, Y.; Wang, Y.; Mandl, G. A.; Maurizio, S. L.; Zhang, H.; Ottenwaelder, X.; Capobianco, J. A.; Sun, L. Cooperative Sensitization Upconversion in Solution Dispersions of Co-Crystal Assemblies of Mononuclear Yb³⁺ and Eu³⁺ Complexes. *Angew. Chem. Int. Ed.* **2023**, *n/a* (n/a), e202304591. <https://doi.org/10.1002/anie.202304591>.

-
- (59) Nonat, A.; Bahamyrou, S.; Lecointre, A.; Przybilla, F.; Mély, Y.; Platas-Iglesias, C.; Camerel, F.; Jeannin, O.; Charbonnière, L. J. Molecular Upconversion in Water in Heteropolynuclear Supramolecular Tb/Yb Assemblies. *J. Am. Chem. Soc.* **2019**, *141* (4), 1568–1576. <https://doi.org/10.1021/jacs.8b10932>.
- (60) Xiao, X.; Haushalter, J. P.; Faris, G. W. Upconversion from Aqueous Phase Lanthanide Chelates. *Opt. Lett.* **2005**, *30* (13), 1674–1676.
- (61) Zhou, Q.; Wirtz, B. M.; Schloemer, T. H.; Burroughs, M. C.; Hu, M.; Narayanan, P.; Lyu, J.; Gallegos, A. O.; Layton, C.; Mai, D. J.; Congreve, D. N. Spatially Controlled Uv Light Generation at Depth Using Upconversion Micelles. *Adv. Mater.* **2023**, *n/a* (n/a), 2301563. <https://doi.org/10.1002/adma.202301563>.
- (62) Demina, P. A.; Khaydukov, K. V.; Babayeva, G.; Varaksa, P. O.; Atanova, A. V.; Stepanov, M. E.; Nikolaeva, M. E.; Krylov, I. V.; Evstratova, I. I.; Pokrovsky, V. S.; Zhigarkov, V. S.; Akasov, R. A.; Egorova, T. V.; Khaydukov, E. V.; Generalova, A. N. Upconversion Nanoparticles Intercalated in Large Polymer Micelles for Tumor Imaging and Chemo/Photothermal Therapy. *Int. J. Mol. Sci.* **2023**, *24* (13), 10574. <https://doi.org/10.3390/ijms241310574>.
- (63) Zhang, K. Y.; Yu, Q.; Wei, H.; Liu, S.; Zhao, Q.; Huang, W. Long-Lived Emissive Probes for Time-Resolved Photoluminescence Bioimaging and Biosensing. *Chem. Rev.* **2018**, *118* (4), 1770–1839. <https://doi.org/10.1021/acs.chemrev.7b00425>.
- (64) Zhang, R.; Yuan, J. Responsive Metal Complex Probes for Time-Gated Luminescence Biosensing and Imaging. *Acc. Chem. Res.* **2020**, *53* (7), 1316–1329. <https://doi.org/10.1021/acs.accounts.0c00172>.
- (65) Lee, L. C.-C.; Lo, K. K.-W. Strategic Design of Luminescent Rhenium(I), Ruthenium(II), and Iridium(III) Complexes as Activity-Based Probes for Bioimaging and Biosensing. *Chem. – Asian J.* **2022**, *17* (22), e202200840. <https://doi.org/10.1002/asia.202200840>.
- (66) Pete, S.; Roy, N.; Kar, B.; Paira, P. Construction of Homo and Heteronuclear Ru(II), Ir(III) and Re(I) Complexes for Target Specific Cancer Therapy. *Coord. Chem. Rev.* **2022**, *460*, 214462. <https://doi.org/10.1016/j.ccr.2022.214462>.
- (67) Zwier, J. M.; Hildebrandt, N. Time-Gated FRET Detection for Multiplexed Biosensing. In *Reviews in Fluorescence 2016*; Geddes, C. D., Ed.; Reviews in Fluorescence; Springer International Publishing: Cham, 2017; pp 17–43. https://doi.org/10.1007/978-3-319-48260-6_3.
- (68) Schroter, A.; Märkl, S.; Weitzel, N.; Hirsch, T. Upconversion Nanocrystals with High Lanthanide Content: Luminescence Loss by Energy Migration versus Luminescence Enhancement by Increased NIR Absorption. *Adv. Funct. Mater.* **2022**, *32* (26), 2113065. <https://doi.org/10.1002/adfm.202113065>.
- (69) Couvreur, P.; Kante, B.; Roland, M.; Speiser, P. Adsorption of Antineoplastic Drugs to Polyalkylcyanoacrylate Nanoparticles and Their Release in Calf Serum. *J. Pharm. Sci.* **1979**, *68* (12), 1521–1524. <https://doi.org/10.1002/jps.2600681215>.
- (70) Fu, S.; Du, C.; Zhang, M.; Tian, A.; Zhang, X. Preparation and Properties of Polymer-Encapsulated Phthalocyanine Blue Pigment via Emulsion Polymerization. *Prog. Org. Coat.* **2012**, *73* (2), 149–154. <https://doi.org/10.1016/j.porgcoat.2011.10.006>.
- (71) Lovell, P. A.; Schork, F. J. Fundamentals of Emulsion Polymerization. *Biomacromolecules* **2020**, *21* (11), 4396–4441. <https://doi.org/10.1021/acs.biomac.0c00769>.

-
- (72) Pavel, F. M. Microemulsion Polymerization. *J. Dispers. Sci. Technol.* **2004**, *25* (1), 1–16. <https://doi.org/10.1081/DIS-120027662>.
- (73) D'Agosto, F.; Rieger, J.; Lansalot, M. RAFT-Mediated Polymerization-Induced Self-Assembly. *Angew. Chem. Int. Ed.* **2020**, *59* (22), 8368–8392. <https://doi.org/10.1002/anie.201911758>.
- (74) Sahoo, S.; Gordievskaya, Y. D.; Bauri, K.; Gavrilov, A. A.; Kramarenko, E. Yu.; De, P. Polymerization-Induced Self-Assembly (PISA) Generated Cholesterol-Based Block Copolymer Nano-Objects in a Nonpolar Solvent: Combined Experimental and Simulation Study. *Macromolecules* **2022**, *55* (4), 1139–1152. <https://doi.org/10.1021/acs.macromol.1c02081>.
- (75) Liu, C.; Hong, C.-Y.; Pan, C.-Y. Polymerization Techniques in Polymerization-Induced Self-Assembly (PISA). *Polym. Chem.* **2020**, *11* (22), 3673–3689. <https://doi.org/10.1039/D0PY00455C>.
- (76) Hunter, S. J.; Penfold, N. J. W.; Jones, E. R.; Zinn, T.; Mykhaylyk, O. O.; Armes, S. P. Synthesis of Thermoresponsive Diblock Copolymer Nano-Objects via RAFT Aqueous Emulsion Polymerization of Hydroxybutyl Methacrylate. *Macromolecules* **2022**, *55* (8), 3051–3062. <https://doi.org/10.1021/acs.macromol.2c00379>.
- (77) Qiu, L.; Han, X.; Xing, C.; Glebe, U. Polymerization-Induced Self-Assembly: An Emerging Tool for Generating Polymer-Based Biohybrid Nanostructures. *Small* **2023**, *19* (18), 2207457. <https://doi.org/10.1002/smll.202207457>.
- (78) Discher, B. M.; Won, Y.-Y.; Ege, D. S.; Lee, J. C.-M.; Bates, F. S.; Discher, D. E.; Hammer, D. A. Polymersomes: Tough Vesicles Made from Diblock Copolymers. *Science* **1999**, *284* (5417), 1143–1146. <https://doi.org/10.1126/science.284.5417.1143>.
- (79) Houga, C.; Giermanska, J.; Lecommandoux, S.; Borsali, R.; Taton, D.; Gnanou, Y.; Le Meins, J.-F. Micelles and Polymersomes Obtained by Self-Assembly of Dextran and Polystyrene Based Block Copolymers. *Biomacromolecules* **2009**, *10* (1), 32–40. <https://doi.org/10.1021/bm800778n>.
- (80) Leong, J.; Teo, J. Y.; Aakalu, V. K.; Yang, Y. Y.; Kong, H. Engineering Polymersomes for Diagnostics and Therapy. *Adv. Healthc. Mater.* **2018**, *7* (8), 1701276. <https://doi.org/10.1002/adhm.201701276>.
- (81) Ghezzi, M.; Pescina, S.; Padula, C.; Santi, P.; Del Favero, E.; Cantù, L.; Nicoli, S. Polymeric Micelles in Drug Delivery: An Insight of the Techniques for Their Characterization and Assessment in Biorelevant Conditions. *J. Controlled Release* **2021**, *332*, 312–336. <https://doi.org/10.1016/j.jconrel.2021.02.031>.
- (82) Bej, R.; Sarkar, J.; Ray, D.; Aswal, V. K.; Ghosh, S. Morphology Regulation in Redox Destructible Amphiphilic Block Copolymers and Impact on Intracellular Drug Delivery. *Macromol. Biosci.* **2018**, *18* (7), 1800057. <https://doi.org/10.1002/mabi.201800057>.
- (83) O'Neil, C. P.; Suzuki, T.; Demurtas, D.; Finka, A.; Hubbell, J. A. A Novel Method for the Encapsulation of Biomolecules into Polymersomes via Direct Hydration. *Langmuir* **2009**, *25* (16), 9025–9029. <https://doi.org/10.1021/la900779t>.
- (84) Liu, G.-Y.; Liu, X.-S.; Wang, S.-S.; Chen, C.-J.; Ji, J. Biomimetic Polymersomes as Carriers for Hydrophilic Quantum Dots. *Langmuir* **2012**, *28* (1), 557–562. <https://doi.org/10.1021/la2033669>.
- (85) Kulkarni, A. A.; Rao, P. S. 2 - Synthesis of Polymeric Nanomaterials for Biomedical Applications. In *Nanomaterials in Tissue Engineering*; Gaharwar, A. K., Sant, S., Hancock,

-
- M. J., Hacking, S. A., Eds.; Woodhead Publishing Series in Biomaterials; Woodhead Publishing, 2013; pp 27–63. <https://doi.org/10.1533/9780857097231.1.27>.
- (86) Mendoza-Muñoz, N.; Alcalá-Alcalá, S.; Quintanar-Guerrero, D. Preparation of Polymer Nanoparticles by the Emulsification-Solvent Evaporation Method: From Vanderhoff's Pioneer Approach to Recent Adaptations. In *Polymer Nanoparticles for Nanomedicines: A Guide for their Design, Preparation and Development*; Vauthier, C., Ponchel, G., Eds.; Springer International Publishing: Cham, 2016; pp 87–121. https://doi.org/10.1007/978-3-319-41421-8_4.
- (87) Lepeltier, E.; Bourgaux, C.; Couvreur, P. Nanoprecipitation and the “Ouzo Effect”: Application to Drug Delivery Devices. *Adv. Drug Deliv. Rev.* **2014**, *71*, 86–97. <https://doi.org/10.1016/j.addr.2013.12.009>.
- (88) Chen, H.; Celik, A. E.; Mutschler, A.; Combes, A.; Runser, A.; Klymchenko, A. S.; Lecommandoux, S.; Serra, C. A.; Reisch, A. Assembly of Fluorescent Polymer Nanoparticles Using Different Microfluidic Mixers. *Langmuir* **2022**, *38* (26), 7945–7955. <https://doi.org/10.1021/acs.langmuir.2c00534>.
- (89) Gericke, M.; Schulze, P.; Heinze, T. Nanoparticles Based on Hydrophobic Polysaccharide Derivatives—Formation Principles, Characterization Techniques, and Biomedical Applications. *Macromol. Biosci.* **2020**, *20* (4), 1900415. <https://doi.org/10.1002/mabi.201900415>.
- (90) Bovone, G.; Cousin, L.; Steiner, F.; Tibbitt, M. W. Solvent Controls Nanoparticle Size during Nanoprecipitation by Limiting Block Copolymer Assembly. *Macromolecules* **2022**, *55* (18), 8040–8048. <https://doi.org/10.1021/acs.macromol.2c00907>.
- (91) Reisch, A.; Runser, A.; Arntz, Y.; Mély, Y.; Klymchenko, A. S. Charge-Controlled Nanoprecipitation as a Modular Approach to Ultrasmall Polymer Nanocarriers: Making Bright and Stable Nanoparticles. *ACS Nano* **2015**, *9* (5), 5104–5116. <https://doi.org/10.1021/acsnano.5b00214>.
- (92) Goubault, C.; Igllicki, D.; Swain, R. A.; McVey, B. F. P.; Lefeuvre, B.; Rault, L.; Nayral, C.; Delpéch, F.; Kahn, M. L.; Chevance, S.; Gauffre, F. Effect of Nanoparticles on Spontaneous Ouzo Emulsification. *J. Colloid Interface Sci.* **2021**, *603*, 572–581. <https://doi.org/10.1016/j.jcis.2021.06.104>.
- (93) Reisch, A.; Heimbürger, D.; Ernst, P.; Runser, A.; Didier, P.; Dujardin, D.; Klymchenko, A. S. Protein-Sized Dye-Loaded Polymer Nanoparticles for Free Particle Diffusion in Cytosol. *Adv. Funct. Mater.* **2018**, *28* (48), 1805157. <https://doi.org/10.1002/adfm.201805157>.
- (94) D'Addio, S. M.; Prud'homme, R. K. Controlling Drug Nanoparticle Formation by Rapid Precipitation. *Adv. Drug Deliv. Rev.* **2011**, *63* (6), 417–426. <https://doi.org/10.1016/j.addr.2011.04.005>.
- (95) Reisch, A.; Trofymchuk, K.; Runser, A.; Fleith, G.; Rawiso, M.; Klymchenko, A. S. Tailoring Fluorescence Brightness and Switching of Nanoparticles through Dye Organization in the Polymer Matrix. *ACS Appl. Mater. Interfaces* **2017**, *9* (49), 43030–43042. <https://doi.org/10.1021/acsami.7b12292>.
- (96) Andreiuk, B.; Reisch, A.; Pivovarenko, V. G.; Klymchenko, A. S. An Aluminium-Based Fluorinated Counterion for Enhanced Encapsulation and Emission of Dyes in Biodegradable Polymer Nanoparticles. *Mater. Chem. Front.* **2017**, *1* (11), 2309–2316. <https://doi.org/10.1039/C7QM00248C>.

-
- (97) Trofymchuk, K.; Valanciunaite, J.; Andreiuk, B.; Reisch, A.; Collot, M.; Klymchenko, A. S. BODIPY-Loaded Polymer Nanoparticles: Chemical Structure of Cargo Defines Leakage from Nanocarrier in Living Cells. *J. Mater. Chem. B* **2019**, *7* (34), 5199–5210. <https://doi.org/10.1039/C8TB02781A>.
- (98) Rosiuk, V.; Runser, A.; Klymchenko, A.; Reisch, A. Controlling Size and Fluorescence of Dye-Loaded Polymer Nanoparticles through Polymer Design. *Langmuir* **2019**, *35* (21), 7009–7017. <https://doi.org/10.1021/acs.langmuir.9b00721>.
- (99) Yan, X.; Bernard, J.; Ganachaud, F. Nanoprecipitation as a Simple and Straightforward Process to Create Complex Polymeric Colloidal Morphologies. *Adv. Colloid Interface Sci.* **2021**, *294*, 102474. <https://doi.org/10.1016/j.cis.2021.102474>.
- (100) A, C.; Kn, T.; As, K.; A, R. Protein-like Particles through Nanoprecipitation of Mixtures of Polymers of Opposite Charge. *J. Colloid Interface Sci.* **2022**, *607* (Pt 2). <https://doi.org/10.1016/j.jcis.2021.09.080>.
- (101) Goubault, C.; Sciortino, F.; Mongin, O.; Jarry, U.; Bostoën, M.; Jakobczyk, H.; Burel, A.; Dutertre, S.; Troadec, M.-B.; Kahn, M. L.; Chevance, S.; Gauffre, F. The Ouzo Effect: A Tool to Elaborate High-Payload Nanocapsules. *J. Controlled Release* **2020**, *324*, 430–439. <https://doi.org/10.1016/j.jconrel.2020.05.023>.
- (102) Casteleiro, B.; Ribeiro, T.; Mariz, I.; Martinho, J. M. G.; Farinha, J. P. S. Encapsulation of Gold Nanoclusters by Photo-Initiated Miniemulsion Polymerization. *Colloids Surf. Physicochem. Eng. Asp.* **2022**, *648*, 129410. <https://doi.org/10.1016/j.colsurfa.2022.129410>.
- (103) Yordanov, G.; Simeonova, M.; Alexandrova, R.; Yoshimura, H.; Dushkin, C. Quantum Dots Tagged Poly(Alkylcyanoacrylate) Nanoparticles Intended for Bioimaging Applications. *Colloids Surf. Physicochem. Eng. Asp.* **2009**, *339* (1), 199–205. <https://doi.org/10.1016/j.colsurfa.2009.02.027>.
- (104) Tamaki, K.; Shimomura, M. Fabrications of Luminescent Polymeric Nanoparticles Containing Lanthanide (Iii) Ion Complexes. *Int. J. Nanosci.* **2002**, *01* (05n06), 533–537. <https://doi.org/10.1142/S0219581X02000620>.
- (105) Gkika, K. S.; Kargaard, A.; Burke, C. S.; Dolan, C.; Heise, A.; Keyes, T. E. Ru(II)/BODIPY Core Co-Encapsulated Ratiometric Nanotools for Intracellular O₂ Sensing in Live Cancer Cells. *RSC Chem. Biol.* **2021**, *2* (5), 1520–1533. <https://doi.org/10.1039/D1CB00102G>.
- (106) Özgür, E.; Patra, H. K.; Turner, A. P. F.; Denizli, A.; Uzun, L. Lanthanide [Terbium(III)]-Doped Molecularly Imprinted Nanoarchitectures for the Fluorimetric Detection of Melatonin. *Ind. Eng. Chem. Res.* **2020**, *59* (36), 16068–16076. <https://doi.org/10.1021/acs.iecr.0c02387>.
- (107) Rothfuss, H.; Knöfel, N. D.; Tzvetkova, P.; Michenfelder, N. C.; Baraban, S.; Unterreiner, A.-N.; Roesky, P. W.; Barner-Kowollik, C. Phenanthroline—A Versatile Ligand for Advanced Functional Polymeric Materials. *Chem. – Eur. J.* **2018**, *24* (66), 17475–17486. <https://doi.org/10.1002/chem.201803692>.
- (108) Kusumaatmaja, A.; Ando, T.; Terada, K.; Hirohara, S.; Nakashima, T.; Kawai, T.; Terashima, T.; Tanihara, M. Synthesis and Photoproperties of Eu(III)-Bearing Star Polymers as Luminescent Materials. *J. Polym. Sci. Part Polym. Chem.* **2013**, *51* (12), 2527–2535. <https://doi.org/10.1002/pola.26652>.

-
- (109) Chen, D.; Luo, Z.; Li, N.; Lee, J. Y.; Xie, J.; Lu, J. Amphiphilic Polymeric Nanocarriers with Luminescent Gold Nanoclusters for Concurrent Bioimaging and Controlled Drug Release. *Adv. Funct. Mater.* **2013**, *23* (35), 4324–4331. <https://doi.org/10.1002/adfm.201300411>.
- (110) Nishiyabu, R.; Hashimoto, N.; Cho, T.; Watanabe, K.; Yasunaga, T.; Endo, A.; Kaneko, K.; Niidome, T.; Murata, M.; Adachi, C.; Katayama, Y.; Hashizume, M.; Kimizuka, N. Nanoparticles of Adaptive Supramolecular Networks Self-Assembled from Nucleotides and Lanthanide Ions. *J. Am. Chem. Soc.* **2009**, *131* (6), 2151–2158. <https://doi.org/10.1021/ja8058843>.
- (111) Cui, J.; Zhang, G.; Xin, L.; Yun, P.; Yan, Y.; Su, F. Functional Nanoscale Metal–Organic Particles Synthesized from a New Vinylimidazole-Based Polymeric Ligand and Dysprosium Ions. *J. Mater. Chem. C* **2018**, *6* (2), 280–289. <https://doi.org/10.1039/C7TC03795C>.
- (112) Zhang, X.; Ballem, M. A.; Ahrén, M.; Suska, A.; Bergman, P.; Uvdal, K. Nanoscale Ln(III)-Carboxylate Coordination Polymers (Ln = Gd, Eu, Yb): Temperature-Controlled Guest Encapsulation and Light Harvesting. *J. Am. Chem. Soc.* **2010**, *132* (30), 10391–10397. <https://doi.org/10.1021/ja102299b>.
- (113) Gao, R.-R.; Dong, W. ATP and Lanthanide Ions Derived Coordination Polymer Nanoparticles as a Novel Family of Versatile Materials: Color-Tunable Emission, Artificial Tongues and Logic Devices. *Microchem. J.* **2021**, *160*, 105753. <https://doi.org/10.1016/j.microc.2020.105753>.
- (114) Li, Y.; Yi, S.; Lei, Z.; Xiao, Y. Amphiphilic Polymer-Encapsulated Au Nanoclusters with Enhanced Emission and Stability for Highly Selective Detection of Hypochlorous Acid. *RSC Adv.* **2021**, *11* (24), 14678–14685. <https://doi.org/10.1039/D1RA01634B>.
- (115) Chan, L.; Huang, Y.; Chen, T. Cancer-Targeted Tri-Block Copolymer Nanoparticles as Payloads of Metal Complexes to Achieve Enhanced Cancer Theragnosis. *J. Mater. Chem. B* **2016**, *4* (26), 4517–4525. <https://doi.org/10.1039/C6TB00514D>.
- (116) Nawrot, K. C.; Zareba, J. K.; Toporkiewicz, M.; Chodaczek, G.; Wawrzynczyk, D.; Kulbacka, J.; Bazylińska, U.; Nyk, M. Polymeric Nanocarriers with Luminescent Colloidal Nanoplatelets as Hydrophilic and Non-Toxic Two-Photon Bioimaging Agents. *Int. J. Nanomedicine* **2021**, *16*, 3649–3660. <https://doi.org/10.2147/IJN.S298300>.
- (117) Bœuf, G.; Roullin, G. V.; Moreau, J.; Van Gulick, L.; Zambrano Pineda, N.; Terryn, C.; Ploton, D.; Andry, M. C.; Chuburu, F.; Dukic, S.; Molinari, M.; Lemerrier, G. Encapsulated Ruthenium(II) Complexes in Biocompatible Poly(D,L-Lactide-Co-Glycolide) Nanoparticles for Application in Photodynamic Therapy. *ChemPlusChem* **2014**, *79* (1), 171–180. <https://doi.org/10.1002/cplu.201300242>.
- (118) Soliman, N.; McKenzie, L. K.; Karges, J.; Bertrand, E.; Tharaud, M.; Jakubaszek, M.; Guérineau, V.; Goud, B.; Hollenstein, M.; Gasser, G.; Thomas, C. M. Ruthenium-Initiated Polymerization of Lactide: A Route to Remarkable Cellular Uptake for Photodynamic Therapy of Cancer. *Chem. Sci.* **2020**, *11* (10), 2657–2663. <https://doi.org/10.1039/C9SC05976H>.
- (119) Cardoso Dos Santos, M.; Runser, A.; Bartenlian, H.; Nonat, A. M.; Charbonnière, L. J.; Klymchenko, A. S.; Hildebrandt, N.; Reisch, A. Lanthanide-Complex-Loaded Polymer Nanoparticles for Background-Free Single-Particle and Live-Cell Imaging. *Chem. Mater.* **2019**, *31* (11), 4034–4041. <https://doi.org/10.1021/acs.chemmater.9b00576>.

-
- (120) Hong-Cai “Joe” Zhou; Kitagawa, S. Metal–Organic Frameworks (MOFs). *Chem. Soc. Rev.* **2014**, *43* (16), 5415–5418. <https://doi.org/10.1039/C4CS90059F>.
- (121) Jin, R.; Zeng, C.; Zhou, M.; Chen, Y. Atomically Precise Colloidal Metal Nanoclusters and Nanoparticles: Fundamentals and Opportunities. *Chem. Rev.* **2016**, *116* (18), 10346–10413. <https://doi.org/10.1021/acs.chemrev.5b00703>.
- (122) Gálico, D. A.; Calado, C. M. S.; Murugesu, M. Lanthanide Molecular Cluster-Aggregates as the next Generation of Optical Materials. *Chem. Sci.* **2023**, *14* (22), 5827–5841. <https://doi.org/10.1039/D3SC01088K>.
- (123) Ikeda, Y.; Nagasaki, Y. PEGylation Technology in Nanomedicine. In *Polymers in Nanomedicine*; Kunugi, S., Yamaoka, T., Eds.; Advances in Polymer Science; Springer: Berlin, Heidelberg, 2012; pp 115–140. https://doi.org/10.1007/12_2011_154.
- (124) Shi, L.; Zhang, J.; Zhao, M.; Tang, S.; Cheng, X.; Zhang, W.; Li, W.; Liu, X.; Peng, H.; Wang, Q. Effects of Polyethylene Glycol on the Surface of Nanoparticles for Targeted Drug Delivery. *Nanoscale* **2021**, *13* (24), 10748–10764. <https://doi.org/10.1039/D1NR02065J>.
- (125) Conrad, J. C.; Robertson, M. L. Shaping the Structure and Response of Surface-Grafted Polymer Brushes via the Molecular Weight Distribution. *JACS Au* **2023**, *3* (2), 333–343. <https://doi.org/10.1021/jacsau.2c00638>.
- (126) Mayo, F. R.; Lewis, F. M. Copolymerization. I. A Basis for Comparing the Behavior of Monomers in Copolymerization; The Copolymerization of Styrene and Methyl Methacrylate. *J. Am. Chem. Soc.* **1944**, *66* (9), 1594–1601. <https://doi.org/10.1021/ja01237a052>.
- (127) Greenley, R. Z. Free Radical Copolymerization Reactivity Ratios. In *The Wiley Database of Polymer Properties*; John Wiley & Sons, Ltd, 2003. <https://doi.org/10.1002/0471532053.bra007>.
- (128) Perrier, S. 50th Anniversary Perspective: RAFT Polymerization—A User Guide. *Macromolecules* **2017**, *50* (19), 7433–7447. <https://doi.org/10.1021/acs.macromol.7b00767>.
- (129) Bhattacharjee, S. DLS and Zeta Potential – What They Are and What They Are Not? *J. Controlled Release* **2016**, *235*, 337–351. <https://doi.org/10.1016/j.jconrel.2016.06.017>.
- (130) Hassan, P. A.; Rana, S.; Verma, G. Making Sense of Brownian Motion: Colloid Characterization by Dynamic Light Scattering. *Langmuir* **2015**, *31* (1), 3–12. <https://doi.org/10.1021/la501789z>.
- (131) Lazzari, S.; Moscatelli, D.; Codari, F.; Salmona, M.; Morbidelli, M.; Diomedede, L. Colloidal Stability of Polymeric Nanoparticles in Biological Fluids. *J. Nanoparticle Res.* **2012**, *14* (6), 920. <https://doi.org/10.1007/s11051-012-0920-7>.
- (132) Khan, S.; Gupta, A.; Verma, N. C.; Nandi, C. K. Kinetics of Protein Adsorption on Gold Nanoparticle with Variable Protein Structure and Nanoparticle Size. *J. Chem. Phys.* **2015**, *143* (16), 164709. <https://doi.org/10.1063/1.4934605>.
- (133) Jiang, Y.; Chen, Z.; Han, Y.; Deb, P.; Gao, H.; Xie, S.; Purohit, P.; Tate, M. W.; Park, J.; Gruner, S. M.; Elser, V.; Muller, D. A. Electron Ptychography of 2D Materials to Deep Sub-Ångström Resolution. *Nature* **2018**, *559* (7714), 343–349. <https://doi.org/10.1038/s41586-018-0298-5>.
- (134) Franken, L. E.; Grünwald, K.; Boekema, E. J.; Stuart, M. C. A. A Technical Introduction to Transmission Electron Microscopy for Soft-Matter: Imaging, Possibilities, Choices, and

-
- Technical Developments. *Small* **2020**, *16* (14), 1906198. <https://doi.org/10.1002/sml.201906198>.
- (135) Ruprecht, J.; Nield, J. Determining the Structure of Biological Macromolecules by Transmission Electron Microscopy, Single Particle Analysis and 3D Reconstruction. *Prog. Biophys. Mol. Biol.* **2001**, *75* (3), 121–164. [https://doi.org/10.1016/S0079-6107\(01\)00004-9](https://doi.org/10.1016/S0079-6107(01)00004-9).
- (136) Danino, D. Cryo-TEM of Soft Molecular Assemblies. *Curr. Opin. Colloid Interface Sci.* **2012**, *17* (6), 316–329. <https://doi.org/10.1016/j.cocis.2012.10.003>.
- (137) Kamble, S.; Agrawal, S.; Cherumukil, S.; Sharma, V.; Jasra, R. V.; Munshi, P. Revisiting Zeta Potential, the Key Feature of Interfacial Phenomena, with Applications and Recent Advancements. *ChemistrySelect* **2022**, *7* (1), e202103084. <https://doi.org/10.1002/slct.202103084>.
- (138) Chandrasekhar, S. Stochastic Problems in Physics and Astronomy. *Rev. Mod. Phys.* **1943**, *15* (1), 1–89. <https://doi.org/10.1103/RevModPhys.15.1>.
- (139) Weibel, N.; Charbonnière, L. J.; Guardigli, M.; Roda, A.; Ziessel, R. Engineering of Highly Luminescent Lanthanide Tags Suitable for Protein Labeling and Time-Resolved Luminescence Imaging. *J. Am. Chem. Soc.* **2004**, *126* (15), 4888–4896. <https://doi.org/10.1021/ja031886k>.
- (140) Clegg, R. M. Fluorescence Resonance Energy Transfer. *Current Opinion in Biotechnology* **1996**.
- (141) Koynov, K.; Butt, H.-J. Fluorescence Correlation Spectroscopy in Colloid and Interface Science. *Curr. Opin. Colloid Interface Sci.* **2012**, *17* (6), 377–387. <https://doi.org/10.1016/j.cocis.2012.09.003>.
- (142) Gill, M. R.; Garcia-Lara, J.; Foster, S. J.; Smythe, C.; Battaglia, G.; Thomas, J. A. A Ruthenium(II) Polypyridyl Complex for Direct Imaging of DNA Structure in Living Cells. *Nat. Chem.* **2009**, *1* (8), 662–667. <https://doi.org/10.1038/nchem.406>.
- (143) Dröge, F.; Noakes, F. F.; Archer, S. A.; Sreedharan, S.; Raza, A.; Robertson, C. C.; MacNeil, S.; Haycock, J. W.; Carson, H.; Meijer, A. J. H. M.; Smythe, C. G. W.; Bernardino de la Serna, J.; Dietzek-Ivanšić, B.; Thomas, J. A. A Dinuclear Osmium(II) Complex Near-Infrared Nanoscopy Probe for Nuclear DNA. *J. Am. Chem. Soc.* **2021**, *143* (48), 20442–20453. <https://doi.org/10.1021/jacs.1c10325>.
- (144) Day, A. H.; Übler, M. H.; Best, H. L.; Lloyd-Evans, E.; Mart, R. J.; Fallis, I. A.; Allemann, R. K.; Al-Wattar, E. A. H.; Keymer, N. I.; Buurma, N. J.; Pope, S. J. A. Targeted Cell Imaging Properties of a Deep Red Luminescent Iridium(III) Complex Conjugated with a c-Myc Signal Peptide. *Chem. Sci.* **2020**, *11* (6), 1599–1606. <https://doi.org/10.1039/C9SC05568A>.
- (145) Holden, L.; Burke, C. S.; Cullinane, D.; Keyes, T. E. Strategies to Promote Permeation and Vectorization, and Reduce Cytotoxicity of Metal Complex Luminophores for Bioimaging and Intracellular Sensing. *RSC Chem. Biol.* **2021**, *2* (4), 1021–1049. <https://doi.org/10.1039/D1CB00049G>.
- (146) Amoroso, A. J.; Coogan, M. P.; Dunne, J. E.; Fernández-Moreira, V.; Hess, J. B.; Hayes, A. J.; Lloyd, D.; Millet, C.; Pope, S. J. A.; Williams, C. Rhenium Fac Tricarbonyl Bisimine Complexes: Biologically Useful Fluorochromes for Cell Imaging Applications. *Chem. Commun.* **2007**, No. 29, 3066–3068. <https://doi.org/10.1039/B706657K>.

-
- (147) Lo, K. K.-W.; Zhang, K. Y.; Li, S. P.-Y. Recent Exploitation of Luminescent Rhenium(I) Tricarbonyl Polypyridine Complexes as Biomolecular and Cellular Probes. *Eur. J. Inorg. Chem.* **2011**, *2011* (24), 3551–3568. <https://doi.org/10.1002/ejic.201100469>.
- (148) Lo, K. K.-W.; Choi, A. W.-T.; Law, W. H.-T. Applications of Luminescent Inorganic and Organometallic Transition Metal Complexes as Biomolecular and Cellular Probes. *Dalton Trans.* **2012**, *41* (20), 6021–6047. <https://doi.org/10.1039/C2DT11892K>.
- (149) Hostachy, S.; Policar, C.; Delsuc, N. Re(I) Carbonyl Complexes: Multimodal Platforms for Inorganic Chemical Biology. *Coord. Chem. Rev.* **2017**, *351*, 172–188. <https://doi.org/10.1016/j.ccr.2017.05.004>.
- (150) Lee, L. C.-C.; Lo, K. K.-W. Strategic Design of Luminescent Rhenium(I), Ruthenium(II), and Iridium(III) Complexes as Activity-Based Probes for Bioimaging and Biosensing. *Chem. – Asian J.* **2022**, *17* (22), e202200840. <https://doi.org/10.1002/asia.202200840>.
- (151) Li, B.; Kwok, K. M.; Zeng, H. C. Versatile Hollow ZSM-5 Nanoreactors Loaded with Tailorable Metal Catalysts for Selective Hydrogenation Reactions. *ACS Appl. Mater. Interfaces* **2021**, *13* (17), 20524–20538. <https://doi.org/10.1021/acsami.1c01916>.
- (152) Salavati-Niasari, M.; Shakouri-Arani, M.; Davar, F. Flexible Ligand Synthesis, Characterization and Catalytic Oxidation of Cyclohexane with Host (Nanocavity of Zeolite-Y)/Guest (Mn(II), Co(II), Ni(II) and Cu(II) Complexes of Tetrahydro-Salophen) Nanocomposite Materials. *Microporous Mesoporous Mater.* **2008**, *116* (1), 77–85. <https://doi.org/10.1016/j.micromeso.2008.03.015>.
- (153) Shilpa, E. R.; Gayathri, V. Encapsulation of Cu(II)[2-(2'-Hydroxyphenyl)Benzimidazole]₂ within Zeolite Nano-Cavity: Structural Properties and Its Catalytic Activity towards Phenol and Styrene Oxidation. *J. Environ. Chem. Eng.* **2016**, *4* (4, Part A), 4194–4206. <https://doi.org/10.1016/j.jece.2016.09.022>.
- (154) Xu, L.; Zhang, J.; Li, Z.; Ma, Q.; Wang, Y.; Cui, F.; Cui, T. In Situ Generation of Ultrasmall Sized and Highly Dispersed CuO Nanoparticles Embedded in Silica Matrix and Their Catalytic Application. *New J. Chem.* **2018**, *43* (1), 520–526. <https://doi.org/10.1039/C8NJ04517H>.
- (155) Zhang, P.; Huang, H.; Huang, J.; Chen, H.; Wang, J.; Qiu, K.; Zhao, D.; Ji, L.; Chao, H. Noncovalent Ruthenium(II) Complexes–Single-Walled Carbon Nanotube Composites for Bimodal Photothermal and Photodynamic Therapy with Near-Infrared Irradiation. *ACS Appl. Mater. Interfaces* **2015**, *7* (41), 23278–23290. <https://doi.org/10.1021/acsami.5b07510>.
- (156) Shen, J.; Kim, H.-C.; Wolfram, J.; Mu, C.; Zhang, W.; Liu, H.; Xie, Y.; Mai, J.; Zhang, H.; Li, Z.; Guevara, M.; Mao, Z.-W.; Shen, H. A Liposome Encapsulated Ruthenium Polypyridine Complex as a Theranostic Platform for Triple-Negative Breast Cancer. *Nano Lett.* **2017**, *17* (5), 2913–2920. <https://doi.org/10.1021/acs.nanolett.7b00132>.
- (157) Lu, M.; Chen, F.; Noy, J.-M.; Lu, H.; Stenzel, M. H. Enhanced Antimetastatic Activity of the Ruthenium Anticancer Drug RAPTA-C Delivered in Fructose-Coated Micelles. *Macromol. Biosci.* **2017**, *17* (10), 1600513. <https://doi.org/10.1002/mabi.201600513>.
- (158) Villemin, E.; Ong, Y. C.; Thomas, C. M.; Gasser, G. Polymer Encapsulation of Ruthenium Complexes for Biological and Medicinal Applications. *Nat. Rev. Chem.* **2019**, *3* (4), 261–282. <https://doi.org/10.1038/s41570-019-0088-0>.
- (159) António, J. P. M.; Gandioso, A.; Nematí, F.; Soliman, N.; Vinck, R.; Sun, F.; Robert, C.; Burckel, P.; Decaudin, D.; Thomas, C. M.; Gasser, G. Polymeric Encapsulation of a

-
- Ruthenium(II) Polypyridyl Complex: From Synthesis to in Vivo Studies against High-Grade Epithelial Ovarian Cancer. *Chem. Sci.* **2023**, *14* (2), 362–371. <https://doi.org/10.1039/D2SC05693C>.
- (160) Aubert, T.; Ledneva, A. Y.; Grasset, F.; Kimoto, K.; Naumov, N. G.; Molard, Y.; Saito, N.; Haneda, H.; Cordier, S. Synthesis and Characterization of A4[Re6Q8L6]@SiO2 Red-Emitting Silica Nanoparticles Based on Re6 Metal Atom Clusters (A = Cs or K, Q = S or Se, and L = OH or CN). *Langmuir* **2010**, *26* (23), 18512–18518. <https://doi.org/10.1021/la103784v>.
- (161) Li, X.; Zhang, Y.; Chen, H.; Sun, J.; Feng, F. Protein Nanocages for Delivery and Release of Luminescent Ruthenium(II) Polypyridyl Complexes. *ACS Appl. Mater. Interfaces* **2016**, *8* (35), 22756–22761. <https://doi.org/10.1021/acsami.6b07038>.
- (162) Caspar, J. V.; Meyer, T. J. Application of the Energy Gap Law to Nonradiative, Excited-State Decay. *J. Phys. Chem.* **1983**, *87* (6), 952–957. <https://doi.org/10.1021/j100229a010>.
- (163) Andreiuk, B.; Reisch, A.; Lindecker, M.; Follain, G.; Peyri ras, N.; Goetz, J. G.; Klymchenko, A. S. Fluorescent Polymer Nanoparticles for Cell Barcoding In Vitro and In Vivo. *Small* **2017**, *13* (38), 1701582. <https://doi.org/10.1002/smll.201701582>.
- (164) Aparin, I. O.; Adarsh, N.; Reisch, A.; Klymchenko, A. S. Bulky Hydrophobic Counterions for Suppressing Aggregation-Caused Quenching of Ionic Dyes in Fluorescent Nanoparticles. In *Handbook of Aggregation-Induced Emission*; John Wiley & Sons, Ltd, 2022; pp 511–540. <https://doi.org/10.1002/9781119643098.ch59>.
- (165) Ishida, H.; Tobita, S.; Hasegawa, Y.; Katoh, R.; Nozaki, K. Recent Advances in Instrumentation for Absolute Emission Quantum Yield Measurements. *Coord. Chem. Rev.* **2010**, *254* (21–22), 2449–2458. <https://doi.org/10.1016/j.ccr.2010.04.006>.
- (166) Onoe, S.; Temma, T.; Shimizu, Y.; Ono, M.; Saji, H. Investigation of Cyanine Dyes for in Vivo Optical Imaging of Altered Mitochondrial Membrane Potential in Tumors. *Cancer Med.* **2014**, *3* (4), 775–786. <https://doi.org/10.1002/cam4.252>.
- (167) Liu, J.-X.; Mei, S.-L.; Chen, X.-H.; Yao, C.-J. Recent Advances of Near-Infrared (NIR) Emissive Metal Complexes Bridged by Ligands with N- and/or O-Donor Sites. *Crystals* **2021**, *11* (2), 155. <https://doi.org/10.3390/cryst11020155>.
- (168) Artem'ev, A. V.; Petyuk, M. Yu.; Berezin, A. S.; Gushchin, A. L.; Sokolov, M. N.; Bagryanskaya, I. Yu. Synthesis and Study of Re(I) Tricarbonyl Complexes Based on Octachloro-1,10-Phenanthroline: Towards Deep Red-to-NIR Emitters. *Polyhedron* **2021**, *209*, 115484. <https://doi.org/10.1016/j.poly.2021.115484>.
- (169) Knighton, R. C.; Dapin, S.; Beer, P. D. Luminescent Anion Sensing by Transition-Metal Dipyriddybenzene Complexes Incorporated into Acyclic, Macrocyclic and Interlocked Hosts. *Chem. – Eur. J.* **2020**, *26* (23), 5288–5296. <https://doi.org/10.1002/chem.202000661>.
- (170) Shakirova, J. R.; Nayeri, S.; Jamali, S.; Porsev, V. V.; Gurzhiy, V. V.; Levin, O. V.; Koshevoy, I. O.; Tunik, S. P. Targeted Synthesis of NIR Luminescent Rhenium Diimine Cis,Trans-[Re(CO)2(L)2]N+ Complexes Containing N-Donor Axial Ligands: Photophysical, Electrochemical, and Theoretical Studies. *ChemPlusChem* **2020**, *85* (11), 2518–2527. <https://doi.org/10.1002/cplu.202000597>.
- (171) Zhang, W.; Liu, Y.; Gao, Q.; Liu, C.; Song, B.; Zhang, R.; Yuan, J. A Ruthenium(II) Complex–Cyanine Energy Transfer Scaffold Based Luminescence Probe for Ratiometric Detection

-
- and Imaging of Mitochondrial Peroxynitrite. *Chem. Commun.* **2018**, *54* (97), 13698–13701. <https://doi.org/10.1039/C8CC08061E>.
- (172) Andreiuk, B.; Reisch, A.; Lindecker, M.; Follain, G.; Peyri ras, N.; Goetz, J. G.; Klymchenko, A. S. Fluorescent Polymer Nanoparticles for Cell Barcoding In Vitro and In Vivo. *Small* **2017**, *13* (38), 1701582. <https://doi.org/10.1002/sml.201701582>.
- (173) Chen, C.; Corry, B.; Huang, L.; Hildebrandt, N. FRET-Modulated Multihybrid Nanoparticles for Brightness-Equalized Single-Wavelength Barcoding. *J. Am. Chem. Soc.* **2019**, *141* (28), 11123–11141. <https://doi.org/10.1021/jacs.9b03383>.
- (174) Hildebrandt, N. How to Apply FRET: From Experimental Design to Data Analysis. In *FRET – F rster Resonance Energy Transfer*; John Wiley & Sons, Ltd, 2013; pp 105–163. <https://doi.org/10.1002/9783527656028.ch05>.
- (175) Wegner, K. D.; Lanh, P. T.; Jennings, T.; Oh, E.; Jain, V.; Fairclough, S. M.; Smith, J. M.; Giovanelli, E.; Lequeux, N.; Pons, T.; Hildebrandt, N. Influence of Luminescence Quantum Yield, Surface Coating, and Functionalization of Quantum Dots on the Sensitivity of Time-Resolved FRET Bioassays. *ACS Appl. Mater. Interfaces* **2013**, *5* (8), 2881–2892. <https://doi.org/10.1021/am3030728>.
- (176) Haase, M.; Sch fer, H. Upconverting Nanoparticles. *Angew. Chem. Int. Ed.* **2011**, *50* (26), 5808–5829. <https://doi.org/10.1002/anie.201005159>.
- (177) Resch-Genger, U.; Gorris, H. H. Perspectives and Challenges of Photon-Upconversion Nanoparticles - Part I: Routes to Brighter Particles and Quantitative Spectroscopic Studies. *Anal. Bioanal. Chem.* **2017**, *409* (25), 5855–5874. <https://doi.org/10.1007/s00216-017-0499-z>.
- (178) Aboshyan-Sorgho, L.; Besnard, C.; Pattison, P.; Kittilstved, K. R.; Aebischer, A.; B nzli, J.-C. G.; Hauser, A.; Piguet, C. Near-Infrared→Visible Light Upconversion in a Molecular Trinuclear d–f–d Complex. *Angew. Chem. Int. Ed.* **2011**, *50* (18), 4108–4112. <https://doi.org/10.1002/anie.201100095>.
- (179) Bolvin, H.; F rstenberg, A.; Golesorkhi, B.; Nozary, H.; Taarit, I.; Piguet, C. Metal-Based Linear Light Upconversion Implemented in Molecular Complexes: Challenges and Perspectives. *Acc. Chem. Res.* **2022**, *55* (3), 442–456. <https://doi.org/10.1021/acs.accounts.1c00685>.
- (180) Nonat, A. M.; Charbonni re, L. J. Upconversion of Light with Molecular and Supramolecular Lanthanide Complexes. *Coord. Chem. Rev.* **2020**, *409*, 213192. <https://doi.org/10.1016/j.ccr.2020.213192>.
- (181) Nonat, A.; Bahamyirou, S.; Lecointre, A.; Przybilla, F.; M ly, Y.; Platas-Iglesias, C.; Camerel, F.; Jeannin, O.; Charbonni re, L. J. Molecular Upconversion in Water in Heteropolynuclear Supramolecular Tb/Yb Assemblies. *J. Am. Chem. Soc.* **2019**, *141* (4), 1568–1576. <https://doi.org/10.1021/jacs.8b10932>.
- (182) Knighton, R. C.; Soro, L. K.; Thor, W.; Strub, J.-M.; Cianf rani, S.; M ly, Y.; Lenertz, M.; Wong, K.-L.; Platas-Iglesias, C.; Przybilla, F.; Charbonni re, L. J. Upconversion in a d–f [RuYb₃] Supramolecular Assembly. *J. Am. Chem. Soc.* **2022**, *144* (29), 13356–13365. <https://doi.org/10.1021/jacs.2c05037>.
- (183) G lico, D. A.; Ovens, J. S.; Sigoli, F. A.; Murugesu, M. Room-Temperature Upconversion in a Nanosized {Ln₁₅} Molecular Cluster-Aggregate. *ACS Nano* **2021**, *15* (3), 5580–5585. <https://doi.org/10.1021/acsnano.1c00580>.

-
- (184) Golesorkhi, B.; Taarit, I.; Bolvin, H.; Nozary, H.; Jiménez, J.-R.; Besnard, C.; Guénée, L.; Fürstenberg, A.; Piguet, C. Molecular Light-Upconversion: We Have Had a Problem! When Excited State Absorption (ESA) Overcomes Energy Transfer Upconversion (ETU) in Cr(III)/Er(III) Complexes. *Dalton Trans.* **2021**, 50 (23), 7955–7968. <https://doi.org/10.1039/D1DT01079D>.
- (185) Golesorkhi, B.; Fürstenberg, A.; Nozary, H.; Piguet, C. Deciphering and Quantifying Linear Light Upconversion in Molecular Erbium Complexes. *Chem. Sci.* **2019**, 10 (28), 6876–6885. <https://doi.org/10.1039/C9SC02068C>.
- (186) Soro, L. K.; Knighton, R. C.; Avecilla, F.; Thor, W.; Przybilla, F.; Jeannin, O.; Esteban-Gomez, D.; Platas-Iglesias, C.; Charbonnière, L. J. Solution-State Cooperative Luminescence Upconversion in Molecular Ytterbium Dimers. *Adv. Opt. Mater.* *n/a* (n/a), 2202307. <https://doi.org/10.1002/adom.202202307>.
- (187) Gálico, D. A.; Calado, C. M. S.; Murugesu, M. Lanthanide Molecular Cluster-Aggregates as the next Generation of Optical Materials. *Chem. Sci.* **2023**, 14 (22), 5827–5841. <https://doi.org/10.1039/D3SC01088K>.
- (188) Knighton, R. C.; Soro, L. K.; Lecointre, A.; Pilet, G.; Fateeva, A.; Pontille, L.; Francés-Soriano, L.; Hildebrandt, N.; Charbonnière, L. J. Upconversion in Molecular Hetero-Nonanuclear Lanthanide Complexes in Solution. *Chem. Commun.* **2021**, 57 (1), 53–56. <https://doi.org/10.1039/D0CC07337G>.
- (189) Knighton, R. C.; Soro, L. K.; Francés-Soriano, L.; Rodríguez-Rodríguez, A.; Pilet, G.; Lenertz, M.; Platas-Iglesias, C.; Hildebrandt, N.; Charbonnière, L. J. Cooperative Luminescence and Cooperative Sensitisation Upconversion of Lanthanide Complexes in Solution. *Angew. Chem. Int. Ed.* **2022**, 61 (4), e202113114. <https://doi.org/10.1002/anie.202113114>.
- (190) Trofymchuk, K.; Valanciunaite, J.; Andreiuk, B.; Reisch, A.; Collot, M.; Klymchenko, A. S. BODIPY-Loaded Polymer Nanoparticles: Chemical Structure of Cargo Defines Leakage from Nanocarrier in Living Cells. *J. Mater. Chem. B* **2019**, 7 (34), 5199–5210. <https://doi.org/10.1039/C8TB02781A>.
- (191) Andreiuk, B.; Reisch, A.; Bernhardt, E.; Klymchenko, A. S. Fighting Aggregation-Caused Quenching and Leakage of Dyes in Fluorescent Polymer Nanoparticles: Universal Role of Counterion. *Chem. – Asian J.* **2019**, 14 (6), 836–846. <https://doi.org/10.1002/asia.201801592>.
- (192) Wilson, B. K.; Prud'homme, R. K. Nanoparticle Size Distribution Quantification from Transmission Electron Microscopy (TEM) of Ruthenium Tetroxide Stained Polymeric Nanoparticles. *J. Colloid Interface Sci.* **2021**, 604, 208–220. <https://doi.org/10.1016/j.jcis.2021.04.081>.
- (193) Bernasconi, C. F.; Kanavarioti, Anastassia. Nucleophilic Additions to Olefins. 19. Abnormally High Intrinsic Barrier in the Reaction of Piperidine and Morpholine with Benzylideneacetylacetone. *J. Am. Chem. Soc.* **1986**, 108 (24), 7744–7751. <https://doi.org/10.1021/ja00284a043>.
- (194) Feng, Y.; Li, Z.; Li, Q.; Yuan, J.; Tu, L.; Ning, L.; Zhang, H. Internal OH – Induced Cascade Quenching of Upconversion Luminescence in NaYF₄:Yb/Er Nanocrystals. *Light Sci. Appl.* **2021**, 10 (1), 105. <https://doi.org/10.1038/s41377-021-00550-5>.

-
- (195) Pini, F.; Francés-Soriano, L.; Andrigo, V.; Natile, M. M.; Hildebrandt, N. Optimizing Upconversion Nanoparticles for FRET Biosensing. *ACS Nano* **2023**. <https://doi.org/10.1021/acsnano.2c12523>.
- (196) Dexter, D. L.; Schulman, J. H. Theory of Concentration Quenching in Inorganic Phosphors. *J. Chem. Phys.* **2004**, *22* (6), 1063–1070. <https://doi.org/10.1063/1.1740265>.
- (197) Baride, A.; May, P. S.; Berry, M. T. Cross-Relaxation from Er³⁺(²H_{11/2},⁴S_{3/2}) and Er³⁺(²H_{9/2}) in β-NaYF₄:Yb,Er and Implications for Modeling Upconversion Dynamics. *J. Phys. Chem. C* **2020**, *124* (3), 2193–2201. <https://doi.org/10.1021/acs.jpcc.9b10163>.
- (198) Schroter, A.; Märkl, S.; Weitzel, N.; Hirsch, T. Upconversion Nanocrystals with High Lanthanide Content: Luminescence Loss by Energy Migration versus Luminescence Enhancement by Increased NIR Absorption. *Adv. Funct. Mater.* *n/a* (n/a), 2113065. <https://doi.org/10.1002/adfm.202113065>.
- (199) Liu, J.; Fu, T.; Shi, C. Spatial Energy Transfer and Migration Model for Upconversion Dynamics in Core–Shell Nanostructures. *J. Phys. Chem. C* **2019**, *123* (14), 9506–9515. <https://doi.org/10.1021/acs.jpcc.8b12300>.
- (200) N’Diaye, M.; Pascaretti-Grizon, F.; Massin, P.; Baslé, M. F.; Chappard, D. Water Absorption of Poly(Methyl Methacrylate) Measured by Vertical Interference Microscopy. *Langmuir* **2012**, *28* (31), 11609–11614. <https://doi.org/10.1021/la302260a>.
- (201) Tian, Y.; Du, E.; Abdelmola, F.; Qiang, Y.; Carlsson, L. A. Rapid Characterization of Water Diffusion in Polymer Specimens Using a Droplet-Based Method. *Langmuir* **2020**, *36* (26), 7309–7314. <https://doi.org/10.1021/acs.langmuir.0c00727>.
- (202) Qiu, X.; Xu, J.; Cardoso Dos Santos, M.; Hildebrandt, N. Multiplexed Biosensing and Bioimaging Using Lanthanide-Based Time-Gated Förster Resonance Energy Transfer. *Acc. Chem. Res.* **2022**, *55* (4), 551–564. <https://doi.org/10.1021/acs.accounts.1c00691>.
- (203) Francés-Soriano, L.; Hildebrandt, N.; Charbonnière, L. J. 8.12 - Lanthanides as Luminescence Imaging Reagents. In *Comprehensive Inorganic Chemistry III (Third Edition)*; Reedijk, J., Poepelmeier, K. R., Eds.; Elsevier: Oxford, 2023; pp 486–510. <https://doi.org/10.1016/B978-0-12-823144-9.00095-9>.
- (204) Xu, R.; Cao, H.; Lin, D.; Yu, B.; Qu, J. Lanthanide-Doped Upconversion Nanoparticles for Biological Super-Resolution Fluorescence Imaging. *Cell Rep. Phys. Sci.* **2022**, *3* (6), 100922. <https://doi.org/10.1016/j.xcrp.2022.100922>.
- (205) Pini, F.; Francés-Soriano, L.; Peruffo, N.; Barbon, A.; Hildebrandt, N.; Natile, M. M. Spatial and Temporal Resolution of Luminescence Quenching in Small Upconversion Nanocrystals. *ACS Appl. Mater. Interfaces* **2022**, *14* (9), 11883–11894. <https://doi.org/10.1021/acsami.1c23498>.
- (206) Ximendes, E.; Benayas, A.; Jaque, D.; Marin, R. Quo Vadis, Nanoparticle-Enabled In Vivo Fluorescence Imaging? *ACS Nano* **2021**, *15* (2), 1917–1941. <https://doi.org/10.1021/acsnano.0c08349>.
- (207) Feng, Z.; Tang, T.; Wu, T.; Yu, X.; Zhang, Y.; Wang, M.; Zheng, J.; Ying, Y.; Chen, S.; Zhou, J.; Fan, X.; Zhang, D.; Li, S.; Zhang, M.; Qian, J. Perfecting and Extending the Near-Infrared Imaging Window. *Light Sci. Appl.* **2021**, *10* (1), 197. <https://doi.org/10.1038/s41377-021-00628-0>.
- (208) Paviolo, C.; Cognet, L. Near-Infrared Nanoscopy with Carbon-Based Nanoparticles for the Exploration of the Brain Extracellular Space. *Neurobiol. Dis.* **2021**, *153*, 105328. <https://doi.org/10.1016/j.nbd.2021.105328>.

-
- (209) Xiao, Y.; Wu, Z.; Yao, Q.; Xie, J. Luminescent Metal Nanoclusters: Biosensing Strategies and Bioimaging Applications. *Aggregate* **2021**, *2* (1), 114–132. <https://doi.org/10.1002/agt2.11>.
- (210) Zheng, J.; Zhou, C.; Yu, M.; Liu, J. Different Sized Luminescent Gold Nanoparticles. *Nanoscale* **2012**, *4* (14), 4073–4083. <https://doi.org/10.1039/C2NR31192E>.
- (211) Porret, E.; Guével, X. L.; Coll, J.-L. Gold Nanoclusters for Biomedical Applications: Toward in Vivo Studies. *J. Mater. Chem. B* **2020**, *8* (11), 2216–2232. <https://doi.org/10.1039/C9TB02767J>.
- (212) Yu, H.; Rao, B.; Jiang, W.; Yang, S.; Zhu, M. The Photoluminescent Metal Nanoclusters with Atomic Precision. *Coord. Chem. Rev.* **2019**, *378*, 595–617. <https://doi.org/10.1016/j.ccr.2017.12.005>.
- (213) Chen, Y.; Montana, D. M.; Wei, H.; Cordero, J. M.; Schneider, M.; Le Guével, X.; Chen, O.; Bruns, O. T.; Bawendi, M. G. Shortwave Infrared in Vivo Imaging with Gold Nanoclusters. *Nano Lett.* **2017**, *17* (10), 6330–6334. <https://doi.org/10.1021/acs.nanolett.7b03070>.
- (214) Guével, X. L.; Wegner, K. D.; Würth, C.; Baulin, V. A.; Musnier, B.; Josserand, V.; Resch-Genger, U.; Coll, J. Tailoring the SWIR Emission of Gold Nanoclusters by Surface Ligand Rigidification and Their Application in 3D Bioimaging. *Chem. Commun.* **2022**, *58* (18), 2967–2970. <https://doi.org/10.1039/D1CC07055J>.
- (215) Li, S.; Ma, Q.; Wang, C.; Yang, K.; Hong, Z.; Chen, Q.; Song, J.; Song, X.; Yang, H. Near-Infrared II Gold Nanocluster Assemblies with Improved Luminescence and Biocompatibility for In Vivo Ratiometric Imaging of H₂S. *Anal. Chem.* **2022**, *94* (5), 2641–2647. <https://doi.org/10.1021/acs.analchem.1c05154>.
- (216) Song, X.; Zhu, W.; Ge, X.; Li, R.; Li, S.; Chen, X.; Song, J.; Xie, J.; Chen, X.; Yang, H. A New Class of NIR-II Gold Nanocluster-Based Protein Biolabels for In Vivo Tumor-Targeted Imaging. *Angew. Chem. Int. Ed.* **2021**, *60* (3), 1306–1312. <https://doi.org/10.1002/anie.202010870>.
- (217) Liu, H.; Hong, G.; Luo, Z.; Chen, J.; Chang, J.; Gong, M.; He, H.; Yang, J.; Yuan, X.; Li, L.; Mu, X.; Wang, J.; Mi, W.; Luo, J.; Xie, J.; Zhang, X.-D. Atomic-Precision Gold Clusters for NIR-II Imaging. *Adv. Mater.* **2019**, *31* (46), 1901015. <https://doi.org/10.1002/adma.201901015>.
- (218) Musnier, B.; Wegner, K. D.; Comby-Zerbino, C.; Trouillet, V.; Jourdan, M.; Häusler, I.; Antoine, R.; Coll, J.-L.; Resch-Genger, U.; Le Guével, X. High Photoluminescence of Shortwave Infrared-Emitting Anisotropic Surface Charged Gold Nanoclusters. *Nanoscale* **2019**, *11* (25), 12092–12096. <https://doi.org/10.1039/c9nr04120f>.
- (219) Kang, X.; Zhu, M. Tailoring the Photoluminescence of Atomically Precise Nanoclusters. *Chem. Soc. Rev.* **2019**, *48* (8), 2422–2457. <https://doi.org/10.1039/C8CS00800K>.
- (220) Cognet, L.; Leduc, C.; Lounis, B. Advances in Live-Cell Single-Particle Tracking and Dynamic Super-Resolution Imaging. *Curr. Opin. Chem. Biol.* **2014**, *20*, 78–85. <https://doi.org/10.1016/j.cbpa.2014.04.015>.
- (221) Shen, H.; Tauzin, L. J.; Baiyasi, R.; Wang, W.; Moringo, N.; Shuang, B.; Landes, C. F. Single Particle Tracking: From Theory to Biophysical Applications. *Chem. Rev.* **2017**, *117* (11), 7331–7376. <https://doi.org/10.1021/acs.chemrev.6b00815>.

-
- (222) Li, Y.; Liu, S.; Yao, T.; Sun, Z.; Jiang, Z.; Huang, Y.; Cheng, H.; Huang, Y.; Jiang, Y.; Xie, Z.; Pan, G.; Yan, W.; Wei, S. Controllable Synthesis of Gold Nanoparticles with Ultrasmall Size and High Monodispersity via Continuous Supplement of Precursor. *Dalton Trans.* **2012**, 41 (38), 11725. <https://doi.org/10.1039/c2dt31270k>.
- (223) Goswami, N.; Yao, Q.; Luo, Z.; Li, J.; Chen, T.; Xie, J. Luminescent Metal Nanoclusters with Aggregation-Induced Emission. *J. Phys. Chem. Lett.* **2016**, 7 (6), 962–975. <https://doi.org/10.1021/acs.jpcclett.5b02765>.
- (224) Kang, X.; Chong, H.; Zhu, M. Au₂₅(SR)₁₈: The Captain of the Great Nanocluster Ship. *Nanoscale* **2018**, 10 (23), 10758–10834. <https://doi.org/10.1039/C8NR02973C>.
- (225) Melnychuk, N.; Egloff, S.; Runser, A.; Reisch, A.; Klymchenko, A. S. Light-Harvesting Nanoparticle Probes for FRET-Based Detection of Oligonucleotides with Single-Molecule Sensitivity. *Angew. Chem. Int. Ed.* **2020**, 59 (17), 6811–6818. <https://doi.org/10.1002/anie.201913804>.
- (226) Roger, K.; Eissa, M.; Elaissari, A.; Cabane, B. Surface Charge of Polymer Particles in Water: The Role of Ionic End-Groups. *Langmuir* **2013**, 29 (36), 11244–11250. <https://doi.org/10.1021/la4019053>.
- (227) Zhang, C.; Pansare, V. J.; Prud'homme, R. K.; Priestley, R. D. Flash Nanoprecipitation of Polystyrene Nanoparticles. *Soft Matter* **2011**, 8 (1), 86–93. <https://doi.org/10.1039/C1SM06182H>.
- (228) Egloff, S.; Runser, A.; Klymchenko, A.; Reisch, A. Size-Dependent Electroporation of Dye-Loaded Polymer Nanoparticles for Efficient and Safe Intracellular Delivery. *Small Methods* **2021**, 5 (2), 2000947. <https://doi.org/10.1002/smtd.202000947>.
- (229) Chandrasekhar, S. Stochastic Problems in Physics and Astronomy. *Rev. Mod. Phys.* **1943**, 15 (1), 1–89. <https://doi.org/10.1103/RevModPhys.15.1>.
- (230) Hoshi, R.; Suzuki, K.; Hasebe, N.; Yoshihara, T.; Tobita, S. Absolute Quantum Yield Measurements of Near-Infrared Emission with Correction for Solvent Absorption. *Anal. Chem.* **2020**, 92 (1), 607–611. <https://doi.org/10.1021/acs.analchem.9b03297>.
- (231) Carr, J. A.; Franke, D.; Caram, J. R.; Perkinson, C. F.; Saif, M.; Askoxylakis, V.; Datta, M.; Fukumura, D.; Jain, R. K.; Bawendi, M. G.; Bruns, O. T. Shortwave Infrared Fluorescence Imaging with the Clinically Approved Near-Infrared Dye Indocyanine Green. *Proc. Natl. Acad. Sci.* **2018**, 115 (17), 4465–4470. <https://doi.org/10.1073/pnas.1718917115>.
- (232) Li, B.; Zhao, M.; Feng, L.; Dou, C.; Ding, S.; Zhou, G.; Lu, L.; Zhang, H.; Chen, F.; Li, X.; Li, G.; Zhao, S.; Jiang, C.; Wang, Y.; Zhao, D.; Cheng, Y.; Zhang, F. Organic NIR-II Molecule with Long Blood Half-Life for in Vivo Dynamic Vascular Imaging. *Nat. Commun.* **2020**, 11 (1), 3102. <https://doi.org/10.1038/s41467-020-16924-z>.
- (233) Li, Q.; Zeman IV, C. J.; Ma, Z.; Schatz, G. C.; Gu, X. W. Bright NIR-II Photoluminescence in Rod-Shaped Icosahedral Gold Nanoclusters. *Small* **2021**, 17 (11), 2007992. <https://doi.org/10.1002/sml.202007992>.
- (234) Li, Y.; Zha, M.; Yang, G.; Wang, S.; Ni, J.-S.; Li, K. NIR-II Fluorescent Brightness Promoted by “Ring Fusion” for the Detection of Intestinal Inflammation. *Chem. – Eur. J.* **2021**, 27 (51), 13085–13091. <https://doi.org/10.1002/chem.202101767>.
- (235) Shi, L.-J.; Zhu, C.-N.; He, H.; Zhu, D.-L.; Zhang, Z.-L.; Pang, D.-W.; Tian, Z.-Q. Near-Infrared Ag₂Se Quantum Dots with Distinct Absorption Features and High Fluorescence Quantum Yields. *RSC Adv.* **2016**, 6 (44), 38183–38186. <https://doi.org/10.1039/C6RA04987G>.

-
- (236) Bruns, O. T.; Bischof, T. S.; Harris, D. K.; Franke, D.; Shi, Y.; Riedemann, L.; Bartelt, A.; Jaworski, F. B.; Carr, J. A.; Rowlands, C. J.; Wilson, M. W. B.; Chen, O.; Wei, H.; Hwang, G. W.; Montana, D. M.; Coropceanu, I.; Achorn, O. B.; Kloepper, J.; Heeren, J.; So, P. T. C.; Fukumura, D.; Jensen, K. F.; Jain, R. K.; Bawendi, M. G. Next-Generation in Vivo Optical Imaging with Short-Wave Infrared Quantum Dots. *Nat. Biomed. Eng.* **2017**, *1* (4), 1–11. <https://doi.org/10.1038/s41551-017-0056>.
- (237) Huang, Y.; Fuksman, L.; Zheng, J. Luminescence Mechanisms of Ultrasmall Gold Nanoparticles. *Dalton Trans.* **2018**, *47* (18), 6267–6273. <https://doi.org/10.1039/C8DT00420J>.
- (238) Le Guével, X. Recent Advances on the Synthesis of Metal Quantum Nanoclusters and Their Application for Bioimaging. *IEEE J. Sel. Top. Quantum Electron.* **2014**, *20* (3), 45–56. <https://doi.org/10.1109/JSTQE.2013.2282275>.
- (239) Zhou, M.; Song, Y. Origins of Visible and Near-Infrared Emissions in [Au₂₅(SR)₁₈]-Nanoclusters. *J. Phys. Chem. Lett.* **2021**, *12* (5), 1514–1519. <https://doi.org/10.1021/acs.jpcclett.1c00120>.
- (240) Luo, Z.; Yuan, X.; Yu, Y.; Zhang, Q.; Leong, D. T.; Lee, J. Y.; Xie, J. From Aggregation-Induced Emission of Au(I)-Thiolate Complexes to Ultrabright Au(0)@Au(I)-Thiolate Core-Shell Nanoclusters. *J. Am. Chem. Soc.* **2012**, *134* (40), 16662–16670. <https://doi.org/10.1021/ja306199p>.
- (241) Wu, Z.; Yao, Q.; Chai, O. J. H.; Ding, N.; Xu, W.; Zang, S.; Xie, J. Unraveling the Impact of Gold(I)-Thiolate Motifs on the Aggregation-Induced Emission of Gold Nanoclusters. *Angew. Chem. Int. Ed.* **2020**, *59* (25), 9934–9939. <https://doi.org/10.1002/anie.201916675>.
- (242) Lu, L.; Li, B.; Ding, S.; Fan, Y.; Wang, S.; Sun, C.; Zhao, M.; Zhao, C.-X.; Zhang, F. NIR-II Bioluminescence for in Vivo High Contrast Imaging and in Situ ATP-Mediated Metastases Tracing. *Nat. Commun.* **2020**, *11* (1), 4192. <https://doi.org/10.1038/s41467-020-18051-1>.
- (243) Musnier, B.; Henry, M.; Vollaie, J.; Coll, J.-L.; Usson, Y.; Josserand, V.; Le Guével, X. Optimization of Spatial Resolution and Scattering Effects for Biomedical Fluorescence Imaging by Using Sub-Regions of the Shortwave Infrared Spectrum. *J. Biophotonics* **2021**, *14* (2), e202000345. <https://doi.org/10.1002/jbio.202000345>.
- (244) Welsher, K.; Liu, Z.; Sherlock, S. P.; Robinson, J. T.; Chen, Z.; Daranciang, D.; Dai, H. A Route to Brightly Fluorescent Carbon Nanotubes for Near-Infrared Imaging in Mice. *Nat. Nanotechnol.* **2009**, *4* (11), 773–780. <https://doi.org/10.1038/nnano.2009.294>.
- (245) Gao, Z.; Danné, N.; Godin, A.; Lounis, B.; Cognet, L. Evaluation of Different Single-Walled Carbon Nanotube Surface Coatings for Single-Particle Tracking Applications in Biological Environments. *Nanomaterials* **2017**, *7* (11), 393. <https://doi.org/10.1126/science.1197321>.
- (246) Godin, A. G.; Varela, J. A.; Gao, Z.; Danné, N.; Dupuis, J. P.; Lounis, B.; Groc, L.; Cognet, L. Single-Nanotube Tracking Reveals the Nanoscale Organization of the Extracellular Space in the Live Brain. *Nat. Nanotechnol.* **2017**, *12* (3), 238–243. <https://doi.org/10.1103/PhysRevE.80.011403>.
- (247) Nandi, S.; Caicedo, K.; Cognet, L. When Super-Resolution Localization Microscopy Meets Carbon Nanotubes. *Nanomaterials* **2022**, *12* (9).

-
- (248) Fakhri, N.; MacKintosh, F. C.; Lounis, B.; Cognet, L.; Pasquali, M. Brownian Motion of Stiff Filaments in a Crowded Environment. *Science* **2010**, *330* (6012), 1804–1807. <https://doi.org/10.1126/science.1197321>.
- (249) Duque, J. G.; Parra-Vasquez, A. N. G.; Behabtu, N.; Green, M. J.; Higginbotham, A. L.; Price, B. K.; Leonard, A. D.; Schmidt, H. K.; Lounis, B.; Tour, J. M.; Doorn, S. K.; Cognet, L.; Pasquali, M. Diameter-Dependent Solubility of Single-Walled Carbon Nanotubes. *ACS Nano* **2010**, *4* (6), 3063–3072. <https://doi.org/10.1021/nn100170f>.
- (250) Le Guével, X.; Wegner, K. D.; Würth, C.; Baulin, V. A.; Musnier, B.; Jossierand, V.; Resch-Genger, U.; Coll, J. Tailoring the SWIR Emission of Gold Nanoclusters by Surface Ligand Rigidification and Their Application in 3D Bioimaging. *Chem. Commun.* **2022**, *58* (18), 2967–2970. <https://doi.org/10.1039/D1CC07055J>.
- (251) Goswami, N.; Yao, Q.; Luo, Z.; Li, J.; Chen, T.; Xie, J. Luminescent Metal Nanoclusters with Aggregation-Induced Emission. *J. Phys. Chem. Lett.* **2016**, *7* (6), 962–975. <https://doi.org/10.1021/acs.jpcclett.5b02765>.
- (252) Soria, F. N.; Paviolo, C.; Doudnikoff, E.; Arotcarena, M.-L.; Lee, A.; Danné, N.; Mandal, A. K.; Gosset, P.; Dehay, B.; Groc, L.; Cognet, L.; Bezard, E. Synucleinopathy Alters Nanoscale Organization and Diffusion in the Brain Extracellular Space through Hyaluronan Remodeling. *Nat. Commun.* **2020**, 1–13. <https://doi.org/10.1038/s41467-020-17328-9>.
- (253) Paviolo, C.; Ferreira, J. S.; Lee, A.; Hunter, D.; Calaresu, I.; Nandi, S.; Groc, L.; Cognet, L. Near-Infrared Carbon Nanotube Tracking Reveals the Nanoscale Extracellular Space around Synapses. *Nano Lett.* **2022**, *22* (17), 6849–6856. <https://doi.org/10.1021/acs.nanolett.1c04259>.
- (254) Volk, A.; Kähler, C. J. Density Model for Aqueous Glycerol Solutions. *Exp. Fluids* **2018**, *59* (5), 75. <https://doi.org/10.1007/s00348-018-2527-y>.
- (255) Cheng, N.-S. Formula for the Viscosity of a Glycerol–Water Mixture. *Ind. Eng. Chem. Res.* **2008**, *47* (9), 3285–3288. <https://doi.org/10.1021/ie071349z>.
- (256) Dobrovolskaia, M. A.; Shurin, M.; Shvedova, A. A. Current Understanding of Interactions between Nanoparticles and the Immune System. *Toxicol. Appl. Pharmacol.* **2016**, *299*, 78–89. <https://doi.org/10.1016/j.taap.2015.12.022>.
- (257) Reisch, A.; Didier, P.; Richert, L.; Oncul, S.; Arntz, Y.; Mély, Y.; Klymchenko, A. S. Collective Fluorescence Switching of Counterion-Assembled Dyes in Polymer Nanoparticles. *Nat. Commun.* **2014**, *5* (1), 1–9. <https://doi.org/10.1038/ncomms5089>.
- (258) Kettler, K.; Veltman, K.; van de Meent, D.; van Wezel, A.; Hendriks, A. J. Cellular Uptake of Nanoparticles as Determined by Particle Properties, Experimental Conditions, and Cell Type. *Environ. Toxicol. Chem.* **2014**, *33* (3), 481–492. <https://doi.org/10.1002/etc.2470>.
- (259) Hao, J.; Chen, J.; Wang, M.; Zhao, J.; Wang, J.; Wang, X.; Li, Y.; Tang, H. Neutrophils, as “Trojan Horses”, Participate in the Delivery of Therapeutical PLGA Nanoparticles into a Tumor Based on the Chemotactic Effect. *Drug Deliv.* **2019**, *27* (1), 1–14. <https://doi.org/10.1080/10717544.2019.1701141>.
- (260) Saito, E.; Kuo, R.; Pearson, R. M.; Gohel, N.; Cheung, B.; King, N. J. C.; Miller, S. D.; Shea, L. D. Designing Drug-Free Biodegradable Nanoparticles to Modulate Inflammatory Monocytes and Neutrophils for Ameliorating Inflammation. *J. Controlled Release* **2019**, *300*, 185–196. <https://doi.org/10.1016/j.jconrel.2019.02.025>.
- (261) Zhao, J. Interplay Among Nitric Oxide and Reactive Oxygen Species. *Plant Signal. Behav.* **2007**, *2* (6), 544–547.

-
- (262) Sadhu, A.; Moriyasu, Y.; Acharya, K.; Bandyopadhyay, M. Nitric Oxide and ROS Mediate Autophagy and Regulate Alternaria Alternata Toxin-Induced Cell Death in Tobacco BY-2 Cells. *Sci. Rep.* **2019**, *9* (1), 8973. <https://doi.org/10.1038/s41598-019-45470-y>.
- (263) Chi, D. S.; Qui, M.; Krishnaswamy, G.; Li, C.; Stone, W. Regulation of Nitric Oxide Production from Macrophages by Lipopolysaccharide and Catecholamines. *Nitric Oxide* **2003**, *8* (2), 127–132. [https://doi.org/10.1016/S1089-8603\(02\)00148-9](https://doi.org/10.1016/S1089-8603(02)00148-9).
- (264) Dey, A. K.; Gonon, A.; Pécheur, E.-I.; Pezet, M.; Villiers, C.; Marche, P. N. Impact of Gold Nanoparticles on the Functions of Macrophages and Dendritic Cells. *Cells* **2021**, *10* (1), 96. <https://doi.org/10.3390/cells10010096>.
- (265) Mauricio, M. D.; Guerra-Ojeda, S.; Marchio, P.; Valles, S. L.; Aldasoro, M.; Escribano-Lopez, I.; Herance, J. R.; Rocha, M.; Vila, J. M.; Victor, V. M. Nanoparticles in Medicine: A Focus on Vascular Oxidative Stress. *Oxid. Med. Cell. Longev.* **2018**, *2018*, 6231482. <https://doi.org/10.1155/2018/6231482>.
- (266) Khalin, I.; Heimbürger, D.; Melnychuk, N.; Collot, M.; Groschup, B.; Hellal, F.; Reisch, A.; Plesnila, N.; Klymchenko, A. S. Ultrabright Fluorescent Polymeric Nanoparticles with a Stealth Pluronic Shell for Live Tracking in the Mouse Brain. *ACS Nano* **2020**, *16*.
- (267) Yue, Y.; Grusenmeyer, T.; Ma, Z.; Zhang, P.; Pham, T. T.; Mague, J. T.; Donahue, J. P.; Schmehl, R. H.; Beratan, D. N.; Rubtsov, I. V. Evaluating the Extent of Intramolecular Charge Transfer in the Excited States of Rhenium(I) Donor–Acceptor Complexes with Time-Resolved Vibrational Spectroscopy. *J. Phys. Chem. B* **2013**, *117* (49), 15903–15916. <https://doi.org/10.1021/jp409628e>.
- (268) Streit, J. K.; Bachilo, S. M.; Ghosh, S.; Lin, C.-W.; Weisman, R. B. Directly Measured Optical Absorption Cross Sections for Structure-Selected Single-Walled Carbon Nanotubes. *Nano Lett.* **2014**, *14* (3), 1530–1536. <https://doi.org/10.1021/nl404791y>.
- (269) Wei, X.; Tanaka, T.; Li, S.; Tsuzuki, M.; Wang, G.; Yao, Z.; Li, L.; Yomogida, Y.; Hirano, A.; Liu, H.; Kataura, H. Photoluminescence Quantum Yield of Single-Wall Carbon Nanotubes Corrected for the Photon Reabsorption Effect. *Nano Lett.* **2020**, *20* (1), 410–417. <https://doi.org/10.1021/acs.nanolett.9b04095>.

Annexes

1. Polymer Characterization

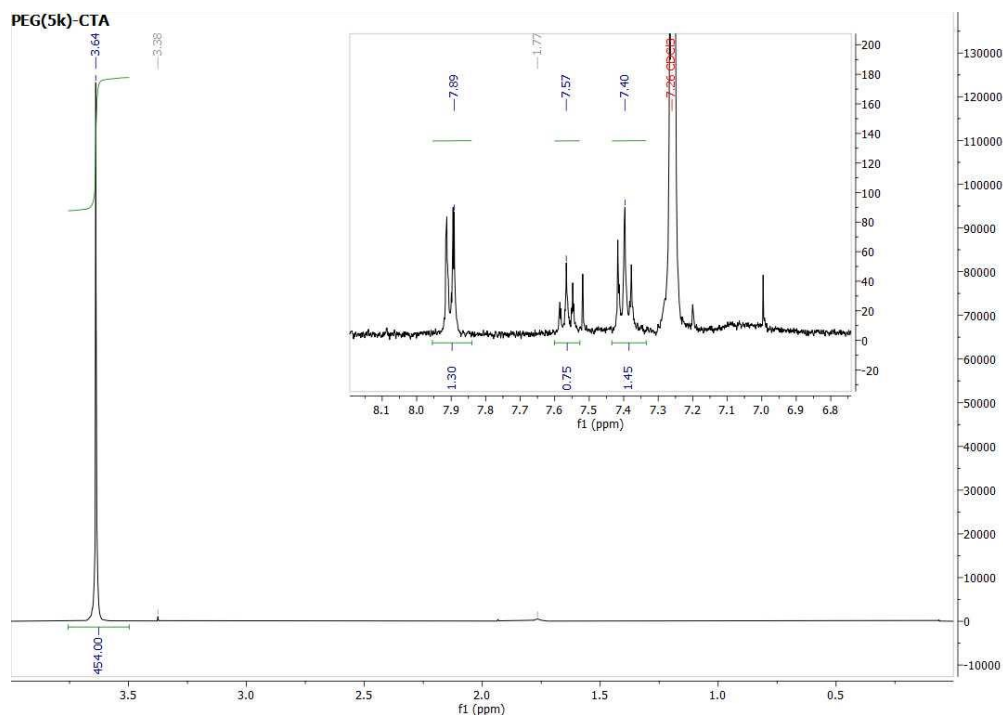


Figure 60: ^1H NMR of coupling reaction between PEG(5k) and CTA

^1H NMR (400 MHz, CDCl_3) δ (ppm): 7.89 (d, 2H), 7.57 (t, 1H), 7.40 (t, 2H), 3.64 (s, 454H).

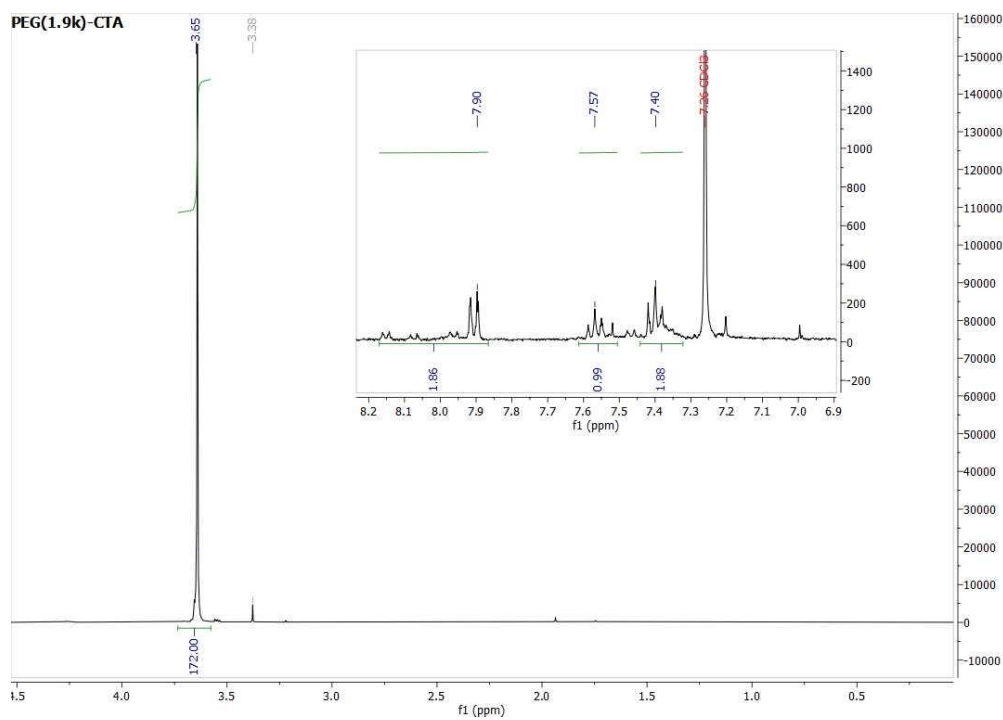


Figure 61 : ^1H NMR of coupling reaction between PEG(1.9k) and CTA

^1H NMR (400 MHz, CDCl_3) δ (ppm): 7.90 (d, 2H), 7.57 (t, 1H), 7.40 (t, 2H), 3.64 (s, 545H).

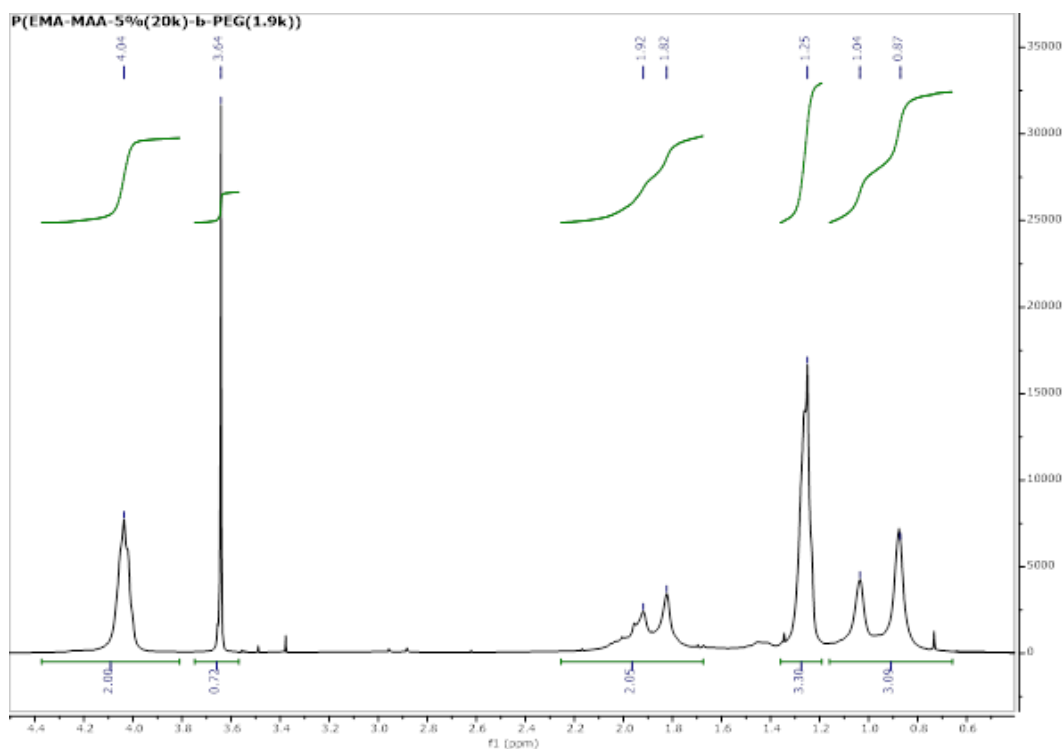


Figure 62: ^1H NMR of P(EMA-COOH-5%)(20k)-b-PEG(1.9k)

^1H NMR (400 MHz, CDCl_3) δ (ppm): 4.04 (m, 2H), 3.64 (s, 0.72H), 1.92 – 1.82 (m, 2H), 1.25 (m, 3H), 1.04 – 0.88 (m, 3H).

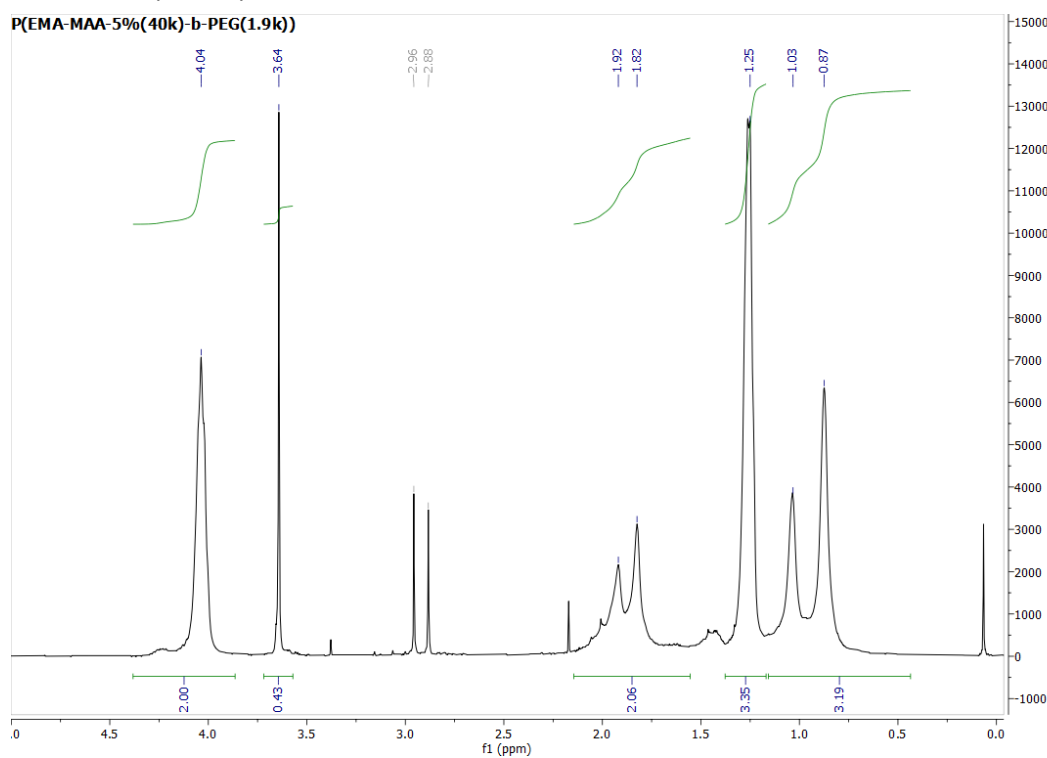


Figure 63: ^1H NMR of P(EMA-COOH-5%)(40k)-b-PEG(1.9k)

^1H NMR (400 MHz, CDCl_3) δ (ppm): 4.04 (m, 2H), 3.64 (s, 0.43H), 1.92 – 1.82 (m, 2H), 1.25 (m, 3H), 1.04 – 0.88 (m, 3H).

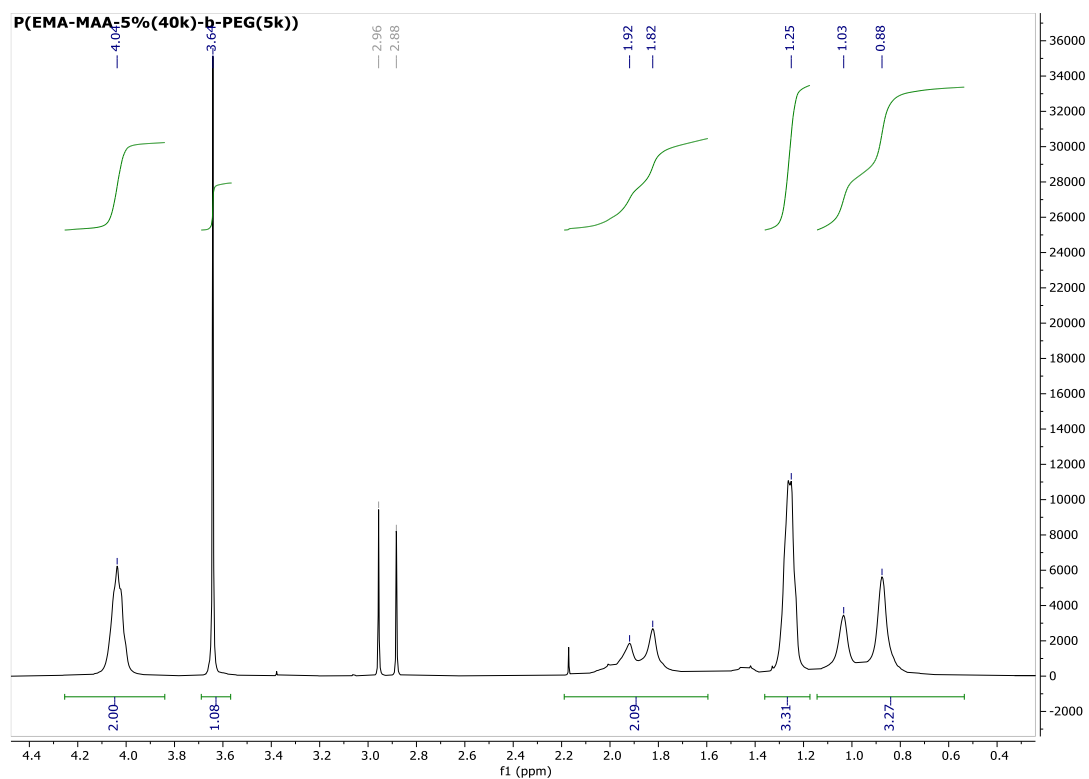


Figure 64: ^1H NMR of P(EMA-COOH-5%)(40k)-b-PEG(5k)

^1H NMR (400 MHz, CDCl_3) δ (ppm): 4.04 (m, 2H), 3.64 (s, 1.08H), 1.92 – 1.82 (m, 2H), 1.25 (m, 3H), 1.04 – 0.88 (m, 3H).

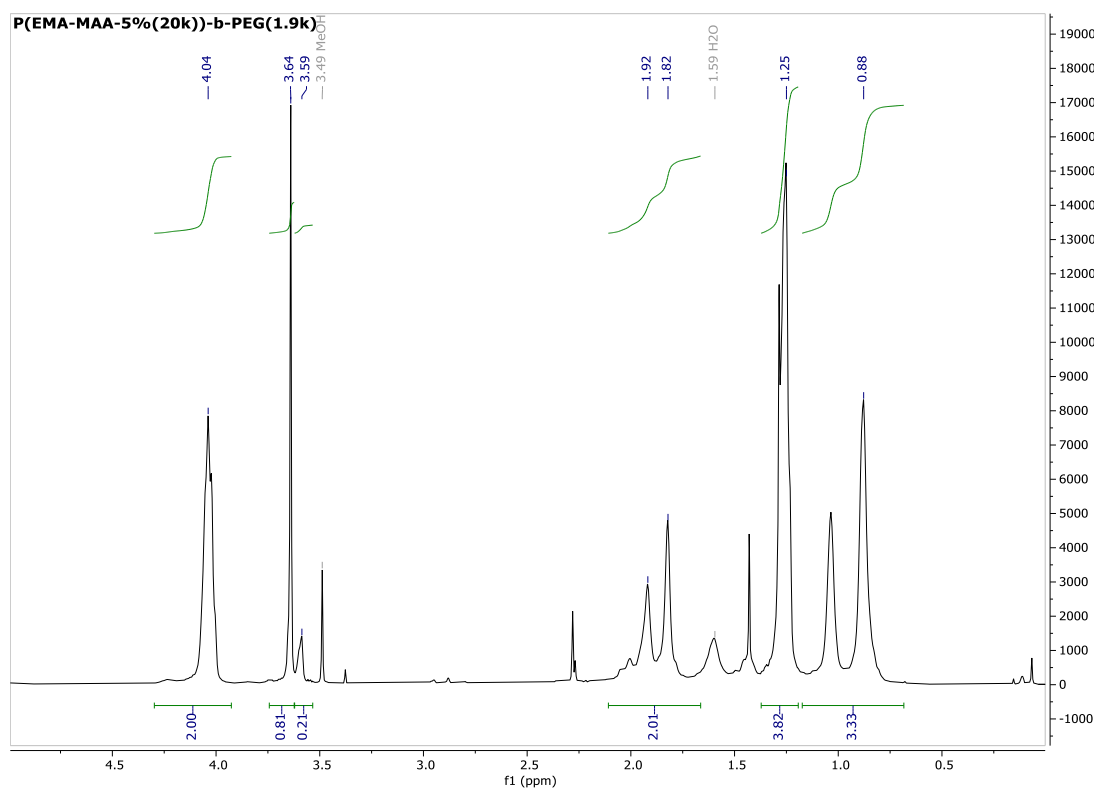


Figure 65: ^1H NMR of P(EMA-COOH-5%)(20k)-b-PEG(1.9k) after methylation

^1H NMR (400 MHz, CDCl_3) δ (ppm): 4.04 (m, 2H), 3.64 (s, 0.81H), 3.59 (s, 0.21H), 1.92 – 1.82 (m, 2H), 1.25 (m, 3H), 1.04 – 0.88 (m, 3H).

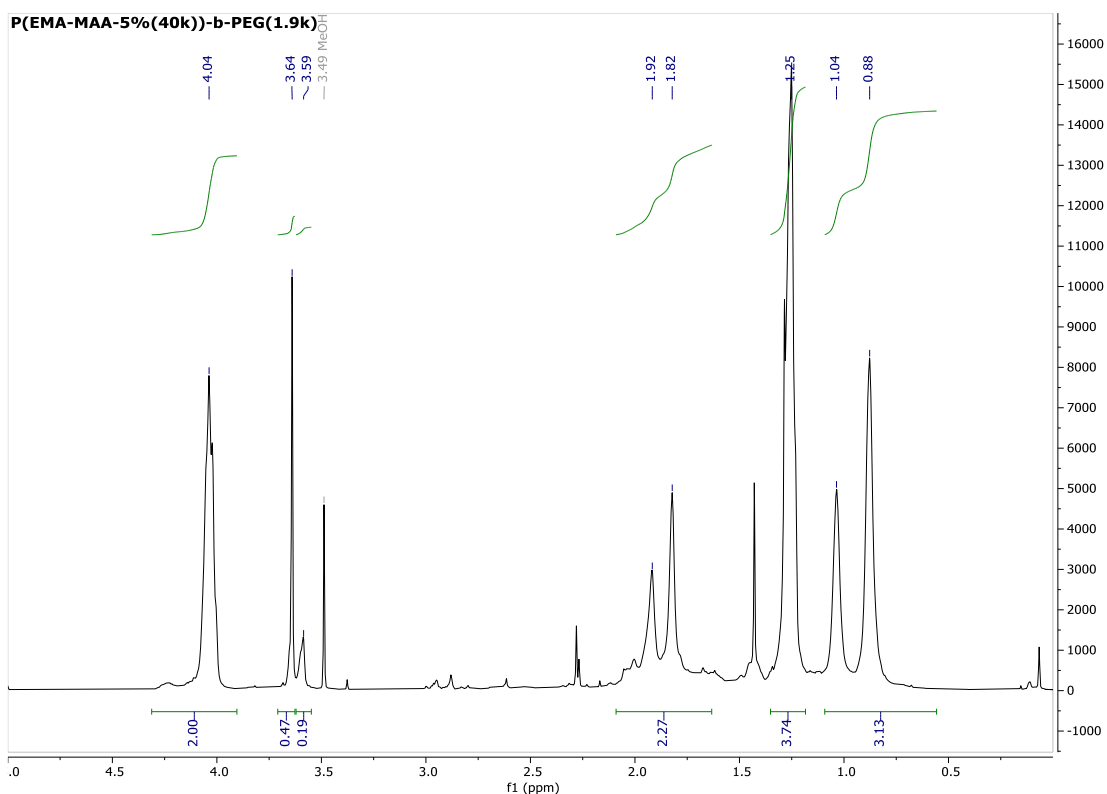


Figure 66: ^1H NMR of $\text{P}(\text{EMA-COOH-5\%})(40\text{k})\text{-b-PEG}(1.9\text{k})$ after methylation

^1H NMR (400 MHz, CDCl_3) δ (ppm): 4.04 (m, 2H), 3.64 (s, 0.47H), 3.59 (s, 0.19H), 1.92 – 1.82 (m, 2H), 1.25 (m, 3H), 1.04 – 0.88 (m, 3H).

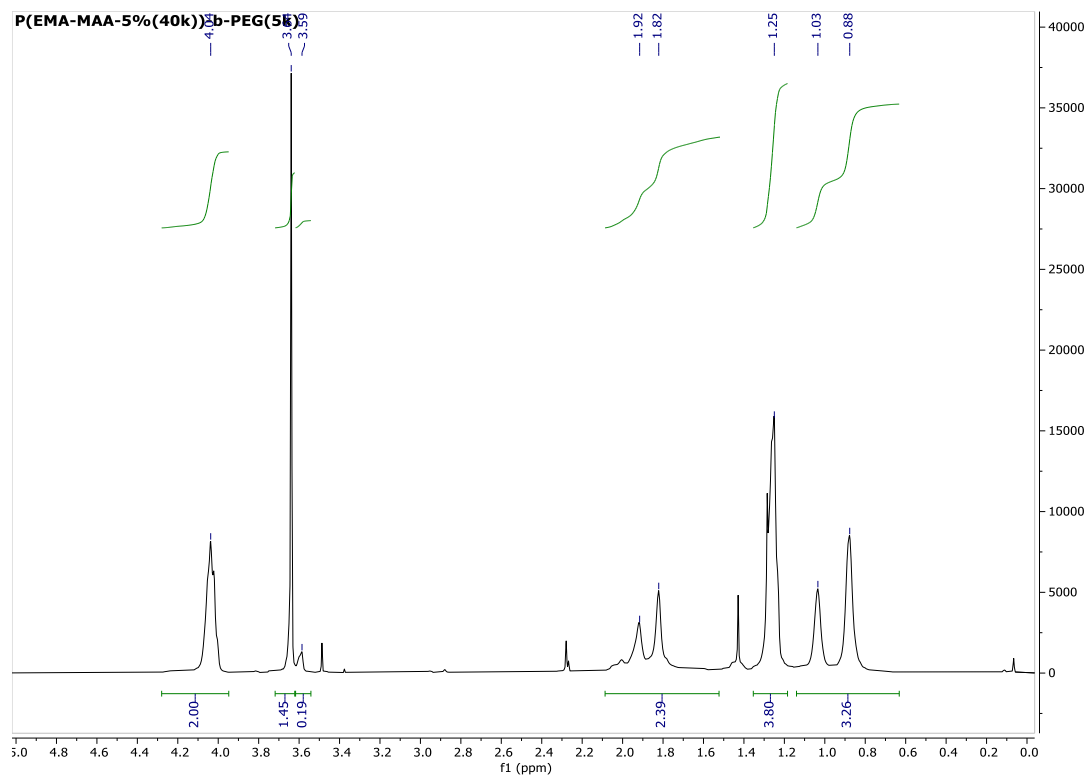


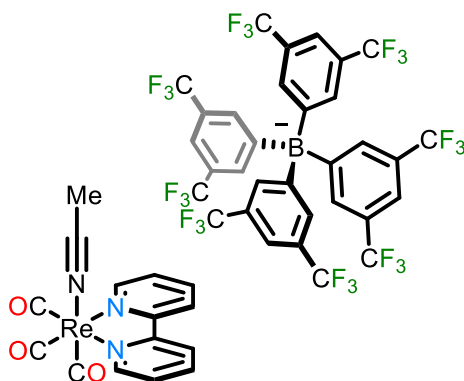
Figure 67: ^1H NMR of $\text{P}(\text{EMA-COOH-5\%})(40\text{k})\text{-b-PEG}(5\text{k})$ after methylation

^1H NMR (400 MHz, CDCl_3) δ (ppm): 4.04 (m, 2H), 3.64 (s, 0.81H), 3.59 (s, 0.19H), 1.92 – 1.82 (m, 2H), 1.25 (m, 3H), 1.04 – 0.88 (m, 3H).

2. Co-encapsulation of organic dyes and metallic complexes for TG Imaging

2.1 Rhenium Loaded PNPs

Synthesis of [Re(2,2'-bipyridine)(CO)₃MeCN] F6-TPB



The compound was synthesised according to an adapted literature procedure.²⁶⁷

[Re(2,2'-bipyridine)(CO)₃Cl] (200 mg, 0.433 mmol, 1.0 eq.) and AgOTf (111 mg, 0.433 mmol, 1.0 eq.) were dissolved in anhydrous CH₂Cl₂ (30 mL) and stirred at ambient temperature for two hours. MeCN (24.8 μL, 0.433 mmol, 1.0 eq.) and Na[BAr^F₄] (384 mg, 0.433 mmol, 1.0 eq.) were added and the reaction stirred at ambient temperature for four hours then cooled to -18 °C for 18 hours. The solution was filtered through a silica plug and layered with pentane (ca. 100 mL) Slow diffusion and filtration gave the title compound as a microcrystalline solid (365 mg, 0.27 mmol, 63%)

¹H NMR (500 MHz, 298 K, CD₃CN) 9.03 (ddd, ³J_{HH} = 5.5, ⁴J_{HH} = 1.6, 0.8, 2H, bipy_H), 8.47 (dt, ³J_{HH} = 8.3, ⁴J_{HH} = 1.1, 2H, bipy_H), 8.28 (td, ³J_{HH} = 7.9, ⁴J_{HH} = 1.5, 2H, bipy_H), 7.73 – 7.71 (m, 2H, bipy_H), 7.73 – 7.71 (m, 8H, Ar^F_H), 7.66 (s, 4H, Ar^F_H), 2.04 (s, 3H, NCC_H₃).

¹³C NMR (126 MHz, 298 K, CD₃CN) 194.4 (s, CO), 191.0 (s, CN), 162.2 (q, ¹J_{CB} = 50, Ar^F), 156.7 (s, Ar), 154.6 (s, Ar), 141.5 (s, Ar), 135.3 (s, Ar), 129.5 (qq, ²J_{FC} = 32, ⁴J_{FC} = 3, Ar^F), 128.7 (s, Ar), 125.0 (q, ¹J_{FC} = 272), 124.9 (s, Ar), 123.1 (s, Ar), 118.3 (sept., ³J_{FC} = 4, Ar^F), 3.5, s, NCC_H₃).

¹¹B NMR spectrum (160 MHz, 298 K, CD₃CN) -6.7 (s, BAr^F₂₄)

¹⁹F NMR spectrum (471 MHz, 298 K, CD₃CN) -63.2 (s, B-{3,5-(C₆H₃(CF₃)₂)₄})

ESI-MS m/z calcd. for [C₁₃H₈N₂O₃Re]⁺ 427.01 found 427.01, corresponding to {M-MeCN-[BAr^F₂₄]⁺}

Anal. Calcd for (C₄₇H₄₃BF₂₄N₃O₃Re) (1330.70 g mol⁻¹): C, 42.42; H, 1.74; N, 3.16. Found: C, 42.46; H, 1.77; N, 3.10.

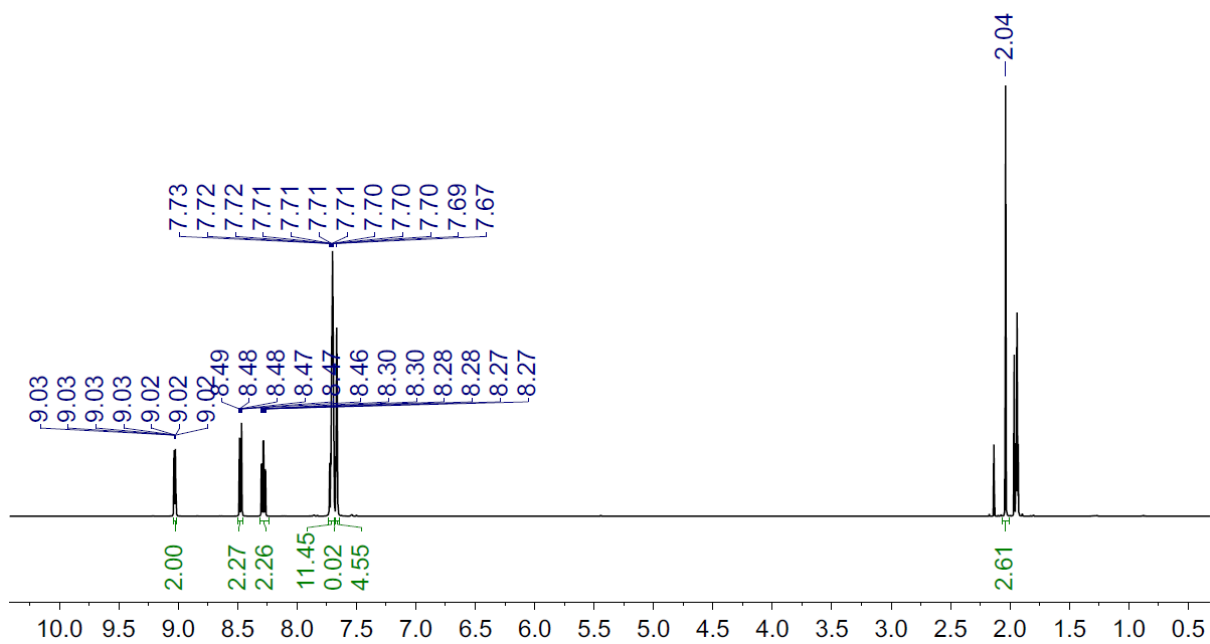


Figure 68. ^1H NMR spectrum (500 MHz, 298 K, CD_3CN)

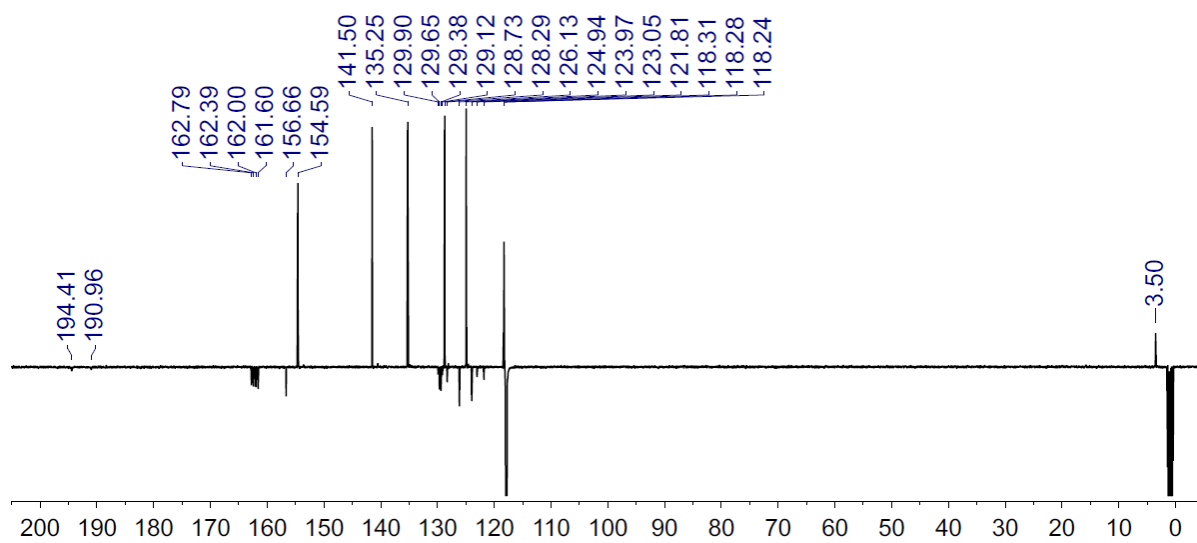


Figure 69. ^{13}C NMR spectrum (126 MHz, 298 K, CD_3CN)

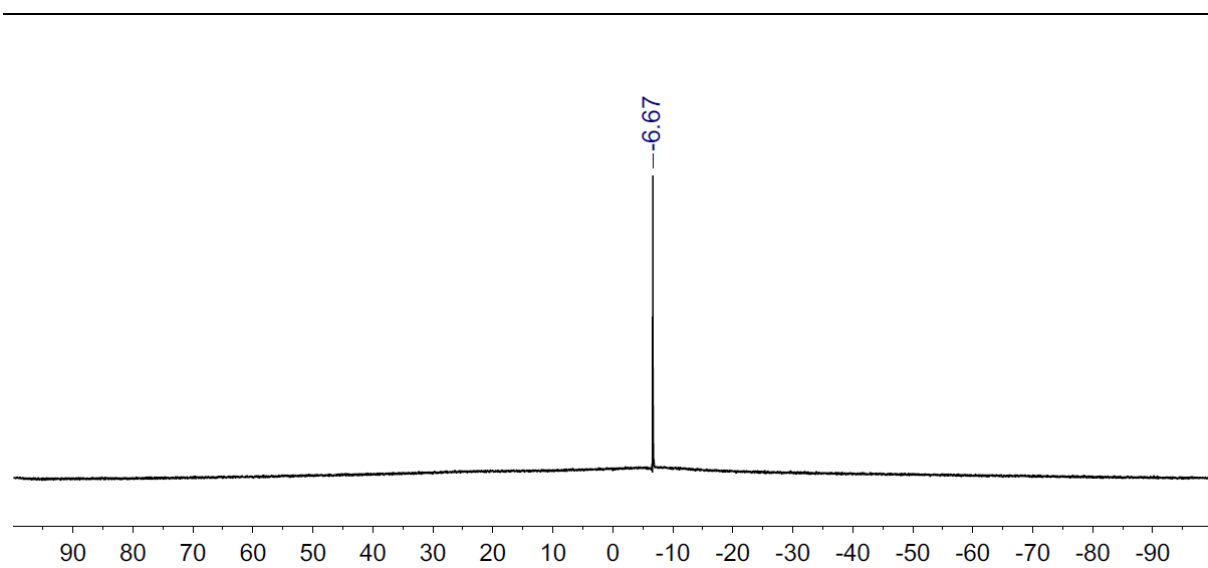


Figure 70. ^{11}B NMR spectrum (160 MHz, 298 K, CD_3CN)

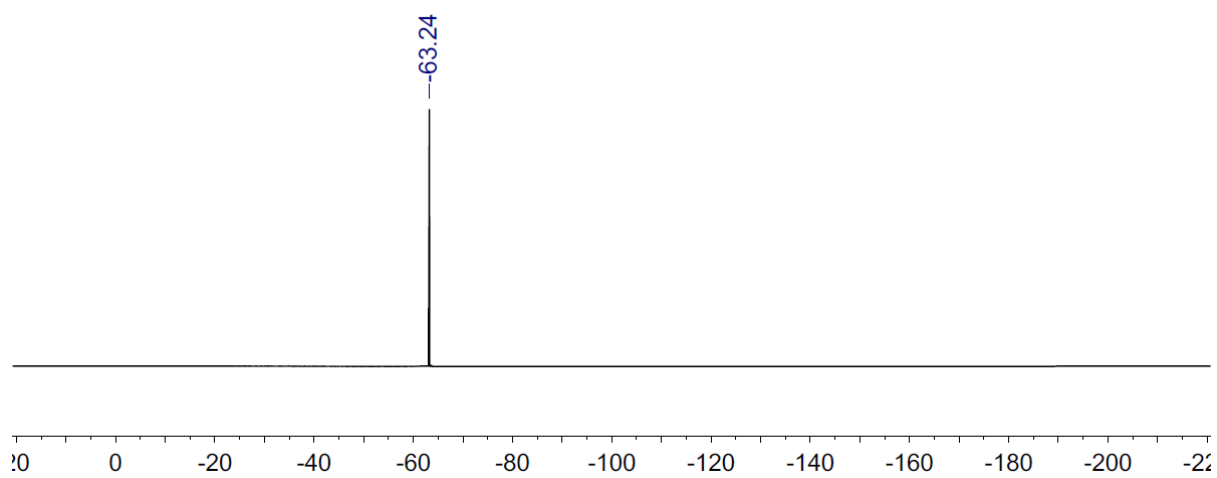


Figure 71. ^{19}F NMR spectrum (471 MHz, 298 K, CD_3CN)

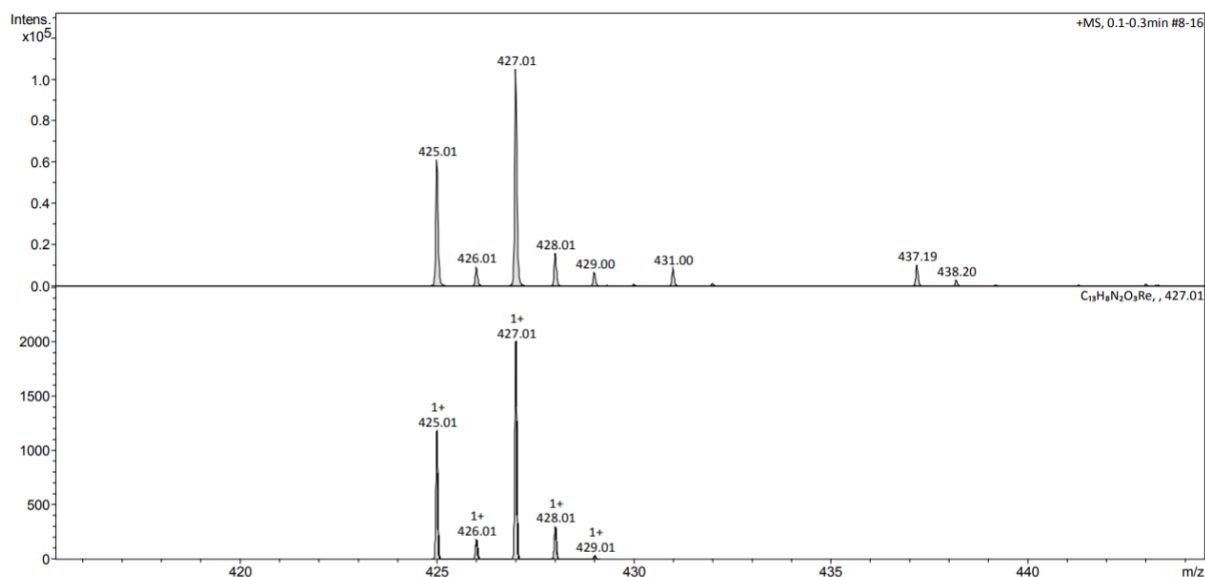
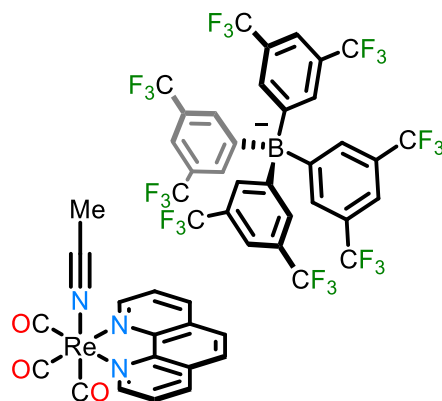


Figure 72: ESI-MS spectrum

Synthesis of [Re(1,10-phenanthroline)(CO)₃MeCN]F6-TPB



The compound was synthesised according to an adapted literature procedure.²⁶⁷

[Re(1,10-phenanthroline)(CO)₃Cl] (210 mg, 0.433 mmol, 1.0 eq.) and AgOTf (111 mg, 0.433 mmol, 1.0 eq.) were dissolved in anhydrous CH₂Cl₂ (30 mL) and stirred at ambient temperature for two hours. MeCN (24.8 μL, 0.433 mmol, 1.0 eq.) and Na[BAr^F₄] (384 mg, 0.433 mmol, 1.0 eq.) were added and the reaction stirred at ambient temperature for four hours then cooled to -18 °C for 18 hours. The solution was filtered through a silica plug and layered with pentane (*ca.* 100 mL) Slow diffusion and filtration gave the title compound as a microcrystalline solid (396 mg, 0.29 mmol, 68%).

¹H NMR (500 MHz, 298 K, CD₃CN) 9.41 (dd, ³J_{HH} = 5.1, ⁴J_{HH} = 1.4, 2H, ArH), 8.81 (dd, ³J_{HH} = 8.3, ⁴J_{HH} = 1.4, 2H, ArH), 8.20 (s, 2H, ArH), 8.00 (dd, ³J_{HH} = 8.3, ³J_{HH} = 5.1, 2H, ArH), 7.69 (s, 8H, Ar^FH), 7.66 (s, 4H, Ar^FH), 1.89 (br.s, 3H, NCCH₃).

¹³C NMR (126 MHz, 298 K, CD₃CN) 162.2 (q, ¹J_{CB} = 50, Ar^F), 155.1 (s, Ar), 140.1 (s, Ar), 135.2 (s, Ar), 131.7 (a, Ar), 129.5 (qq, ²J_{FC} = 32, ⁴J_{FC} = 3, Ar^F), 128.4 (s, Ar), 126.8 (s, Ar), 125.0 (q, ¹J_{FC} = 272), 118.3 (sept., ³J_{FC} = 4, Ar^F), remaining quaternary and exchanging resonances undetected.

¹¹B NMR spectrum (160 MHz, 298 K, CD₃CN) -6.7 (s, BAr^F₂₄)

^{19}F NMR spectrum (471 MHz, 298 K, CD_3CN) -63.2 (s, B-{3,5-($\text{C}_6\text{H}_3(\text{CF}_3)_2$) $_4$)

ESI-MS m/z calcd. for $[\text{C}_{15}\text{H}_8\text{N}_2\text{O}_3\text{Re}]^+$ 451.01 found 451.01, corresponding to {M-MeCN-[$\text{BAR}^{\text{F}}_{24}$] $^+$ }

Anal. Calcd for $(\text{C}_{49}\text{H}_{43}\text{BF}_{24}\text{N}_3\text{O}_3\text{Re})$ (1354.72 g mol^{-1}): C, 43.44; H, 1.71; N, 3.10. Found: C, 43.42; H, 1.73; N, 3.02.

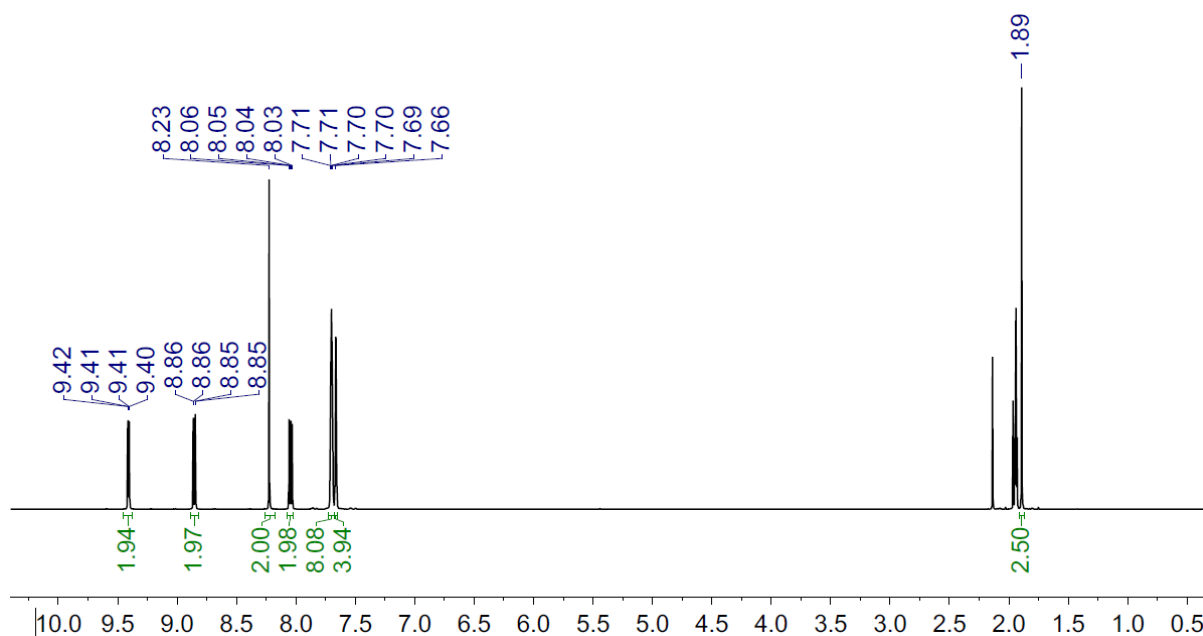


Figure 73: ^1H NMR spectrum (500 MHz, 298 K, CD_3CN)

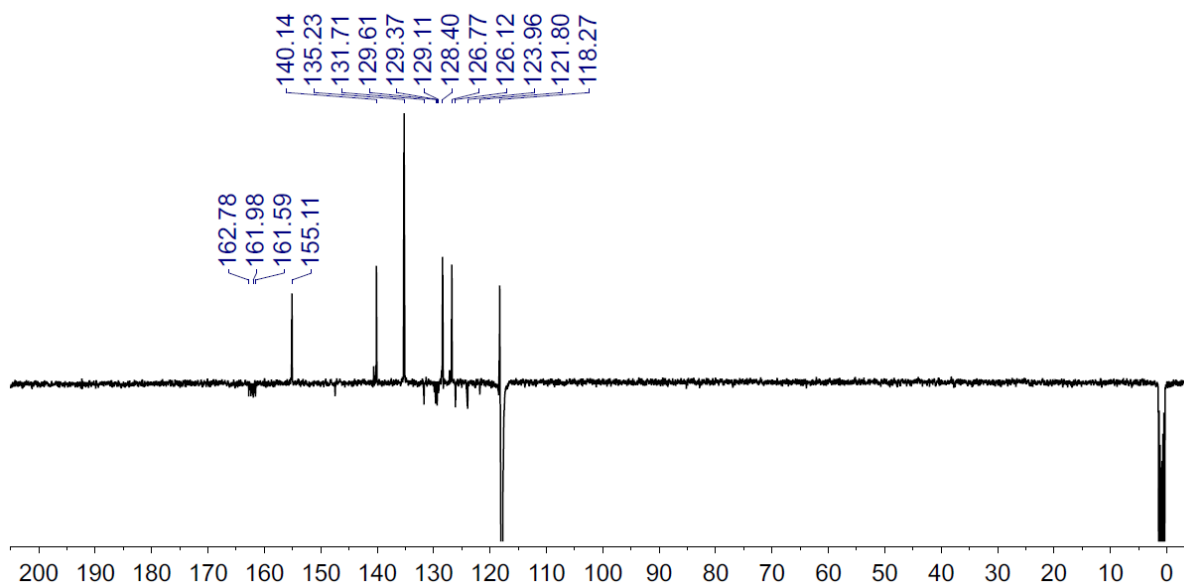


Figure 74: ^{13}C NMR spectrum (126 MHz, 298 K, CD_3CN)

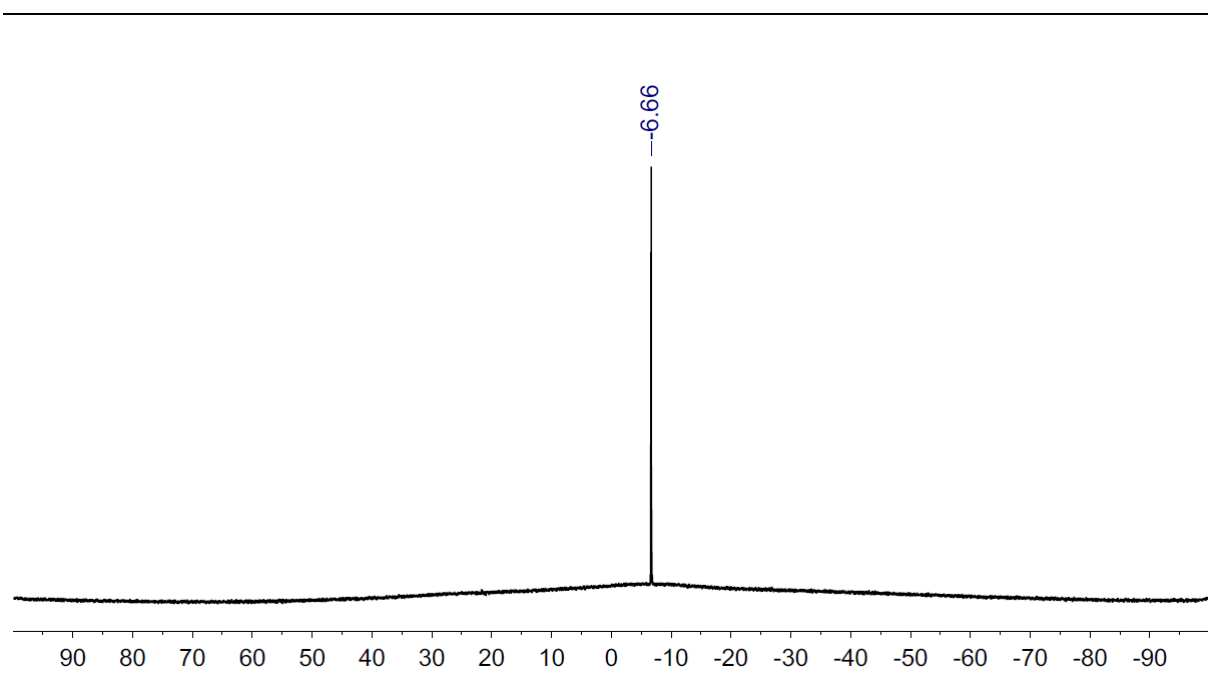


Figure 75: ^{11}B NMR spectrum (160 MHz, 298 K, CD_3CN)

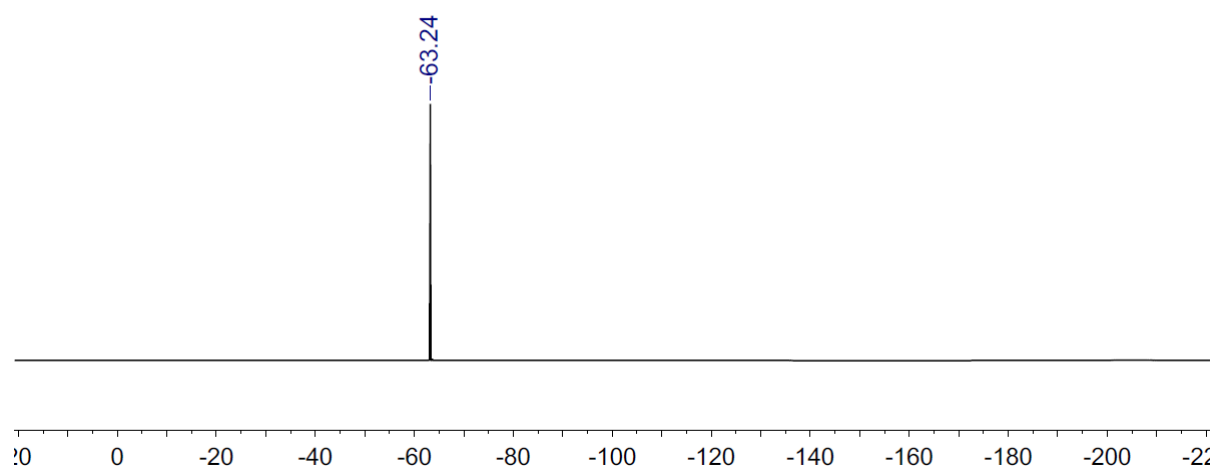


Figure S76: ^{19}F NMR spectrum (471 MHz, 298 K, CD_3CN)

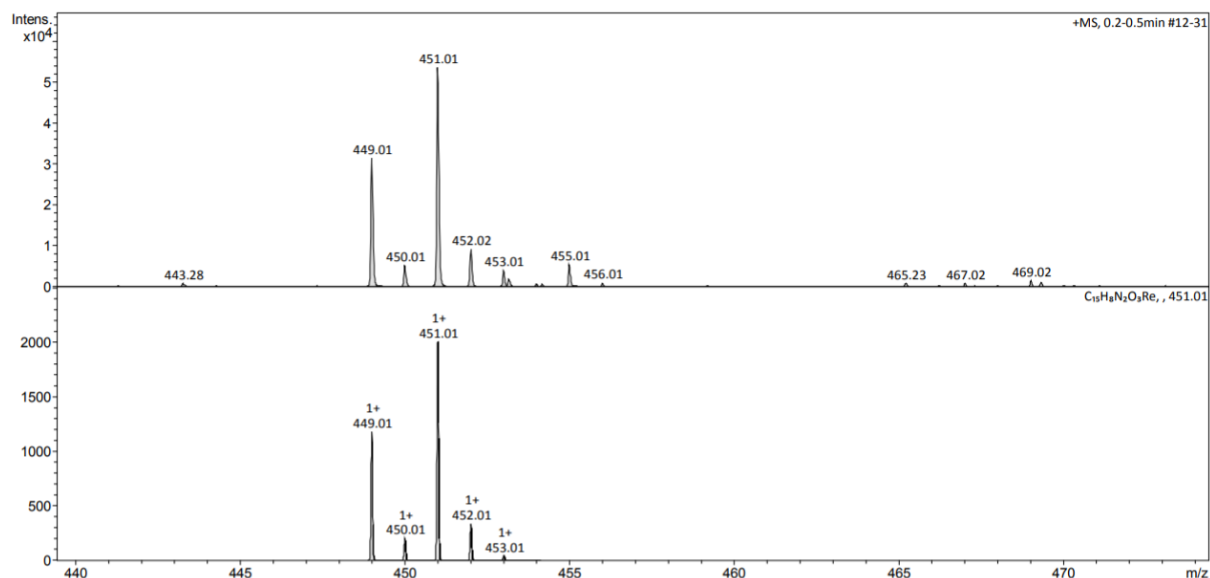


Figure 77: ESI-MS spectrum

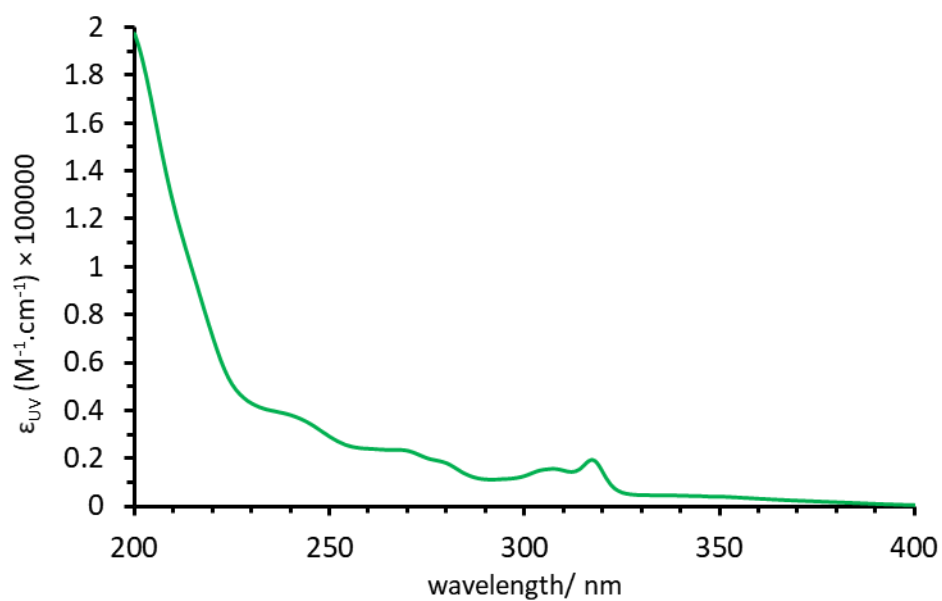


Figure 78: Absorption spectra of Re(bipy) ([Re(2,2'-bipyridine)(CO)₃](MeCN)]F6-TPB) in aerated MeCN

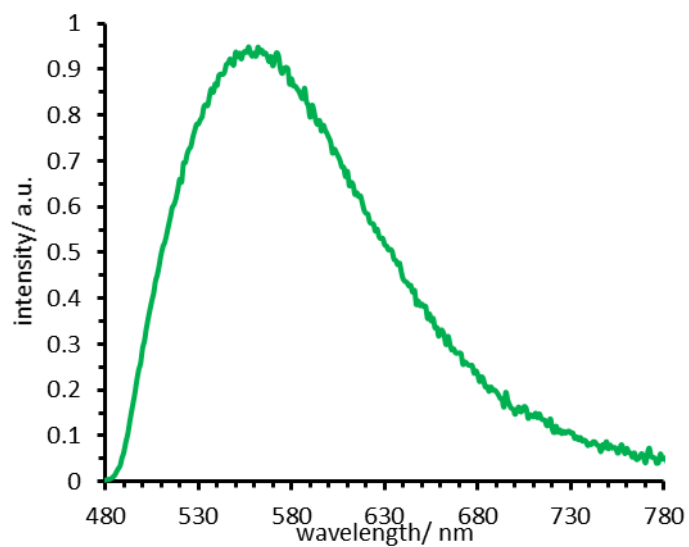


Figure 79: Emission spectra of $\text{Re}(\text{bipy})$ ($[\text{Re}(2,2'\text{-bipyridine})(\text{CO})_3](\text{MeCN})\text{F6-TPB}$) in aerated MeCN ($\lambda_{\text{exc}} = 320$ nm)

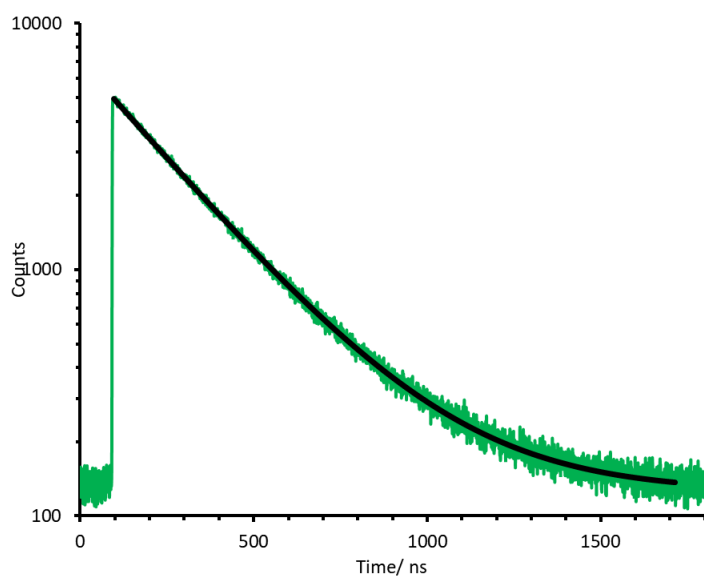


Figure 80: PL decays of $\text{Re}(\text{bipy})$ ($[\text{Re}(2,2'\text{-bipyridine})(\text{CO})_3](\text{MeCN})\text{F6-TPB}$) in aerated MeCN ($\lambda_{\text{em}} = 303$ nm; decay signal in green, monoexponential fit in black)

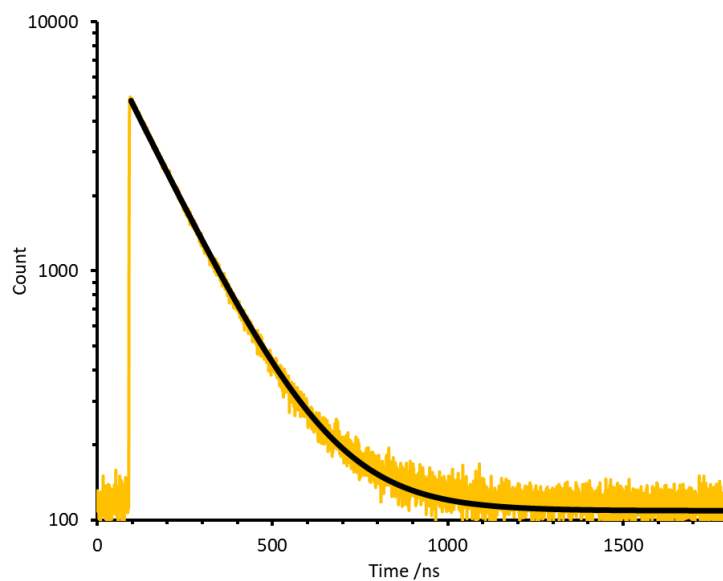


Figure 81: PL decays of $\text{Re}(\text{phen})$ ($[\text{Re}(1,10\text{-phenanthroline})(\text{CO})_3](\text{MeCN})\text{F6-TPB}$) in aerated MeCN ($\lambda_{em} = 303$ nm; decay signal in green, monoexponential fit in black)

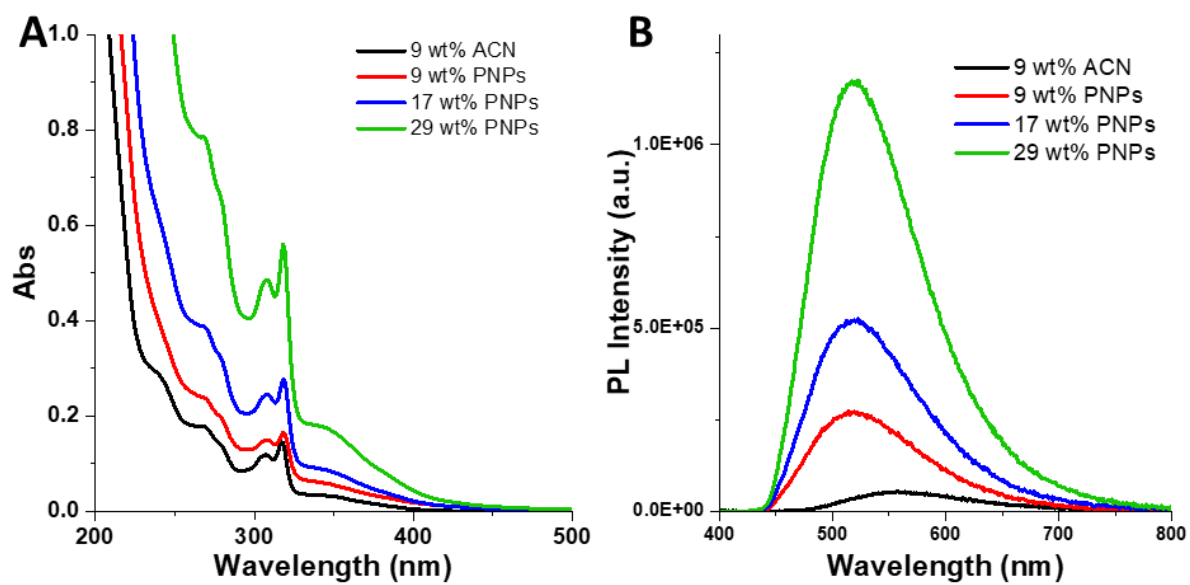


Figure 82: A) Absorption and B) emission spectra of the $\text{Re}(\text{bipy})$ loaded PNPs

2.2 Co-encapsulation of rhenium complex and cyanine dyes

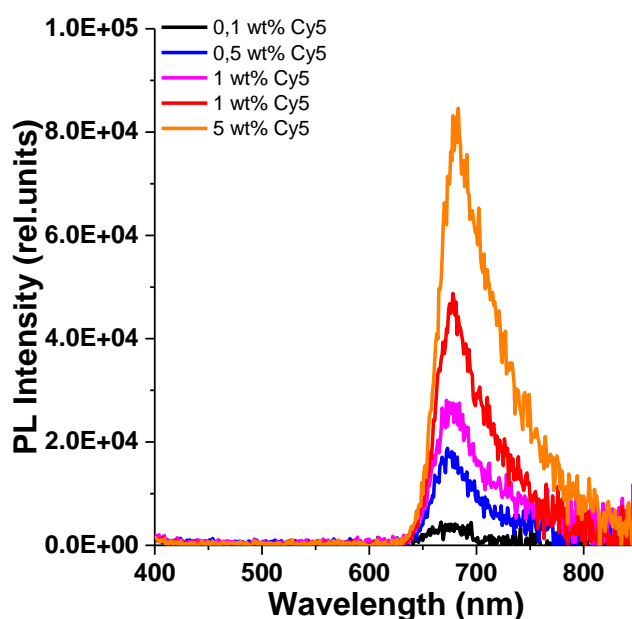


Figure 83: PL emission spectra of the Cy5 loaded NPs, $\lambda_{ex} = 292 \text{ nm}$

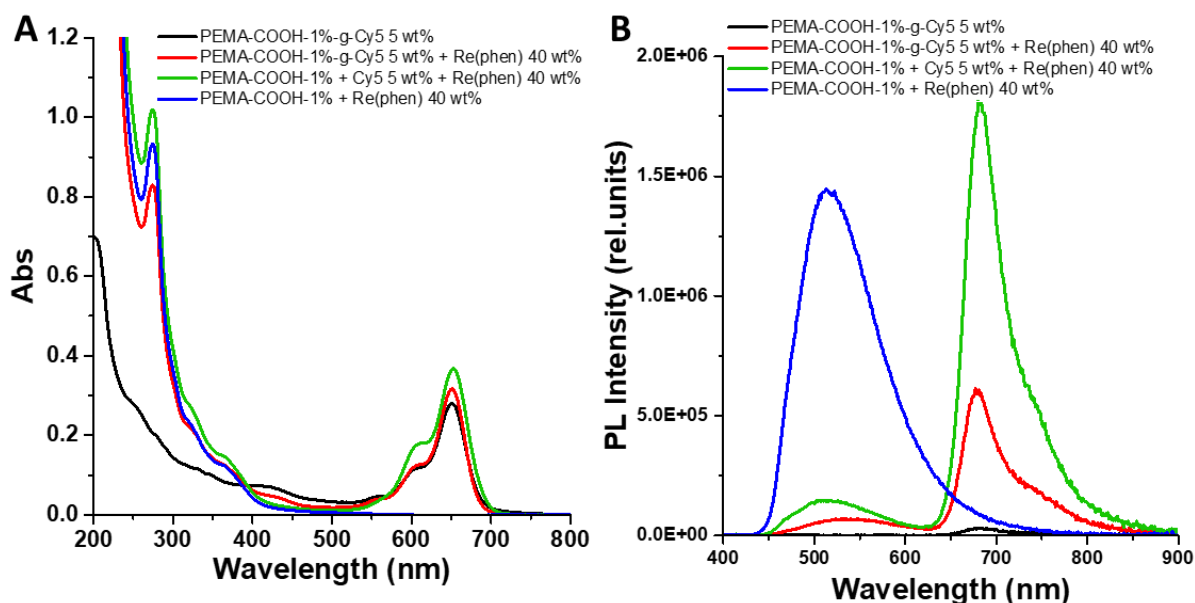


Figure 84: A) Absorbance and B) PL emission spectra of the Re(phen)/Cy5 loaded PNPs with Cy5-grafted polymer

PL Decay Fitting

For the Re donor and Cy5 acceptor PL decays in the 0 to 14 μs detection range, all PL decay curves were fit using the following multi-exponential intensity decay function:

$$I = \sum_i A_i \exp\left(-\frac{t}{\tau_i}\right) = A \sum_i \alpha_i \exp\left(-\frac{t}{\tau_i}\right) \quad (21)$$

where A is the total amplitude and α_i are the amplitude fractions ($\sum \alpha_i = 1$).

The PL decay curve of the pure donor (Re-NPs PEMA-COOH 1% at 40% [Re(phen)]) was fit using a double-exponential decay function, which led to the amplitude fractions α_{D0} and α_{D1} , the PL decay times τ_{D0} and τ_{D1} (with $\tau_{D0} > \tau_{D1}$) and a resulting amplitude-averaged PL decay time of the pure donor (in the absence of the acceptor) $\langle \tau_D \rangle$ using equation 9 :

$$\langle \tau_D \rangle = \alpha_{D0} \tau_{D0} + \alpha_{D1} \tau_{D1} \quad (22)$$

The FRET-quenched decay curves in the Re donor detection channel were fit using a triple-exponential decay function, leading to the amplitude fractions α_{DA*1} , α_{DA*2} , and α_{DA*3} and the PL decay times τ_{DA1} , τ_{DA2} , and τ_{DA3} , for which the third decay time component was fixed to $\tau_{DA3} = \tau_{D0}$ in order to take into account the emission of unquenched donors.

For the calculation of the average donor decay time in the presence of the acceptor $\langle \tau_{DA} \rangle$, only the first two amplitudes and decay times were used (as the third component represents unquenched donors). Therefore, the amplitude fractions must be redefined for these two decay times τ_{DA1} and τ_{DA2} :

$$\alpha_{DA1} = \frac{\alpha_{DA*1}}{\alpha_{DA*1} + \alpha_{DA*2}} \quad \text{and} \quad \alpha_{DA2} = \frac{\alpha_{DA*1}}{\alpha_{DA*1} + \alpha_{DA*2}} \quad (23)$$

As the unquenched donor possesses two decay time components (τ_{D1} and τ_{D0}), $\langle \tau_{DA} \rangle$ must be corrected for the shorter time component (τ_{D1}). As this shorter decay time of the “pure” donor has the same time range as the FRET-quenched decay times, the use of an additional exponential for the fit procedure leads to inconsistent fit results. We therefore, applied a correction factor z_D (the fraction of unquenched donors in the short-time components), which is determined by comparing the amplitude fractions of τ_{D0} and τ_{DA3} ($\tau_{DA3} = \tau_{D0}$) multiplied by the amplitude fraction α_{D1}

$$z_D = \alpha_{D1} (\alpha_{DA*3} / \alpha_{D0}) \quad (24)$$

The average FRET-quenched decay time is then

$$\langle \tau_{DA} \rangle = \frac{\alpha_{DA1} \tau_{DA1} + \alpha_{DA2} \tau_{DA2} - z_D \tau_{D1}}{1 - z_D} \quad (25)$$

and the average FRET-efficiency is

$$\langle E_{FRET} \rangle = 1 - \frac{\langle \tau_{DA} \rangle}{\langle \tau_D \rangle} \quad (26)$$

The FRET-sensitized decay curves in the Cy5 acceptor detection channel for the long window measurements were fit using a triple-exponential decay function, leading to the amplitude fractions α_{AD*1} , α_{AD*2} , and α_{AD*3} and the PL decay times τ_{AD1} , τ_{AD2} , and τ_{AD3} , for which the third decay time component was fixed to $\tau_{AD3} = \tau_{D0}$.

For the calculation of the average acceptor decay time in the presence of the donor $\langle \tau_{AD} \rangle$, only the first two amplitudes and decay times were used (as the third component represents unquenched donors). Therefore, the amplitude fractions must be redefined for these two decay times τ_{AD1} and τ_{AD2} and also corrected by the FRET rates k_{FRETi} to consider the FRET efficiency-dependent excitation of the acceptors:

$$\alpha_{AD1} = \frac{\frac{\alpha_{AD*1}}{k_{FRET1}}}{\left(\frac{\alpha_{AD*1}}{k_{FRET1}}\right) + \left(\frac{\alpha_{AD*2}}{k_{FRET2}}\right)} \quad \text{and} \quad \alpha_{AD2} = \frac{\frac{\alpha_{AD*2}}{k_{FRET1}}}{\left(\frac{\alpha_{AD*1}}{k_{FRET1}}\right) + \left(\frac{\alpha_{AD*2}}{k_{FRET2}}\right)} \quad (27)$$

Where:

$$k_{\text{FRET}i} = \frac{1}{\tau_{\text{AD}i}} - \frac{1}{\langle \tau_{\text{D}} \rangle} \quad (28)$$

The correction factor z_A (the fraction of unquenched donors in the short time components) is almost negligible but is still taken into account for a correct treatment in case of long window measurements (for the short window measurements, z_A was taken as zero).

$$z_A = \alpha_{\text{D}1}(\alpha_{\text{AD}*3}/\alpha_{\text{D}0}) \quad (29)$$

The corrected averaged FRET sensitized decay time can then be calculated by:

$$\langle \tau_{\text{AD}} \rangle = \frac{\alpha_{\text{AD}1} \tau_{\text{AD}1} + \alpha_{\text{AD}2} \tau_{\text{AD}2} - z_A \tau_{\text{D}1}}{1 - z_A} \quad (30)$$

And then we can calculate the average FRET efficiency by:

$$\langle E_{\text{FRET}} \rangle = 1 - \frac{\langle \tau_{\text{AD}} \rangle}{\langle \tau_{\text{D}} \rangle} \quad (31)$$

For the short time window, all PL decay curves were fit using multiexponential intensity decay functions with a starting time point of $t_0 = 1.64$ ns, which corresponded to a short delay between the start of the actual PL decay (at $t = 0$) and the start of the fit. The PL intensity decay is then defined by:

$$I = \sum_i A_{i-\text{Fit}} \exp\left(-\frac{(t-t_0)}{\tau_i}\right) = \sum_i A_i \exp\left(-\frac{t}{\tau_i}\right) \quad (32)$$

When using tail fits that start after $t = 0$, the obtained pre-exponential factors are not correct for the complete decay that starts at $t = 0$. Although the lifetimes do not change, the single amplitudes ($A_{i-\text{FIT}}$) must be corrected to yield the correct amplitudes (A_i)¹⁷⁴:

$$I = A_{i-\text{FIT}} \cdot \exp\left(-\frac{(t-t_0)}{\tau}\right) = A_i \cdot \exp\left(-\frac{t}{\tau}\right) \Rightarrow A_i = A_{i-\text{FIT}} \cdot \exp\left(-\frac{t_0}{\tau}\right) \quad (33)$$

After correcting the amplitudes, the fits were plotted using equation 21, where C is the background intensity, A_1 and A_2 are the corrected amplitudes, τ_1 and τ_2 are the first and second lifetime components, t is the time and $I(t)$ is the time-dependent PL intensity.

$$I(t) = A_1 \cdot \exp\left(-\frac{t}{\tau_1}\right) + A_2 \cdot \exp\left(-\frac{t}{\tau_2}\right) + C \quad (34)$$

Table 7 : Fit (from Re(phen) PL decay curves) lifetimes (τ) and amplitude fractions (α) and calculated correction factors (z_D), amplitude averaged FRET lifetimes ($\langle \tau_{\text{DA}} \rangle$), average FRET efficiencies ($\langle E_{\text{FRET}} \rangle$), overall amplitude-averaged lifetimes ($\langle \tau \rangle$), lifetime system-averaged FRET efficiencies ($\langle E^*_{\text{FRET}} \rangle$), and intensity system-averaged FRET efficiencies ($\text{int.} \langle E^*_{\text{FRET}} \rangle$).

Cy5	$\tau_{\text{DA}1}$ (μs)	$\alpha_{\text{DA}1}$	$\tau_{\text{DA}2}$ (μs)	$\alpha_{\text{DA}2}$	$\alpha_{\text{DA}0}$	rel. errors
0.1%	0.64	0.28	1.52	0.72	0.61	18%
0.5%	0.34	0.31	1.27	0.69	0.34	10%
1.0%	0.24	0.40	1.14	0.60	0.20	6%
2.0%	0.11	0.37	0.74	0.63	0.13	4%
5.0%	0.05	0.50	0.43	0.50	0.10	3%

Cy5	z_D	$\langle \tau_{DA} \rangle$ (μs)	$\langle E_{FRET} \rangle$	$\langle \tau \rangle$ (μs)	$\langle E^*_{FRET} \rangle$	int. $\langle E^*_{FRET} \rangle$
0.1%	0.22 ± 0.12	1.31 ± 0.74	0.64 ± 0.40	3.26 ± 1.17	0.10 ± 0.04	0.08 ± 0.02
0.5%	0.12 ± 0.04	0.95 ± 0.27	0.74 ± 0.25	2.16 ± 0.43	0.40 ± 0.10	0.41 ± 0.08
1.0%	0.072 ± 0.013	0.76 ± 0.12	0.79 ± 0.17	1.52 ± 0.18	0.58 ± 0.10	0.60 ± 0.12
2.0%	0.047 ± 0.006	0.47 ± 0.05	0.87 ± 0.15	1.02 ± 0.08	0.72 ± 0.10	0.80 ± 0.16
5.0%	0.037 ± 0.003	0.20 ± 0.02	0.94 ± 0.15	0.67 ± 0.04	0.81 ± 0.10	0.92 ± 0.18

Relative errors provided in the table are related to τ and α and were estimated. Errors for z_D , $\langle \tau_{DA} \rangle$, $\langle E_{FRET} \rangle$, $\langle \tau \rangle$, $\langle E^*_{FRET} \rangle$, and int. $\langle E^*_{FRET} \rangle$ (intensity calculated system-averaged FRET efficiency with intensity errors estimated as 10%) were calculated using error propagation.

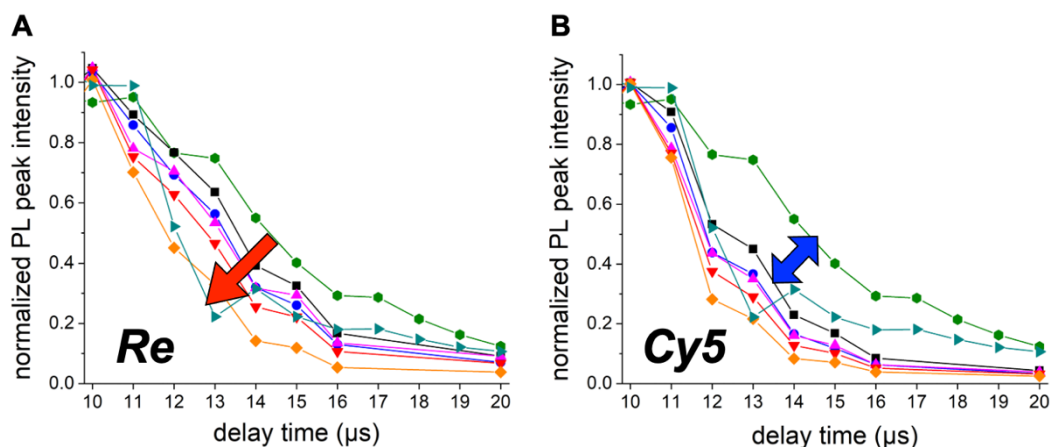


Figure 85: Normalized PL peak intensities of Re NPs loaded with different amounts of Cy5 (Black: 0.1% Cy5; blue: 0.5% Cy5; magenta: 1% Cy5; red: 2% Cy5; orange: 5% Cy5.) as a function of delay time. Excitation wavelength $\lambda_{ex} = 303$ nm; gate time: $20 \mu s$. The green data points (Re NP without Cy5) and dark cyan data points (NPs with 5% Cy5 and without Re represent the instrument flash lamp decay) were measured only for Re and Cy peak intensities, respectively. They are shown in both graphs for orientation. A) Re donor peak intensity shows a progressive intensity decrease with increasing fractions of Cy5 acceptor as indicated by the red arrow. B) Cy5 acceptor peak intensity is independent of the Cy5 fraction and all curves have approximately the same intensities as the flash lamp decay. Blue arrow indicates the difference to the Re decay, which is approximately the same for all curves.

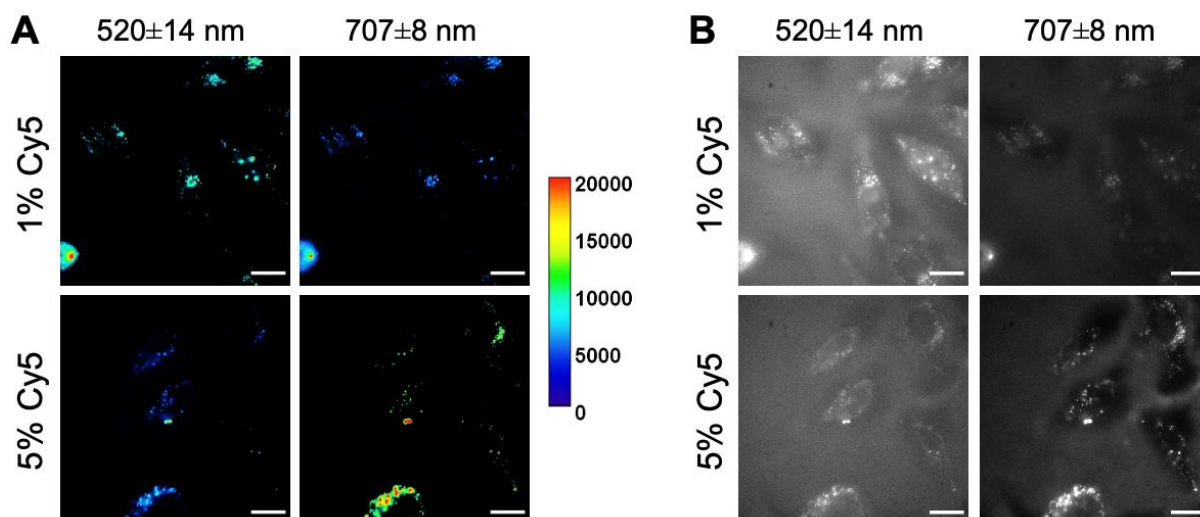


Figure 86: Live cell fluorescence images of HeLa cells after 3h of incubation with 10 $\mu\text{g/ml}$ Re-NPs PEMA-COOH 1% at 40% [Re(phen)] loaded with 1 wt% and 5 wt% of Cy5. Excitation (λ_{ex}) at 320 ± 20 nm and emission (λ_{em}) at 520 ± 14 nm for the Re donor channel and 707 ± 8 nm for the Cy5 acceptor channel. **A:** Fluorescence intensity (color-coded intensities shown on the right) comparison of Re and Cy5 emission. The images were treated with ImageJ, such that the threshold was adjusted and the autofluorescence at 520 ± 14 nm (taken from an image of cells without NPs and excited/detected using the same parameters) was subtracted. **B:** Raw images, which show the strong autofluorescence intensity at 520 ± 14 nm. Images were acquired using an Olympus IX83 microscope, Andor EMCCD camera with 500 ms acquisition time and 500-fold EM gain, and continuous wave illumination with an 82 W X-Cite light source. Scale bars in all pictures: 20 μm .

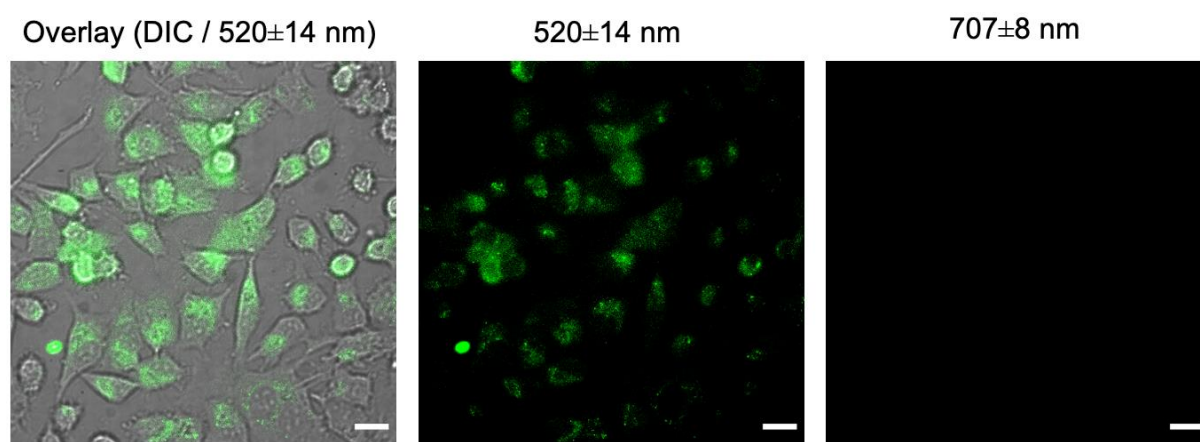


Figure 87: Control images of HeLa cells incubated for 3h with 10 $\mu\text{g/ml}$ Re-NPs (PEMA-COOH 1% at 40% [Re(phen)]). Excitation (λ_{ex}) at 320 ± 20 nm and emission (λ_{em}) at 520 ± 14 nm (green) and 707 ± 8 nm. Images were acquired using an Olympus IX83 microscope, Andor EMCCD camera with 500 ms acquisition time and 500-fold EM gain, and continuous wave illumination with an 82 W X-Cite light source. Scale bars in all images: 20 μm

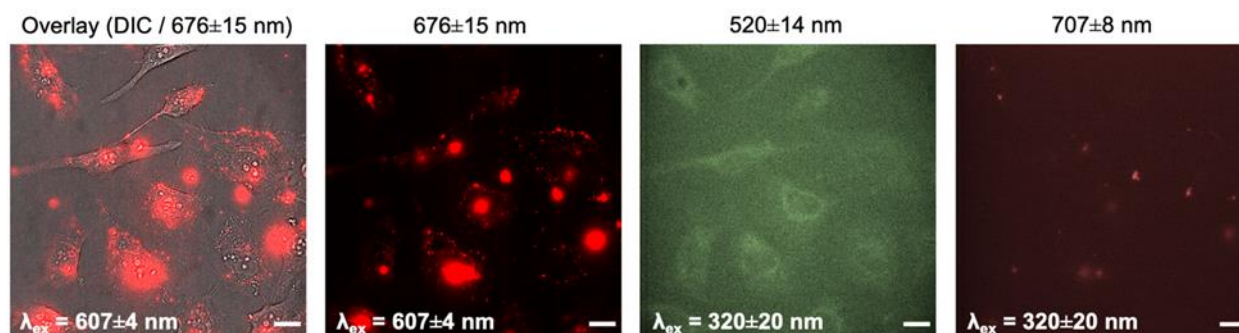


Figure 88: Control images of HeLa cells incubated for 3h with 4 $\mu\text{g}/\text{mL}$ Cy5-NPs (PEMA-COOH 1% loaded with 5% Cy5). Direct excitation of Cy5 at 607 ± 4 nm and emission detection at 676 ± 15 nm resulted in strong fluorescence signals, whereas excitation at 320 ± 20 nm resulted in the detection of significant autofluorescence at 520 ± 14 nm and very faint Cy5 emission at 707 ± 8 nm. The contrast and brightness of both images on the right was adjusted to visualize the signals. Therefore, the background is also stronger. Images were acquired using an Olympus IX83 microscope, Andor EMCCD camera with 50 ms acquisition time and 50-fold EM gain, and continuous wave illumination with a 10 W X-Cite light source. Scale bars in all images: 20 μm .

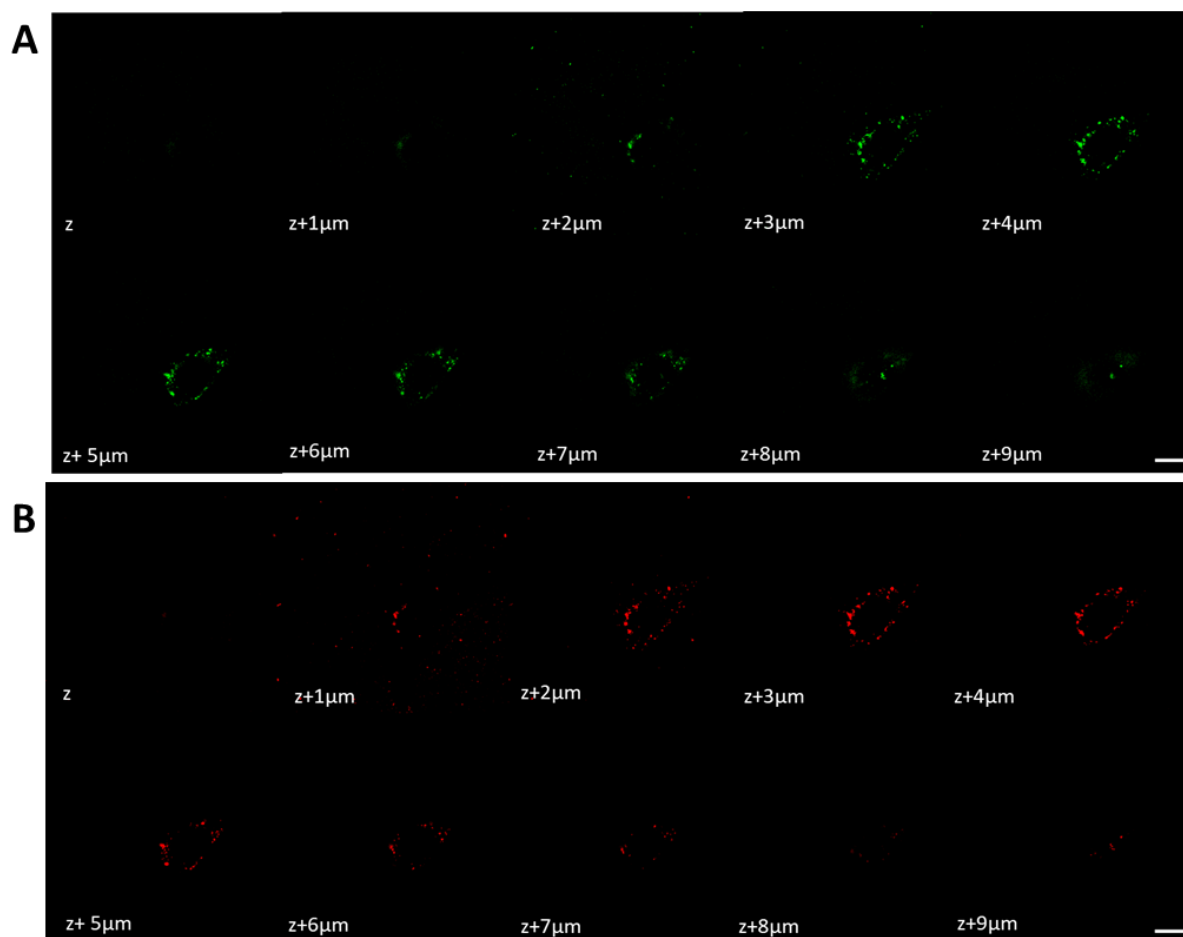


Figure 89: A z-scan imaging (in steps of 1 μm) across HeLa cells incubated with 40% Re+ 5% Cy5 for 3h at 10 $\mu\text{g}/\text{mL}$, excitation (λ_{ex}) at 320 ± 20 nm, and emission (λ_{em}) at A) 520 ± 14 nm (green) for the donor channel and B) 707 ± 8 nm (red) for the acceptor channel. Images of the NPs were acquired using an Olympus IX83 microscope with EMCCD camera (Andor) with an acquisition time of 500ms, x500 EM gain, and illuminated with continuous wave illumination source at a power of 82W. Scale bar: 20 μm

3. Molecular Up-conversion within PNPs for Live-Cell Imaging

3.1 Formulation and optimisation

				Emission	
				Pas d'émission	
				Non testé	
				Pas de particule	
				X	

Copolymères			
Loading 10% - ACN	Water	Buffer	
PEMA75-HEMA25-COOH1%	X		119
PEMA50-HEMA50-COOH1%	X		X
PEMA25-HEMA75-COOH1%	X		197
PEMA50-HEMA50-COOH1% bloc	X		211

PEMA-SO ₃ H1%		
ACN	Water	Buffer
1%	12	95
2%	19	78
5%	17	124
10%	21	
20%	62	
40%	X	

PEMA-SO ₃ H1%		
Water	ACN/MeOH 50%/50%	
5%	18	
10%	21	
20%	X	
40%	X	

PEMA-SO ₃ H1%		
ACN	Water	Buffer
1%	94	32
2%	112	34
5%	100	46
10%	160	49

PLGA		
ACN	Water/MeOH 50%/50%	Water/MeOH 75%/25%
5%	X	153

PEMA-SO ₃ H1%/PEMA		
ACN	Water	Buffer
1%	X	
2%	X	
5%	X	
10%	X	

PEMA-SO ₃ H1%/PEMA		
Water	ACN/MeOH 50%/50%	MeOH
5%	300	263

PEMA-SO ₃ H1%/PEMA		
ACN	Water	Buffer
5%	19	X
10%	20	X
20%	20	X
40%	29	?
50%	125	?
60%	X	?

PEMA-SO ₃ H5%		
ACN	NaCl 5 mM	NaCl 10 mM
5%	X	X
10%	X	X
20%	X	X

PEMA-SO ₃ H2%		
ACN	Water	
5%	61	
10%	53	
20%	46	
40%	55	

PEMA-SO ₃ H2%		
Water		
5%	15	
10%	17	
20%	65	
40%	153	

PEMA-SO ₃ H5%/PEMA		
ACN	NaCl 5 mM	NaCl 10 mM
5%	X	X
10%	X	X
20%	X	X

PEMA-SO ₃ H1%/PEMA		
ACN	Water	Buffer
5%	35	19
10%	213	43
20%	X	X
40%	96	100

PEMA-SO ₃ H5%/PEMA		
ACN	NaCl 5 mM	NaCl 10 mM
5%	X	X
10%	X	X
20%	X	X

PEMA-SO ₃ H1%/PEMA		
ACN	Water	Buffer
5%	18	24
10%	17	24
20%	19	25
40%	X	X

PEMA-SO ₃ H1%/PEMA		
ACN	Water	Buffer
5%	35	19
10%	213	43
20%	X	X
40%	96	100

PEMA-SO ₃ H1%/PEMA		
ACN	Water	Buffer
5%	18	24
10%	17	24
20%	19	25
40%	X	X

PEMA-SO ₃ H1%/PEMA		
ACN	Water	Buffer
5%	18	24
10%	17	24
20%	19	25
40%	X	X

PEMA-SO ₃ H1%/PEMA		
ACN	Water	Buffer
5%	18	24
10%	17	24
20%	19	25
40%	X	X

PEMA-SO ₃ H1%/PEMA		
ACN	Water	Buffer
5%	18	24
10%	17	24
20%	19	25
40%	X	X

PEMA-SO ₃ H1%/PEMA		
ACN	Water	Buffer
5%	18	24
10%	17	24
20%	19	25
40%	X	X

PEMA-SO ₃ H1%/PEMA		
ACN	Water	Buffer
5%	18	24
10%	17	24
20%	19	25
40%	X	X

PEMA-SO ₃ H1%/PEMA		
ACN	Water	Buffer
5%	18	24
10%	17	24
20%	19	25
40%	X	X

PEMA-SO ₃ H1%/PEMA		
ACN	Water	Buffer
5%	18	24
10%	17	24
20%	19	25
40%	X	X

PEMA-SO ₃ H1%/PEMA		
ACN	Water	Buffer
5%	18	24
10%	17	24
20%	19	25
40%	X	X

PEMA-SO ₃ H1%/PEMA		
ACN	Water	Buffer
5%	18	24
10%	17	24
20%	19	25
40%	X	X

PEMA-SO ₃ H1%/PEMA		
ACN	Water	Buffer
5%	18	24
10%	17	24
20%	19	25
40%	X	X

PEMA-SO ₃ H1%/PEMA		
ACN	Water	Buffer
5%	18	24
10%	17	24
20%	19	25
40%	X	X

PEMA-SO ₃ H1%/PEMA		
ACN	Water	Buffer
5%	18	24
10%	17	24
20%	19	25
40%	X	X

PEMA-SO ₃ H1%/PEMA		
ACN	Water	Buffer
5%	18	24
10%	17	24
20%	19	25
40%	X	X

PEMA-SO ₃ H1%/PEMA		
ACN	Water	Buffer
5%	18	24
10%	17	24
20%	19	25
40%	X	X

PEMA-SO ₃ H1%/PEMA		
ACN	Water	Buffer
5%	18	24
10%	17	24
20%	19	25
40%	X	X

PEMA-SO ₃ H1%/PEMA		
ACN	Water	Buffer
5%	18	24
10%	17	24
20%	19	25
40%	X	X

PEMA-SO ₃ H1%/PEMA		
ACN	Water	Buffer
5%	18	24
10%	17	24
20%	19	25
40%	X	X

PEMA-SO ₃ H1%/PEMA		
ACN	Water	Buffer
5%	18	24
10%	17	24
20%	19	25
40%	X	X

PEMA-SO ₃ H1%/PEMA		
ACN	Water	Buffer
5%	18	24
10%	17	24
20%	19	25
40%	X	X

PEMA-SO ₃ H1%/PEMA		
ACN	Water	Buffer
5%	18	24
10%	17	24
20%	19	25
40%	X	X

PEMA-SO ₃ H1%/PEMA		
ACN	Water	Buffer
5%	18	24
10%	17	24
20%	19	25
40%	X	X

PEMA-SO ₃ H1%/PEMA		
ACN	Water	Buffer
5%	18	24
10%	17	24
20%	19	25
40%	X	X

PEMA-SO ₃ H1%/PEMA		
ACN	Water	Buffer
5%	18	24
10%	17	24
20%	19	25
40%	X	X

PEMA-SO ₃ H1%/PEMA		
ACN	Water	Buffer
5%	18	24
10%	17	24
20%	19	25
40%	X	X

PEMA-SO ₃ H1%/PEMA		
ACN	Water	Buffer
5%	18	24
10%	17	24
20%	19	25
40%	X	X

PEMA-SO ₃ H1%/PEMA		
ACN	Water	Buffer
5%	18	24
10%	17	24
20%	19	25
40%	X	X

PEMA-SO ₃ H1%/PEMA		
ACN	Water	Buffer
5%	18	24
10%	17	24
20%	19	25
40%	X	X

PEMA-SO ₃ H1%/PEMA		
ACN	Water	Buffer
5%	18	24
10%	17	24
20%	19	25
40%	X	X

PEMA-SO ₃ H1%/PEMA		
ACN	Water	Buffer
5%	18	24
10%	17	24
20%	19	25
40%	X	X

PEMA-SO ₃ H1%/PEMA		
ACN	Water	Buffer
5%	18	24
10%	17	24
20%	19	25
40%	X	X

PEMA-SO ₃ H1%/PEMA		
ACN	Water	Buffer
5%	18	24
10%	17	24
20%	19	25
40%	X	X

PEMA-SO ₃ H1%/PEMA		
ACN	Water	Buffer
5%	18	24
10%	17	24
20%	19	25
40%	X	X

PEMA-SO ₃ H1%/PEMA		
ACN	Water	Buffer
5%	18	24
10%	17	24
20%	19	25
40%	X	X

PEMA-SO ₃ H1%/PEMA		
ACN	Water	Buffer
5%	18	24
10%	17	24
20%	19	25
40%	X	X

PEMA-SO ₃ H1%/PEMA		
ACN	Water	Buffer
5%	18	24
10%	17	24
20%	19	25
40%	X	X

PEMA-SO ₃ H1%/PEMA		
ACN	Water	Buffer
5%	18	24
10%	17	24
20%	19	25
40%	X	X

PEMA-SO ₃ H1%/PEMA		
ACN	Water	Buffer
5%	18	24
10%	17	24
20%	19	25
40%	X	X

PEMA-SO ₃ H1%/PEMA		
ACN	Water	Buffer
5%	18	24
10%	17	24
20%	19	25
40%	X	X

PEMA-SO ₃ H1%/PEMA		
ACN	Water	Buffer
5%	18	24
10%	17	24
20%	19	25
40%	X	X

PEMA-SO ₃ H1%/PEMA		
ACN	Water	Buffer
5%	18	24
10%	17	24
20%	19	25
40%	X	X

PEMA-SO ₃ H1%/PEMA		
ACN	Water	Buffer
5%	18	24
10%	17	24
20%	19	25
40%	X	X

PEMA-SO ₃ H1%/PEMA		
ACN	Water	Buffer
5%	18	24
10%	17	24
20%	19	25
40%	X	X

PEMA-SO ₃ H1%/PEMA		
ACN	Water	Buffer

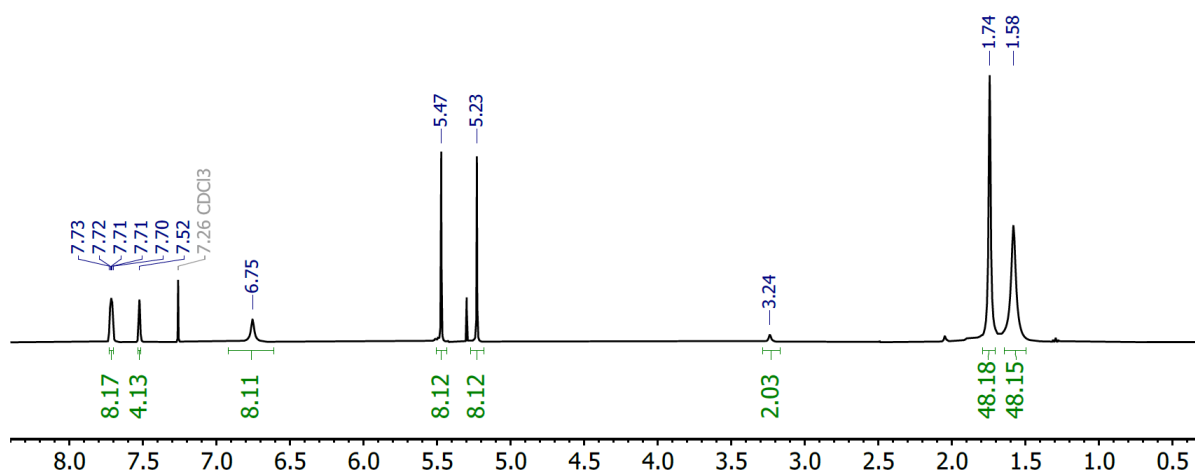


Figure 91: ^1H NMR (400 MHz, 298 K, CDCl_3) of $[\text{Y}_9(\text{acac})_{16}(\text{OH})_{10}](\text{F6-TPB})$

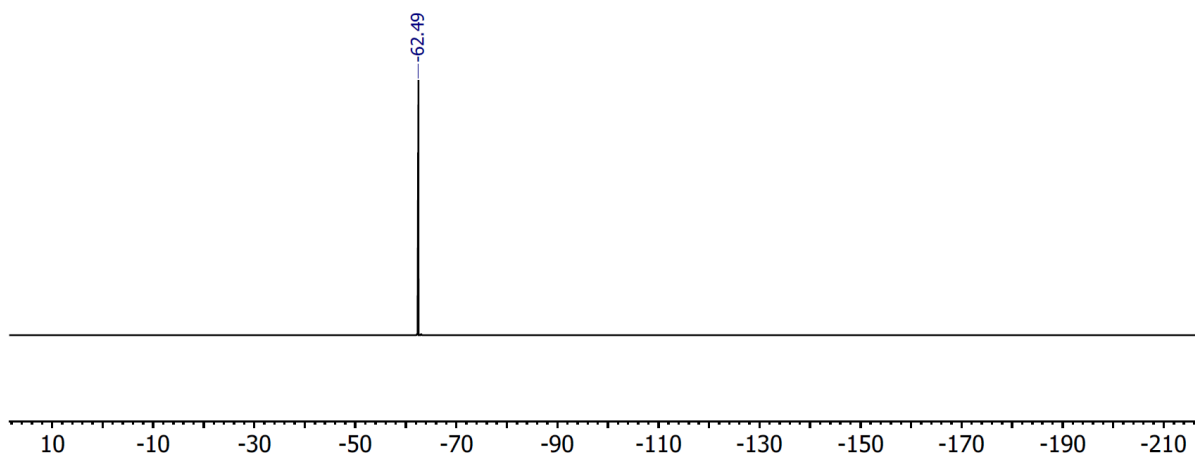


Figure 92: ^{19}F NMR (377 MHz, 298 K, CDCl_3) of $[\text{Y}_9(\text{acac})_{16}(\text{OH})_{10}](\text{F6-TPB})$

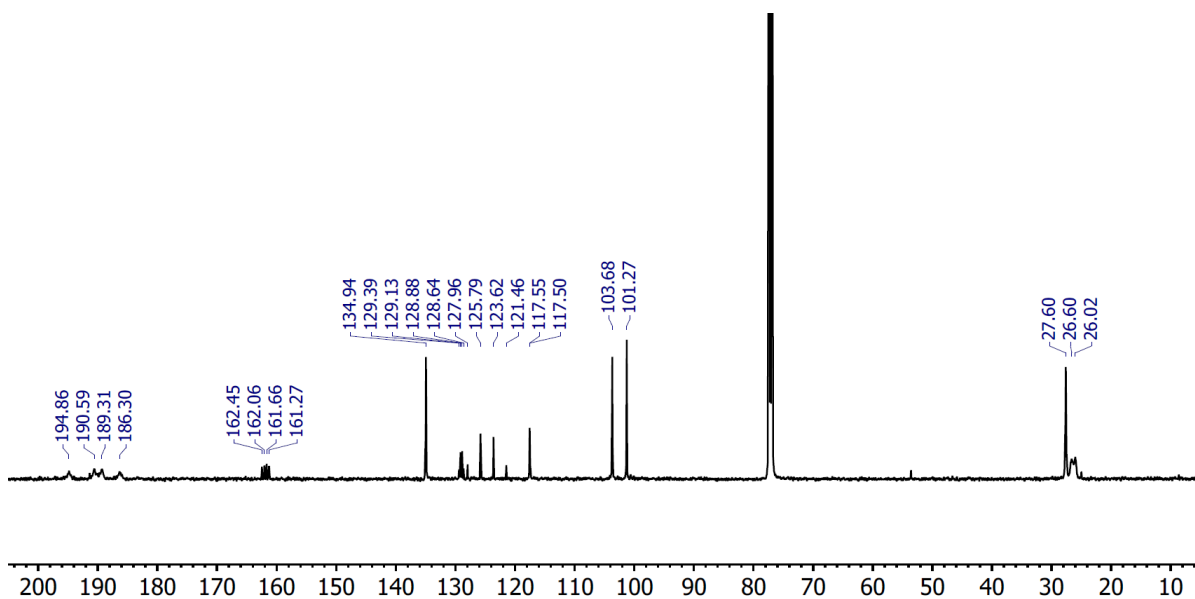


Figure 93: ^{13}C NMR (126 MHz, 298 K, CDCl_3) of $[\text{Y}_9(\text{acac})_{16}(\text{OH})_{10}](\text{F6-TPB})$

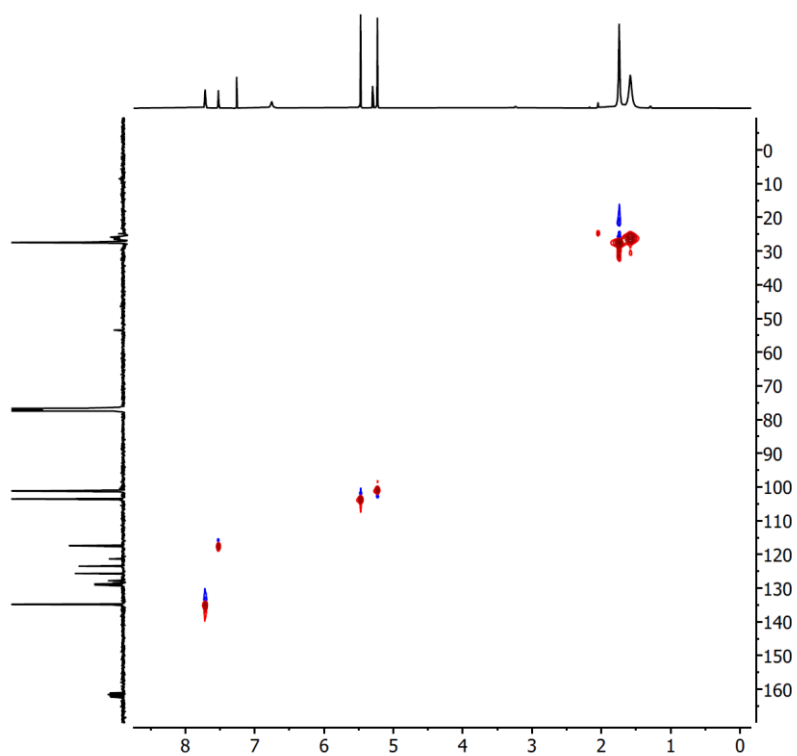


Figure 94: ^1H - ^{13}C HSQC NMR (500 MHz, 298 K, CDCl_3) of $[\text{Y}_9(\text{acac})_{16}(\text{OH})_{10}](\text{F6-TPB})$

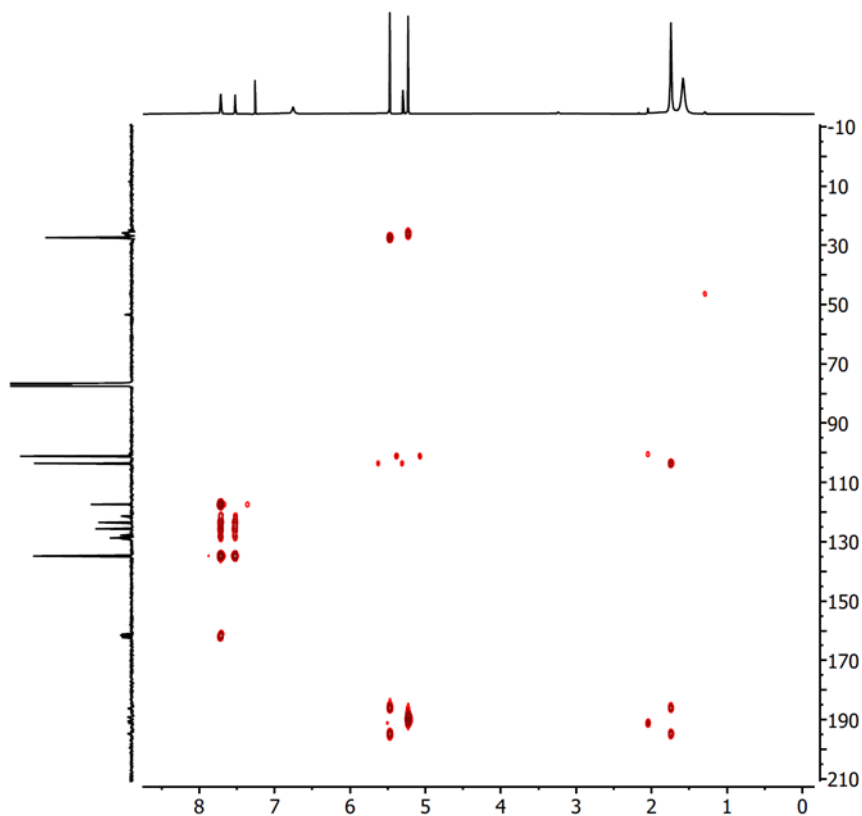


Figure 95: ^1H - ^{13}C HMBC NMR (500 MHz, 298 K, CDCl_3) of $[\text{Y}_9(\text{acac})_{16}(\text{OH})_{10}](\text{F6-TPB})$

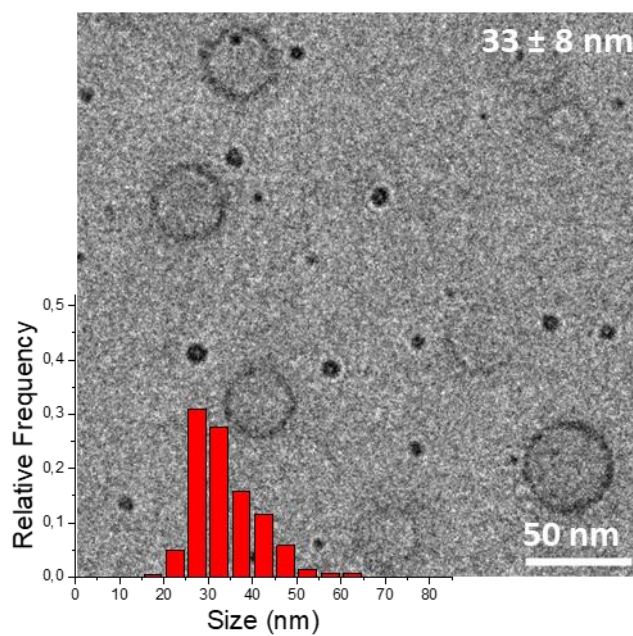


Figure 96: TEM picture of PEMA-COOH-5% NPs loaded with 38 wt% $[\text{Y}_5\text{Tb}_4(\text{acac})_{16}(\text{OD})_{10}](\text{F6-TPB})$ prepared in phosphate buffer

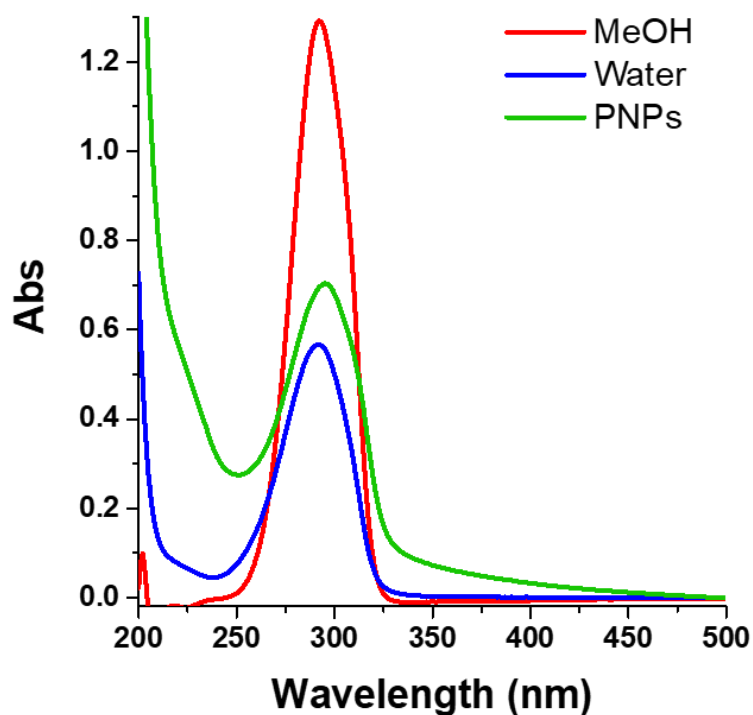


Figure 97: Absorbance spectra of the acac ligands from $[Yb_5Tb_4acac_{16}(OD)_{10}](F6-TPB)$ in methanol, water or inside PNPs

Table 8: Theoretical and calculated concentration of the $[Yb_5Tb_4acac_{16}(OD)_{10}](F6-TPB)$ complex inside the PNPs. α : using ϵ_{ligand} in methanol

Loading	PEMA-COOH-5%		PMMA-SO ₃ H-1%	
	Calculated Concentration ^a	Theoretical Concentration	Calculated Concentration ^a	Theoretical Concentration
9 wt%	0.00184	0.004	7.78092E-4	0.002
17 wt%	0.00412	0.008	0.00169	0.004
29 wt%	0.0085	0.016	0.00326	0.008
38 wt%	0.01242	0.024	0.00476	0.012
44 wt%	0.00879	0.032	0.00656	0.016
50 wt%	0.00955	0.04	0.00778	0.02

3.2 Characterization in deuterated media

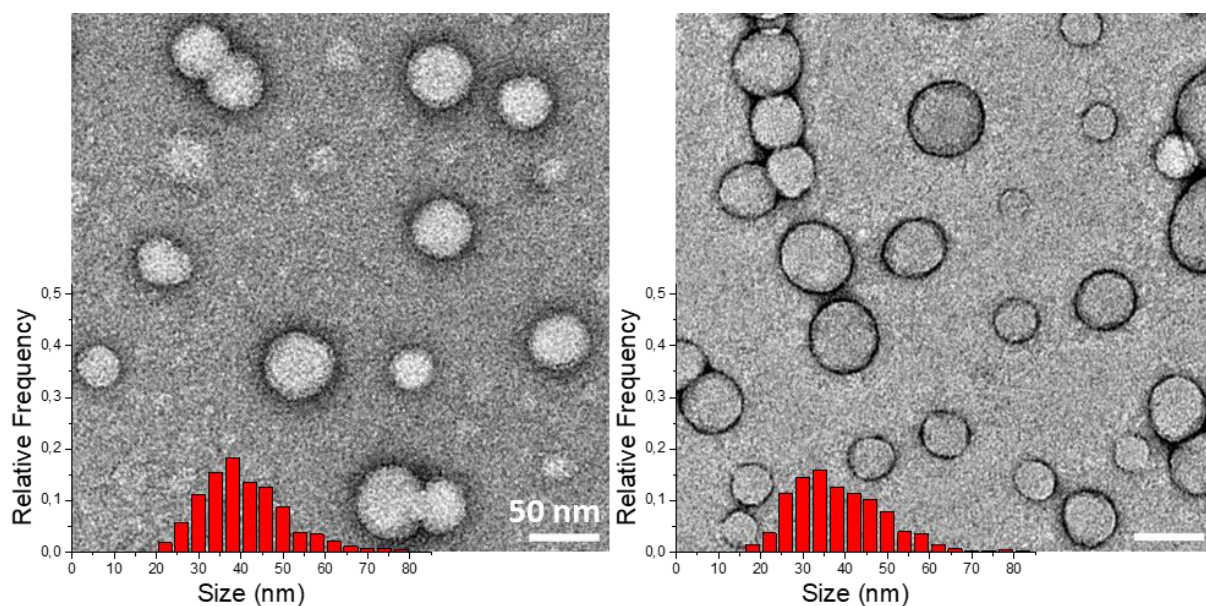


Figure 98: TEM pictures of PEMA-COOH-5% NPs loaded with 9 wt% (left) and 17 wt% (right) of $[Yb_5Tb_4(acac)_{16}(OD)_{10}](F6-TPB)$ prepared in deuterated phosphate buffer.

Table 9: Size, number of complexes and average distance between the complexes inside the PNPs

	Size DLS (nm)	Size TEM (nm)	Number of dye per NP	Distance Inter-Complex (nm)
10% in PEMA-COOH-5%	83 ± 15	41 ± 11	597	2,17
20% in PEMA-COOH-5%	93 ± 18	39 ± 11	941	1,78
60% in PEMA-COOH-5%	96 ± 9	36 ± 11	1666	1,36
60% in PMMA-SO3H-1%	48 ± 12	18 ± 4	225	1,32

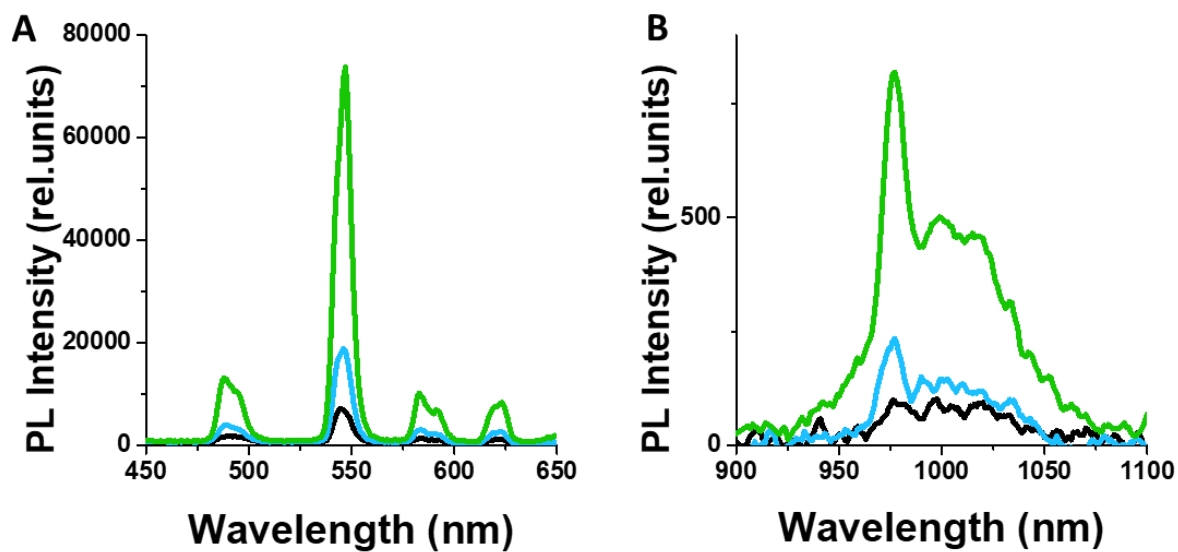


Figure 99 : Absolute emission spectra of A) Tb and B) Yb when loaded inside PEMA-COOH-5% PNPs.

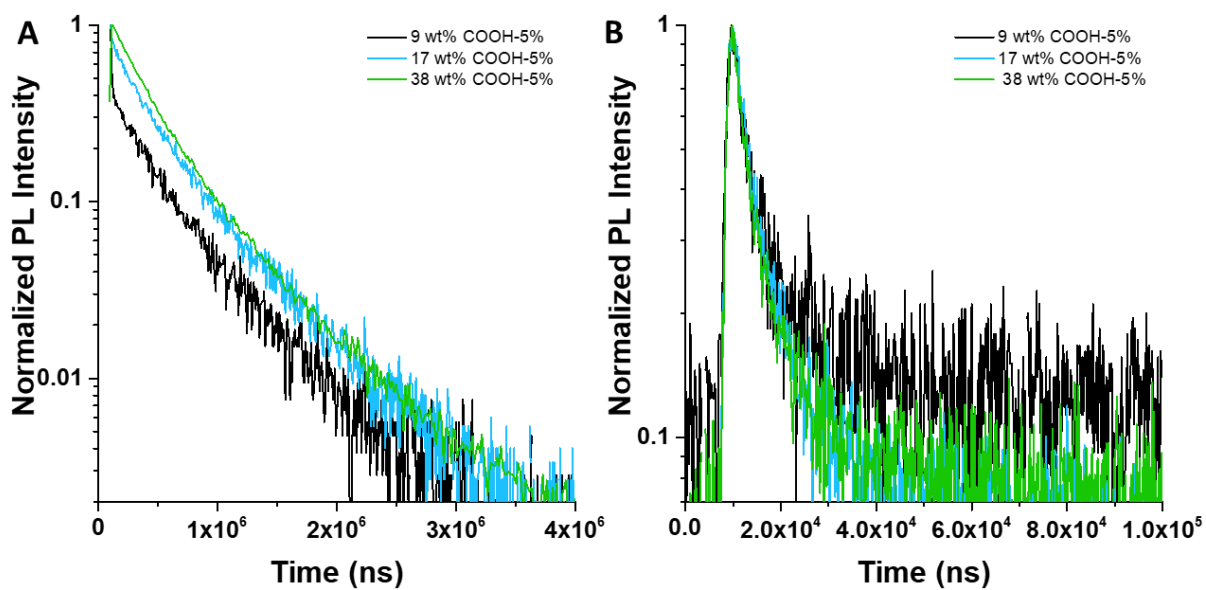


Figure 100: Normalized PL Decay curves for the downshifting emission of A) Tb and B) Yb for different PEMA-COOH-5% PNPs, $\lambda_{ex} = 340 \text{ nm}$

Table 10: Calculated lifetimes for different NPs in deuterated aqueous media. a) Reported from⁵⁷

	Amplitude Average Lifetime (μ s) Tb	Amplitude Average Lifetime (μ s) Yb
9 wt% PEMA-COOH-5%	457.3	5.2
17 wt% PEMA-COOH-5%	486.5	7.7
38 wt% PEMA-COOH-5%	474.9	4.7
9 wt% PMMA-SO ₃ H-1%	414.2	8.6
17 wt% PMMA-SO ₃ H-1%	422.2	8.1
38 wt% PMMA-SO ₃ H-1%	443.0	9.4
50 wt% PMMA-SO ₃ H-1%	408.3	48.9
[Yb ₅ Tb ₄ (acac) ₁₆ (OD) ₁₀](OD)	0.9 ^a	49 ^a

Amplitude Average Lifetime $\langle \tau \rangle$ calculated with:

$$\langle \tau \rangle_f = \sum_i^n f_i \tau_i$$

$$f_i = \frac{\alpha_i \tau_i}{\sum_i^n \alpha_i \tau_i}$$

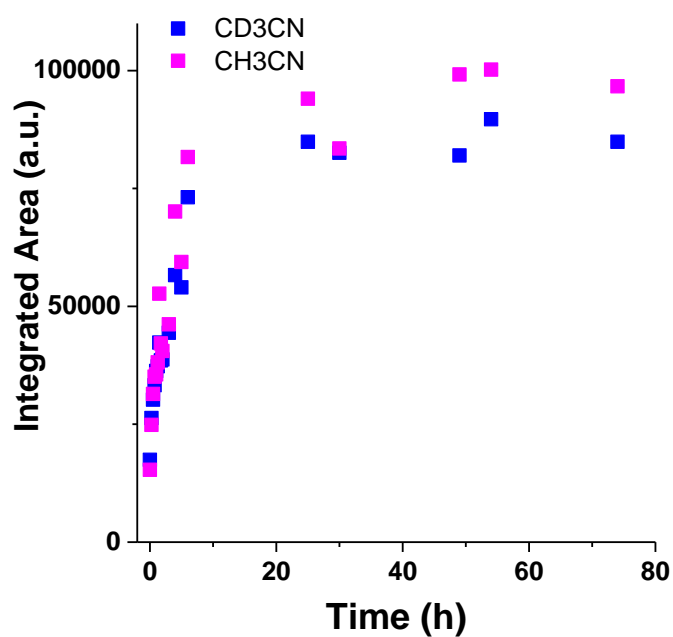


Figure 101: Relative intensities of UC PL for PEMA-COOH 5% NPs loaded with 38 wt% [Yb₅Tb₄(acac)₁₆(OD)₁₀](F6-TPB) prepared in either using deuterated or non-deuterated acetonitrile over time Evolution of the area of UC emission over time

3.3 Imaging

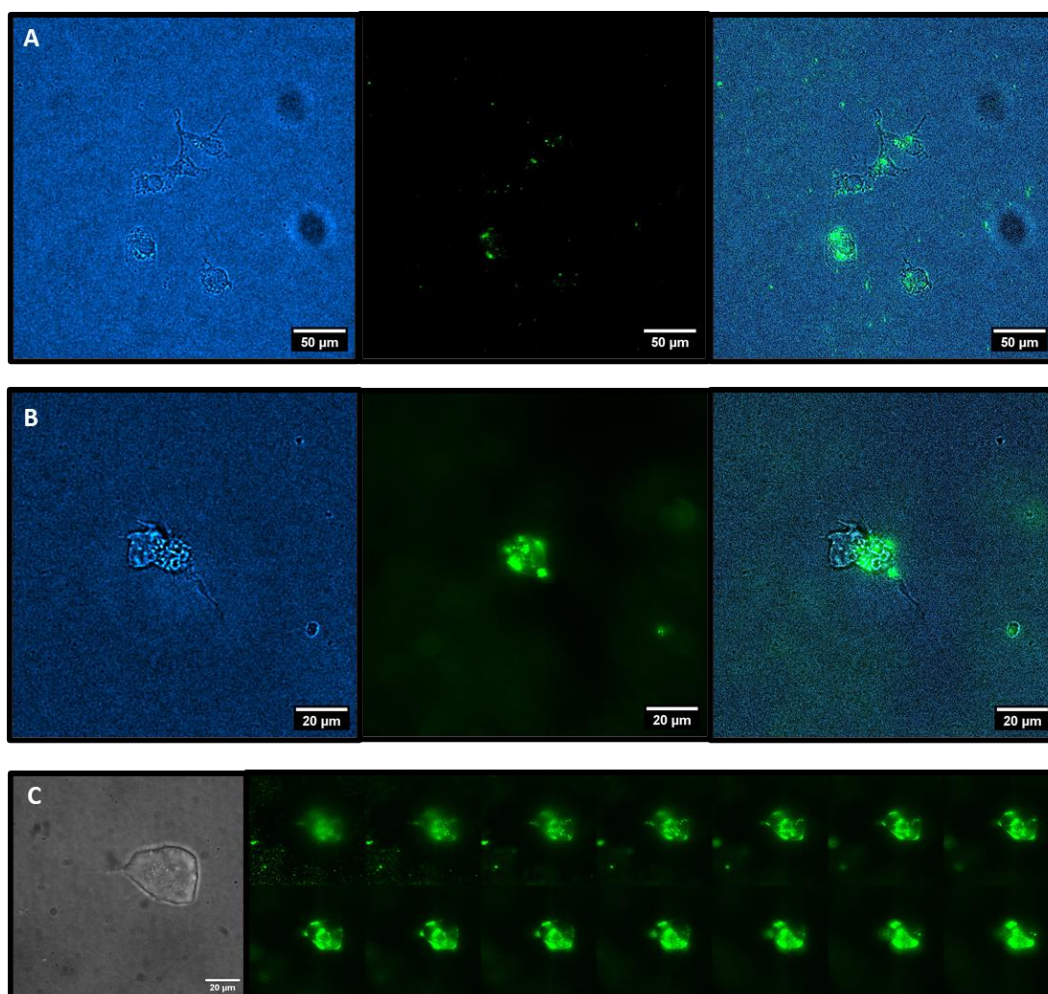


Figure 102: DIC, green channel under 980 nm excitation and composite image of inorganic UCNPs in Cos7 cells with (A) 40x and (B) 100x magnification. (C) Reference DIC image and scan along z-axis of green channel for inorganic UCNPs

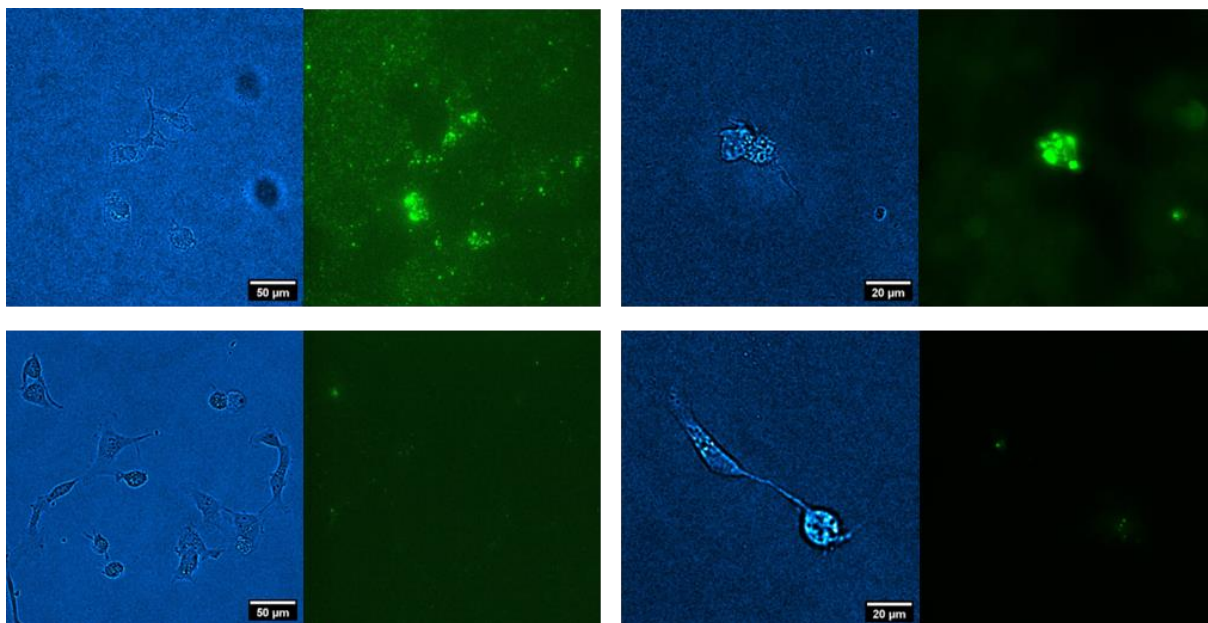


Figure 103: DIC and raw fluorescence images of inorganic (upper row) and polymeric UCNPs

4. Gold Nanoclusters loaded PNPs for SWIR Imaging

4.1 AuNCs encapsulation

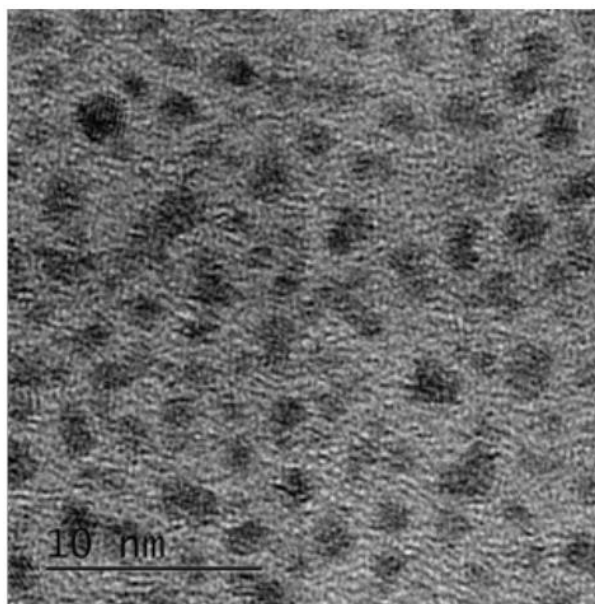


Figure 104: High resolution TEM of AuNCs with DDT ligands dispersed in ethanol. Average size 1.84 ± 0.32 nm.

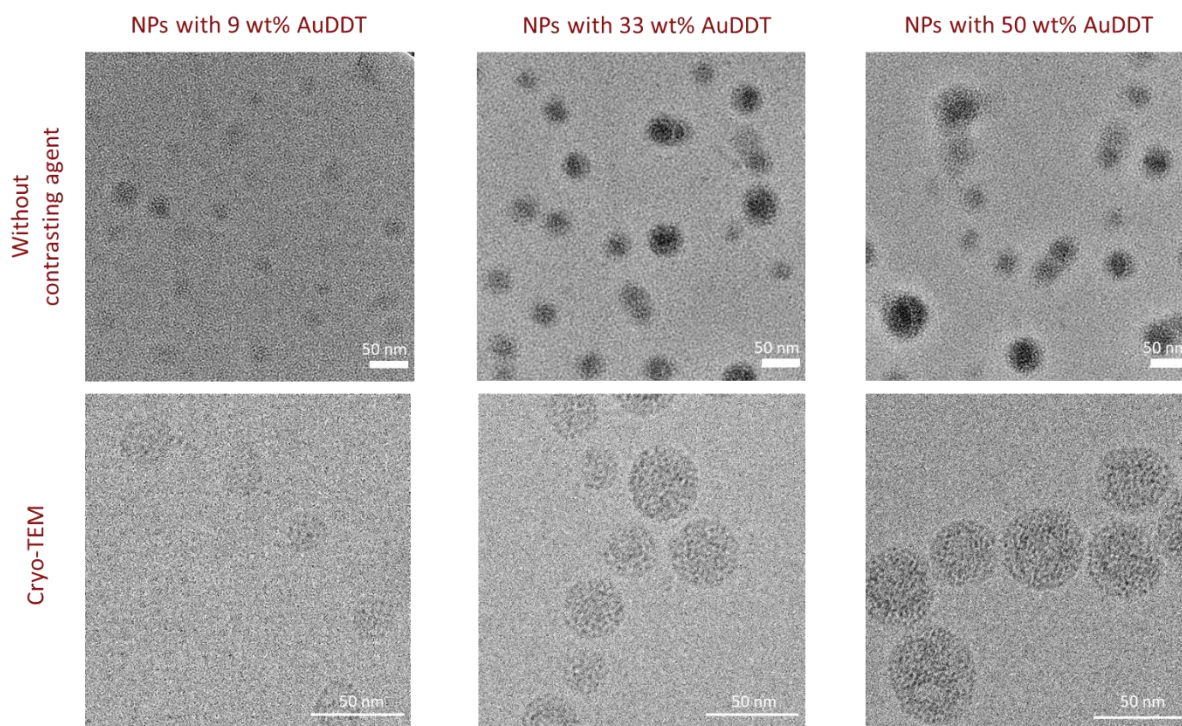


Figure 105: Transmission electron micrographs (top row) and cryo-TEM images (bottom row) of NPs

4.2 Photophysical characterizations

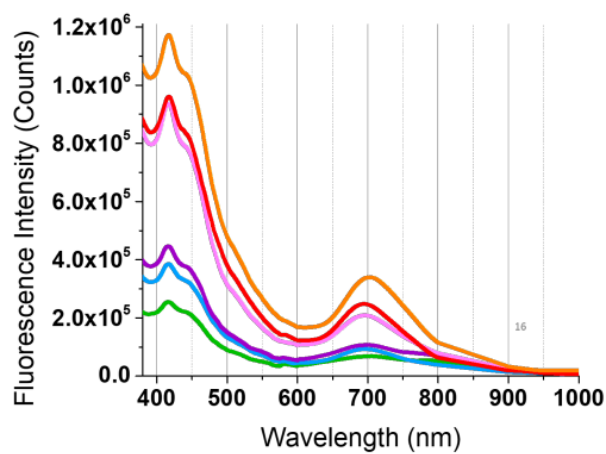


Figure 106: PL excitation spectra of AuPNPs. green 9 wt%, blue: 17 wt%, purple: 23 wt%, magenta: 33 wt%, red: 43 wt%, orange: 50 wt%

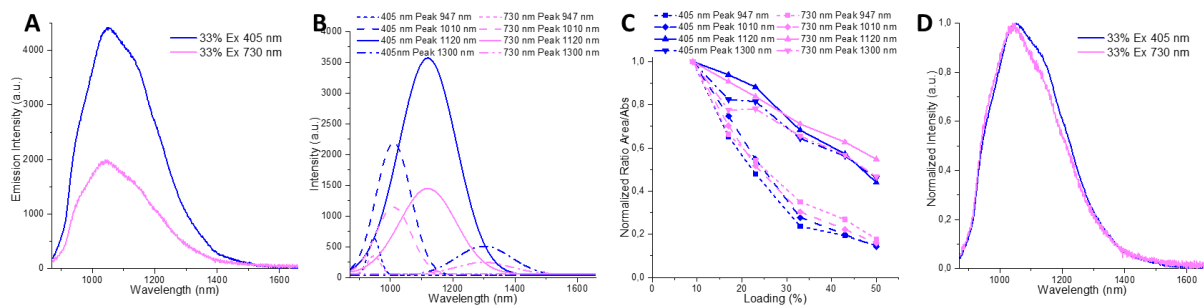


Figure 107: Influence of excitation wavelengths on the PL emission. Absolute A), normalized B), and deconvoluted C) emission spectra for NPs loaded with 33 wt% of AuNCs made from PEMA-COOH 5%. D) Normalized emission to absorption ratios for NPs loaded with different amounts of AuNCs excited either at 405 nm or 730 nm.

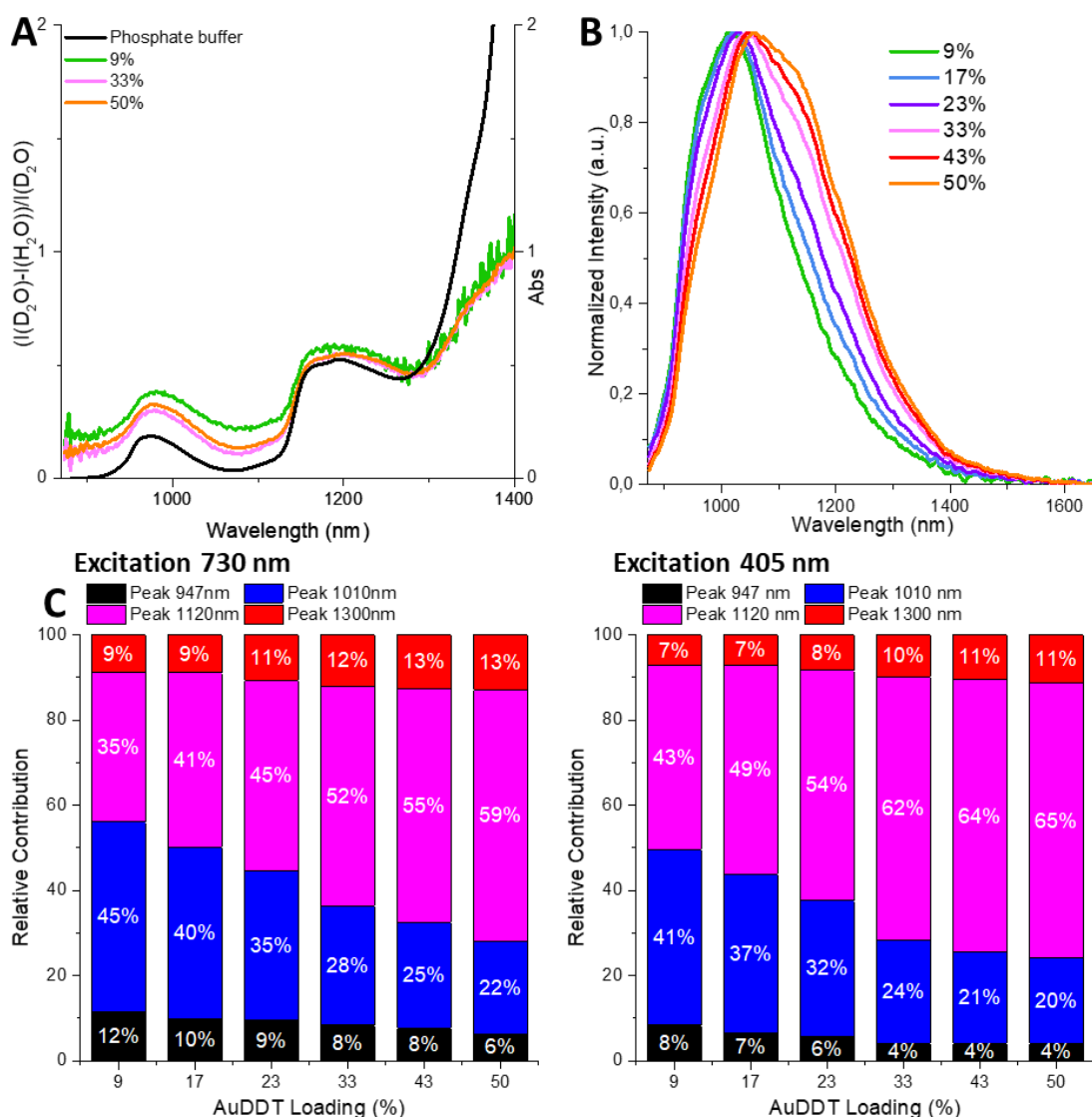


Figure 108: A) In black: absorption spectrum of phosphate buffer in the 900 – 1400 nm range. In color: Normalized difference between emission spectra recorded in D₂O and H₂O for solutions of PNPs loaded with different amounts of AuNCs ($\lambda_{ex} = 730$ nm). B) Normalized PL emission spectra of NPs loaded with different amounts of AuNCs ($\lambda_{ex} = 730$ nm). C) Relative contributions of the different peaks to the emission of NPs with different loadings of AuNCs as obtained after deconvolution ($\lambda_{ex} = 730$ nm or 405 nm)

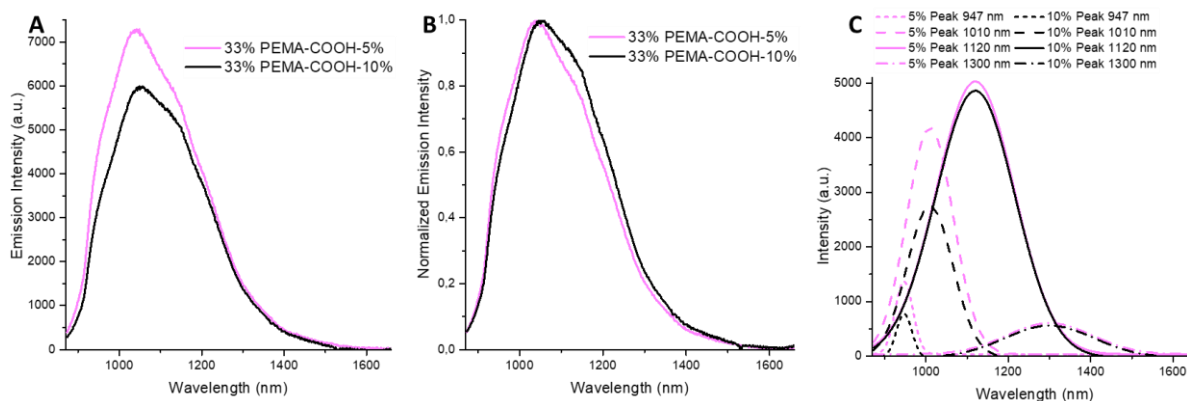


Figure 109: Influence of NP size on emission properties. A) Absolute, B) normalized, and C) deconvoluted emission spectra ($\lambda_{\text{exc}} = 730 \text{ nm}$) of NPs loaded with 33 wt% of AuNCs made from either PEMA-COOH 5% ($49 \pm 6 \text{ nm}$) or 10% ($25 \pm 3 \text{ nm}$)

Table 11 : Summary of characteristics of some NIR-II contrast agents in water

Contrast agent	Type	$\lambda_{\text{exc.}}$ (nm)	$\lambda_{\text{em.}}$ (nm)	ϵ ($\text{M}^{-1} \cdot \text{cm}^{-1}$)	QY ^a (%)	Brightness $\text{M}^{-1} \cdot \text{cm}^{-1}$ ^c	Ref.
ICG	dye	785	1000-1300	1.5×10^5	0.9	6.5×10^1	[31]
IR-E1050	dye	785	1000-1300	0.8×10^4	0.2	1.0×10^1	[31]
LZ-1105	dye	1021	1060	1.08×10^5	0.06	6.5×10^1	[32]
Gold nanorods	nanorods	680	990	1.5×10^4	8	1.2×10^3	[33]
TTQP	AIE based NPs	683	1078	3.29×10^4	8	2.7×10^4	[34]
Ag ₂ Se QDs	quantum dots	800-930	1000	5.5×10^4	23 ^b	1.2×10^4	[35a]
AuPNPs	nanohybrids	730	900- 1400	2.0×10^8	0.4	7.6×10^5	

a) In water, where not noted otherwise; b) in C_2Cl_4 ; c) calculated according to brightness = $\epsilon \times \text{QY}$.

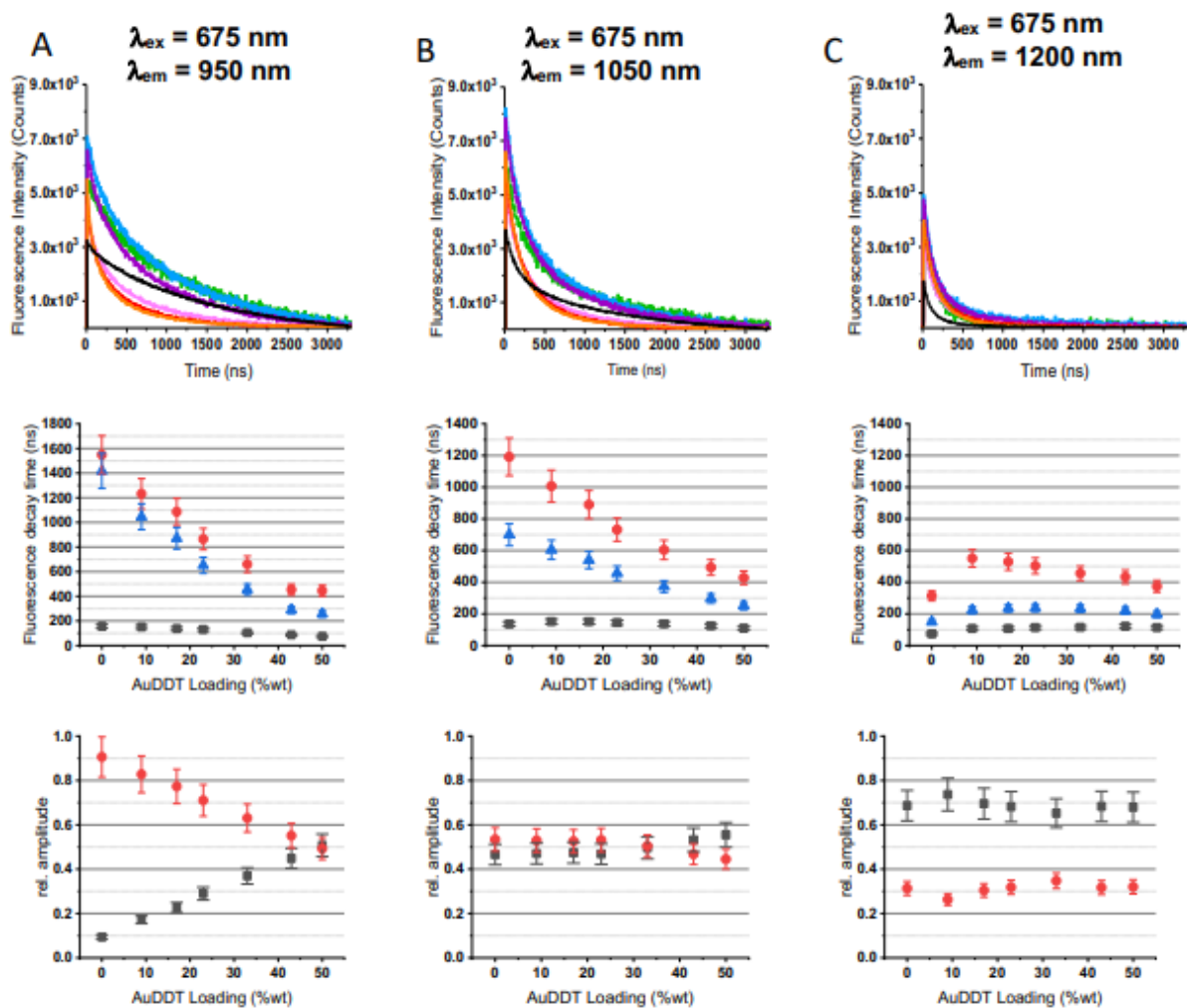


Figure 110: Intensity-comparable (the curves from each graph were normalized for similar excitation intensity and similar absorption and background was subtracted) PL decays (top row - black: AuNCs; orange: 50 wt%, red: 43 wt%; magenta: 33 wt%; purple: 23 wt%; blue: 17 wt%; green: 9 wt%), fit PL decay times (black: t_1 ; red: t_2 ; blue: t_3), and fit amplitude fractions (black: x_1 ; red: x_2) of AuNCs (in ethanol) and AuNC loaded NPs (in D2O) for excitation at 675 nm and emission at different wavelengths (A: 950 nm, B: 1050 nm, and C: 1200 nm)

4.3 Brightness evaluation for *in vivo* applications

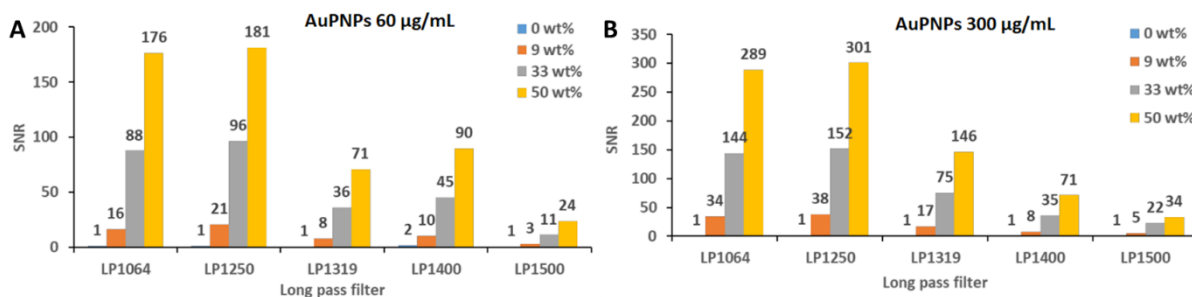


Figure 111: Signal-to-noise ratio (SNR) of AuPNP solutions A) 60 µg/mL and B) 300 µg/mL at different AuNC loadings. $\lambda_{ex} = 808$ nm.

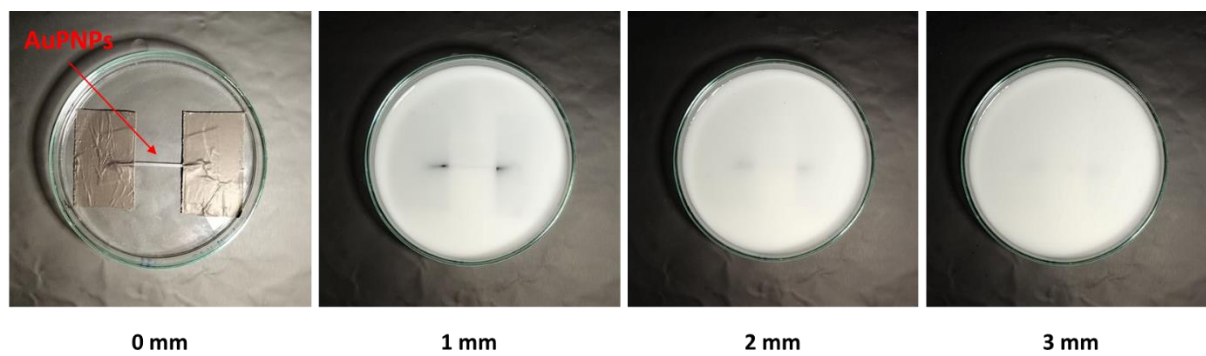


Figure 112: Protocol for capillary PL imaging of AuPNPs at different depth from 0 to 3 mm of 1% intralipid solution

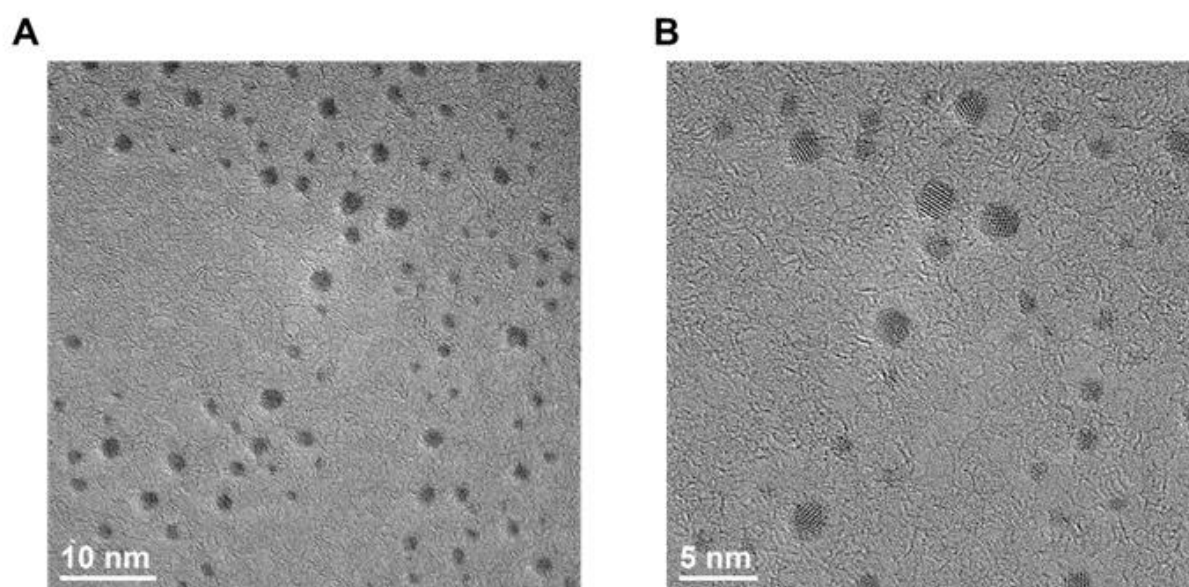


Figure 113: TEM images of hydrophilic AuNCs at two different magnifications for SPT

Table 12 : Characteristics of the different NPs used for SPT in SWIR

NP type	ϵ per NP elemental constituent [M ⁻¹ .cm ⁻¹] ^{a)}	Size [nm]	N: Number of AuNC/C per NP	$\epsilon*N$: extinction coefficient per NP (M ⁻¹ .cm ⁻¹) ^{a)}	QY (%)	Brightness (M ⁻¹ .cm ⁻¹) ^{a)}
AuNCs ^{b)}	4 050	2-3	1	4 050	6.5	263
AuPNPs	10 000 per AuNC	26 (diameter)	240	2.1E+6	0.65	1.4E+04
(7,5) SWCNTs	1 600 per C atom ^{c)}	400 (length) ^{d)}	39 000	6,5E+7	0.21 ^{e)}	1.3E+05

^{a)} excitation at 660 nm; ^{b)} in water from reference²⁵⁰; ^{c)} from reference²⁶⁸ for (7,5) nanotubes at their S_{22} transition (660nm) ^{d)} as a mean length value ^{e)} derived from reference²⁶⁹ after correction due to the use in this study of phospholipid-PEG as a biocompatible surfactant for SWCNTs instead of sodium cholate used in reference²⁶⁹ which generates brighter nanotubes.

4.4 Biointerfacing

The cytotoxicity and immunotoxicity experiments were made by Dr. X. Le Guével and Iryna Moskalevska in the IAB in Grenoble.

Cell culture: Both the J774.1A murine macrophage cell line (ATCC) and the NIH-3 T3 murine embryonic fibroblast cell line (ATCC) were cultured in DMEM supplemented with 10 % foetal calf serum at 37 °C, 5 % CO₂.

Cytotoxicity: Cytotoxicity was assessed by two different methods: PrestoBlue™ and lactic dehydrogenase (LDH) release assay. Cells were seeded in 96 well-plates at 3000 cells/well for J774.1A and 5000 cells/well for 3 T3. After 24 h, cells were treated with different concentrations of nanoparticles (5, 10, 25, 50 and 100 µg/mL for PEMA NPs) for 24 or 48 h. PrestoBlue™ (ThermoFisher cat n° A13261) was added at 1:10 and incubated for 3 h. The absorbance was read at 570 nm using a 595 nm reference with the Sunrise™ reader (Tecan). The released LDH from cells with damaged membranes was quantified using the CytoTox-ONE assay kit according to the manufacturer's protocol (Promega cat n° G7891). The fluorescence signal was read at 590 nm for an excitation at 560 nm with CLARIOstar® Microplate Reader (BMG Labtech).

Cellular uptake: The intracellular fate of the nanocarriers was studied by live-cell confocal microscopy. J774.1A cells were seeded at 5x10⁴ cells/mL in 4-well LabTeck and after 24 h incubated with Au-PEMA NPs (50 µg/mL) for 24 h. Actin was labelled with AlexaFluor488-phalloidine™ (ThermoFischer A12379). Cell membrane was labelled with Cell mask green

plasma membrane™ (Thermofisher cat n°: C37608). All confocal measures were done using an LSM710 NLO confocal microscope (Carl Zeiss) with an objective Plan APOchromat 20×/0.8NA in air and an objective Plan APOchromat 63×/1.4NA in oil. Near-infrared signal from Au NCs was captured using APD detector with a 405 nm excitation and a LP750 filter. Image treatment was done using the ImageJ software.

The gold uptake quantification was determined by ICP-MS. Cells were mineralized at atmospheric pressure in aqua regia (nitric acid and hydrochloric acid in a molar ratio of 1:3, for 48 h at room temperature. The mineralization is diluted to reach a concentration of 2 % of aqua regia before analysis. Standard solutions were prepared in aqua regia 2 % (v/v).

Immunotoxicity: J774.1A were seeded at 2.5×10^5 cells/mL. After 2 h, the cells were treated with different concentrations of nanocarriers (10 and 50 µg/mL) for 24 h. The nanocarrier exposed cells were stimulated with *E. coli* lipopolysaccharide (LPS) at 2 µg/mL for 24 h at 37 °C, 5 % CO₂. Macrophages were identified by the expression of markers CD11b (BioLegend cat n°: 101226) and F4/80 (BioLegend cat n°: 123152), and their activation was evaluated by the expression of I-A^b (BioLegend cat n°: 116410) and CD86 (BioLegend cat n°: 105008). Live cells were selected by Zombie Violet™ staining (BioLegend cat n°: 423113). Fluorescence labelled cells were analysed by flow cytometry using LSR II (BD Biosciences) using FCS Express V6 software (De Novo Software).

Cytokines production was measured in the supernatant of cell cultures using IL-6, TNF-α, and IL-10 mouse ELISA kits following the manufacturer's protocols (Thermofisher cat n°: 887064, 88732488, 88710588). The absorbance was read with CLARIOstar® Microplate Reader (BMG Labtech) at 450 nm using 570 nm as a reference. The NO production was evaluated by measuring the nitrite concentration in the cell culture supernatant using Griess assay. 50 µL of supernatant was incubated with the same volume of Sulphanilamide 1 % (w/v) (Sigma cat n°: S9251) for 10 min under shaking at 37 °C. 50 µL of *N*-alpha-naphthyl-ethylenediamine (NED) 0.1 % (w/v) (Sigma cat n°: 222488) was added and incubated for 10 min at 37 °C in the dark. The absorbance was read with CLARIOstar® Microplate Reader (BMG Labtech) at 540 nm. Production of ROS in the cell culture supernatant was estimated following the manufacturer's protocol (ENZO ROS/superoxide detection kit ref: ENZ-51010).

Statistical analysis: The values are presented by mean ± standard error of mean (SEM). At least three independent experiments were performed. Data were tested for normality and the appropriate statistic test was chosen. The statistical analysis was performed by Kruskal-Wallis test for multiple means comparisons of non-parametric data using GraphPad Prism software version 8.0. The probability was set at *p-value < 0.05, **p-value < 0.01, ***p-value < 0.001.

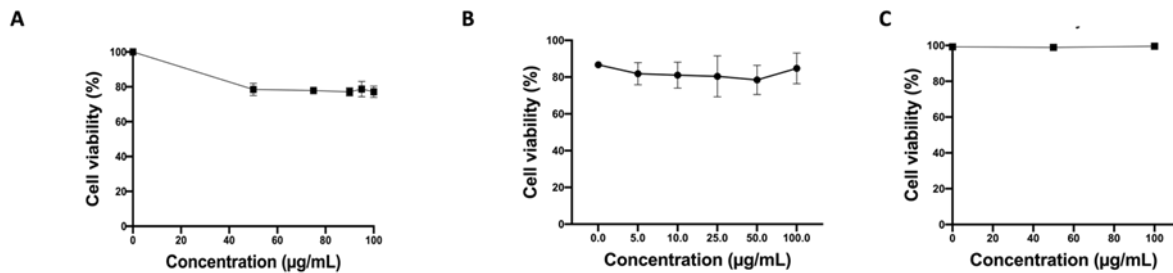


Figure 114: A) LDH assays on J774.1 cells at 24h with different concentrations of AuPNPs. B) PrestoBlue assays and C) LDH assays on NIH-3T3 cells lines at 24h with different concentrations of AuPNPs.

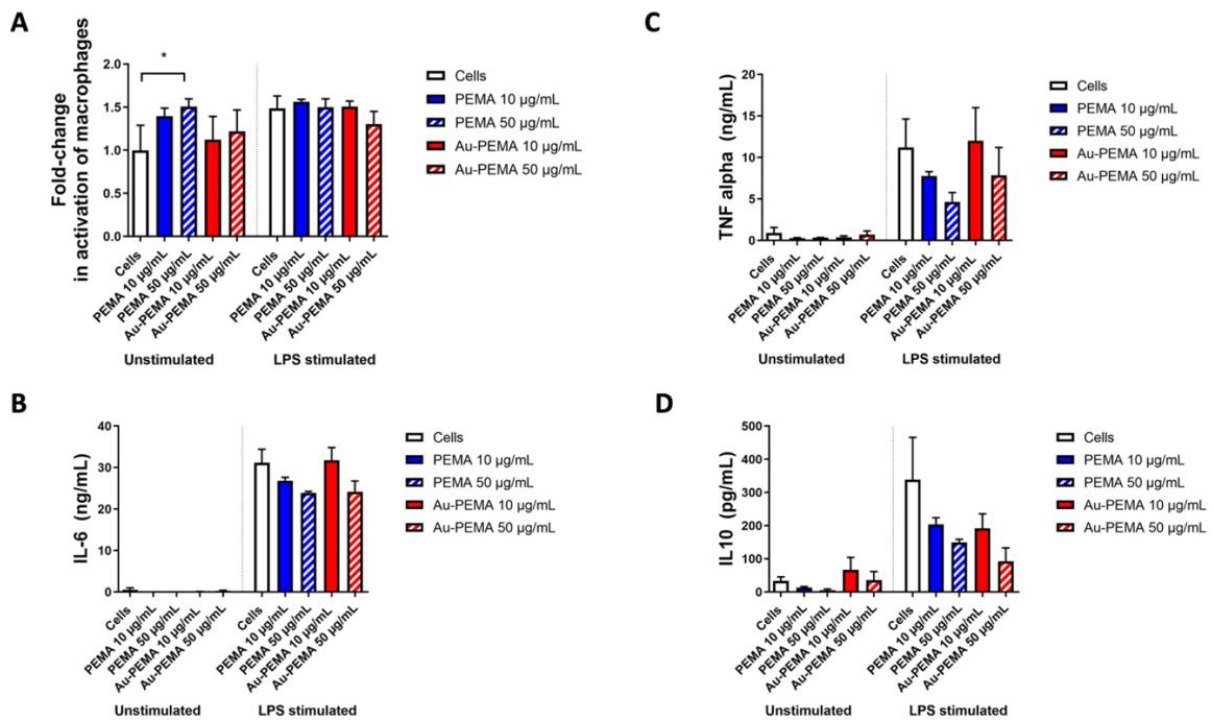


Figure 115: Effect of the Au-PEMA NPs on macrophage activation. A) Percentage of activated J774.1A macrophages determined as the percentage of cells expressing the CD86 and MHCII markers after a 24 h exposure to NPs, followed by a 24 h of LPS stimulation. Secretion of cytokines B) IL-6, C) TNF- α and D) IL-10 by J774.1A after a 24 h exposure to NPs, followed by a 24 h of LPS stimulation. Mean \pm SE. PEMA control groups n = 3; other groups n = 7-8.

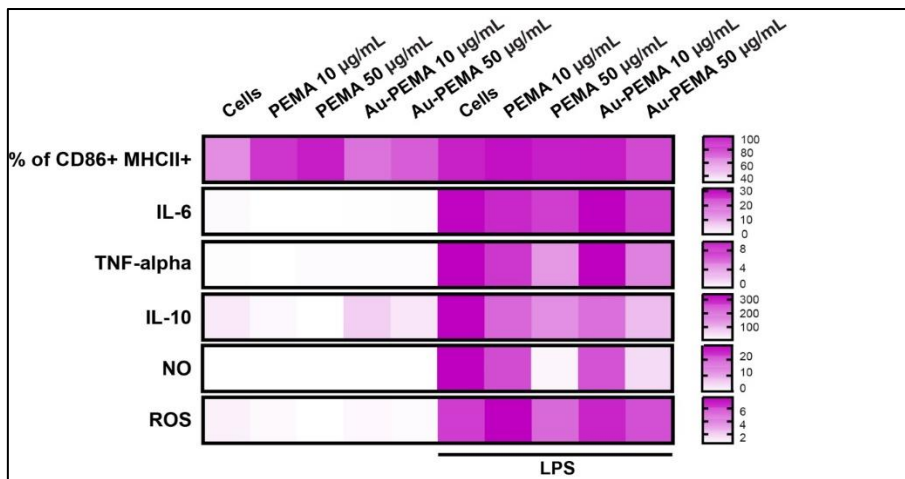


Figure 116 : Heat map representing effects of NPs on J774.1A macrophage activation, cytokines, NO and ROS production. Data are presented as mean value.

1. Introduction

L'utilisation de la luminescence en bioimagerie et détection est aujourd'hui largement répandue, car elle permet d'atteindre une haute résolution à différentes échelles, est rapide, sensible et spécifique¹. Augmenter le rapport signal sur bruit permet d'améliorer la qualité d'une image ou la limite de détection d'un objet. Pour y arriver la conception des sondes luminescentes joue un rôle clé. D'un côté, des sondes dont la brillance est très grande vont permettre d'augmenter le signal et ainsi démarquer l'objet d'intérêt au sein d'un milieu biologique. D'un autre côté, différents types de sondes utilisant des phénomènes de luminescence peu présents dans les milieux biologiques ont été développés, permettant une réduction du bruit de fond, notamment dû à l'autofluorescence. On peut citer notamment des nanoclusters d'or avec une émission dans la région proche infra-rouge II (NIR II ou SWIR, 1000 à 1700 nm)², des complexes de métaux de transition montrant des temps de vie de luminescence supérieurs à ceux des molécules biologiques³ ou encore des composés à base de lanthanides, en forme de nanoparticules ou de complexes, ayant une émission par conversion ascendante⁴. En revanche, la solubilité et la stabilité de ces émetteurs est généralement très limitée en milieu aqueux, ce qui freine grandement leur application dans des milieux biologiques complexes. Pour permettre le transfert de ces propriétés lumineuses en milieu aqueux, l'encapsulation de ces luminophores dans des nanoparticules polymériques (NP) peut être envisagée. La nanoprécipitation, qui utilise l'effet Ouzo⁵, est une méthode qui a été largement utilisée dans notre laboratoire avec des fluorophores organiques car elle permet de préserver le caractère lumineux de l'objet encapsulé et de découpler les propriétés de surfaces, régies elles par les polymères utilisés^{6,7}. De plus, il est possible de cette manière de rassembler un très grand nombre d'entités lumineuses dans un petit espace, augmentant drastiquement la brillance de l'objet final.

L'objectif de ma thèse a été de formuler des NP chargées en luminophores afin d'obtenir des nano-objets avec des modes de luminescence variés en milieu biologique, pour des applications en bioimagerie et biodétection. J'ai choisi trois types d'émetteurs très différents pour l'encapsulation : (i) des complexes de rhénium ayant de longs temps de vie de luminescence ainsi que (ii) des complexes nonanucléaires de lanthanides émettant en up-conversion et (iii) des nanoclusters d'or émettant dans le proche infrarouge.



Figure 117: Schéma de la nanoprécipitation

Lors de ces travaux de thèse, j'ai travaillé sur la synthèse et la caractérisation de NP luminescentes brillantes. Pour cela, je me suis intéressée aux concentrations en luminophores qu'il était possible d'encapsuler, ainsi que à l'optimisation de leur encapsulation. J'ai ensuite étudié les propriétés physico-chimiques telles que la taille ou les propriétés de surface des NP. J'ai aussi cherché à caractériser leurs propriétés photophysiques telles que l'absorbance, l'émission en conversion ascendante et/ou descendante ou leur temps de vie de luminescence. Enfin j'ai cherché à évaluer leur comportement et stabilité dans des milieux biologiques complexes.

2. Nanoparticules pour l'imagerie résolue dans le temps

Dans un premier temps, je me suis intéressée à un complexe de rhénium (noté Re(phen), Figure 118A), candidat potentiel pour l'imagerie à déclenchement périodique. On cherche dans ce cas à acquérir des images sur un temps correspondant au temps de vie de la sonde (quelques μs ou ms). Le déclenchement de l'acquisition est commencé après le temps de vie de fluorescence des milieux biologiques, supprimant ainsi l'autofluorescence (quelques ns). J'ai cherché à l'encapsuler dans des nanoparticules polymériques grâce à la nanoprécipitation (Figure 118B) et ai pu obtenir des NP dont les tailles ont été déterminées par mesure de la diffusion dynamique de la lumière (DLS). Ces NP peuvent être synthétisées avec de hauts taux de charge et le complexe est encapsulé dans des polymères avec des structures et propriétés variées. Ces variations dans la nature du polymère utilisé permettent de contrôler la taille des NP, indépendamment de la concentration en Re(phen) encapsulée (Figure 118C).

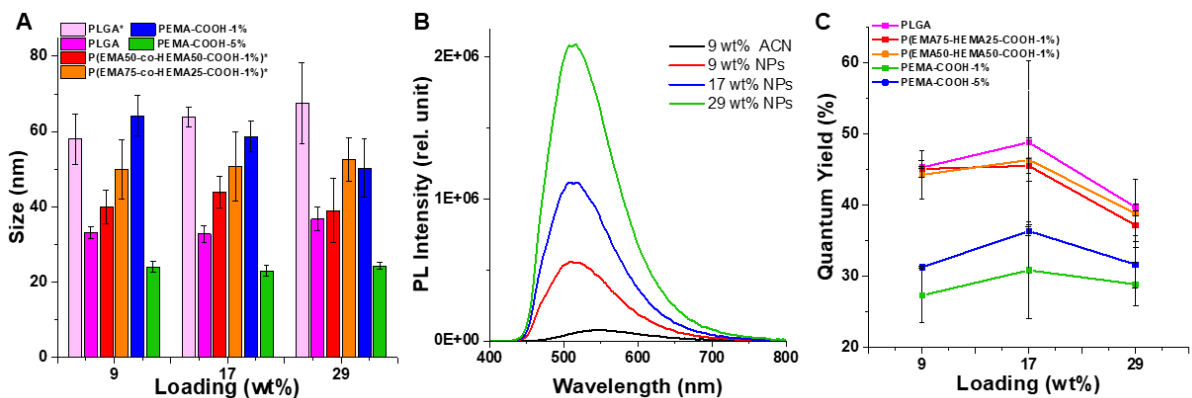


Figure 118 : A) Structure de Re(phen) et des polymères utilisés en nanopréciptation B) Schéma de la technique de nanopréciptation C) Taille des NP obtenues avec différents polymères et pour différentes concentrations en complexe de rhénium

Les NP obtenues présentent des spectres d'absorption et d'émission ayant une forme similaire à ceux du Re(phen) en solution organique. Le rendement quantique de Re(phen) a montré une nette augmentation lorsque ce dernier est dans les nanoparticules ce qui permet d'améliorer leur brillance. Des expériences de co-encapsulation utilisant le phénomène de transfert d'énergie par résonance de type Förster (FRET) dans les NP ont été réalisées. Pour cela, une concentration donnée de Re(phen) a été co-encapsulée avec différentes concentrations de 1,1-Dioctadecyl-3,3,3-tetraméthylindodicarbocyanine (abrégée Cy5) puis les spectres d'émission des différentes NP ont été réalisés (Figure 119A). On peut y voir une augmentation de l'efficacité du transfert d'énergie lorsque l'on augmente la quantité de Cy5, confirmant la co-encapsulation.

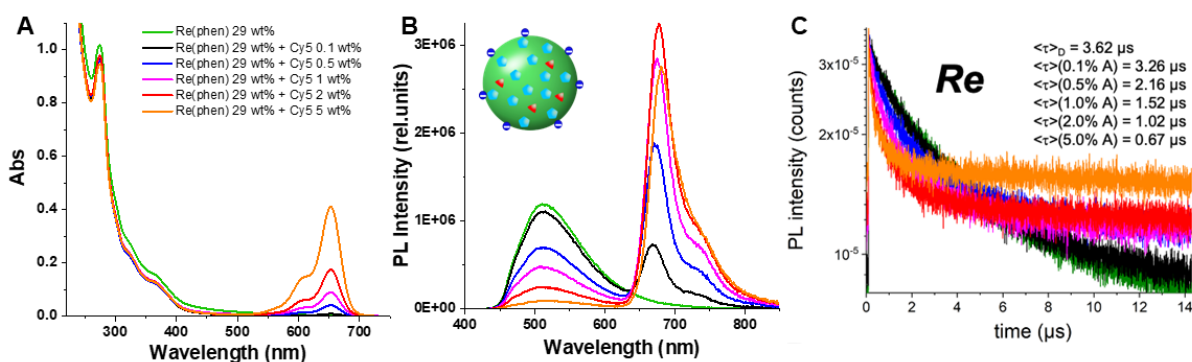


Figure 119 : A) Spectres d'émission, excitation 292 nm, et courbes de décroissance de temps de vie de fluorescence pour le canal B) de Re(phen) (515 ± 8 nm) et C) de Cy5 (700 ± 8 nm) des NP chargés avec Re(phen) et différentes concentrations en Cy5

Cette co-encapsulation a permis de déplacer la gamme d'émission des NP vers le proche infrarouge, région connue pour son autofluorescence réduite, donnant une propriété intéressante pour une application en milieu biologique de ces NP. La caractérisation photophysique des NP a été complétée par la mesure de leurs temps de vie de fluorescence. Le temps de vie de fluorescence de Re(phen) a pu être augmenté grâce à son encapsulation

dans les NP, passant d'environ 200ns à 3.6 μ s (Figure 119B). La bonne co-encapsulation avec la Cy5 a également pu être montrée avec ces analyses, les temps de vie de fluorescence de Re(phen) diminuant avec l'augmentation de la proportion en Cy5. Ce phénomène a également pu être observé lors de l'observation des temps de vie dans le canal de Cy5 (Figure 119C) et est le résultat d'une très grande efficacité du FRET entre les deux complexes. Ces différentes caractérisations mettent en avant la complexité de ces systèmes ainsi que les différents paramètres à prendre en compte leur design.

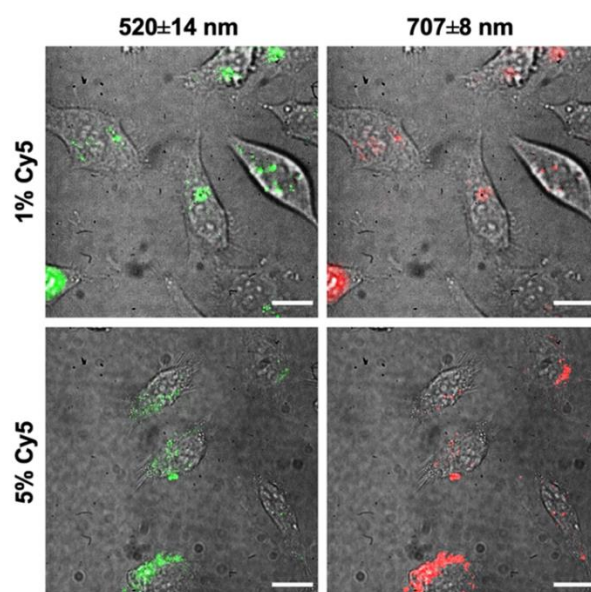


Figure 120: Imageire cellulaire de nanoparticules charges avec 29 wt% Re(phen) and 1 or 5 wt% Cy5. excitation (λ_{exc}) a 320 ± 20 nm et émission (λ_{em}) a 520 ± 14 nm (vert) pour le canal du donneur, et 707 ± 8 nm (rouge) pour le canal de l'accepteur. Les images montrent la superposition entre les images en lumière transmise et celles de fluorescence. Echelle 20 μ m

La grande réduction des temps de vie de fluorescence due à la co-encapsulation des complexes de rhénium avec des molécules de cyanine a empêché la possibilité de réaliser de l'imagerie à déclenchement périodique. Cependant, ces sondes ont pu être utilisées pour l'imagerie de cellules vivantes.

3. Nanoparticules pour l'imagerie en conversion ascendante

Knighton *et al.*⁸ ont développé des complexes contenant 9 atomes de lanthanides entourés de ligands acétylacétonates, exhibant un phénomène de conversion ascendante (up-conversion) moléculaire, c'est à dire l'émission d'une lumière dans le visible lorsqu'ils sont excités dans le proche infrarouge. Dans ce cas, les atomes d'ytterbium sont excités et transmettent leur énergie aux atomes de terbium selon un mécanisme coopératif, résultant en une émission du terbium dans le visible. Ces résultats ont pu être observés dans un solvant organique, cependant l'Up-Conversion moléculaire reste encore inédite en milieu aqueux, rendant

difficile son application en bioimagerie. L'encapsulation de ces complexes dans des NP a été proposée comme solution pour protéger ces complexes nona-nucléaires (notés Yb_5Tb_4) tout en transférant leurs propriétés lumineuses dans l'eau.

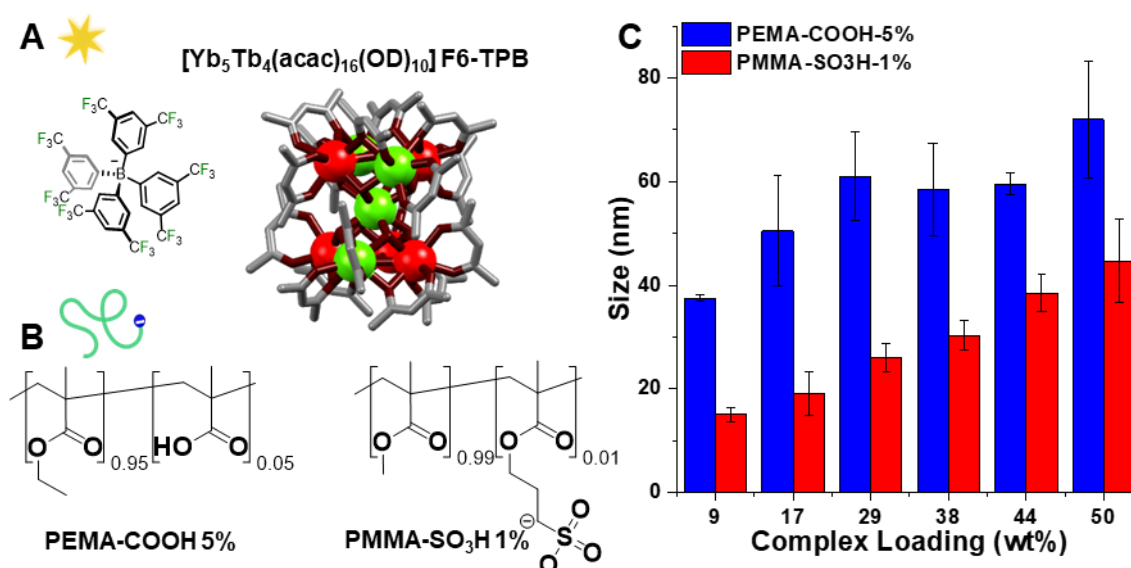


Figure 121: A) Structure du complexe étudié B) Structure des polymères utilisés C) Taille des différentes nanoparticules préparées

Le travail d'encapsulation de ces composés s'est révélée être un réel défi, qui a pu être relevé grâce à une équilibrage du caractère hydrophobe entre les polymères et le complexe à encapsuler. Notamment, l'échange du contre-ion hydrophile d'origine du complexe pour un contre-ion plus hydrophobe et encombrant a permis d'augmenter la quantité encapsulée, atteignant une concentration maximale de 38 % en masse. La taille des NP obtenues a été mesurée en DLS mais également en Microscopie Electronique à Transmission (TEM), montrant des objets entre 15 et 45 nm selon le polymère utilisé.

Les propriétés photophysiques de ces NP ont été étudiées en milieu aqueux deutéré et non deutéré. Les milieux deutérés ont des énergies vibrationnelles différents des non deutérés qui favorisent les transitions radiatives et augmentent ainsi la luminescence des NP. L'étude spectroscopique de ces systèmes a montré non seulement une différence d'intensité mais également de stabilité dans la luminescence de ces NP. En complément, une étude spectroscopique résolue dans le temps a permis d'analyser l'évolution des temps de vie de luminescence des Yb_5Tb_4 encapsulés en fonction de leur concentration en NP.

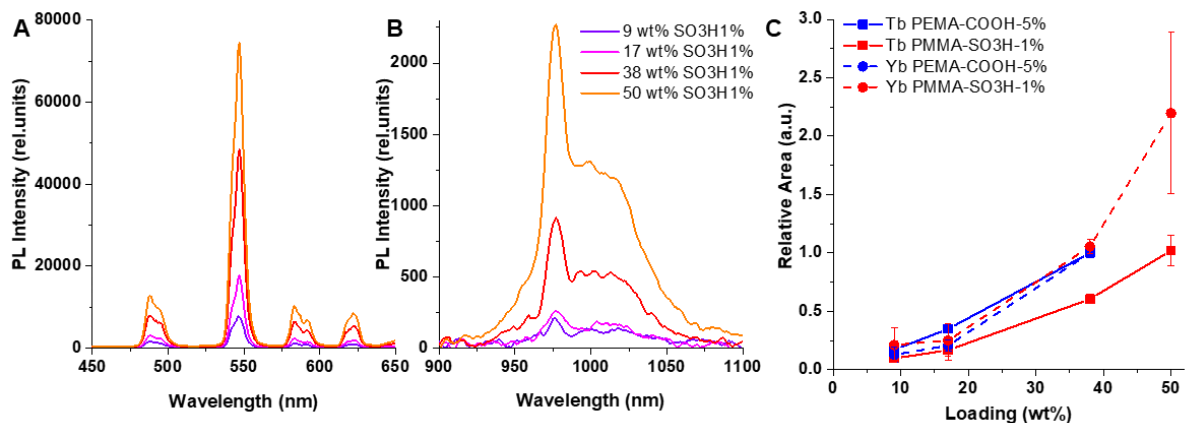


Figure 122 : A) Structure du complexe de lanthanides B) Image TEM (échelle 50 nm) et C) Spectre d'UC dans l'eau (orange) et l'eau deutérée (vert) des NP contenant 38 % Yb_5Tb_4 dans PEMA-COOH-5%, excitation 980 nm. D) Imagerie de fluorescence des cellules Hela marquées avec les NP contenant 38 % Yb_5Tb_4 dans PEMA-COOH-5%, excitation 980 nm. Echelle 20 μ m.

Avec une excitation à 980 nm, il a été possible d'observer de la photoluminescence dans le visible, confirmant la capacité des nanoparticules à émettre en up-conversion dans un milieu aqueux deutéré mais aussi protique. L'étude de l'évolution du signal de ces NP dans le temps a permis de montrer une augmentation du signal dans les premières heures après leur synthèse et également qu'il est possible de les stocker sur une durée de plusieurs semaines dans l'eau deutérée sans dégradation de leurs propriétés.

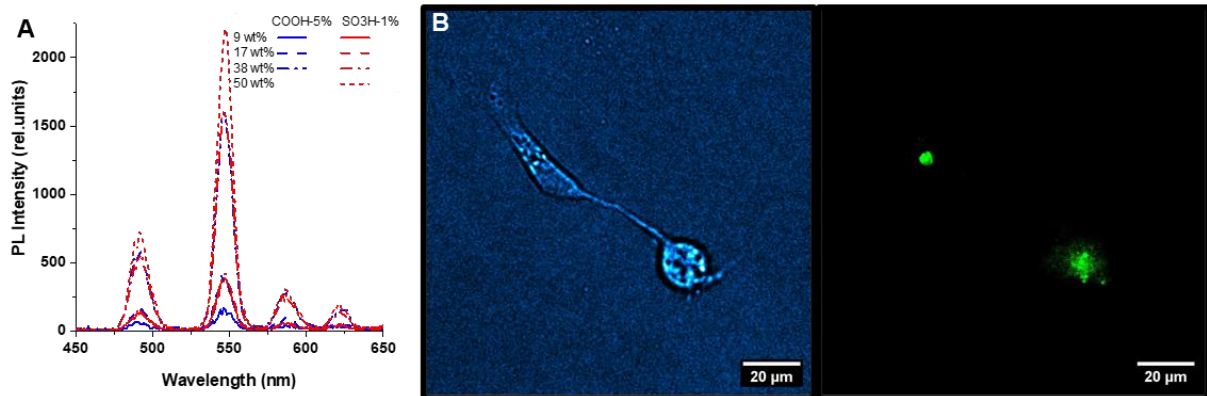


Figure 123: A) Signal d'up-conversion de différentes formulations de nanoparticules B) Images en lumière transmise (gauche) et de luminescence utilisant la conversion ascendante de cellules Hela incubées avec des nanoparticules

Afin d'attester leur potentiel pour être utilisés en bioimagerie, des cellules de type Hela ont été incubées avec les NP pendant 3h pour permettre leur endocytose. Les cellules marquées ont été observées en microscopie de fluorescence, utilisant un laser 980 nm comme source d'excitation et une fenêtre d'observation dans le visible et permettant ainsi de valider la possibilité d'imagerie en milieu biologique complexe.

4. Nanoparticules pour l'imagerie dans le proche infrarouge

Un troisième type d'imagerie permettant de limiter l'autofluorescence est l'imagerie dans le proche infrarouge, c'est-à-dire à des longueurs d'onde entre 1000 à 1700 nm. En effet, les tissus absorbent faiblement dans cette région du spectre lumineux, permettant une plus grande pénétration de la lumière incidente ainsi qu'une diffusion réduite de la lumière émise. Par conséquent, l'image obtenue en imagerie SWIR aura une meilleure sensibilité associée à une meilleure résolution. Un des défis dans le développement de cette imagerie est le manque d'agents de contrastes brillants en milieu aqueux⁹. Nous avons choisi d'utiliser des clusters d'or, connus pour leur biocompatibilité, comme émetteurs dans le SWIR. En effet, leur gamme de luminescence est dépendante du nombre d'atomes d'or qui les compose¹⁰ et peut être adaptée pour émettre jusque dans cette région.

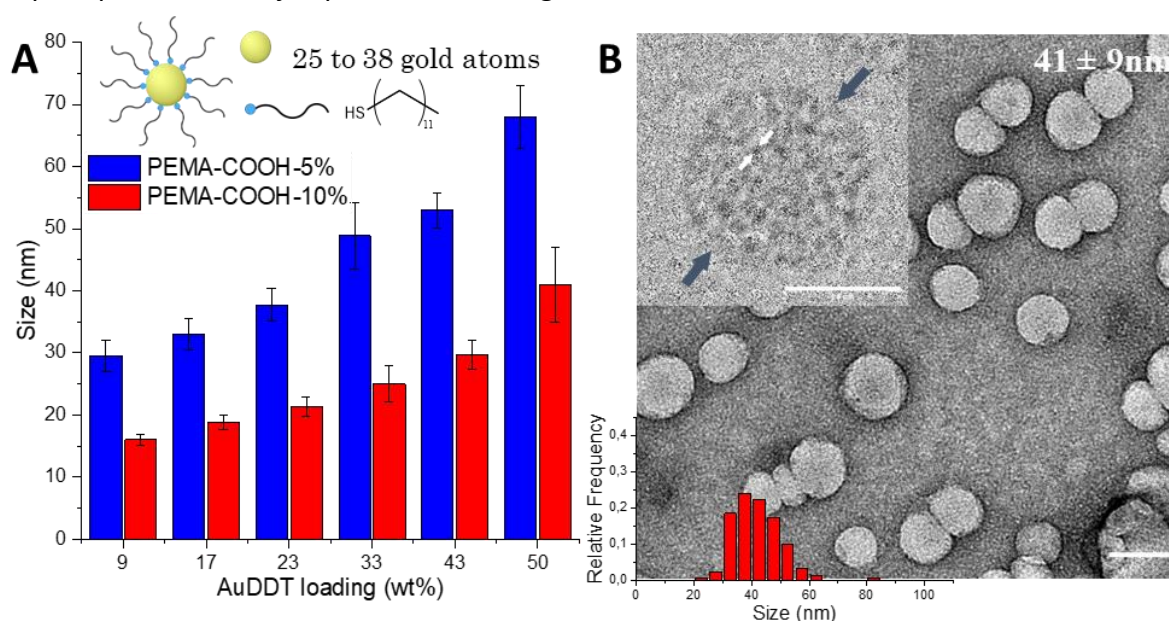


Figure 124 : Tailles mesurées en DLS des NP chargées en AuNC. En haut à gauche : schéma descriptif des AuNC. B) Images TEM (échelle 50 nm) et Cryo TEM (en haut à gauche, échelle 20 nm) des NP avec une charge de 33 %. C) Spectres d'émission des NP avec différentes concentrations en AuNC, excitation 730 nm. D) Luminescence (au-delà de 1064 nm) des NP dans un capillaire à différentes profondeurs en solution intra lipidique.

Nous avons cherché à encapsuler des nanoclusters d'or (AuNC) composés de 25 atomes d'or et capés de chaînes aliphatiques dans des NP polymériques. Leur taille moyenne étant de deux nanomètres, le challenge était de réussir à produire des NP avec une grande concentration en AuNC, tout en gardant une taille inférieure à une centaine de nanomètres. L'encapsulation des nanoclusters a pu être réalisée en atteignant une concentration de 50 % en masse, qui a été confirmée par des mesures en ICP et en absorbance, avec une taille d'environ 70 nm, d'après des mesures en DLS et ces valeurs ont pu être confirmées en TEM. Pour une concentration en AuNC donnée, il est possible de faire varier la taille des NP en jouant sur la chimie des polymères utilisés et notamment sur leur taux de charge. Il a été possible de synthétiser des NP d'environ 70 nm, contenant jusqu'à 14 000 nanoclusters. En cryo-TEM (Figure 124B, inset) il était possible d'observer les AuNC encapsulés au sein de la nanoparticule. A faible

concentration dans la NP, ces nanoclusters peuvent être distingués de manière individuelle et sont assez espacés, tandis qu'à haute concentration, les clusters sont plus nombreux et plus proches les uns des autres.

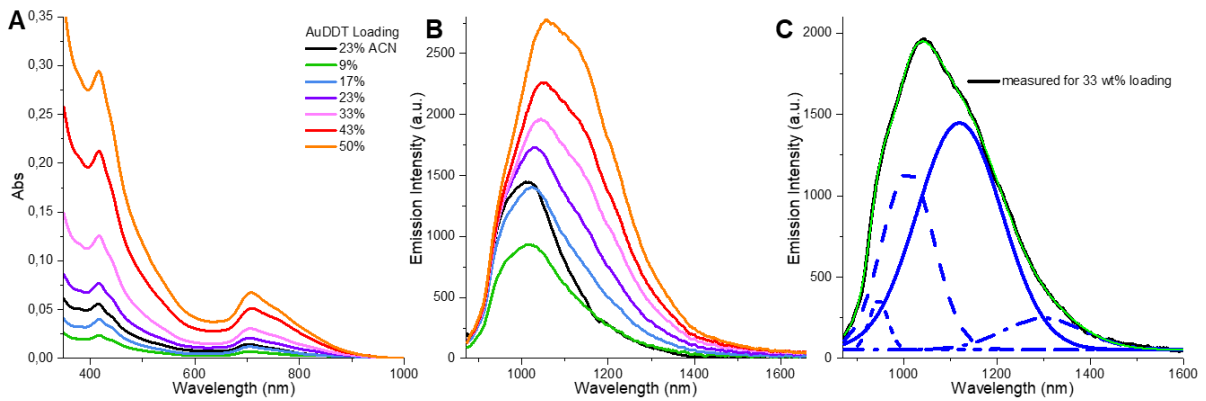


Figure 125: A) Spectres d'absorbance et B) spectres d'émission de nanoparticules chargées avec différentes concentrations en clusters d'or C) Déconvolution spectrale du spectre d'émission des nanoparticules

L'étude de leurs propriétés photophysiques a montré une émission entre 850 et 1400 nm, qui augmente avec la concentration en nanoclusters. La brillance de ces NP a pu être évaluée et est jusqu'à 100 fois supérieure aux autres agents de contrastes actuellement décrits dans la littérature. Un décalage vers les plus grandes longueurs d'onde de l'émission est observé lorsque la concentration en nanoclusters dans les nanoparticules est augmentée. Pour comprendre ce phénomène, une déconvolution spectrale a été appliquée sur tous les spectres d'émission et l'analyse de ces données a montré une perte de luminescence accrue pour les plus petites longueurs d'onde.

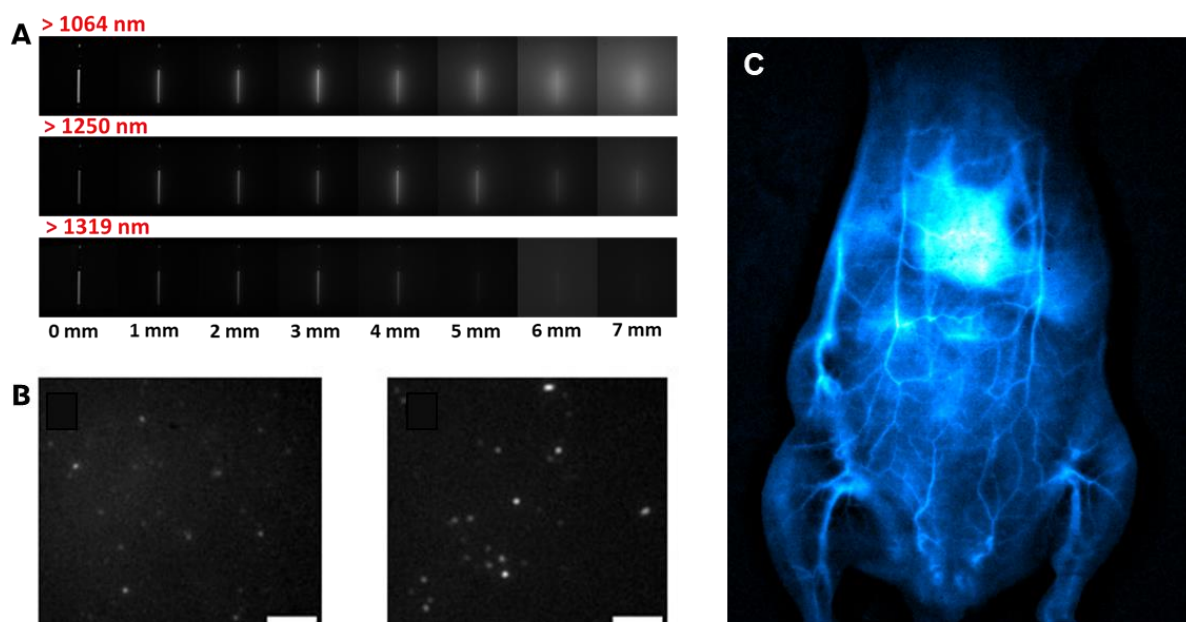


Figure 126 : A) Imagerie en phantom de capillaire sanguin B) Imagerie de superlocalisation des nanoparticules (gauche) et des nanotubes de carbone (droite) C) Imagerie in vivo des vaisseaux sanguins d'une souris

Pour confirmer leur potentiel pour l'imagerie SWIR, les NP ont été introduits dans un capillaire imitant un vaisseau sanguin et ont été recouverts de différentes épaisseurs de solution intra lipidiques. L'imagerie de ce capillaire a été réalisée dans le SWIR, la sensibilité et la résolution ont été estimées bonnes jusqu'à une profondeur de 4 mm. Ces NP ont également été étudiées par imagerie de super-résolution, qui permet d'observer les NP au niveau de la particule individuelle. Ces études ont donc permis de prouver la grande brillance des NP en solution mais aussi leur potentiel pour le suivi de particules uniques.

5. Conclusion générale

Au cours de mes projets de thèse, j'ai réussi à synthétiser des NP contenant des luminophores aux propriétés variées, que ce soit d'un point de vue physico-chimique ou photophysiques. Ces différents systèmes m'ont permis de mieux comprendre les différents défis qui se posent lors de la formulation des NP, ainsi que les outils à ma disposition pour encapsuler de manière efficace et homogène ces luminophores. La structure des polymères utilisés joue un rôle majeur dans la capacité d'encapsulation mais aussi dans les propriétés de surface des NP obtenues. Si certaines tendances générales peuvent être émises lors de l'étude de l'encapsulation des différents luminophores, c.-à-d. le lien taille des NP/ nombre de charge sur le polymère, il est à noter que le résultat de la combinaison polymère/luminophore reste unique, un même polymère ne donnant pas les mêmes NP selon ce qui est encapsulé.

Il a été possible de réaliser diverses caractérisations photophysiques des systèmes, leur absorbance, émission de luminescence ascendante ou descendante ou encore leurs temps de vie ayant été étudiés. Ces études ont permis de confirmer la capacité de la matrice polymérique à protéger les luminophores et à transférer leurs uniques propriétés en milieu aqueux. D'une part, les NP chargées en Re(phen) sont un excellent outil pour comprendre les enjeux et difficultés à relever pour obtenir des systèmes avec une brillance performante. D'autre part, les NP contenant les complexes de lanthanide sont le premier exemple reporté de système de conversion ascendante moléculaire à émettre en milieu aqueux. Finalement, il a été possible de repousser la limite de brillance dans le SWIR grâce à l'élaboration des NP chargées en AuNC. Des différents systèmes formulés, il a d'ores et déjà été possible de confirmer leur potentiel pour de l'imagerie en SWIR ou en up-conversion. La modification de leurs propriétés de surface pour améliorer leur stabilité et leur spécificité pour des applications en milieu biologique complexe est encore en cours d'amélioration.

Conception et caractérisation de nanoparticules polymériques luminescentes pour la bioimagerie et la biodétection

Résumé

La luminescence est très utilisée dans les domaines de la bioimagerie et la biodétection. L'utilisation d'agents de contrastes est nécessaire pour améliorer les performances de ce type d'imagerie et obtenir une sensibilité et une résolution satisfaisante. Un besoin important existe de développer des sondes plus brillantes ainsi que de lutter contre l'autofluorescence naturelle des milieux biologiques complexes. Pour cela l'utilisation de modes de luminescence absents des milieux biologiques est une attrayante solution. L'imagerie dans le proche infrarouge, la détection à déclenchement périodique ainsi que le processus de conversion ascendante sont les trois modes de luminescence choisis pour le développement de nouveaux agents de contraste. Dans ce contexte, la synthèse par nanoprécipitation de nanoparticules polymériques encapsulant de grandes quantités de luminophores a été réalisée. Une caractérisation physico-chimique ainsi que photophysique des sondes obtenues a permis de prouver l'apparition des modes de luminescence recherchés ainsi que montrer leur grande brillance. Des expériences en modèle phantom, en cellule ou encore *in vivo* ont mis en lumière leur potentiel pour la bioimagerie et la biodétection.

Mots clé : Nanoparticules polymériques, Luminescence, Bioimagerie

Abstract

Luminescence is widely used for medical application such as bioimaging and sensing. Contrasting agents are required to enhance the abilities of this type of detection, in order to obtain a satisfactory sensitivity and resolution. There is an important need to develop brighter probes to overcome the natural autofluorescence of complex biological media. To do so, alternative luminescent mode absent in biological media are an attractive solution. Shortwave Infrared imaging, Time-Gated detection and Up-conversion process are the three chosen modes for the development of new contrasting agents. In this context, the synthesis through nanoprecipitation of polymeric nanoparticles loaded with high amount of luminophores has been achieved. A physico-chemical study associated with a photophysical characterization of the obtained probes enabled to prove their ability to present the PL properties wanted. Experiment in phantom model, in living cells or *in vivo* enlightened the nanoparticles potential for bioimaging and biosensing.

Key words: Polymeric Nanoparticles, Luminescence, Bioimaging